RADIATIVE-CONVECTIVE PANELS AND A COOLING SYSTEM FOR CONCENTRATING SOLAR POWER

by

Ana Dyreson

A dissertation submitted in partial fulfillment of
the requirements for the degree of

Doctor of Philosophy

(Mechanical Engineering)

at the

UNIVERSITY OF WISCONSIN–MADISON

2018

Date of final oral examination: 8/23/18

The dissertation is approved by the following members of the Final Oral Committee:
Franklin Miller, Associate Professor, Mechanical Engineering
S.A. Klein, Professor Emeritus, Mechanical Engineering
Greg Nellis, Professor, Mechanical Engineering
Doug Reindl, Professor, Mechanical Engineering
Victor Zavala, Associate Professor, Chemical and Biological Engineering

ACKNOWLEDGMENTS

I am thankful to my advisors Franklin Miller and Sandy Klein who exemplify the dedication to students that every professor should have. Advice from staff at Dow Chemical and their financial support of this project ass invaluable. Outside advice from Mike Erbes (SimTech) and Ty Neises (NREL) was extremely critical to what I learned and accomplished. Solar Lab friends, past and present, make graduate school interesting and I am grateful for their company on this journey. I would be remiss if I didn't recognize my immediate and extended family that made finishing a PhD with a tiny baby possible - especially, of course, Devon.

To baby Elden. Whether you are an artist or an astronaut, you can go to school wherever you want as long as it is the University of Wisconsin.

CONTENTS

Contents ii

List of Tables ix

List of Figures xii

Abstract xvii

1 Introduction 1
- *1.1 CSP and the energy-water problem* . . . 1
- *1.2 Nighttime radiative-convective panels for solar power plant cooling* . 6
- *1.3 Initial technical assessment* . . . 6
- *1.4 Initial cost estimations* . . . 8
- *1.5 Research Goals* . . . 12

2 Literature Review 14
- *2.1 Radiative-convective panels* . . . 14
- *2.2 CSP cooling* . . . 40

3 Heat transfer model of radiative-convective panels 55
- *3.1 Modeling heat transfer from radiative-convective panels* . . . 55
- *3.2 Results* . . . 70

4 Rankine power cycle modeling 100
- *4.1 Modeling a benchmark power cycle with IPSEpro* . . . 100
- *4.2 Results and validation for benchmark cycle* . . . 123
- *4.3 Modeling a custom power cycle* . . . 129
- *4.4 Results for custom power cycles* . . . 136
- *4.5 Approximation of Power Cycle in System Adviser Model* . . . 143

5 CSP with nighttime cooling assessment 152

5.1 Modeling the radiative-convective CSP cooling system in SAM . . . 152
5.2 Implementation of radiative cooled and air-cooled plant models . . . 160
5.3 Results . . . 178

6 Conclusion 190
6.1 The potential for radiative cooling of CSP power plants . . . 190
6.2 Future Work . . . 191

A Appendix: Power cycle regression coefficients 194

B Appendix: Feasibility study paper 197

C Appendix: Radiator modeling paper 223

Bibliography 238

NOMENCLATURE

α	thermal diffusivity m/s^2
Δh_s	isentropic enthalpy change, expansion from bowl to ELEP J/kg
$\Delta h_{s,x}$	isentropic enthalpy change, expansion from inlet to exhaust J/kg
ΔT_{CW}	temperature drop of cooling water at design C
$\dot{m}$	flow rate kg/sec
$\dot{m}^*$	dimensionless mass flow rate -
$\dot{m}_i$, $\dot{m}_o$	mass flow rate on tube side (i), shell side (o) kg/sec
$\dot{m}_{cond}$	condenser mass flow rate kg/sec
$\dot{m}_{HTF}$	mass flow rate of HTF kg/sec
$\dot{m}_{tube}$	mass flow rate in tube kg/sec
$\dot{Q}$	thermal input MWth
$\dot{q}_{cond}$	rate of conduction heat transfer from one node to another in x or y direction, W
$\dot{q}_{conv,int}$	rate of internal convection heat transfer from the fluid in tube, W
$\dot{q}_{conv,tube}$	rate of convection heat transfer from the surface of the tube, W
$\dot{q}_{conv}$	rate of convection heat transfer from the the panel to surroundings (top, bottom), W
$\dot{q}_{fluid}$	rate of change of internal energy of the fluid, W
$\dot{Q}_{in}$*	dimensionless thermal input -
$\dot{Q}_{net}$	net heat transfer rate W/m^2
$\dot{q}_{rad,tube}$	rate of radiation heat transfer from the surface of the tube, W
$\dot{q}_{rad}$	rate of radiation heat transfer from the the panel to surroundings (top, bottom), W
$\dot{Q}_{rej,design}$	power cycle heat rejection at design MWth
$\dot{W}$	power output MW
$\dot{W}^*$	dimensionless power output -
ϵ	emissivity - (b back, t top, g ground)
ϵ_s	effective emissivity of the sky
ϵ_{HX}	heat exchanger effectiveness -

ϵ_{rad}	radiator effectiveness -
η_{design}	power cycle design point efficiency -
η_{exp}	isentropic expansion efficiency -
η_{PV}	PV panel efficiency -
η_{tot}	isentropic efficiency including inlet to exhaust-
κ	ratio of tube and shell side mass flow rates -
μ	viscosity $kg/m-s$
ν	kinematic viscosity m/s^2
ρ	density kg/m^3
σ	Stefan-Boltzmann constant W/m^2-K^4
$\tau\alpha$	transmittance-absorbance product -
τ_s	shear stress Pa
A	area m^2
A_c	area of panel m^2
A_i,A_o	heat transfer area of tube (i) and shell side (o) m^2
A_{field}	total surface area of radiator field panels m^2
A_{row}	total surface area of row of radiative panels connected in series m^2
A_{solar}	total surface area of heliostats m^2
C	constant for Zukauskas correlation
C_2	ratio of maximum to average velocity on shell side -
C_f	local friction factor -
C_i, C_o	constant -
c_p	specific heat J/kg-K
C_y	cost in year y $
D	tube diameter m
DNI	direct normal irradiance W/m^2
dx	node width in lateral direction, m
dy	node width in flow direction, m
F	fin efficiency -
f	friction factor -
F'	collector efficiency -

F_R	collector heat removal factor -
F'_R	collector-heat exchanger factor -
f_{cloud}	cloudiness fraction -
f_{pv}	convection factor for PV panel -
F_W	correction factor for condenser water temperature (also M material, C cleanliness)-
h	convection coefficient W/m^2-K ($\bar{h}$ is average)
H_0	Constant for SCC extraction line for low pressure turbine Btu/lb
h_c	convection coefficient W/m^2-K (t top, b bottom)
h_i, h_o	internal convection in tube side (i) and shell side (o) W/m^2-K
h_r	radiation coefficient W/m^2-K (t top, b bottom)
h_{bowl}	enthalpy at turbine bowl J/kg
h_{ELEP}	enthalpy at expansion line end point (ELEP) J/kg
h_{out}	enthalpy after exhaust J/kg
$height_c$	height of rectangular channel m
hrs_{CTES}	hours of cold side storage -
hrs_{night}	hours of shortest night in year
I_T	plane-of-array radiation W/m^2
k	conductivity W/m-K
k_i,k_o	fluid conductivity on tube (i) and shell side (o) W/m-K
L	length m
L_c	characteristic length m
$L_{section}$	length of individual panel section m
m_z	constant for Zukauskas correlation
$m_{storage}$	mass of water storage kg
N	project lifetime for economic analysis in years
n	number of tubes in parallel -
N_p	number of rows in parallel in field -
Nu	Nusselt number - (Nu_x is local value, $\bar{Nu}$ is average)
Nu_i,Nu_o	Nusselt number of tube (i) and shell side (o) -
p	pressure -

P_c	Cycle condensing pressure Pa
PPT	pinch point temperature difference C
Pr	Prandtl number -
Pr_i, Pr_o	Prandtl number on tube side, shell side -
Pr_s	Prandtl number evaluted at surface temperature -
Q_u	heat transfer rate W
Q_y	energy produced in year y kWh
$Q_{r,t}$	Radiation heat flux from the top of panel W
R_o	Constant for SCC extraction line for low pressure turbine 1/K
Re	Reynolds number -, (Re_x is local value)
Re_i	Reynolds number on tube side (ref reference condition) -
$Re_{D,max}$	Reynolds number evaluated at maximum velocity on shell side -
S	sky radiance W/m^2
s	entropy J/kg-K
S_{down}	downward longwave radiation W/m^2
T	temperature K
t	hours after midnight, hr
$T*$	approximate adiabatic temperature, i.e. adiabatic temperature, K
T^*_{in}	dimensionless HTF inlet temperature -
T_a	ambient air dry bulb temperature K
T_g	temperature of ground K
T_p	Plate temperature K
T_s	effective sky temperature K
T_{ad}	exact adiabatic temperature K
T_{cold}, T_{warm}	cold tank temperature, warm tank temperature, design value (o), initial value (i) C
T_{CW}	cooling water temperature C
$T_{dp,C}$	ambient dew point temperature C
T_f	fluid temperature K (i inlet, o outlet)
$T_{i,j}$	node temperature K
T_{pv}	temperature of PV panel K

th	plate thickness m
TI	Turbulence intensity of wind
u	wind speed m/s
u_m	mean velocity m/s
u_∞	free stream velocity m/s
U_{cond}	condenser conductance W/m^2-K
U_L	loss factor W/m^2-K
$U_{x,i}$	uncertainty in variable x_i, units same as x_i
UA	conductance-area product (spht superheater, $evap$ evaporator, $econ$ economizer, FWH feedwater heater, FWH_{cond} condensing section of feedwater heater, ref reference condition) W/K
V	velocity m/s
v_{tube}	velocity in tube m/s
W	tube-to-tube spacing m
w_c	width of rectangular channel m
x	position from edge of plate m
Y	dimensionless response variable -
Y_{INT}	interaction effect on variable Y -
Y_{ME}	main effect on variable Y -

LIST OF TABLES

1.1 Summary of plant size parameters for 250 MW CSP plant 8
1.2 Estimated component costs for 250 MW CSP plant (million $) 10

2.1 Effect of convection uncertainty on annual cooling. 31
2.2 Radiative cooling heat fluxes from literature. 35

3.1 Sign of loss coefficient depending on reference temperature and ambient. 64
3.2 Geometry and wind speed conditions tested for radiators. 69
3.3 Conditions and assumptions made for comparison of radiator models . 70
3.4 Physical characteristics of Lordan LSC-F collector used in experiments 72
3.5 Uncertainties included in experimental design. 75
3.6 Model results for baseline condition 84
3.7 Contributions to total uncertainty in $T_{f,o}$ =317.32 of 0.31°C. 85
3.8 Contributions to total uncertainty in ΔT =1.98 of 0.22°C. The inlet temperature has little effect on the temperature drop. 85
3.9 Contributions to total uncertainty in Q =829.9 W of 82.5 W. The mass flow rate has little effect on overall heat transfer. 85

4.1 Key cycle design outputs for comparison. 123
4.2 The design values of the three main factors for the low pressure cycle. . 131
4.3 Series of cycle simulations required to represent cycle fully using two factor interactions. A variable can be set at its low value (-), design point (0) high value (+), or varied from low to high. 144
4.4 The range of the three factors are shown; note that the pressure limitations used for the interaction effect with temperature and pressure in the high pressure cycle is 2.75 - 7.75 in Hg even though the correlations are used over the complete range. 149

4.5 The error between the full IPSE cycle runs for all cases available and the approximations are shown for normalized gross power. Including the interaction effects reduces the error. 151

5.1 The inputs required in SAM to run the custom radiative cooled cycle are shown along with any nomenclature used in this document and clarifying notes. 155
5.2 Three SAM cases for solar power tower plant configurations were tested for both radiative- and air-cooled plants. 160
5.3 Key power cycle inputs for SAM are provided that differentiate the two systems. The high and low backpressure cycles are those described in IPSEpro modeling in Chapter 4. 161
5.4 24 different designs are shown. The performance of eight different radiator designs (A-H) was tested using 2015 Las Vegas weather data. All 24 designs were used to test the effectiveness at design conditions. The range of tube velocities is 0.25-1.37 m/s (0.8-4.5 ft/s). 163
5.5 Final dimensions. 166
5.6 For each plant, given the peak summer storage requirement, the radiator multiplier is shown which provides reasonable field performance. . . . 167
5.7 Flow requirement and pressure drop examples. 170
5.8 The pumping power requirement for the smallest system is summarized. 171
5.9 Summary of hourly data before quality control. 174
5.10 Statistical summary of the hourly input data for Desert Rock Station from 2015, after to infilling the missing hourly data. 174
5.11 The trade off between pumping and performance is tested in annual simulations. The LCOE is reduced by 0.01 cent/ kWh. 189

A.1 Effects of temperature for the low pressure cycle. 194
A.2 Effects of temperature for high pressure cycle. 194
A.3 Pressure effects for the low pressure cycle for min pressure to 16090 Pa. 195
A.4 Pressure effects for the low pressure cycle from 16090 Pa to max pressure. 195
A.5 Pressure effects for the high pressure cycle. 195

A.6 Mass flow effects for the low pressure cycle. 196
A.7 Mass flow effects for high pressure cycle. 196

LIST OF FIGURES

1.1 Water consumption of different generators. 2
1.2 Thermoelectric cooling constraint map of US. 3
1.3 CSP plant cooling systems installed since 2007. 4
1.4 Cost breakdowns of air- and radiative-cooled parabolic trough CSP. . . 11
1.5 Cooling system cost for parabolic trough. 11

2.1 Duration curves of unmet cooling load based on convection uncertainty. 31
2.2 Distribution of wind speeds as measured in Las Vegas, Nevada. 33
2.3 Eicker and Dalibard [2011] heat fluxes. 36
2.4 Comparison of low water use cooling options. 47

3.1 Panel cross section with temperature profile. 56
3.2 Roll bond cross section with inset. 65
3.3 Finite differences model. 66
3.4 Example of finite differences model. 71
3.5 Ambient conditions. 72
3.6 Comparison of wind measurement and convection uncertainty, high measurement uncertainty. 77
3.7 Comparison of wind measurement and convection uncertainty, low measurement uncertainty. 78
3.8 The measured inlet temperature, measured outlet temperature, and modeled outlet temperature are provided. 79
3.9 Results of model validation 80
3.10 Results of model validation by radiation versus convection. 81
3.11 Roll bond geometry as modeled 82
3.12 Increasing uncertainty in temperature drop with increasing wind speed. 86
3.13 Increasing uncertainty in temperature drop with increasing inlet temperatures and wind speeds. 87
3.14 Fraction of heat transfer by radiation versus inlet temperature. 88

3.15 The fraction of heat transfer by radiation varies with ambient conditions and inlet temperature; here the radiation fraction is shown for a medium wind speed of 3.1 m/s. 89
3.16 The fraction of heat transfer by radiation varies with ambient conditions and inlet temperature; here the radiation fraction is shown for a low wind speed of 1.5 m/s. 90
3.17 The rate of change of the radiation heat transfer with respect to inlet temperature varies with the cube of inlet temperature. A surface area A of one is assumed. 91
3.18 The rate of change of the convection heat transfer with respect to inlet temperature varies depends strongly on wind speed. A surface area A of one is assumed. 91
3.19 Fraction of radiation by heat transfer for simple annual model. 93
3.20 Comparison of radiator models for 17 different designs. 96
3.21 For 17 different radiator designs, the error in the heat transfer compared to the numerical model is plotted against the ratio F_R. 97
3.22 Comparison of radiator models using annual simulations. 98

4.1 The process diagram and results for a water-cooled 100 MW power block and HTF delivery based on example plant per Yildiz. 103
4.2 The process diagram shows the specific inputs values used for each component. 104
4.3 Exhaust loss curve example. 108
4.4 Condenser in IPSE. 109
4.5 Closed feedwater heater. 110
4.6 Open feedwater heater. 111
4.7 Detail of HTF loops and solar steam generator train and reheater from IPSE process model. 111
4.8 The gross efficiency is maximum at full load and decreases towards lower load cases and higher cooling water temperatures. 125

4.9 The condensing pressure decreases according to cooling water temperature and load fraction. 126
4.10 The exhaust losses reflect the exhaust loss curve for the last stage turbine blade. The last stage turbine blade was chosen so that at 28 °C cooling water temperature and 100 % load, exhaust losses are near the minimum level. 127
4.11 The HTF mass flow rate is directly related to the load fraction. 128
4.12 The HTF return temperature is related to the load fraction and the system is controlled to maintain a minimum of 250 °C temperature at low loads. 129
4.13 Selection of turbine for exhaust losses. 131
4.14 IPSE model for lower pressure cycle. 133
4.15 IPSEp model of high pressure cycle. 134
4.16 IPSE model for high pressure cycle with ACC model. 135
4.17 The last stage leaving velocity is exceeds 426 m/s only for high load cases (>1) and low condensing pressures for the 5.16 m^2 turbine at the design HTF temperature of 566 C. 137
4.18 The last stage leaving velocity exceeds 426 m/s for the lower condensing pressures for the 3.06 m^2 turbine at the design HTF temperature of 566 C. 138
4.19 The exhaust losses at the 5.16 m^2 turbine for HTF delivery temperature of 566 °C are shown for a range of mass flow rate (loads) and condensing pressures. 139
4.20 The exhaust losses at the 3.06 m^2 turbine for HTF delivery temperature of 566 °C are shown for a range of mass flow rate (loads) and condensing pressures. 139
4.21 The efficiency with the 5.16 m^2 turbine for HTF delivery temperature of 566 °C are shown for a range of mass flow rate (loads) and condensing pressures. 140
4.22 The efficiency with the 3.06 m^2 turbine for HTF delivery temperature of 566 °C are shown for a range of mass flow rate (loads) and condensing pressures. 140

4.23 The two cycles have different efficiency profiles at full load and 566 °C HTF temperature. 141
4.24 The efficiency profiles of both cycles where y-axis starts at 0.35 efficiency to emphasize the differences between the cycles. 141
4.25 The condensing pressure effect for a simple Rankine Cycle with constant turbine efficiency for hot side temperature of 566 °C is shown. 142
4.26 The main effects of pressure for the low pressure / 5.16 m^2 cycle. . . . 146
4.27 The main effects of temperature for the lower pressure/ 5.16 m^2 cycle. . 146
4.28 The main effects of mass flow for the low pressure/ 5.16 m^2 cycle. . . . 147
4.29 The main effects of pressure for the high pressure/ 3.06 m^2 cycle. . . . 147
4.30 The main effects of temperature for the high pressure/ 3.06 m^2 cycle. . 148
4.31 The main effects of mass flow for the high pressure / 3.06 m^2 cycle. . . 148
4.32 The error between the approximation of the cycle and the full IPSE runs at 566 °C HTF temperature is shown for the low pressure (5.16 m^2) cycle. 150
4.33 The error between the approximation of the cycle and the full IPSE runs at 566 °C HTF temperature is shown for the high pressure (3.06 m^2) cycle. Axis same as previous figure for comparison. 151

5.1 System layout with stratified tank, glycol loop. 153
5.2 System layout with two tank cold storage, direct water cooling field. . . 154
5.3 The effectiveness of panels during one year of nighttime operation is correlated to the wind speed. 164
5.4 The dimensionless group relates to the effectiveness of the radiator panel using geometry parameters and the loss coefficient. The mass flow rate is that of the water side of the heat exchanger between the field and cold storage. 165
5.5 The heat transfer for turbulent flow is slightly better but pumping loads increase significantly. 167
5.6 The length of the radiator panels tested depending on the cold storage size and radiator multiplier is shown for the peaking plant. 169
5.7 Radiator field example layout. 169

5.8 Pumping power example results. 172
5.9 Energy results of peak plant. 179
5.10 Energy as percent of ACC baseline for peak plant. 180
5.11 The gross and net output for an intermediate plant relative to the air-cooled cycle are shown. 180
5.12 The gross and net output for a baseload plant relative to the air-cooled cycle are shown. 181
5.13 The LCOE for a peak plant of the smallest radiative-cooled system size makes this configuration cost-competitive. 182
5.14 The increase in total direct costs for a Peak radiative-cooled plant compared to an air-cooled plant. 183
5.15 The increase in total direct costs for a Intermediate radiative-cooled plant compared to an air-cooled plant. 184
5.16 The increase in total direct costs for a Baseload radiative-cooled plant compared to an air-cooled plant. 184
5.17 The cost of each configuration for a peak power plant is shown along with the estimated radiative-cooling cost to reach LCOE competitiveness with air-cooling. 185
5.18 The cost of each configuration for a Intermediate power plant is shown along with the estimated radiative-cooling cost to reach LCOE competitiveness with air-cooling. 186
5.19 The cost of each configuration for a Baseload power plant is shown along with the estimated radiative-cooling cost to reach LCOE competitiveness with air-cooling. 186
5.20 The LCOE of the peak power plant with the initial cost estimations and a 20% decrease in costs is shown. More configurations reach cost-competitiveness. 187
5.21 The tube pressure drop, radiator effectiveness, and radiator-HX combined effectiveness are shown for varying CR. The minimum capacitance rate is the glycol side. 189

ABSTRACT

Cooling of concentrating solar power (CSP) plants is a classic example of the connection between energy and water systems. While CSP is both renewable and flexible, it historically used water for cooling the steam cycle. But as water constraints become tighter, especially in deserts where CSP is located, new CSP plants use air-cooled condensers. Air cooling, however, decreases plant energy performance. This work considers an alternative dry cooling system that takes advantage of the low nighttime temperatures and clear skies in the desert. In the proposed system, fluid is circulated during the night through a field of black radiative panels in a closed loop. The fluid is cooled by radiation to the night sky and convection to the ambient air. Water storage tanks allow use of the cooled fluid on demand. The objective of this work is to compare air- and radiative- cooled solar power tower plants. An analytical model for the radiative panel was detailed and validated. Rankine power cycle models were created for the air-cooled and radiative-cooled systems to fully account for off-design operation. In particular, exhaust losses at the last stage turbine were included. The results show that the thermal efficiency of the cycle is not as strongly dependent on condensing pressure as simple cycle models would predict. The system is modeled in annual simulations which use industry-standard models of the solar field, receiver, and thermal energy storage systems. Three systems are modeled: a peaking plant with very little thermal storage, a baseload plant with enough storage to run nearly constantly, and an intermediate plant. Annual hourly simulations show the gross energy production is up to 4% higher for radiative cooling. The net energy production, after accounting for pumping the fluid, is up to 6% higher. The levelized cost of energy of the radiative-cooled system is higher than the air-cooled system except for the peaking plant, which is not currently a typical CSP configuration. This thesis showed that radiative-cooling costs are likely too high to make it cost-effective for current CSP plants, but the system has energy benefits that may make it useful for other applications.

1 INTRODUCTION

1.1 CSP and the energy-water problem

The importance of the energy-water nexus in thermoelectric power generation is shown by quantifying the total water use of the power sector as well as the individual water intensities of different thermoelectric power plants. According to the USGS [Maupin et al., 2010], the three largest categories of water withdrawals in the US are thermoelectric power, irrigation, and public supply, and those categories account for 90% of water withdrawals. Thermoelectric power supply is the single largest withdrawal load at 45% of the total. The water footprint of thermoelectric generated power from the 2010 USGS report was 72 L (19 gallons) withdrawal per kWh. Notably this does not include hydroelectric power. This is a *withdrawal* (not consumption) number representative of all types of cooling systems. The largest withdrawals are for once-through type cooling systems that withdraw large volumes of water for cooling, warm the water, and return it to the source, which sometimes harms aquatic life. The water consumption of electricity produced in the US is estimated to be on the order of 1.9 L (0.5 gallon) per kWh [Diehl and Harris, 2014]. Macknick et al. [2012] reviews and consolidates the range of data points from literature for water footprints of different electricity generation sources in the US. They point to the importance of the issue as some states have begun to address water use in power generation and recent drought has already lead to water constraints on electricity production. Compiling data from many sources, they estimate the median and range of water withdrawal and consumption for all major electricity generation sources (see Figure 1.1 for consumption by cooling type). Parabolic trough CSP with evaporative cooling is among the most water intensive of all renewable and non-renewable sources (reasons are discussed in this section). The median water consumption for wet-cooled parabolic trough CSP is 3.3 L per kWh (0.3 L dry-cooled).

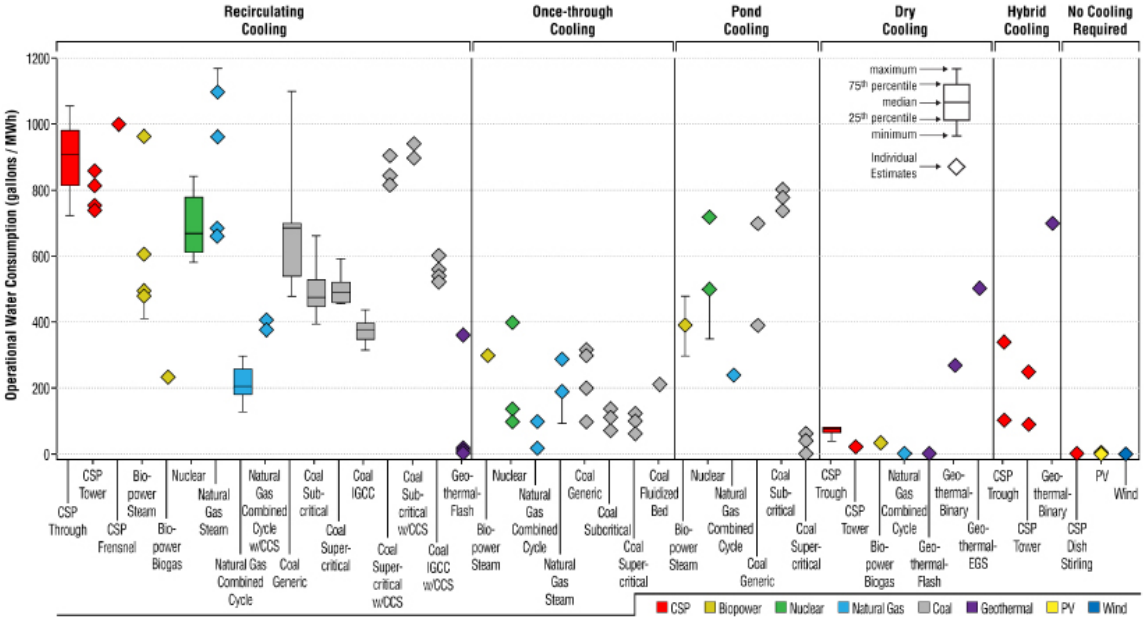

Figure 1.1: Macknick et al. [2012] summarizes water consumption data from many different data sources.

The desert southwest of the US is a water-constrained area and also has some of the best solar resources in the continent. Figure 1.2 shows a thermoelectric cooling constraint index determined by EPRI Goldstein [2003] that incorporated water constraints as well as projections for new generation. The southern California and Nevada areas where CSP plants are most common are highly constrained. Their index showed the most widespread high values were for the west and southwest, though high index values were sprinkled through the southeast and northwest as well.

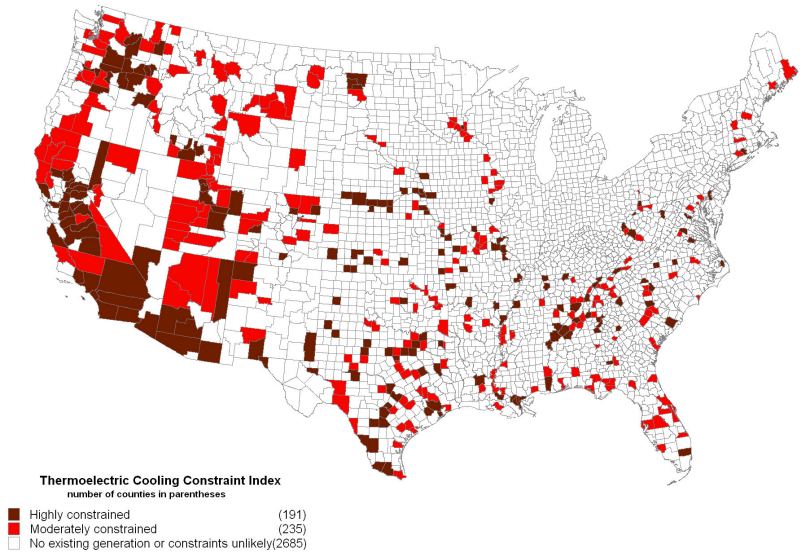

Figure 1.2: A thermoelectric cooling constraint index was determined and mapped by EPRI [Goldstein, 2003] to highlight for water-energy constrained areas in the US.

CSP power plants have typically used evaporative cooling in cooling towers to cool a liquid stream that is circulated through a condenser to provide heat rejection from the power cycle. (Here this is also referred to as wet cooling though other types of wet cooling exist.) Recently, more plants employ air-cooled condensers to reduce water use as shown in Figure 1.3.

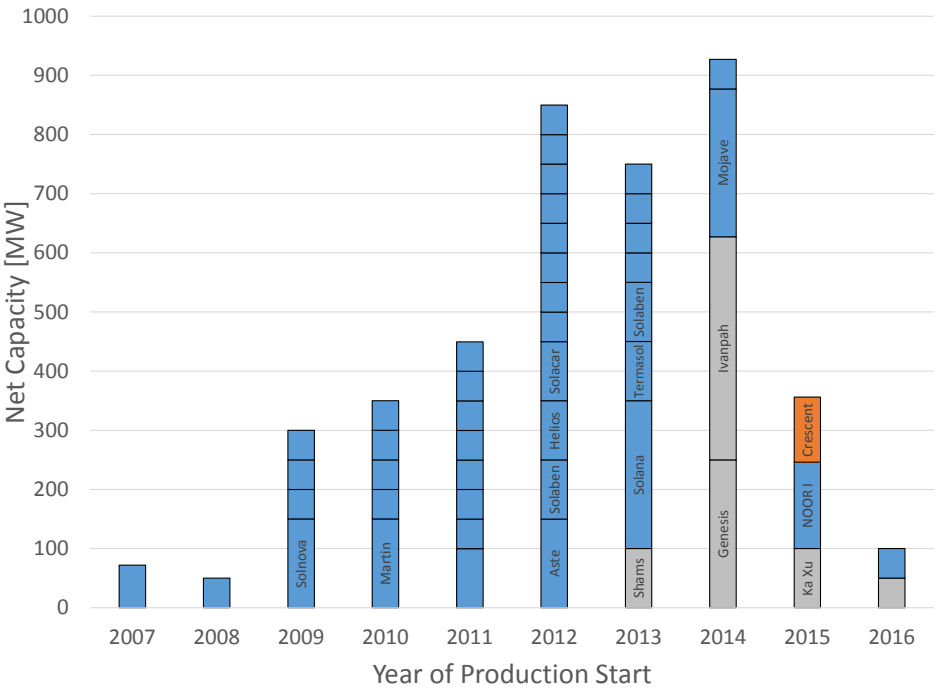

Figure 1.3: Operational parabolic trough and power tower CSP plants since 2007 trend towards dry or hybrid wet-dry systems. Blue indicates cooling towers are used, grey indicates air-cooled condensers, and orange indicates hybrid. Data obtained from NREL.

When choosing between air-cooled condensers and cooling towers, there is a trade off between performance and water usage. The performance comparison is summarized in Section 2.2.1. First, a high level discussion of the water use of CSP and other power plants is considered.

A 2001 report to the US Congress [USDOE, 2001] used the value of 2.2 L (0.57 gallons) per kWh for solar thermal power plants with evaporative cooling. Turchi et al. [2010] considers water consumption of wet and dry-cooled parabolic trough

CSP plants and finds that the cooling tower is the only significant component, dwarfing the of other ancillary water usage. Water consumption is decreased by 90% for dry compared to wet cooling. In their analysis wet-cooled plants consumed 3.5 L per kWh compared to 0.3 L per kWh for dry-cooled. These estimates for cooling tower water consumption can be confirmed from first principles using the enthalpy of vaporization of water and a power plant thermal efficiency between and 0.35 and 0.45, giving water consumption of 2.8 and 1.8 L per kWh, respectively. Example values for design point thermal efficiencies in parabolic trough plants are 0.4 [Zhang et al., 2013] and .36 to .38 [Turchi et al., 2010]; off design operation is less efficient.

CSP power plant water use can be compared to other thermoelectric power plants and other land uses. The water consumption of wet-cooled steam power plants is considered by Diehl and Harris. They estimate the water consumption for coal power plants in the US using recirculating cooling towers is 1.7 L (0.43 gallons) per kWh produced - the lowest end of the first principles estimates for CSP. Turchi et al. [2010] compare CSP to coal-fired Rankine cycles (2 L per kWh). The CSP cycles use more water because of lower efficiency and more off-design operation. Water consumption of CSP plants is compared to agriculture and golf courses on a water per land area basis (also in Bracken et al. [2015]) and it is shown that even CSP with wet cooling is less than half as water intensive these other land uses. Regardless, the magnitude of the overall water withdrawals by the thermoelectric power generation sector (approximately 45% of the total withdrawals per Diehl and Harris [2014]), makes the water usage of CSP important.

The CSP water issue is addressed in several other contexts. Bracken et al. [2015] provide a CSP overview, a review of permitting issues in the Southwest US, a water use summary, and a case study of three CSP plants where water use was a significant issue in project development. The complexities of the water permitting issue detailed in that report highlight the importance of the water issue for CSP. Several reports to Congress have highlighted the importance of this issue to the public perception and support for CSP (Carter and Campbell [2009] and USDOE [2001]). Burkhardt et al. [2011] compares life cycle impacts of cooling alternatives for

CSP in Daggett. In addition to the power plant's water consumption they quantify another 0.5 L per kWh due to manufacturing.

1.2 Nighttime radiative-convective panels for solar power plant cooling

This dissertation considers black panels for passive cooling and assesses their use for dry cooling of concentrating solar power plants. Uncovered, black panels with circulating channels are used to cool fluid at night. This work specifically considers such panels used for the cooling system of a CSP plant. In order to provide cooling on demand, a cold water storage system is required to store the cold fluid. The benefits of such a system depend on the impacts on the power plant throughout the year, thus a detailed, hourly annual simulation is required that captures the details of both the radiative cooling and the power plant off-design operation.

1.3 Initial technical assessment

An initial feasibility assessment of this proposal is in Dyreson and Miller [2016]. That work was a simplified comparison of the proposed system to an air-cooled CSP plant. The CSP plant was a parabolic trough power plant. Though solar power tower plants are more efficient, the trough plant was first studied because of the possibility of putting the black radiative panels on the same structure as the parabolic trough mirrors. In concept, the mirror side could face upward during the day and the black panel could face upward at night. Ultimately, this configuration was not pursued but remains an interesting potential design. The main simplification was that the heat rejection required from the radiative cooled system was that of an air-cooled system; thus any condensing pressure effects of changing the cold sink temperature were not considered. The analysis determined that the night sky radiator system could provide most of the required cooling for a typical CSP

power plant without adjusting the plant's schedule or operating points. The results identified uncertainties in the simple model. The key results were:

- The annual cooling from a radiator field closely matches the annual heat rejection required from a CSP plant with a solar multiple of two when the solar aperture area and radiator surface areas are equal. (The solar multiple (SM) is the ratio of the thermal output of the solar field to the thermal input for the power cycle at design). During some hours in the summer, the radiator system provides less than 50% of required cooling but it provides 100% of the cooling during the winter. In actual implementation the power block's operation would be adjusted so that heat rejection load matches available cooling, but this analysis shows that the amount of cooling available is reasonable for a CSP plant.
- Radiation and convection both contribute to the heat rejection; radiation is not dominating in all conditions.
- The two critical uncertainties in the model of radiator performance are night sky temperature and convection coefficient, though over the course of the year the system can provide a majority of the required cooling even with the most conservative assumptions.
- The condensing temperatures, which are likely achievable with cold storage charged by radiators, are lower than with an air-cooled system during midday and higher during morning and evening hours.

After completion of the feasibility study, the cost of the technology for use in a parabolic trough power CSP plant was assessed. These initial cost estimates for a single power plant example informed the design of the system in the more detailed work within this thesis.

1.4 Initial cost estimations

As an initial estimate of costs, 250 MW air-cooled CSP plant costs were estimated from Kurup and Turchi [2015]. This estimating method uses unit costs for each component that are scaled per acre, square meter surface area, MW output, etc. Using a solar multiple of 2, the field area is approximately 2 million square meters. The basic specifications of the plant are in Table 1.1.

Table 1.1: Summary of plant size parameters for 250 MW CSP plant

Basic plant compoments	
2,000,000	Field size [m^2]
250	capacity, gross [MW]
225	capacity, net (10% parasitics) [MW]
4,167	[MWth]
5	Collector width [m] as in Dyreson and Miller (2016)
15	Row spacing [m] (SAM default)
1.4	Non-solar land multiplier (SAM default)
2,076	Total footprint [acres]
Night sky cooling components	
2,000,000	Radiatior field area [m^2]
494	Total radiative surface area [acres]
1 to 3	Non-radiator land multiplier
1.89E+08	Cold storage volume [gallons]

The power block cost ($288 million) is adjusted for night time cooling by removing the estimated air-cooled condenser cost. The air-cooled condenser (ACC) cost was scaled from the cost for the ACC in a 350 MW coal plant EPRI [2004]. To this reduced cost the radiator field and cold storage cost was added. The cost of radiator panels was estimated using two vendor quotes for small commercial sized roll-bond panels ($12 to 20 per m^2). Land area for the radiator cooling field was estimated from by applying a multiplier to the radiative surface area. The lower land area estimate assumes no additional land is required. The higher estimate assumes that row spacing requirements for cleaning and maintenance are the same

as for the solar collectors. Note that in order to co-construct the solar collectors and radiator field, a complete redesign of the collectors would be required and so although this would minimize the land area requirement, it is not considered here. The cold storage is the more expensive part of the cooling system - cost estimates obtained from industry experts were $0.5 to 0.7 per gallon for individual tanks of about 12 million gallons [Andrepont, 2016]. Here a range of $0.5 to $1 per gallon was used. The total tank size would be 189 million gallons based on the initial work scaled directly from the smaller plant in the feasibility analysis which assumed two, fully mixed tanks. The low end was based on half of this volume assuming stratified tanks. The initial cost estimations completed are shown in Table 1.2 and Figure 1.4.

Table 1.2: Estimated component costs for 250 MW CSP plant (million $)

	Air-cooled baseline	Night sky cooling (low end)	Night sky cooling (high end)	Source
Site improvements	$ 60	$ 60	$ 60	Kurup & Turchi
Solar field	$ 490	$ 490	$ 490	Sunshot Vision 2016 Update
HTF system	$ 160	$ 160	$ 160	Kurup & Turchi
Thermal storage	$ 313	$ 313	$ 313	Kurup & Turchi
Balance of plant	$ 30	$ 30	$ 30	Kurup & Turchi
Power plant	$ 288	$ 325	$ 429	Kurup & Turchi
Less ACC	$ -	$ (34)	$ (31)	EPRI (2004)
Plus roll-bond panels	$ -	$ 24	$ 40	Vendor range
Plus cold storage	$ -	$ 47	$ 132	$0.5-0.7 /gal
Contingency	$ 94	$ 96	$ 108	SAM default
EPC & Owner costs	$ 158	$ 162	$ 181	SAM default
Land	$ 21	$ 21	$ 21	SAM default
Radiator system land	$ -	$ 5	$ 15	1-3x radiative surface area
Sales tax	$ 57	$ 59	$ 66	SAM default
Subtotal direct costs	$ 1,434	$ 1,474	$ 1,646	
Total	$ 1,670	$ 1,721	$ 1,928	
per MWe net	$ 7.42	$ 7.65	$ 8.57	
Percent increase	-	3%	15%	

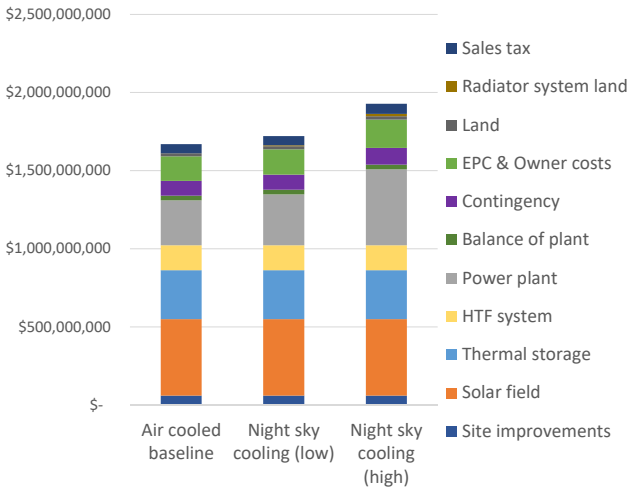

Figure 1.4: The costs of a baseline air-cooled plant is compared to upper and low ends of a radiatively cooled plant. The largest part of the cost increase is the cold storage system in the nighttime cooling system.

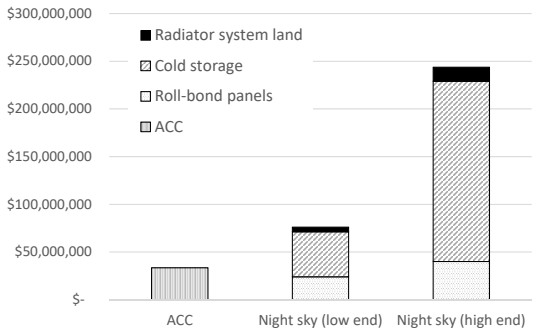

Figure 1.5: Night sky cooling at least doubles the ACC cost. Cold storage is the cost driver.

This first cost estimate suggests that cost of the night sky cooling system adds 3 to 15% to the basic air-cooled plant. The radiator cost is likely conservative because it is based on vendor quotes for small scale, small quantity units. This analysis informs the design because the cost of the cold storage system dominates. It will be important to minimize the size of the cold storage by using stratified water tanks. In order to justify the night sky cooling system, the initial cost estimate points to at least a 3% increase in energy output required compared to air cooling (via performance improvements of reduced condensing temperature and lower parasitic loads). In addition to first costs, operational costs and energy sales revenues ultimately factor in to the comparison. Though not included in this scope, work on optimizing the plant operation can also inform the design, as in Dowling et al. [2016].

1.5 Research Goals

Nighttime radiation-enhanced cooling from non-selective surfaces that are uncovered from ambient convection is a simple, but as of yet unexplored dry cooling method for power plants. The heat transfer problem includes fundamental forced convection heat transfer, something that is well studied but not easy to predict under ambient conditions. The radiation heat transfer depends on the effective sky temperature, available from measurements in a few locations. The cooled water temperature is coupled to the power plant operation (according to condensing temperature), adding complexity to the system operation. There are a multitude of heat transfer, thermodynamic, and optimization problems which could be explored.

The research questions selected focus on assessing the practicality of the radiative panels with cold storage for power plant cooling. Because water concerns have deterred new CSP plants from using wet cooling, the system is primarily compared to air cooled condensers. The central research question was: **What is the potential of a black, uncovered radiator panel system with cold storage to provide cooling for CSP power plants? What are the economic and energy benefits of the system (if any) compared to air cooled condensers?** To answer this question, the goals of this thesis were as follows:

1. Complete a feasibility assessment of radiative-convective cooling for CSP.
2. Identify the appropriate modeling method for the radiative-convective panels.
3. Capture the condensing pressure effects in the Rankine power cycle with adequate detail to compare different cooling systems.
4. Create a system-level simulation that can be used to compare a radiative-cooled power plant with cold storage to an air-cooled plant capturing condensing pressure, parasitic losses, and costs.

Toward these goals, Chapter 3 considers the modeling the heat transfer from uncovered, black panels. Existing literature is used to validate the models. Chapter 4 focuses on modeling the performance of a steam cycle power plant under varying operating conditions in order to capture the off-design performance effects of different cooling systems. Chapter 5 uses the radiative panel model and power plant model in existing CSP system models using System Advisor Model to compare the proposed radiative cooling system with cold storage to air-cooling for CSP. Chapter 2 first presents the relevant literature.

2 LITERATURE REVIEW

This literature review is in two parts. First, background material related to radiative-convective panels is provided. Radiation and convection concepts are covered separately, followed by applications of radiative-convective cooling panels. Second, literature that is useful for comparing CSP cooling systems is described.

2.1 Radiative-convective panels

2.1.1 Radiative cooling

The proposed night sky cooling system relies partly on the radiation exchange between a warm panel and the cold night sky. This section outlines the theory of radiation cooling and reviews previous work on radiation cooling both for power plants and for building comfort cooling.

Background and theory

Radiation cooling is the heat exchange between an object and its colder surroundings resulting in a net cooling effect. The colder surroundings are ideally the atmosphere, assuming the object does not have any radiation exchange with other warm objects (i.e., a view factor of one to the sky). An object's radiation is known based on its emissivity and temperature. The incoming radiation from the sky (radiance S) can be measured and is typically characterized by an effective black body sky temperature T_s or an effective emissivity ϵ_s at the ambient temperature (T_a). The relationships between the sky radiance and the effective sky temperature and emissivity are:

$$S = \sigma T_s^4 \tag{2.1}$$

$$S = \epsilon_s \sigma T_a^4 \tag{2.2}$$

Thus either effective sky temperature or emissivity can be used to characterize the radiance of the sky. Then the radiation exchange between an object (temperature T and emissivity ϵ) and the sky can be written as:

$$\dot{Q}_{net} = \epsilon\sigma(T^4 - T_s^4) \tag{2.3}$$

Though the focus of works cited in this section is on black body radiating surfaces, also included are proposals for radiation from selective surfaces. The same concepts are employed except that the surface properties are spectral such that reflection and emission vary by wavelength. The reason for using selective surfaces is to reflect short wave radiation from the sun to allow net radiation cooling during daytime hours. Selective surfaces can also be used to optimize the emission during the night based on the fact that the atmosphere is transparent to radiation in the atmospheric window of approximately 8-14 micrometers. For discussions of the theory and potential of radiation cooling from selective surfaces see the early works of Berdahl et al. [1983] and Catalanotti et al. [1975].

Sky temperature estimates and measurements

Sky temperature is most commonly measured with a pyrgeometer. A pyrgeometer measures the incoming long wave radiation that then allows calculation of effective sky temperature or emissivity per equation 2.2 or 2.1. The pyrgeometer is a pyranometer where the solar (short wave) radiation is filtered by a screen with a cut-in wavelength of typically around 4 micrometers. Others have proposed alternative measurements (Berger et al. [1984], Gliah et al. [2011], Cooper et al. [1981]) but pyrgeometers are commercially available and are the most common source of data. In particular Gliah et al. [2011] provides a summary of sky temperature measurement techniques and the shortcomings of the pyrgeometer method. However to date a better method has not been vetted and a good pyrgeometer such as Kipp & Zonen CGR4 claims uncertainty of less than 3% in daily insolation [Kipp&Zonen, 2014]. Pyrgeometer measurements are not widely available in the way that other weather data are. For international sites, the BSRN Network makes available some

data (bsrn.awi.de). For US sites, SURFRAD (esrl.noaa.gov/gmd/grad/surfrad) provides data including a location at Las Vegas, Nevada that is useful for the current work because it is a realistic location for CSP plants.

Because measurements of effective sky temperature are not readily available en mass at weather stations nor in typical meteorological year (TMY) datasets, many have attempted to correlate sky temperature to ambient conditions. Several correlations are available for sky temperature under clear skies and some correlations also consider partly cloudy conditions. During completely cloudy periods the sky temperature can be approximated by the ambient temperature. Aubinet [1994] and Eicker and Dalibard [2011] provide full treatments of the available correlations.

Along with a detailed review of the available sky emissivity correlations for both clear and non-clear conditions, Eicker and Dalibard [2011] provide a comparison to measurements for the purpose of a study of photovoltaic-thermal (PVT) panels. The authors compare modeled sky temperatures to pyrgeometer measurements in Germany for a short period of time. The non-clear models all use some quantity to represent cloudiness that is based on daytime radiation, so they do not account for changing cloudiness overnight. They find that clear sky temperature models are reasonably accurate but only during clear conditions, while cloudy sky models are marginal in cloudy conditions and poor in clear conditions. So no single model can be used to predict sky emissivity for all conditions.

One often cited clear sky emissivity model is Berdahl and Martin [1984]. They provide apparent emissivity for clear sky based on a correlation from six different locations over the course of several years. This model also performed well during clear periods tested by Eicker and Dalibard [2011]. A pyrgeometer was used to estimate sky emissivity during clear periods. The locations have a variety of climates but two locations are potential CSP sites: Tucson, AZ and Boulder City, NV. The clear sky emissivity is correlated to dew point temperature. The correlation for apparent emissivity to dew point temperature was fit based on monthly average data and then a cosine function was fit to this data to account for day-night differences, based on previous work that showed the emissivity differences would be 0.016, with the larger emissivities at night. The effective sky temperature (T_s) based on the Berdahl

sky emissivity correlation is [Duffie and Beckman, 2013]:

$$T_s = T_a \left(0.711 + 0.0056 T_{dp,C} + 0.000073 T_{dp,C}^2 + 0.013 \cos\left(15t\right)\right)^{1/4} \tag{2.4}$$

The same authors also propose a sky emissivity correlation accounting for cloudiness conditions [Martin and Berdahl, 1984] but the performance of that model in hourly predictions of effective sky temperature is poor based on the work of Eicker and Dalibard [2011].

Vidhi [2014] use experimental data from measured sky temperatures (pyrgeometer) in Colorado to compare common clear sky emissivity correlations. Though several models have similar error, the lowest error is that of Berdahl and Martin [1984].

2.1.2 Forced convection over flat plates

Radiation cooling can be either enhanced or diminished by convection effects, so it is equally important to understand the convection as it is to understand the radiation. A flat, uncovered radiator panel exposed to ambient wind is subject to combined free and forced convection, with forced convection dominating under any significant wind speed. This section describes external forced convection heat transfer theory and reviews relevant experimental work.

Uninterrupted plate

Convection from a panel due to outdoor winds is approximated by forced convection over an uninterrupted flat plate. This section includes a brief summary of theory and discussion of experimental results. For a full treatment see heat transfer texts and handbooks (for example Nellis and Klein [2009], Incropera and DeWitt [2002], Hewitt [2008]).

The difference between the surface temperature and the free stream temperature drives heat transfer between the surface and free stream. The resistance to heat

transfer is characterized by the size of the boundary layer. Initially the boundary layer is small and the resistance to heat transfer is low. As the flow field develops the boundary layer grows and the resistance increases. Initially the boundary layer is laminar. Eventually the boundary layer transitions to turbulence and the resistance to heat transfer is related to the size of the viscous sublayer within the turbulent boundary. The transition from laminar to turbulent flow (that is in fact not a discrete change but a transition) decreases the resistance to heat transfer, but the turbulent boundary layer continues to grow and so the resistance to heat transfer increases from the initial minimum value. The thermal boundary layer growth is related to the momentum boundary layer growth. A few definitions are required. Reynolds number is the ratio of inertial to viscous forces $Re_x = \frac{\rho u_\infty x}{\mu}$. Prandtl number is the ratio of the momentum diffusivity to the thermal diffusivity $Pr = \frac{\nu}{\alpha}$. The local (as opposed to area-average) Nusselt number is the dimensionless heat transfer coefficient defined as:

$$Nu_x = \frac{hx}{k} \tag{2.5}$$

where h is the local heat transfer coefficient, x is the position from the entrance of the flow on the plate, and k is the conductivity of the fluid. The local friction factor C_f is the dimensionless shear stress:

$$C_f = \frac{2\tau_s}{\rho u_\infty^2} \tag{2.6}$$

where τ_s is the shear stress, ρ is the density of the fluid, and u_∞ is the free stream velocity.

Experimental work by many (described in this section) has shown that turbulent conditions are generally present in flow of ambient wind over a plate. One common form of the standard forced convection correlation for turbulent flow over a flat plate is summarized here. An experimentally derived friction factor for turbulent flow over a smooth flat plate is [H. Schlichting, 1979]:

$$C_f = 0.0592 Re_x^{-0.2} \tag{2.7}$$

The modified Reynolds analogy or Chilton-Colburn analogy describes the relationship between the momentum boundary layer and thermal boundary layer for fluids with Prandtl numbers close to 1 when viscous dissipation can be neglected and the pressure gradient in the flow direction is small. This leads to a relationship between the Nusselt number and friction factor:

$$Nu_x = \frac{C_f}{2} Pr^{1/3} Re_x \tag{2.8}$$

The local Nusselt number for a smooth flat plate is then:

$$Nu_x = 0.0296 Re_x^{4/5} Pr^{1/3} \tag{2.9}$$

This equation applies for turbulent conditions up to Re_x of 1e8 and Prandtl numbers for 0.6 to 60 [Nellis and Klein, 2009].

The average Nusselt number is determined by integration of the local value over the length of the plate. Since turbulent conditions are assumed to exist through the entire plate in this case, the initial laminar region is not considered and the average Nusselt number is related to the Prandtl number and average Reynolds number per:

$$\bar{Nu} = 0.037 Re^{4/5} Pr^{1/3} \tag{2.10}$$

Other versions of this equation exist because different empirical correlations for friction factor can be used or other methods can be used to approximate the Nusselt number. The above relation is for an isothermal plate. A correlation for local Nusselt number for forced convection over a plate with a constant heat flux (instead of constant temperature) under turbulent conditions is:

$$Nu_x = 0.0308 Re_x^{4/5} Pr^{1/3} \tag{2.11}$$

The Prandtl number range is from 0.6 to 60. Because a radiator that is cooling a fluid over its length is in fact neither isothermal nor characterized by constant heat flux, either form is equally relevant. Since the two are very close, the isothermal version is used here.

Immediately a few differences from theory are apparent: the cooling panel may have fluid channels that are not flush with the plate so it is not truly a flat plate, and the boundary layer development is influenced by the surface roughness and turbulence of ambient wind. Experimental work reviewed in the following sections demonstrates the applicability (and limitations) of applying the turbulent forced convection theory to real outdoor conditions.

Relevant experimental work - uninterrupted plate

A great deal of experimental work has been completed to predict the heat transfer coefficient for flow over a flat plate both in wind tunnels and outdoor conditions. Many have completed tests for convection from solar thermal panels or PV panels, which resemble the convection from the surface of the radiator panel relatively well. One difference is that solar collectors are generally tilted for optimal solar radiation exposure, not flat for maximum view to the sky as radiators would be. However, correlations are useful because they often consider a range of orientations including completely horizontal.

A review of this literature provides three general conclusions: 1) flow in ambient conditions is generally turbulent and 2) the flat plate correlation described in equation 2.10 is more accurate and generalizable than correlations made to an individual experiment and 3) all predictions of forced convection coefficients should be considered approximations. The first two conclusions are discussed in this section. The third conclusion, that all predictions are approximations, is apparent in the literature in general. For example Incropera and DeWitt [2002] state that errors of up to 25% should be expected in general for flat plate correlations and in particular for expression 2.7 the accuracy is 15%. This uncertainty is in part due to uncertainty in measurement of heat transfer coefficients and in part because any real wind will have a specific flow field and free stream turbulence.

Empirical correlations for flow over flat plate

Palyvos [2008] provides a review paper of convection over flat plates for application

in building thermal energy analysis and roof-mounted solar. This review paper includes the equations for 38 linear correlations for heat transfer coefficient to velocity, 18 power law correlations to velocity, 20 equations correlated to Reynolds and Prandtl number per boundary layer theory, and 15 correlations to velocity and plate length. From the linear equations the author proposes a simple equation that could serve as an initial estimate of convection, while not being specifically tuned to any one experiment.

$$\bar{h} = 4.2 + 3.5V \tag{2.12}$$

Here V is the wind velocity component parallel to the plate in m/s. The average maximum deviation of this equation to each of the empirical linear relations is 18%.

Palyvos concludes that field measurements should be pursued, that wind velocity measurement should be standardized, and that most importantly the use of any of the existing correlations should be done only with an understanding of the applicability of a given correlation.

Example of empirically derived linear correlation

Sharples and Charlesworth [1998] is an often-cited experimental work that provides data for convection in real ambient conditions. Their experiment uses a residential solar collector-sized heating element on the roof of a building to provide data that is as close as possible to the real operating conditions of solar collectors. The roof had a 35°pitch. The wind speed measurement was taken 1.5 m above and several meters away from the test element. Air temperature was measured with a shielded thermocouple. Short and long wave radiation were measured to isolate convection from radiation. The experiments were completed in periods of generally overcast skies with good winds. The daytime and nighttime conditions did not give different heat transfer coefficient results.

Both linear and power fits were made to the data at each of several wind incidence angles. For a head-on wind, the correlation is:

$$\bar{h} = 2.2V + 8.3 \tag{2.13}$$

The study finds reasonable agreement with the correlation of Test et al. [1981], developed under similar conditions, and some agreement with other correlations as well. Their correlation well describes the conditions of the test it was developed under but does not incorporate the influence of effective plate length (either due to varying wind direction or actual plate size differences), and therefore does not reflect the fact that the local heat transfer coefficient varies along plate length according to boundary layer theory.

A return to boundary layer theory

The question of choosing the best convection heat transfer correlation for flat plates, specifically solar collectors, is reviewed by Sartori [2006], concluding in unambiguous terms that correlations based on boundary layer theory are the only relevant correlations for general use.

On the topic of turbulent versus laminar conditions, Sartori cites literature that suggests that the conditions of flow over a blunt-edged solar collector would never be truly laminar. Though no original experimental work is included in this work, by examination of available experimental work the author shows that several have observed that real wind conditions are turbulent.

After reviewing available correlations that have been made using either linear or power regressions to measured heat transfer coefficient in terms of wind speed and (in some cases) also length of plate, Sartori emphasizes that these correlations do not generally reflect boundary layer theory and so are not relevant outside of the specific geometry and conditions under which they were tested. Boundary layer theory shows that the local heat transfer coefficient decreases along plate length, and so a correlation for average heat transfer coefficient must account for effective plate length. The effective length of a plate should consider the variable outdoor wind direction because the path of the wind over the plate determines how much time the boundary layer has to develop. Sartori creates simplified versions of the

basic flat plate correlations for laminar, transition, and turbulent regions over a flat plate. Beginning with equation 2.10, Sartori uses properties of air at a mean fluid temperature of 40°C to estimate the average heat transfer coefficient based only on the length of the plate in the wind direction L in meters and the wind velocity V in m/s.

$$\bar{h} = 5.74 V^{4/5} L^{-1/5} \tag{2.14}$$

The accuracy of the correlation is tested using experimental work by others. The equation consistently matches the experimental results as well as the related site-specific correlations better than other correlations. In addition Sartori made data available (through comments on a journal article [Sartori, 2011]) comparing experimental results to a number of correlations and shows superior accuracy of the Sartori equation under several different wind speeds from two experimental studies.

Experimental work reinforcing correlations based on boundary layer theory

Kaplani and Kaplanis [2014] study the impact of convection over PV panels on panel temperature. The temperature of the PV panel is modeled with the relation:

$$T_{pv} = T_a + f_{pv} I_T \tag{2.15}$$

Where T_a is the ambient temperature, I_T is the plane-of-array radiation, and f_{pv} is a factor that includes the effects of convection on a tilted panel per the following definition:

$$f_{pv} = \frac{(\tau\alpha) - \eta_{pv}}{U_{L,f} - U_{L,b}} \tag{2.16}$$

Where $(\tau\alpha)$ is the transmittance-absorbance product, η_{pv} is the efficiency of the PV panel, and $U_{L,f}$ and $U_{L,b}$ are the front and back loss coefficients.

A number of correlations are used in the analytical model and the resulting f is compared to experimental data. The PV panel tested was one in an array of four panels, each 1.49 by 0.674 m. The panels are two-axis tracking and experimental data included a range of angles down to 15°from horizontal (but never completely horizontal). One year of data was monitored and the analysis is based on the clear sky days only.

The authors choose the set of Sartori correlations (laminar, transition, and turbulent) as well as the Kendoush equation Kendoush [2009]. The Kendoush equation is also an analytically derived equation for convection that accounts for the wind direction and plate length. In this work the wind regime for the Sartori correlations was not always assumed to be turbulent. Instead the wind regime was selected based on the Reynolds number and assumed turbulent if there were obstacles directly in the flow path. The heat transfer coefficient was not calculated but the model predicts the f factor to the satisfaction of the authors using either Sartori or Kendoush equation for the forced convection on the windward side of a PV panel, with a RMSE of 0.004 m^2K per W. To understand the significance of this error, consider radiation from 100 to 1000 W/m^2 . The RMSE reported would result in a 0.4 to 4°C error in the temperature of the PV panel. With the temperature sensitivity of the panel used in the experiments, the impact on efficiency would be up to 2%.

Other empirically derived correlations for forced convection were tested including that of Sharples and Charlesworth [1998] but resulted in poor performance of the model. The authors conclude that this is in part due to the empirical nature of the correlations.

It is notable that the flow is not assumed to be turbulent given the conclusion of Sartori that outdoor flow over a blunt flat plate is always turbulent. However since the model was not run assuming only turbulent flow it is not known if the fit of f to the experimental data would have been improved with the turbulent assumption.

Experimental work reinforcing assumption of turbulence

Neises [2011] modeled the temperature of a PV panel and also used experimental

data. Though the convection heat transfer coefficient was not measured, the impact of the convection correlation used in the model was tested by changing the correlation and examining the error in modeled PV power and PV panel temperature compared to measured values. Neises compared four models for forced convection including two laminar and two turbulent models. The flat plate turbulent equation, Equation 2.10, and another version of the turbulent forced convection equation were used. The two turbulent forced convection equations were more accurate than the laminar correlations, so turbulent conditions are assumed to exist even in low wind speeds. Since the two turbulent forced convection equations had similar impact on the accuracy of the PV model, the more simple version, Equation 2.10, was chosen. It is worth noting that a complete model including the laminar-turbulent transition was not tested.

Experimental work contradicting correlations based on boundary layer theory

McColl et al. [2015] also models PV panel temperature and compares to measurements as part of a study on PV cooling methods. In this case the correlation of Sharples and Charlesworth [1998] is compared to the Sartori equations (laminar, transition, and turbulent) and to fundamental equations, that are essentially the same as the Sartori equations. Based on one day of data, the correlation of Sharples provides much more accurate PV panel temperature than those based on fundamentals. The standard deviation of the predicted panel temperature for this single day were 2.2, 9.0, and 6.9°C, for the Sharples, Sartori, and fundamental correlations, respectively. In particular the panel temperature prediction is poor at low wind speeds when convection is predicted by the Sartori or fundamental correlations. The panel size was 1.485 by 0.655 m and the panel was oriented at a stationary south-facing position. The Sharples correlation may be best in this case because likely the panel size in the Sharples test was similar to that in the current case, and the authors assumed laminar and transition flows exist though the work of Sartori and others shows outdoor wind is likely turbulent, thus under predicting cooling

by convection in low wind speeds. This study is included here as it is contradictory to the conclusions of Kaplani and Kaplanis [2014] and, to some extent Neises [2011], though the McColl work uses a shorter period of data, one day, than the others.

Interrupted plate

The uninterrupted plate model is based on a free stream air flow and the development of a boundary layer over the length of a single flat plate. However, in the proposed radiative field described, the majority of the panels experience an incoming flow field affected by the previous panels. This is often described as an interrupted plate. Existing studies of interrupted plates relate to heat exchangers, PV panels, and solar concentrators. For heat exchangers, understanding the fundamental flow characteristics of plate-fin heat exchangers began with analysis (experimental and analytical) of flow over multiple plates aligned in a row and also in staggered arrays. For PV power plants, convection effects impact the temperature of the panel, which is relevant since the a higher temperature leads to a lower panel efficiency. Though studies have considered convection over individual PV panels (as described in Section 2.1.2), work on the convection effect within a large field of PV panels was not found in this literature review (perhaps because the temperature-efficiency effect is not a primary performance concern). Solar concentrators for CSP plants of both trough and tower type have been studied because wind loading can be a significant issue and leads to overdesigned collectors and high costs. Interest in reducing collector cost has led to both experimental work (wind tunnel and outdoor) and CFD analysis of individual concentrators as well as intra-field effects. Collectors positioned inside of the field or shielded by fencing have lower wind loads. This section summarizes relevant literature for intra-field momentum and thermal boundary layer effects from these different applications.

Relevant results - interrupted plate

Cur and Sparrow [1978] investigate the effects of two flat plates arranged in series in a wind tunnel. The heat transfer coefficient is obtained by analogy to mass transfer

for tests for geometries typical of heat exchangers. These were thickness:length ratios (0.04 to 0.12), spacing:length ratios (0.25 to 2), and Reynolds numbers (1,100 to 13,600). The wind tunnel results are not directly applicable because they use a hydraulic diameter that relates to the wind tunnel duct size, but the qualitative characteristics of the flow field are still useful. In some experiments both fore and aft plates participated in heat (mass) transfer, while in other experiments the first plate was there only for development of the momentum boundary layer but did not participate in heat (mass) transfer. The second plate heat transfer coefficient compared to the first depends on the effects of spacing thickness, and Reynolds number. Applying these results to the radiative-convective cooling panels with large spacing (up to 15 m row spacing for 5 m wide radiators if installed on the back of solar collectors as in the concept of the original feasibility study in the current work) and small thickness relative to plate length (i.e. th=2 mm and characteristic length of plate at least 5 m), the second plate will have a heat transfer coefficient approximately the same as the first as long as the Reynolds number is high (>5,500). If Re is lower, the heat transfer coefficient from first to second plate (10-50 %). Thus knowledge of the flow regime is important. Cur and Sparrow [1979] extend previous work (two plates) to an array of plates. The development of a 'periodic fully developed' regime occurs when there are many plates. Mass transfer experiments on a small duct with a series of plates were completed to measure heat transfer characteristics by analogy. In this study the plate spacing was kept uniform at spacing = length of plate. The Reynolds number and plate thickness were varied as in the previous study. Results showed that thermal development was achieved by the eighth plate and that the periodic flow condition typically had a lower heat transfer coefficient than the first plate, though the decrease was moderate - less than 20%. (As in Cur and Sparrow [1978], the first to second plate differences can be either positive or negative, depending on the thickness of the plate and flow conditions.) These results suggest that when the wind approaches an array of plates from the direction perpendicular to the length of the plate, a degradation of 20% could be applied to the heat transfer coefficient to conservatively estimate the effect of multiple plates on the predicted heat transfer coefficient. When the wind

approaches from the direction parallel to the length of the plate, the heat transfer coefficient would be expected to degrade along the path. These results also suggest that increasing the thickness of the plate could serve to augment the heat transfer coefficient, possibly more than making up for the degradation. Increasing the plate thickness would increase the turbulence at the start of each plate. It is worth noting that the results were for spacing-to-length ratio of one and the wind tunnel flow was not representative of outdoor conditions, which are more turbulent.

Specifically for solar panels on building rooftops, Kind et al. [1983] used scaled experiments of a pitched roof with an array of solar panels in simulated outdoor wind conditions (turbulent flow). In addition to showing that general correlations do not well predict behavior in outdoor conditions, they also show how the convection coefficient varies over multiple plates and with varying wind directions. If the wind approaches along the array's length, their results show a 20% decrease in heat transfer coefficient from the first to the final panel. They note that the results are not applicable when there is significant wake from surrounding objects or in any case when the geometry is different than the described experiment.

Camargo et al. [2009] complete a paired experimental and numerical study of convection over multiple heated plates. The spacing between places was approximately equal to the plate length in the flow direction. The plate thickness to length ratio was about 0.25. Over a range of Reynolds numbers (2,000 to 20,000), the heat transfer coefficient measured at the second plate was lower than at the first plate, but did not degrade significantly more by the fourth plate. The difference between the first and second plate heat transfer coefficients was related to the Reynolds number; higher flow rates led to higher differences. This is consistent with Cur and Sparrow [1978] for related geometry (high thickness:length and spacing:length approximately unity). The degradation was about 20%.

Relevant CFD methods - interrupted plate

This section reviews some of the work where computational fluid dynamics (CFD) methods are used to model flow around heliostats and PV panels. The study of

wind loading over the field can inform the study of heat transfer coefficient over the field. Ho [2014] provide an overview of the use of CFD for CSP systems. For collectors, their review of the literature summarized the use of CFD for single heliostat or parabolic trough collectors. In high wind conditions, parabolic trough collectors typically are stowed at a position about 60 degrees from upward facing, while heliostats are stowed horizontally with the mirror facing down. CFD was used, often along with experiments, to examine the wind loading over heliostats for different orientations (stowed or not) and for different facet spacing (spacing between individual mirrors mounted on a single heliostat).

Wu et al. [2010] complete numerical and experimental studies of the gap effect on heliostat wind loads. The 'gap' is the spacing between individual facets or heliostat mirror panels that make up a single tracking heliostat. The numerical model is in ANSYS Fluent. Due to the complexity of the geometry, a two dimensional simplification is made. The inlet conditions used a velocity boundary layer and the exit was a static pressure. The energy equation was not solved because the temperature field was not important. The steady Reynolds-average Navier-Stokes (RANS) equations were solved. A k-ω model was implemented for turbulence as it is accurate for free shear flows. The results show that the gap effect is not important when designing for wind load and numerical and experimental results agree.

Sment and Ho [2013] measure wind speeds in a heliostat field to observe the wind loading and wind turbulence intensity within the field. Their wind loading measurements generally agree with the results of Peterka et al. [1986] which showed a reduction in the wind load from the first to the later rows of heliostats. Three positions were tested including the stow position, which is nearly horizontal. The wind load measurements for the horizontal position were not reported (likely because the projected area was zero into the wind). Turbulence intensity (TI) was found to increase significantly from the first to the later heliostat rows (0.1 to 0.5 TI), specifically when the heliostats were horizontal the turbulence intensity doubled (to 0.2 TI). The wind speed measurements were at 32 Hz sampling rate and measurement heights were 4, 7, and 10 m depending on the location. A CFD model using SolidWorks was also completed but the direct comparison of model to

experiment was not successful.

Jubayer et al. [2016] complete a CFD analysis and wind tunnel testing of convection from a single ground mounted PV panel. A single ground mounted panel at an angle of 25°is studied with two different wind directions and three different Reynolds numbers. Free stream turbulence is known to increase the heat transfer. The CFD model used a nonuniform grid with increasing grid sizes further away from the panel except toward the ground. The inlet conditions used surface roughness and turbulence intensity profiles. The OpenFOAM software was used. The turbulence model was the shear stress transport (SST) k-ω model. The wind tunnel measurements use a boundary layer tunnel to better approximate outdoor conditions. Though velocity profiles do not match exactly, agreement is reasonable. This work showed that the heat transfer from a ground mounted panel is higher (12%) than that from a roof-mounted by comparison to previous results.

Capturing intra-field convection effects

Some initial estimates are made to determine the potential impacts on the radiative cooling system proposed. Based on the literature review, the convection coefficient correlation for single flat plate has an uncertainty of approximately $\pm$ 20% and the forced convection over the panels within the field may be about 20% lower than that of the first panels on the edge of the field. These bounds are applied to the annual simulation of the system from Dyreson and Miller [2016] using the adiabatic analytical model as described in Chapter 3. Figure 2.1 and Table 2.1 detail the results of the annual hourly simulations. As an upper bound on the strength of convection, 'convection uncertainty (+)' is determined by augmenting the convective heat transfer coefficient by 20% every hour. As a lower bound, 'convection uncertainty (-) and intrafield effect (-)' is determined by derating the convective heat transfer coefficient by 36% every hour (1- 80% uncertainty x 80 % intrafield penalty). If convection accounts for half of the heat transfer, the overall penalty for the convection uncertainty and intrafield effects would be consistently about 36% . However the annual penalty estimates in Table 2.1 is less than this for a

few reasons. First, during the winter there is excess cooling available so the system can meet cooling demand despite the decrease in convection estimates. Second, this panel design uses a long 200 m length in order to mirror the collector field geometry , so it is overdesigned for most conditions.

Table 2.1: The cooling provided using the radiator field area equal to the collector field area is decreased by up to 5% over the year. The month of June is also shown to illustrate that the penalty is larger in the summer. There is no decrease in heat transfer in the winter but in the month of June heat transfer can be decreased by up to 10%. Two uncertainty cases are analyzed as bounds. The case for wind approaching along the 200m length is also considered as an extreme case; if the characteristic length for convection heat transfer is 200 m for one section of radiator and if the turbulent boundary layer is not interrupted along this length, the heat transfer coefficient would decrease along the entire length.

Case	Annual cooling met (%)	June cooling met (%)
Baseline	94	86
'h' (-20%), intra-field effect (-20%)	91	79
'h' (+20%)	95	88
Assume wind along 200m length	89	76

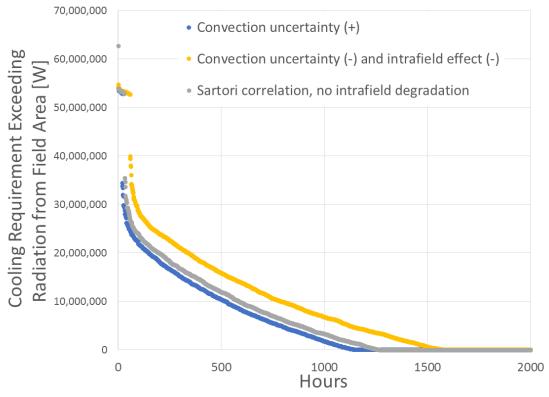

Figure 2.1: Duration curves of the unmet cooling load for a CSP plant operated as an air-cooled plant with radiative cooling provided using only an area equal to the solar field aperture area.

These bounds do not change the feasibility analysis significantly from the original conclusions in Dyreson and Miller [2016]; the radiator area is approximately adequate for cooling provision and the power plant operation should be considered to fully appreciate how a radiative cooling system might compare to an air-cooled system.

Wind speed variations and impact on convection

This section considers the impacts of sub-hourly wind speed variations. The simplified boundary layer version of the Sartori correlation is:

$$\bar{h} = 5.74 V^{4/5} L^{-1/5} \tag{2.17}$$

In solar data sets , the wind speed is often reported as the hourly average, and this is a typical modeling timescale for CSP. Using wind speed measurements at a timescale on the order of one hour, the distribution of wind speeds has a typical Weibull distribution.

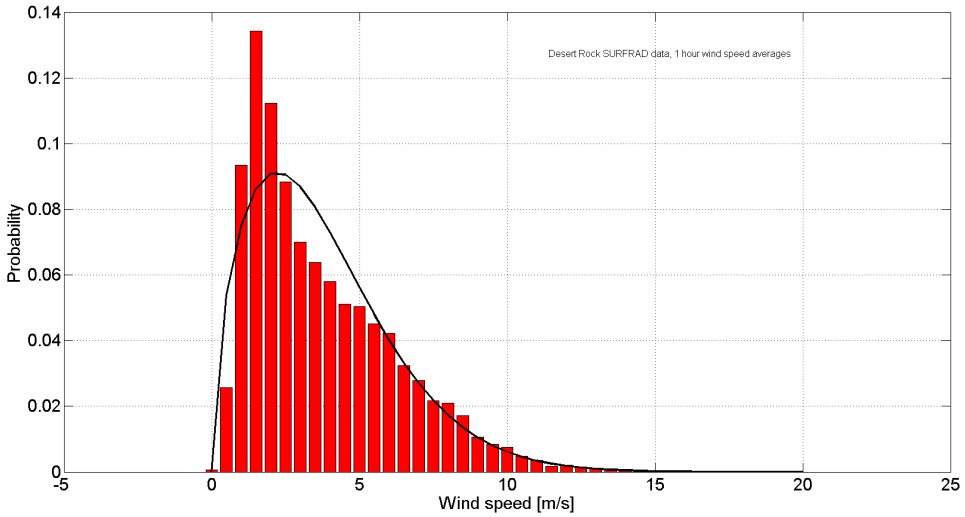

Figure 2.2: Wind speeds measured at the Desert Rock site in the SURFRAD network are reported at one minute values and here averaged hourly to produce histogram of the hourly averages compared to a Weibull distribution.

However on smaller timescales, outdoor wind is turbulent. Turbulence is described by turbulence intensity (TI) as the ratio of the standard deviation of wind speeds to average of wind speeds:

$$TI = \frac{std}{\bar{u}} \tag{2.18}$$

Measurements are typically made on at least 1 Hz sampling rates with averaging timescales of something less than one hour; usually ten minutes. The ten minute timescale is a convention in wind energy engineering as it relates to the response times of wind turbines. Turbulent fluctuations are normally distributed instead of having a skewed distribution like the longer term measurements. Manwell et al. [2009]. This means that using hourly averages results in a conservative estimate of convective heat transfer because the convective heat transfer coefficient favors

the higher wind speeds. Sub-hourly data are not necessary for modeling the heat transfer from radiative-convective panels which operate on longer timescales.

2.1.3 Radiative cooling applications

Radiative cooling has been investigated in detail for building cooling and a few publications consider radiative cooling for power plants. A fundamental difference between these two categories is the temperature of the radiator object. For comfort cooling a building is maintained below ambient while a power plant condenser generally operates above ambient unless the cooling system allows cooling below ambient (such as a cooling tower which approaches ambient wet bulb). This section summarizes the relevant literature as it pertains to the current work.

Radiative cooling for comfort cooling

As summarized by Eicker and Dalibard [2011], substantial work has been done on passive radiation cooling for buildings. Systems proposed use open tanks, dedicated thermal panels, and PVT panels. (PVT panels are typically used to cool PV panels and to collect thermal energy during the day but as a passive cooling panel they can be used at night to cool water.) In this section several works that can inform the proposed radiative enhanced cooling system are discussed, mostly those that use uncovered non-selective surfaces. These works provide interesting insights into experiences with uncovered black surfaces for water cooling but importantly they are focused on conditions that exist when the cooling load is a building. A summary of heat fluxes from experiments is provided in Table 2.2. The heat flux depends on the ambient temperature, sky temperature, wind speed, and radiator surface temperature, but the magnitude of the heat flux for applications for comfort cooling are on the order of 100 W/m^2 . Raising the inlet temperature in one study showed the potential for higher heat fluxes.

Table 2.2: Heat fluxes measured from black, uncovered radiators at night under different operating conditions range widely underlining the importance of operating temperature and ambient conditions. Fluxes are approximate as they are in some cases interpreted from graphs in the original literature.

Reference	Temperature	Location,Month	Heat Flux [W/m^2]
Eicker and Dalibard [2011]	Inlet 20-40°C	Spain, June	30-210
Tevar et al. [2015]	Comfort cooling	Spain, July	64
Erell and Etzion [2000]	Inlet 20°C	Israel, July	88
Eicker and Dalibard [2011]	Inlet 15-20°C	Germany, Oct.	100-120
Eicker and Dalibard [2011]	Inlet 35-55°C	Germany, Nov.	200-800
Hosseinzadeh and Taherian [2012]	Outlet 15-23°C	Iran, Nov.	23-52

Hosseinzadeh and Taherian [2012] operate two serpentine solar collectors without glazing along with a water storage system to test the potential for building cooling in Iran. The cooling achieved was between 23-52 W/m^2 under a variety of ambient and flow conditions. The solar collector is a 1 mm thick iron plate with copper tubes. The panel is insulated on the back. Their model, like many flat panel radiative cooling models, is created using the formulation of Duffie and Beckman [2013] for solar collectors.

Kimball [1985] tested radiative cooling panels in Phoenix, Arizona. Several configurations were tested including an uncovered, black panel. In this experiment a radiator with copper tubing was kept at a uniform temperature with electric heating. The heat flux obtained from the radiators at different operating temperatures was examined. The model was extrapolated to consider annual performance at different locations under a variety of operating conditions. The experimental heat fluxes are not reported. The authors normalize all results by ideal radiator performance where an ideal radiator is a covered radiator with a radiator surface having perfect reflectivity outside of the atmospheric window and perfect emissivity within it.

Eicker and Dalibard [2011] use a PVT panel with the cover removed to provide nighttime cooling. Both modeling and experimental work are completed. The

PVT panels' cooling performance is modeled using a modified solar collector approach including estimates for night sky temperature and convection coefficients. This model is first validated with a prototype experiment using commercially available PVT modules. Experimentation included measurements of inlet and exit temperatures, ambient conditions, and sky temperature (via pyrgeometer). The PVT panels had surface area of 0.67 m^2 and the circulating tube inner diameter was 8 mm. The uncovered emissivity was 0.8978. The prototype experiment was completed in November in Stuttgart, Germany for two nights. The cooling power available at night was between 100 and 120 W/m^2 . Water was cooled less than 5°C and flow rates were 23-28 kg per m^2 per hour. Incoming water temperatures were between 15 and 20°C. The impact of varying the incoming water temperature was also examined for incoming water temperatures over 50°C during a separate two day period in October. Results comparing heat fluxes based on the water-to-sky temperature difference are in Figure 2.3. The heat flux is higher as the inlet water temperature increases above the sky temperature.

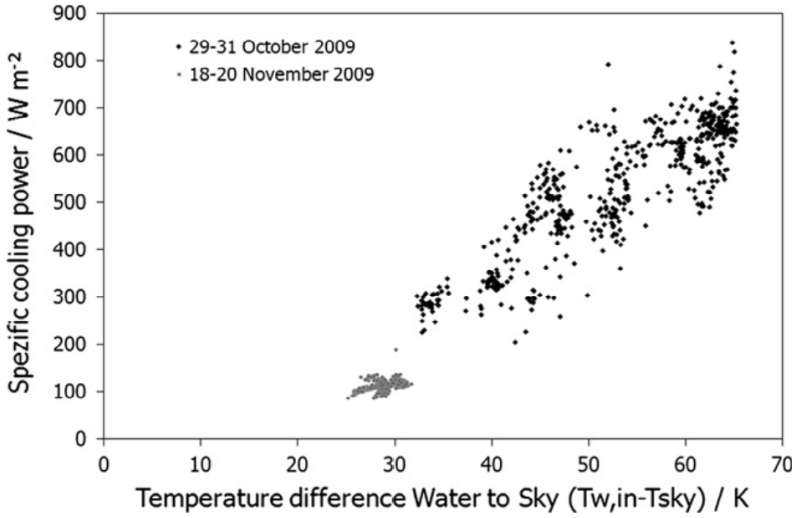

Figure 2.3: Eicker and Dalibard [2011] heat fluxes.

Eicker and Dalibard [2011] also install a different set of PVT panels in a model home. These PVT panels consisted of copper tubes (ID 15 mm) fastened with aluminum strips to the back of PV modules with a high conductivity glue. The area of one panel is 2.8 m^2 and the mass flow rate is 20 kg per m^2 per hour. Several operating modes were tested in Madrid, Spain in June. The average cooling power when the uncovered PVT panel was cooling from a storage tank (approximately 40°C) at night was 40-70 W/m^2 . It is notable that the heat flux from the Spain system was much less than from the prototype system, but the ambient temperatures in the October and November periods in Germany were down to 5°C at night while in Spain they were about 20°C at minimum. This in addition to the different PVT panel geometries likely accounts for the differences in performance.

Erell and Etzion [2000] propose flat plate solar collectors to provide nighttime cooling for a building. They begin by outlining the differences between a solar collector and a flat plate radiator: mechanical pumping is required for a radiator (natural circulation not possible), convection effects can work to the advantage of the radiator instead of being considered a loss mechanism so a cover is not necessarily best, and the heat flux is significantly less and so the ideal solar collector geometry is not the ideal radiator geometry. The authors use the solar collector model in Duffie and Beckman [2013] to model an uncovered radiator where the radiation term is linearized. They note that the loss coefficient U_L in the solar collector model can not be assumed constant as convection plays a more significant role and varies with wind speed. They describe the effects of the solar collector parameters based on radiator and ambient temperatures: tube spacing W, fin efficiency F, collector efficiency F', mass flow rate, and loss coefficient U_L. An experiment is also completed wherein three different radiators were tested. Two were conventional solar collectors except they had no convection shields (one insulated on bottom one not) and the third radiator had copper tubes with finned surfaces as in a car radiator. Though the exact range of test conditions and dates is not provided, the authors state that a range of conditions were tested, and at least some of them were in July in Israel. Operating temperatures were around 20°C. They suggest that the typical finned plate geometry may not be optimal for cooling performance depending on

the ambient conditions and propose a radiator consisting only of pipes.

Tevar et al. [2015] present experimental results from three different 'radio-convective' panels designed for use in building cooling. Experiments were completed in Almeria in Spain. The three uncovered panels tested were 1) panel with complex geometry and high emissivity 2) selective absorbency plate and 3) white metallic panel. The emissivity for the three are 0.9, 0.02, and 0.05, respectively, chosen to cover a wide range. The very low emissivity panel was useful to isolate convection and conduction effects from radiation. The range of conditions over the 15 nights in July included in the test covered clear to cloudy skies and winds from 0 to 4 m/s. The high emissivity panel provided maximum cooling of 63.7 W/m^2 . The experimental results compared well with the theoretical, which were based on solar collector calculations as in Duffie and Beckman [2013]. Though the temperature of the test was not provided, since the application is specifically for building cooling it is assumed to be low.

One consideration in implementation of radiative cooling systems is dew accumulation. In fact in some places a radiating surface is used to collect water at night [Smith, Geoffrey B., Granqvist, 2011]. Water on a radiative surface reduces the cooling potential because water is an infrared absorber. The accumulation of dew depends on the climate and how cold the radiator operates. According to Smith it is not a major problem and can be handled with slotted surfaces as needed. In the current application for cooling in a dry climate, dew accumulation is expected to be minimal. The condensation and, later, evaporation of the water is expected to have little effect on the overall heat rejection from the panels overall.

Radiative cooling for power plants

Zeyghami and Khalili [2015] propose using a selective surface to provide daytime radiative cooling as supplemental cooling for air-cooled supercritical carbon dioxide cycles for solar thermal power. The selective surface reflects solar insolation and emits in the atmospheric window of 8 -13 micrometers. Based on modeled operation, the net output of the cycles is improved by 3 to 8% depending on cycle configuration

(recompression or not) and hot temperature (500 to 800°C). They note that the largest improvements from reducing cycle condensing temperature are for lower temperature cycles. Peak radiative cooling is 135 W/m^2 .

Olwi et al. [1992] propose a white covered pond to provide passive cooling for thermal power plants in the desert both day and night. One typical day (September) is modeled using hourly steady-state conditions. Water at 50°C enters the pond in the upper layer that is separated by a screen from the lower (cold) layer of water. The sky temperature estimate is based on correlation to dewpoint. A net heat rejection is available all day, although higher at night. According to the model, the total available heat rejection is about 150 W/m^2 (about 50 W/m^2 radiation and 100 W/m^2 convection). The experimental implementation of this model [Sabbagh et al., 1993] showed that the average heat rejection by radiation was about 50 W/m^2 . During the day the upper layer of water is heated, but the authors suggest that in operation this hot water would be 'drawn away'. (The method of eventually cooling this water is not stated, and throwing it away would negate the water saving benefits of a dry-cooled system.) The major problem encountered during testing was that it was difficult to prevent an air gap from being present between the water in the pond and the cover, increasing the resistance to heat transfer. The analysis in the Olwi et al. [1992] lacks a sufficiently long analysis period (only one day) and the feasibility of the system did not include discussion of the pond size required for heat rejection for a power plant-scale system. Regardless, the poor performance in the experiments of Sabbagh et al. [1993] show that it is not a promising method of providing cooling.

Similar to the work of Olwi et al. [1992], a nighttime cooling system for a supercritical organic Rankine cycle was proposed by Vidhi [2014] using radiative cooling from a covered or uncovered pond. Due to a lack of experimental data the results were inconclusive, but it is expected that a cooling pond would be subject to the same problems of daytime heat gain and lack of good heat transfer through pond cover as found by the experimental work of Sabbagh et al. [1993].

Du Marchie Van Voorthuysen and Roes [2013] propose radiating surfaces within the parabolic trough structure of the solar collectors. These radiating surfaces would

provide cooling both day and night using selective surfaces. The radiating surfaces are aluminum mirrors coated in titanium dioxide in order to be transparent to far infrared radiation. The surfaces are also cooled by convection to ambient air. Water would circulate from the condenser through a water tube below the parabolic trough and be stored in a cold storage basin. This water tube would be thermally connected to the cold radiating surfaces with heat tubes. The total insolation for a June day along with average daytime temperature, nighttime temperature, average sky temperature suppression (25°C), and two point estimates for wind speeds are used to analyze the performance. The average heat flux from the radiating surfaces is found to be sufficient to cool a 33% efficient Rankine power cycle fueled by the parabolic trough solar plant. Unlike the current proposed radiative cooling system, the design of Du Marchie Van Voorthuysen and Roes [2013] requires adding complexity to the parabolic trough design that would likely reduce their efficiency from their current best designs. The parabolic troughs solar field is already the most expensive part of a CSP power plant [USDOE, 2012]. The analysis in the paper is limited in that off-design conditions, heat tube performance, condenser performance, and cold water storage tank size were not addressed.

2.2 CSP cooling

2.2.1 CSP power plant cooling

This section summarizes current and proposed systems for CSP cooling and compares their attributes.

Wet and dry cooling

Cooling towers, air cooling, and hybrid systems are the three options typically considered for CSP plants. Though eliminating water usage for cooling, air-cooled condenser systems don't perform as well as wet-cooled systems. An air-cooled system will suffer from either a thermal efficiency penalty or a parasitic load penalty

or both. The performance penalty is because the condensing temperature of an air-cooled system is limited by the outdoor dry bulb temperature (for CSP this issue is magnified in the hot desert during the day). Wet-cooled systems, however, can approach the wet bulb temperature instead, allowing for lower condensing temperatures and therefore higher efficiency in the Rankine steam cycle. The parasitic load penalty for an air-cooled system arises from the fact that it is more energy-intensive to move air than to pump water for cooling. But the thermal efficiency and parasitic load penalties are complex because the two offer a trade-off. In designing the air-cooled system, a larger air-cooled condenser can be used to approach the design day dry bulb temperature more closely at a capital cost and parasitic load penalty. In turn, the parasitic loads on an air-cooled system can be reduced by using a smaller condenser (fewer fans) and accepting a lower thermal efficiency due to higher condensing temperatures. The trade-off requires annual simulations in order to account for the off-design operation of systems.

Section 2.2.1 surveys the literature comparing evaporative cooling towers, air-cooled and hybrid systems (here referred to as wet, dry, and hybrid) and provides a more detailed discussion of the modeling. The performance penalties are highly dependent on how the systems are designed and compared. Though it is now recognized that a levelized cost of energy (LCOE) does not account for the true value of CSP with energy storage and regulating capacity, comparisons often use this metric [Dowling et al., 2017]. A penalty for air cooling is predicted in all of the literature cited in this section; the increase in LCOE predicted ranges from 3 to 9%.

Alternative cooling systems

Because the energy-water issue for CSP power plants is critical, some have proposed alternative cooling systems. In this section alternative cooling systems are summarized including their performance, water use, and cost.

Hybrid wet-dry cooling

Wagner and Kutscher [2010] analyze a hybrid cooling system composed of parallel evaporative cooling tower and air-cooled condenser for CSP and such a system is implemented at the Crescent Dunes power tower plant [SolarReserve, 2015]. The system as proposed by Wagner and Kutscher splits the steam mass flow rate exiting the turbine between the ACC and a heat exchanger using the cooling tower.

Nighttime air cooling

Muñoz et al. [2012] propose an air-cooled condenser that operates at night with cold storage at a CSP plant, taking advantage of low nighttime ambient temperatures in the desert. The authors model a 50 MW CSP power plant that uses a steam-to-water condenser. The cold water is provided using a water-to-air compact heat exchanger. The primary operating mode is to use the compact heat exchanger during the nighttime hours, when ambient temperature is lower than during the day. This cooled water is then stored in cold storage and pumped to the power cycle when it operates. As needed, cooling can also be provided directly from the water-to-air heat exchanger without being stored. The model considered a single nighttime steady state operating condition and a single daytime steady state operating condition. The impacts of varying the day-to-night temperature difference, storage volume, hours of storage, and hours of sunlight were studied. Overall, a six percent increase in cycle efficiency was observed compared to a typical air-cooled cycle. This performance improvement was due to the decrease in turbine back pressure that was possible since the stored water was colder than the day time ambient air. The system's advantage over an air-cooled system was significant for day to night temperature differences of at least 20°C. The added parasitic loads of the water storage system are accounted for and the net efficiency is improved compared to air cooling.

Underground channels for pre-cooling

Goswami [2011] analyzes using underground channels to pre-cool air for an air-cooled condenser at a CSP plant. The basic premise is to circulate air in underground channels and then use an air-to-condensate heat exchanger. An 80 MW power plant was modeled. The solar collector field area was about one square mile, while one tenth of a square mile was required for the underground channels. Lower condenser inlet air temperatures were obtained than is possible with a typical air-cooled system. The decrease in air temperatures was a few degrees, up to 7°C. The net power output of the plant, accounting for the air circulation fans, was higher. Goswami's underground cooling system would suffer from long term performance degradation as the ground was warmed by circulation of air. In addition the cost of underground channels large enough to circulate volumes of air for power plant cooling, as well as the associated ducting to the condenser, in addition to the already high cost of an air-cooled condenser, would be prohibitive and this concept is not further explored for the purpose of the current work.

Vidhi [2014] considers the same for supercritical organic Rankine cycles. Also considered are hybrid cooling systems made up of underground cooling, air cooling, ground loop water cooling, and radiative pond cooling (see also Section 2.1.3).

Spray and deluge enhancements to air cooling

Spray and deluge cooling can be used to augment the performance of air-cooled condensers. Spray cooling the inlet air to air-cooled condensers has been proposed to improve their performance for combined cycle power plants [EPRI, 2003]. A report to Congress references an analysis of spray cooling at a SEGS plant in Daggett, CA, USA [USDOE, 2001]. Spray cooling uses fine mists sprayed onto the inlet air of an air-cooled condenser to reduce the dry bulb temperature of the air by humidification. The application of the spray should be fine tuned to minimize water use and scaling of the condenser surface as well as other maintenance impacts of the unevaporated water. Deluge cooling uses water sprayed on air-cooled condenser surfaces to reduce the effective heat sink temperature as well as increase the heat

transfer coefficient at the surface [Poullikkas et al., 2011]. Spray and deluge cooling have not been studied widely for CSP. In addition these methods still require water consumption. Water use could be minimized by using only during peak summer periods, but in that case the impact is small overall.

Heller cycle indirect air cooling

The indirect cooling system called the Heller cycle has received some attention for CSP cooling (USDOE [2001], Poullikkas et al. [2011], Colmenar-Santos et al. [2014]). In an indirect air-cooled system the steam exiting the turbine in the power cycle is cooled by a fluid that is then cooled externally. The critical component of the Heller cycle is the direct injection of cooling water into the steam cycle after the turbine. The steam is condensed directly by contact with the water at a water-to-steam mass ratio of 20 or higher. A portion of this water continues to the boiler feedwater and the remainder is cooled with a dry cooling tower. Configurations of the air side cooling could include a natural or forced draft dry tower with some augmentation by spray cooling, deluge cooling, or hybrid wet-dry system.

The typical Heller cycle uses this direct contact spray condenser (or barometric condenser or jet condenser) and a natural draft dry cooling tower. In a dry cooling tower water circulates in air-to-water heat exchangers around the base of a large tower and natural convection creates air movement from the bottom to the top, cooling the water to approach the dry bulb temperature. The cooling water is pumped from the condensing pressure to slightly above atmospheric pressure to avoid air leaking into the water. Cooled water is moved back to the power cycle and an energy recovery turbine is used as the water goes back down to the cycle low side pressure.

Many Heller systems have been implemented outside of the US [EPRI, 2004] but most of the information available on the systems and their performance benefits is from the manufacturers such as Balogh and Szabo [2008]. EPRI [2004] provides the most objective comparison to air-cooled systems, though their analysis still uses manufacturer performance estimates. The EPRI report considers the cost and

performance of a 500 MW coal plant with Heller cycle cooling augmented by deluge cooling and a 750 MW combined cycle plant with Heller cycle cooling (no deluge cooling). The 500 MW cycle with Heller system had a slightly higher energy output (+0.5% gross and +1.3% net) compared to ACC. The 750 MW combined cycle plant with Heller system also had slightly higher energy output (+0.2% gross and +0.5% net) compared to ACC. The improvement in net output above gross is due to the reduction in parasitic loads for the natural draft cooling tower compared to ACC with fans. The gross improvement of both plants over air-cooled is less straight forward as both operate against the ambient dry bulb temperatures. One reason for the slight improvement may be that the turbine back pressure is not limited by the minimum pressure limits of steam ducting to an ACC.

According to cost information comparisons provided by the manufacturer, the Heller system would have a higher initial cost but due to higher plant output and lower operating costs, the total cost of the Heller cycle is less than that of the ACC. The EPRI report concludes that the Heller cycle is worth considering when dry cooling is required though the choice is highly dependent on actual costs. Downsides to choosing a natural draft system are that the height required for a natural draft tower makes them only effective for large plants and the visibility of the tall cooling tower may be not be acceptable depending on location (though wet cooling towers also have such issues due to a visible plume).

PV power for ACC parasitic load

Carter and Campbell [2009] suggest using photovoltaics (PV) to provide fan power for air-cooled systems but a review of the literature found no analysis.

Other alternative cooling systems

A report to Congress also suggests the use of non-freshwater water sources for wet cooling but notes that availability of such water is limited and uncertain [Carter and Campbell, 2009].

Work is currently underway by Martin and Pavlish (in USDOE [2013]) for a desiccant-based cooling system for CSP plants to reduce water usage compared to wet cooling. Nighttime use of the desiccant system can use the inherent energy storage in the material to take advantage of the night temperatures. At this time there are no results available to discern the merits of this proposal.

Damerau et al. [2011] consider water use of CSP in Africa. They use simple approximations of plant performance to compare the impacts of wet, dry, Heller, hybrid, and spray systems. The analysis included the performance impacts of global climate change temperature increases (1.5% to 3% increase in cooling water demand). For wet or hybrid systems, the water source is dependent on the location and could be freshwater, treated waste water, or desalinated seawater. The LCOE for different locations, cooling types, and temperature projections are compared. The results are examined in terms of the time to cost parity with coal and gas and it is found that CSP with alternative cooling systems lags one to two years behind wet-cooled CSP for reaching cost parity with those fuels.

Finally, several have proposed methods that utilize radiative cooling. These are summarized in Section 2.1.3.

Comparison of alternatives

Figure 2.4 sketches how the major low-water use cooling systems compare in terms of gross cycle efficiency and parasitic power requirements. Standard air cooling (forced draft air-cooled condensers) is the benchmark; it is currently feasible and any new technology should demonstrate improved performance and/or decreased cost to be viable. Night sky cooling with radiation, the focus of the current work, is also included. Though the systems vary in their maturity and the analysis that has been completed in the literature varies widely in its level of detail, one can observe the potential benefits of each.

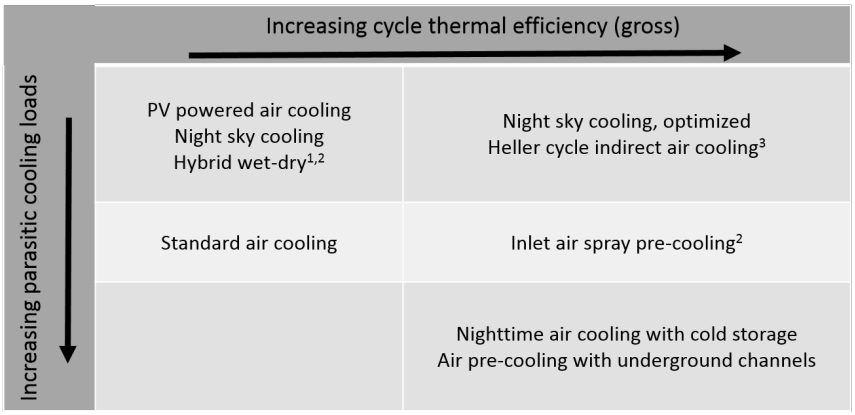

[1] The fraction of wet vs dry cooling capacity in the parallel system changes the parasitic cooling loads and water use. A typical value might be 15% wet cooling capacity/85% air cooling.
[2]Incurrs some water use for cooling, though still less than evaporative cooling with cooling towers.
[3]Heller cycle indirect air cooling can be implemented in a number of configurations. If using dry, natural draft cooling towers the system would have lower parasitic loads than an all air cooled system.

Figure 2.4: Low water use cooling options that have been described in the literature can be roughly categorized by cycle efficiency and parasitic loads. Night sky cooling has low parasitic loads and, when optimized, could offer high cycle gross efficiency.

2.2.2 Rankine cycle design and modeling

This section reviews Rankine cycle models which have been used to assess CSP power plants.

Yildiz [2017] provides a 'Bankability Report' which is a new effort by the SolarPACES organization to provide standardization of CSP power plant assessments to increase the reliability of the economic assessments. Appendix D of this work provides guidance on the power cycle modeling. Performance is typically captured at a range of HTF temperature, HTF flow rate, and ambient temperatures in matricies. A reference heat cycle is described and modeled in process software (not specified). The configuration represents state of the art for a 100 MW plant with six feedwater preheaters for regeneration, HP and LP turbines, and sliding evaporator pressure down to 30 bar (for part load conditions).

SAM is software that simulates renewable power plants including CSP (see Wagner and Gilman [2011] and NREL). SAM uses a multi-step process to regress the part load operation of the power cycle based on the operation at design point (from an Engineering Equation Solver EES [Klein, 2016] model) and off-design operation based on process simulation software (not specified). The simulations are based on Wagner [2008], where a design of experiments approach is used to capture up to two variable interactions. (See also Chapter 4 of this thesis).

Shinners [2014] completes off design modeling of three different CSP plant configurations. EES was used to model the performance of each cycle under various operating conditions including off-design performance of turbines and heat exchange components. The turbine was modeled following methods from Patnode [2006], which uses a correlation for turbine efficiency degradation by according to mass flow rate. A a Stodola's law relationship between pressure drop and mass flow rate is used. The part load efficiency of the turbines was related to mass flow rate - mass flow rates much lower than the reference value lead to significant turbine efficiency degradations. Then the performance under different configurations was regressed based on HTF flow rate and temperature, and cooling water flow rate and temperature. The output variables were power, HTF return temperature, and

cooling water return temperature. The cooling water flow was tested for incoming cold water temperatures of 20 to 35 C (293 to 308 K). The cooling water flow rate is tested for 1200 to 1600 kg/sec. The correlations were implemented in TRANSYS in order to run annual models.

Dyreby et al. [2014] use a constant polytropic efficiency for turbines in SCO2 cycles as a more fair comparison between cycles operating with different pressure ratios. Polytropic efficiencies of 0.8 and 0.9 were tested. In his thesis, Dyreby [2014] uses off-design models of radial turbines where the turbine efficiency is related to the ratio of tip speed to spouting velocity. (The spouting velocity is the ideal velocity if expansion through turbine is isentropic.) The off design turbine model is relevant for up to 50 MW radial turbines.

2.2.3 CSP cooling analysis

This section summarizes studies which compare cooling systems for CSP power plants.

Wet versus dry cooled

Kelly [2006] determines the optimal design for a dry-cooled parabolic trough plant and the LCOE difference between dry and wet-cooled plants. To determine the optimal ACC size and dry-cooled plant design, the dry plant was modeled in detail in GateCycle packaged software [GE]. The power block was an 80 MW plant without thermal energy storage with six steam extraction points and reheat based on the AndaSol power plant. Six different inlet temperature differences (ITD - the difference between the condensing temperature and the ambient air temperature) were used to model the air-cooled system in GateCycle. The model calculated the turbine power and the parasitic cooling load at each ambient dry bulb temperature condition assuming full load operation. The annual output of each of the different designs was determined using bin data of the temperatures during sunlight hours (as their design did not have thermal energy storage). The economic analysis included cost estimates of the systems (the six different condenser sizes

corresponding to different ITD requirements) and these costs were applied to a range of energy prices ($ 0.06 to 0.14 / kWh). Air-cooled condenser costs were based on a correlation for $ per MW cost to ITD. An optimal ITD of approximately 35-40°F is chosen for the dry-cooled plant based on net value. This is notably higher than typical for fossil fueled plants because without thermal energy storage, the solar plant very seldom operates at peak power and design point conditions, so a lower ITD (larger condenser) would not be justified. The optimal ITD for net value assuming full load operation is not affected by the price of energy, though if time of day pricing were applied this would change the result. The impact of upper limits on condenser pressure are also shown to be minimal by additional analysis of the lowest LCOE dry-cooled case (40 °F ITD).

To compare the LCOE for the wet- and dry-cooled systems, the Excelergy program (correlations based on actual performance data from the SEGS power plants) is used to analyze off-design operation of both wet- and dry-cooled plants. Default values are used, thus no longer capturing the GateCycle model for the air-cooled plant. Annual results show that the air-cooled plants have 91- 96% of the annual output of the wet-cooled plant. The LCOE increase for an air-cooled plant was 8 to 9% assuming a water cost of $1.40 per 1,000 gallons. The water cost would have to be ten times higher to make the LCOE equal for the two plant types.

Air-cooled preliminary study for SEGS VI

Patnode [2006] examines an air-cooled alternative for the water-cooled SEGS VI plant located in California. The noted advantages are water conservation as well as optical performance improvement of the solar field when the humid air from the existing cooling towers is eliminated. The performance penalty is considered. An air-cooled system is designed by using performance characteristics of a condenser from literature and choosing the optimal number of such condenser units to maximize the net power output accounting for the parasitic fan penalties associated with reducing the condensing pressure. This optimization is completed for design conditions. Annual variations are examined by using design conditions for each

month and determining the condensing pressure that is achievable with the existing cooling tower or the alternative air-cooled system. The plant operation is simulated in detail for one day in June. A simple cost benefit analysis based on the single day of operation was done. The LCOE of the reduction in power output of the plant when air-cooled is used to estimate the cost (the added cost of the air-cooled condenser was not accounted for) and the benefit is estimated by the savings due to water cost savings. In this limited framework, the benefits did not justify the costs.

Multiple CSP plant designs

Turchi et al. [2010] details a comparison between wet, dry and hybrid cooling systems' cost and performance. The work consolidates and builds on detailed work by WorleyParsons (WorleyParsons [2009a], WorleyParsons [2009b], WorleyParsons [2010]). Thirteen plant designs are compared over three different locations in the Southwest US (Las Vegas, Nevada, Daggett, California, and Alamosa, Colorado). The levelized cost of energy (LCOE) increased for dry cooling compared to wet by 3 to 8%. Water usage of the plant decreased by 90%. Performance modeling was done with GateCycle software.

The report provides detailed discussion of how power plant designs can be compared for different cooling systems. Two paradigms are presented for comparing CSP cooling systems: fixed solar field size, or fixed electricity output at design. (Other literature in this section compares power plants with fixed solar fields.)

For Las Vegas, Nevada and Daggett, California sites, the ACC cost per MW net output at design conditions is optimized by varying ITD. In both cases an ITD of 25 °F (14 C) was selected. The analysis also considered year round operation and found that when optimizing ACC cost per MWh, the ITD was minimized for 25 to 32 °F. It is noted that ITD selection is sensitive to solar field costs and thermal energy storage size. The 14 °ITD is on the low side.

When comparing a wet and dry plant in Daggett, CA and requiring the same net output at design point, the air-cooled plant must have a larger solar field and power block than the wet-cooled plant because its thermal efficiency is lower at

design conditions. However when off-design operation is considered, the dry plant actually produces more energy over the course of the year because during many hours of the year the dry bulb temperature is much lower than design point so the oversized solar field and turbine provide higher output. The parasitic power from the air-cooled system is about double that of the water cooled system and the plant cost is much higher due to the ACC itself as well as the over sized field and turbine. A comparison at the Las Vegas, NV location found similar results and a LCOE increase of 6.3% was attributed to the switch from wet to dry cooling, in this case assuming a constant solar field size instead of a constant plant output at design conditions. The Alamosa, CO site was unique in that it is a high elevation site with a lower solar resource. Because the labor rates were at this site are lower, the cost penalty for dry cooling compared to wet is lower and the LCOE increase is less. Further modeling is done with the System Advisor Model (SAM) to examine time of day impacts on LCOE but those impacts were small. Specifically an energy price schedule favoring peak periods was implemented for the dry and wet-cooled plants. The turbine was allowed to operate over its rated capacity up to 105% during the peak price period.

Wet, dry, and hybrid cooling analysis

A comparison of air-cooled, cooling tower, and hybrid cooled performance for a CSP power plant is provided by Wagner and Kutscher [2010]. SAM is used to model the 95 MW_t solar field and IPSEpro [SimTech, 2017] is used to model the 35 MW_e (gross) power Rankine cycle with five steam extraction points. (Here MW_t and MW_e are used to distinguish the thermal and electrical energy in the CSP system.) The boiler pressure is allowed to vary with HTF temperature.

System optimization accounted for the relative benefits of a low turbine back pressure (for higher first law efficiency in the cycle) and the increased parasitic fan loads that are required to maintain low back pressures. Important results from the annual simulation are that the wet-cooled plant's efficiency was 2.5% higher than the air-cooled plant and the wet-cooled plant produced 7% more energy over

the year for the same solar field size. The parasitic load penalty for air cooling did not occur because the turbine's back pressure in the air-cooled plant was selected to reduce the parasitic load penalty. In this case a lower thermal efficiency was accepted so that the parasitic loads were the same as the wet-cooled plant.

Moser et al. [2013] studies how a parabolic trough plant with air-cooling can be operated considering sensitivity to dry bulb air temperature. An optimization is done the results show preference for night time operation. The off-design performance of the steam turbine are not provided but are based on characteristic lines from a manufacturer.

2.2.4 Cooling for supercritical CO2 cycles

Supercritical CO2 Brayton cycles offer some advantages compared to superheated steam Rankine cycles. The turbomachinery size is significantly smaller due to the fluid properties of supercritical CO2. Higher cycle efficiencies can be obtained with sCO2 Brayton once the source temperature exceeds 550°C Dyreby et al. [2014]. Both cycles can use air cooling and there is current interest in sCO2 for CSP power cycles, so some notes on these cycles are of interest though sCO2 is not considered in the analysis in this thesis.

The use of air cooling for SCO2 Brayton cycles is often highlighted because other fluids considered for supercritical Brayton cycles have critical temperatures too low for ambient temperature sinks to be useful (CO2 31.1°C and 7.39 MPa, Helium -268°C and 0.228 MPa, Air -141°C and 2.79 MPa). Water, on the other hand, has very high critical temperature and pressure, requiring very high temperature heat sources and high strength materials for operating pressures of a supercritical water cycle (373.9°C and 22.1 MPa). But many also highlight the special benefits of air cooling a sCO2 Brayton cycle compared to a Rankine cycle. Hruska et al. [2016] find that the air-cooled SCO2 Brayton cycle requires a smaller air-cooled heat exchanger and higher cycle efficiency than the air-cooled steam Rankine cycle. Conversely, Cheang et al. [2015] conclude that steam Rankine cycles are more efficient and, when considering the total plant cost, are more cost effective than SCO2 cycles for

solar applications. Conboy et al. [2014] consider nuclear applications and show that SCO2 Brayton with air cooling is beneficial.

Hruska et al. [2016] compare Rankine and SCO2 Brayton cycles by fixing the heat source temperature at 700 °C and requiring equivalent power output. Both cycles are relatively simple (Rankine with single feedwater heater and Brayton with regeneration - no recompression.) Using the same size heat exchanger, the Brayton cycle is shown to achieve lower condensing temperatures and therefore higher efficiencies.

3 HEAT TRANSFER MODEL OF RADIATIVE-CONVECTIVE PANELS

This chapter details the modeling and validation of the heat transfer from uncovered radiative-convective panels. Passive cooling for both homes and industry continues to see attention in the literature due to its energy and, in the case of power plant cooling, water saving potential. The results presented here and the provided heat transfer code are useful for modelers investigating potential for passive cooling systems for both comfort cooling and industrial applications.

The first section details the three models: two analytical models and a numerical model. The models apply to uncovered, high conductivity, high emissivity plates with single pass circulating fluid and can be extended to include other plate geometries (see Duffie and Beckman [2013] or Bliss [1959] for other geometries). The second section provides validation of the models using existing data, compares the three models, and describes an experimental design for testing the models. Based on the results herein, the analytical model based on the classic solar collector model by Duffie and Beckman [2013] as modified by Ito and Miura [1989] is recommended. It is more accurate than the classic formulation of the analytical model for a variety of designs and operating conditions. In addition, it is more computationally efficient than a finite differences model.

3.1 Modeling heat transfer from radiative-convective panels

Three models are presented.

3.1.1 Basic analytical formulation

The first of three models included in this work is an analytical model closely based on the solar model from Duffie and Beckman [2013] as detailed by Eicker and Dalibard [2011] for radiative-convective cooling panels. One notable difference,

discussed further in Section 3.1.2, is that the reference temperature here is the effective sky temperature T_s instead of ambient. The general equation for useful heat loss rate is written in terms of the temperature difference $(T_p - T_s)$.

$$Q_u = A_c U_{L,s}(T_p - T_s) \tag{3.1}$$

Where T_p is the representative temperature of the plate, $U_{L,s}$ is the overall loss coefficient, and A_c is the area of the collector surface.

Figure 3.1 shows a cross section of a radiative-convective panel that is uncovered and uninsulated and example temperature profiles along the lateral (x) and flow (y) directions. Tubes in the panel circulate the cooling fluid. The geometry of the collector is described by the number of tubes in parallel in one collector n, the center-to-center distance between tubes W, the tube diameter D, the length of the plate L, and the thickness of the absorber plate th. The area of the collector surface is $A_c = nWL$.

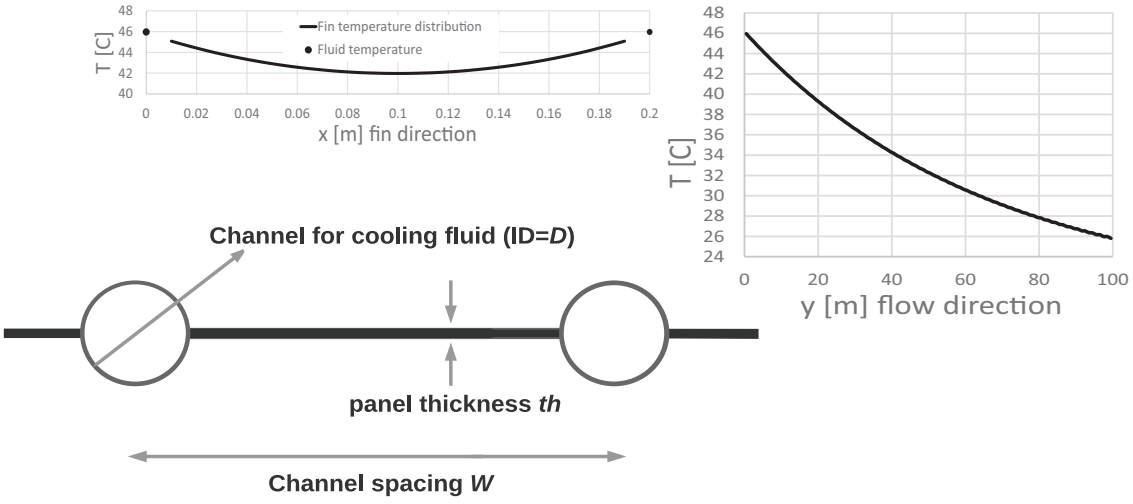

Figure 3.1: A cross section of a radiative-convective panel (bottom left). The temperature is lowest in the midpoint between tubes (top left). The temperature of the fluid in the tubes decreases along the panel length (right).

Radiative and convective heat transfer coefficients are defined relative to the difference between the plate temperature and the effective sky temperature. The radiation heat transfer from the top of the collector to the effective night sky T_s is determined by radiation transfer between a small convex object (plate) and a large enclosure (sky). Only the emissivity (ϵ) of the small surface, in this case the panel, is relevant; the large enclosure acts as a blackbody. Dividing the heat flux rate by $(T_p - T_s)$ to reference the plate-sky temperature difference, the radiation coefficient relative to the sky temperature is:

$$h_{r,t} = \sigma \cdot \epsilon \cdot \frac{T_p^4 - T_s^4}{T_p - T_s} = \sigma \cdot \epsilon \cdot (T_p^2 + T_s^2)(T_p + T_s) \tag{3.2}$$

The Stephan-Boltzmann constant is σ. Other formulations linearize the heat transfer coefficient as described in Duffie and Beckman [2013], but the formulation in Equation 3.2 is simply an algebraic operation and does not make any approximations to linearize radiation heat transfer. Assuming that the radiator surface is exposed to the ground on the back side, the radiation heat transfer from the bottom of the plate to the ground temperature (T_g) is based on radiation exchange between two flat infinite plates. The panel back has emissivity ϵ_b and the ground has emissivity ϵ_g. The heat transfer coefficient relative to the sky temperature is:

$$h_{r,b} = \sigma \cdot \frac{1}{\frac{1}{\epsilon_b} + \frac{1}{\epsilon_g} - 1} \cdot \frac{T_p^4 - T_g^4}{T_p - T_s} \tag{3.3}$$

The convection coefficients from the top ($h_{c,t}$ to ambient air) and bottom ($h_{c,b}$ to ground) are determined from convection correlations for a given condition per standard methods. Depending on the conditions the convection may be forced or free (natural). The coefficients are normalized to the plate-sky temperature difference:

$$h_{c,t,s} = h_{c,t} \frac{T_p - T_a}{T_p - T_s} \tag{3.4}$$

$$h_{c,b,s} = h_{c,b} \frac{T_p - T_g}{T_p - T_s} \tag{3.5}$$

Radiation and convection act in parallel for heat transfer from the top of the panel and bottom of the panel. With these four resistances acting in parallel relative to the temperature difference ($T_p - T_s$), the overall loss coefficient ($U_{L,s}$) is a sum of the four individual coefficients.

$$U_{L,s} = h_{r,t} + h_{c,t,s} + h_{r,b} + h_{c,b,s} \tag{3.6}$$

A fin analysis is used to model the temperature variation between tubes. The collector efficiency (F') combines the traditional fin efficiency (F) with the resistance of the tube wall and internal flow resistance to represent the lateral direction temperature variation in the x-direction as in Figure 3.1 (inset). The reader is referred to Duffie and Beckman for F and F'.

Next the temperature distribution in the flow direction (y-direction) is examined. The fluid outlet temperature ($T_{f,o}$) at $y = L$ is then written (using $A_c = nWL$) :

$$T_{f,o} - T_s = (T_{f,i} - T_s) exp(-\frac{A_c F' U_{L,s}}{\dot{m} c_p}) \tag{3.7}$$

Where the inlet temperature is $T_{f,i}$, the mass flow rate is $\dot{m}$, and the specific heat capacity of the fluid is c_p. As noted in Duffie and Beckman [2013], this distribution of temperatures assumes that the fin efficiency and loss coefficient are constant over the flow direction of the plate. The collector heat removal factor (F_R) is defined to account for the flow direction temperature variation in the y-direction as in Figure 3.1 (inset). F_R is the ratio of the useful heat rejection to the useful heat rejection that would take place if the whole collector were at temperature $T_{f,i}$ and the loss coefficient was unchanged.

$$F_R = \frac{\dot{m} c_p (T_{f,i} - T_{f,o})}{A_c U_{L,s} (T_{f,i} - T_s)} \tag{3.8}$$

For reference an effectiveness relative to the sink temperature (here T_s) and rela-

tionship to F_R is:

$$\epsilon_{rad} = \frac{Q}{Q_{max}} = \frac{T_{f,i} - T_{f,o}}{T_{f,i} - T_s} = F_R \frac{A_c U_{L,s}}{\dot{m} c_p} \tag{3.9}$$

Equations 3.8 and 3.7 can be used to eliminate $T_{f,o}$ and $T_{f,i}$ and finally write the heat removal factor as:

$$F_R = \frac{\dot{m} c_p}{A_c U_{L,s}} (1 - exp(-\frac{A_c U_{L,s} F'}{\dot{m} c_p})) \tag{3.10}$$

The total heat rejection is then written in terms of F_R, A_c, $U_{L,s}$, T_s and the inlet fluid temperature $T_{f,i}$:

$$Q_u = F_R A_c U_{L,s} (T_{f,i} - T_s) \tag{3.11}$$

Finally the outlet temperature is determined from the total heat rejection:

$$Q_u = \dot{m} c_p (T_{f,i} - T_{f,o}) \tag{3.12}$$

The collector operation is thus parameterized so that given inlet temperature, mass flow rate, geometry, and ambient conditions, the total heat rejection can be determined. An iterative solution method is required because of the dependence of $U_{L,s}$ on the plate mean temperature. Equations 3.1, 3.10, 3.11, and 3.12 are solve iteratively along with the formulations for $U_{L,s}$, F, and F', appropriate for given geometry and taking into account wind conditions.

In order to most accurately evaluate fluid properties in the tubes, a mean fluid temperature is calculated by Duffie & Beckman. In this work the mean fluid temperature is estimated by the inlet fluid temperature because fluid property differences along the tube are not critical for the problem.

3.1.2 Analytical formulation using adiabatic reference temperature

In this section the adiabatic temperature is defined and used as a reference temperature in a reformulated solar collector model instead of the sky temperature. The

issue of reference temperature choice and implications for modeling are discussed.

Adiabatic temperature concept

Ito and Miura Ito and Miura [1989] present an adiabatic minimum temperature (or adiabatic temperature) that provides realistic sink temperature reflecting the strength of radiation and convection heat transfer to the ambient. The adiabatic temperature is the surface temperature at which there is zero net heat transfer. For a plate being cooled, the adiabatic temperature provides a lower bound for the desirable outlet temperature; if the outlet temperature is less than the adiabatic minimum, the plate begins to approach the adiabatic state.

To derive the adiabatic temperature, the total heat transfer is written using expanded and linearized radiation terms. Radiation heat transfer is linearized using the average of the plate and ambient temperatures ($\bar{T}_{p,a}$) (as in Nellis and Klein [2009] and other texts). The radiation from the top of the panel to the sky is expanded and linearized:

$$Q_{r,t} = \sigma\epsilon\left(T_p^4 - T_s^4\right) = \sigma\epsilon\left(T_p^4 - T_a^4\right) + \sigma\epsilon\left(T_a^4 - T_s^4\right) = \sigma\epsilon(T_a^4 - T_s^4) + \sigma\epsilon 4\bar{T}_{p,a}^3(T_p - T_a) \tag{3.13}$$

The radiation to the ground is treated similarly. Summing the radiation and convection to the top and bottom and collecting terms in $(T_p - T_a)$, the heat transfer rate is:

$$Q_u = A_c\sigma\epsilon(T_a^4 - T_s^4) + A_c\sigma\frac{1}{\frac{1}{\epsilon_b} + \frac{1}{\epsilon_g} - 1}(T_a^4 - T_g^4) + h_{c,b}A_c(T_a - T_g) + A_c\left(4\sigma\epsilon\bar{T}_{p,a}^3 + 4\sigma\frac{1}{\frac{1}{\epsilon_b} + \frac{1}{\epsilon_g} - 1}\bar{T}_{p,a}^3 + h_{c,b} + h_{c,t}\right)(T_p - T_a) \tag{3.14}$$

When the plate temperature equals the adiabatic temperature (T_{ad}), the total rate of heat transfer Q_u is zero. These substitutions ($Q_u = 0$ and $T_p = T_{ad}$) are made in Equation 3.14. Because the radiation terms have been linearized for $(T_p - T_a)$, it

is simple to then solve for the adiabatic temperature, except that the average of the adiabatic and ambient ($\bar{T}_{ad,a}$) remains. For the case of an uninsulated, uncovered panel, the adiabatic temperature is given by Equation 3.15:

$$T_{ad} = T_a - \frac{\sigma\epsilon(T_a^4 - T_s^4) + \sigma\frac{1}{\frac{1}{\epsilon_b}+\frac{1}{\epsilon_g}-1}(T_a^4 - T_g^4) + h_{c,b}(T_a - T_g)}{4\sigma\left(\epsilon + \frac{1}{\frac{1}{\epsilon_b}+\frac{1}{\epsilon_g}-1}\right)\bar{T}_{ad,a}^3 + h_{c,b} + h_{c,t}} \tag{3.15}$$

Note that this equation is implicit in adiabatic temperature because the radiation heat transfer rate depends on the surface temperature. Given ambient conditions and convection coefficients, one can solve iteratively for the adiabatic temperature. Free convection coefficients do depend on the plate temperature, but since free convection is typically small compared to forced and to the radiation heat transfer, approximations for plate temperature are acceptable.

The adiabatic temperature provides a physically meaningful temperature on which to base the analytical solution; it is always less than the ambient dry bulb temperature and greater than the sky temperature. The adiabatic temperature is closer to the air temperature for higher wind speeds and it approaches the sky temperature when the wind is calm.

Adiabatic reference temperature model

An analytical formulation based on that of Ito and Miura is presented. Ito and Miura estimate that $\bar{T}_{ad,a} = T_a$ in Equation 3.15 in order to implement the solar collector model. That approximation is not good when the adiabatic temperature is far from the ambient, which occurs when the radiation heat transfer is strong compared to convection. In the current formulation, instead the adiabatic temperature is replaced with the plate temperature in Equation 3.15 (in the term $\bar{T}_{ad,a}$) . This is a closer approximation, and the model is proven by comparison to the finite difference model in this Chapter. With this substitution, the approximate adiabatic minimum temperature (T^*) is:

$$T^* = T_a - \frac{\sigma\epsilon(T_a^4 - T_s^4) + \sigma\frac{1}{\frac{1}{\epsilon_b}+\frac{1}{\epsilon_g}-1}(T_a^4 - T_g^4) + h_{c,b}(T_a - T_g)}{4\sigma\left(\epsilon + \frac{1}{\frac{1}{\epsilon_b}+\frac{1}{\epsilon_g}-1}\right)\bar{T}_{p,a}^3 + h_{c,b} + h_{c,t}} \tag{3.16}$$

The overall heat transfer coefficient using the adiabatic minimum as the reference temperature is defined as:

$$U_L^* = 4\sigma\left(\epsilon + \frac{1}{\frac{1}{\epsilon_b}+\frac{1}{\epsilon_g}-1}\right)\bar{T}_{p,a}^3 + h_{c,b} + h_{c,t} \tag{3.17}$$

The analytical model in Section 3.1.1 is applied to account for flow-direction and fin-direction temperature profiles using temperature difference $(T_p - T^*)$ instead of $(T_p - T_s)$. The fin efficiency, collector efficiency, and heat removal factor are defined with T_s replaced with T^* and U_L is replaced with U_L^* as appropriate. Substituting the overall heat loss coefficient Equation 3.17 and adiabatic temperature Equation 3.15 into Equation 3.1, the resulting heat transfer is indeed equivalent to Equation 3.14, the heat flux from a surface at temperature T_p.

The model is implemented by first estimating the plate temperature with the inlet fluid temperature in Equations 3.16 and 3.17. Implementation of the collector model then gives an estimate of the plate temperature. Iterations are repeated until the plate temperature converges.

Importance of thermal sink reference temperature choice

The analytical model allows for both radiation heat transfer (to the effective sky temperature) and convection heat transfer (to the ambient air temperature) in a single loss coefficient by normalizing both the radiation and convection heat transfer coefficients to a single reference temperature. In Duffie and Beckman [2013], the reference temperature is the ambient T_a and the heat transfer coefficients are referenced to the plate-ambient temperature difference. Sections 3.1.1 and 3.1.2 show that the analytical model can also be formulated using the effective sky

temperature or the adiabatic minimum temperature. When applying the collector model for cooling applications, the choice of reference temperature becomes an important consideration. (This is not an issue for solar hot water collectors where losses are small compared to gains in the heat transfer.)

For a given choice of reference temperature, there is a related loss coefficient (U_L, U_L^*, or $U_{L,s}$, for ambient, adiabatic, or sky temperature references, respectively). Under some conditions, the loss coefficient can be negative. Table 3.1 summarizes how the sign of the loss coefficient for each model depends on the plate temperature with reference to the ambient, adiabatic and sky temperatures. A model based on the adiabatic temperature has a positive loss coefficient U_L^* in any condition, while using the other two reference temperatures can, at times, result in a negative loss coefficient. Computationally, it is more difficult to find the solution to a problem where the loss coefficient may be either positive or negative. The effective sky temperature reference model has a positive loss coefficient in any cooling condition. The ambient air temperature reference has a negative loss coefficient during some net cooling conditions, so it is not implemented in the solar collector model in this paper.

Table 3.1: Depending on the plate temperature's value compared to the ambient and adiabatic temperatures, the loss coefficient can be negative. Here ambient (T_a and U_L), sky (T_s and $U_{L,s}$), and adiabatic minimum (T^* and U_L^*) are shown. The loss coefficient will be positive regardless of the choice of reference temperature when both radiation and convection are cooling the surface. When there is convective heating combined with radiative cooling, the loss coefficient can be negative.

	$T_s < T^* < T_a < T_p$	$T_s < T^* < T_p < T_a$	$T_s < T_p < T^* < T_a$
	Cooling by convection & radiation	Net cooling; convection heating + radiation cooling	Net heating; convection heating + radiation cooling
$Q_u = A_c U_L (T_p - T_a)$	$0 < U_L$	$U_L < 0$	$0 < U_L$
$Q_u = A_c U_{L,s} (T_p - T_s)$	$0 < U_{L,s}$		$U_{L,s} < 0$
$Q_u = A_c U_L^* (T_p - T^*)$	$0 < U_L^*$		

The solar collector model has been implemented for radiative-convective cooling applications in different ways in the literature. For example Eicker and Dalibard [2011] and Farmahini Farahani et al. [2010] use the ambient temperature while Ito and Miura [1989] use the adiabatic temperature. When applying a model, it is important to understand how radiation is accounted for and what thermal sink temperature has been defined.

3.1.3 Finite difference model

A two dimensional finite difference model of the radiative-convective panel solves the combined heat transfer problem numerically. This model is implemented here for validation of the analytical models because, with an adequately discretized grid, there are no assumptions made about the temperature distribution as is required in the analytical model (see Section 3.1.1). For the purpose of the model validation here, it was assumed that skies were clear (cloudiness fraction equal to zero). Figure 3.2 shows the cross section of a radiator and indicates the reduction of the problem based on symmetry to one single half-tube and fin section. Edge effects are assumed

minimal and are not included. Figure 3.3 shows a top view of the same section of the radiator. The fin is modeled with nodes indexed by i in the x-direction and j in the y-direction. The fin tip, which is the midpoint between two tubes, is modeled as adiabatic.

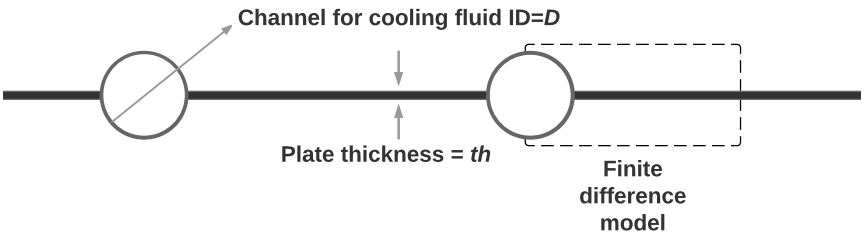

Figure 3.2: A cross section of the roll bond radiator panel is shown along with the section which is modeled in the two dimensional finite difference model.

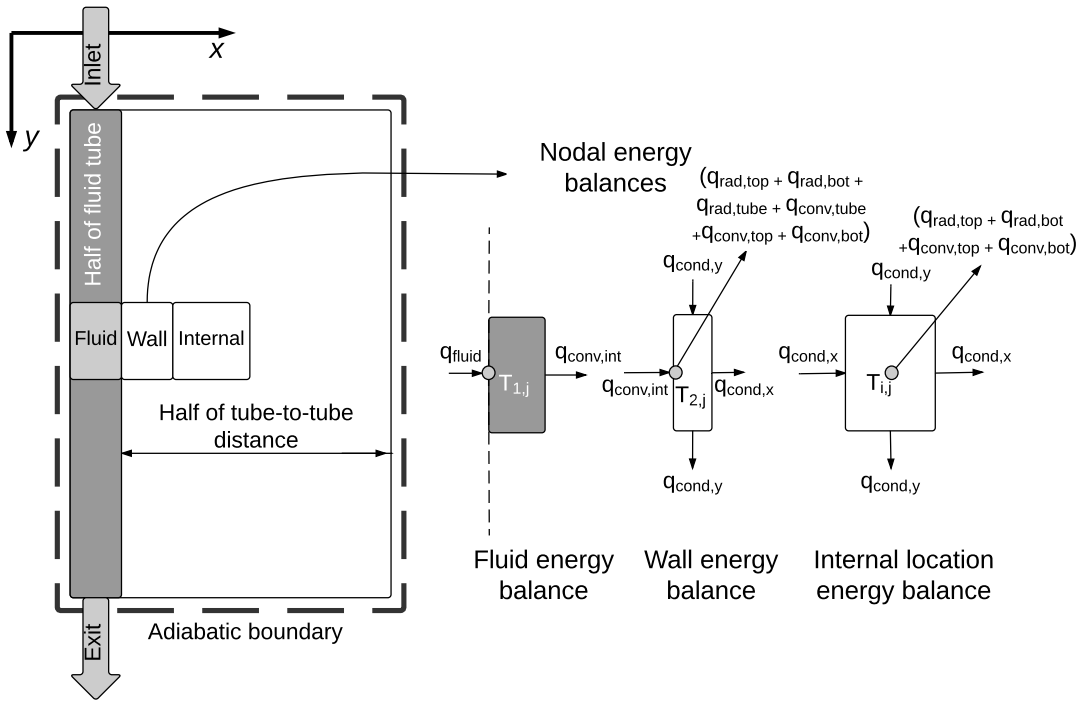

Figure 3.3: A top view of one section of the radiator panel shows examples of the energy balances completed depending on node location (insets in the figure).

On any given node at location (i, j) with temperature $T_{i,j}$, radiation and convection heat rates are determined from the node temperature. An energy balance on each control volume using two point finite differences for the temperature gradient is completed. The energy balance for any control volume can include convection to ambient, radiation to sky, conduction between adjacent nodes, and convection from fluid. Figure 3.3 shows the three main control volume types and the heat transfer modes included. The distance between nodes in the x-direction is dx (except the distance from the first fluid node to the second wall node, which is exactly a distance of half of the tube diameter). The distance between nodes in the y-direction is dy.

A conduction term in the x-direction on an internal control volume is:

$$\dot{q}_{cond,x} = k dy th \frac{1}{dx} \left(T_{i-1,j} - T_{i,j}\right) \tag{3.18}$$

Likewise a conduction term in the y-direction is:

$$\dot{q}_{cond,y} = k dx th \frac{1}{dy} \left(T_{i,j-1} - T_{i,j}\right) \tag{3.19}$$

The radiation heat transfer from the top of the panel on an internal control volume $\dot{q}_{rad,top}$ is determined from:

$$\dot{q}_{rad,top} = \sigma\epsilon(1 - f_{cloud}) dx dy \left(T_{i,j}^4 - T_s^4\right) + \sigma\epsilon f_{cloud} dx dy \left(T_{i,j}^4 - T_a^4\right) \tag{3.20}$$

Where the portion of the sky that is considered cloudy f_{cloud} has an temperature of the dry bulb, not sky temperature. The convection heat transfer from the top is:

$$\dot{q}_{conv,top} = h_{c,t} dy dx \left(T_{i,j} - T_a\right) \tag{3.21}$$

Radiation from the bottom of the panel to the ground is based on radiation exchange between two parallel surfaces:

$$\dot{q}_{rad,bot} = \frac{\sigma}{1/\epsilon_p + 1/\epsilon_g - 1} dy dx \left(T_{i,j}^4 - T_g^4\right) \tag{3.22}$$

Convection from the bottom of the panel to the air is:

$$\dot{q}_{conv,bot} = h_{c,b} dy dx \left(T_{i,j} - T_a\right) \tag{3.23}$$

At the fluid node, the rate of change in internal energy of the fluid is:

$$\dot{q}_{fluid} = \dot{m} c_p \Delta T \tag{3.24}$$

Internal forced convection in the tube is based on the temperature difference between the fluid ($T_{1,j}$) and tube, which is assumed to be at the temperature of the

bordering wall node ($T_{2,j}$). The area for heat transfer is half of the tube circumference times the control volume length dy.

$$\dot{q}_{conv,int} = h_{fi}\frac{\pi D}{2}dy\,(T_{1,j} - T_{2,j}) \tag{3.25}$$

Energy balances in two dimensions are completed on each control volume, including convection, conduction, and radiation terms as appropriate depending on location. These energy balances are shown in Figure 3.3 for the fluid control volume, wall control volume, and generic internal control volume. Note that at the wall node, the energy balance includes convection and radiation from the projected half surface of the tube (radius), since this area is also exposed to the same ambient conditions and the tube is assumed to be at the same temperature as the wall node. The special radiation and convection terms for the tube surface (top and bottom together) are:

$$\dot{q}_{rad,tube} = \sigma\epsilon(1 - f_{cloud})\frac{D}{2}dy\left(T_{i,j}^4 - T_s^4\right) + \sigma\epsilon f_{cloud}\frac{D}{2}dy\left(T_{i,j}^4 - T_a^4\right)$$

$$+ \frac{\sigma}{1/\epsilon_p + 1/\epsilon_g - 1}\frac{D}{2}dy\left(T_{i,j}^4 - T_g^4\right) \tag{3.26}$$

$$\dot{q}_{conv,tube} = h_{c,t}\frac{D}{2}dy\,(T_{i,j} - T_a) + h_{c,b}\frac{D}{2}dy\,(T_{i,j} - T_g) \tag{3.27}$$

In addition the control volume at the wall and is half the size of the internal control volumes so that the node is located exactly at the tube edge. The control volume at the edge of the fin (rightmost) is also half the size of the internal control volumes. To reflect this, in the energy balances at these locations the area $dxth$ in the y-direction conduction terms (Equation 3.19) is replaced by $\frac{dx}{2}th$. In Equations 3.20, 3.21, 3.22, 3.23, the surface area $dxdy$ is replaced by $\frac{dx}{2}dy$.

Nodes at the mid-point between tubes (adiabatic fin tip) or at the beginning or ending radiator surfaces are considered adiabatic and so conduction terms are zero as appropriate on the boundaries. On the right side, the conduction term $\dot{q}_{cond,x}$ is

zero exiting the node towards the right. On the top, the conduction term $\dot{q}_{cond,y}$ is zero entering the node. On the bottom, the conduction term $\dot{q}_{cond,y}$ is zero exiting the node.

Because the numerical model accuracy depends on the number of nodes used to model the panel, first a test is completed to determine what node density would be accurate enough for a range of radiator sizes and designs. The panel geometries, flow rates tested are shown in Table 3.2 and represent a range of designs from large installations to small, roof-mounted cooling systems.

Table 3.2: Geometry and wind speed conditions tested along with fin efficiency for designs # 1 to 17. (F, F_R, and $\epsilon_{rad}$are provided for reference to the analytical models and are calculated using adiabatic temperature as reference temperature.)

	1	2	3	4	5	6	7	8	9	10	11	12	13	14	15	16	17
L [m]	100	200	200	200	200	2	5	5	5	100	200	200	200	2	5	5	5
W [m]	0.2	0.2	0.2	0.1	0.2	0.1	0.2	0.2	0.2	0.2	0.2	0.2	0.2	0.1	0.2	0.2	0.2
th [mm]	2	2	2	0.2	2	2	2	2	2	0.2	0.2	0.2	0.2	0.2	0.2	0.2	0.2
$\dot{m}$ [kg/s]	2.25	2.25	4.5	4.5	1	0.03	0.01	0.03	0.03	2.25	2.25	4.5	1	0.03	0.01	0.03	0.03
D [cm]	2	2	2	2	2	1.59	1.59	1.59	1.59	2	2	2	2	1.59	1.59	1.59	1.59
u [m/s]	3.1	3.1	3.1	3.1	3.1	1.5	1.5	1.5	6	3.1	3.1	3.1	3.1	1.5	1.5	1.5	6
n [-]	50	50	50	50	50	12	12	12	12	50	50	50	50	12	12	12	12
F_R [-]	0.47	0.29	0.47	0.60	0.13	0.73	0.24	0.46	0.29	0.38	0.26	0.38	0.13	0.66	0.22	0.37	0.23
F [-]	0.92	0.92	0.92	0.84	0.92	0.98	0.93	0.93	0.86	0.57	0.57	0.57	0.57	0.84	0.59	0.59	0.44
ϵ_{rad} [-]	0.77	0.95	0.78	0.54	0.99	0.21	0.93	0.59	0.74	0.62	0.86	0.63	0.97	0.19	0.86	0.48	0.60

Table 3.3 documents the ambient conditions, materials, and convection assumptions that are used to demonstrate the radiator models in this section. These ambient conditions are typical of those in the analysis of Dyreson and Miller [2016] in the desert region of Daggett, California, USA.

Table 3.3: Conditions and assumptions made for comparison of radiator models

	Symbol	Value for model testing
Ambient dry bulb temperature [K]	T_a	299.3
Effective sky temperature [K]	T_s	280.9
Wind direction	-	Across width W
Inlet water temperature [K]	T_{in}	319.3
Plate emissivity, top	ϵ	0.95
Plate emissivity, bottom	ϵ_b	0.07
Ground emissivity	ϵ_g	0.9
Convection coefficient, top [W/m^2-K]	$h_{c,t}$	For turbulent flow per Sartori [2006]
Convection coefficient, bottom [W/m^2-K]	$h_{c,b}$	Correlation for heated plate
Conductivity of plate [W/m-K]	—	235

Each of the 17 designs are modeled with different node layouts from two to 20 in the fin direction (x) and five to 200 in the flow direction (y). The percent error is calculated for each design and node layout relative to the highest density grid (x=20, y=200) model.

The density of the baseline model (20 nodes in fin direction and 200 in flow direction) was selected because the heat transfer from a radiator converged within $\pm$0.2% at or below this density for all designs; in other words this was more nodes than necessary. The error in the varying node layouts for the 17 different designs was examined and a model with ten nodes in the fin direction and 20 in the flow direction was within 0.2% error for all of the designs. The 10 x 20 node model was chosen as the minimum grid density for the numerical model.

3.2 Results

After validating one of the models with existing data, the three models are compared and an experimental design is considered.

3.2.1 Validation of finite differences model from literature

From the literature summarized in Chapter 2, some experimental data was available to test the panel models.

The results of Eicker and Dalibard [2011] are compared to the results of a year long model of radiation operation Dyreson and Miller [2016] by plotting on the same axis. Figure 3.4 shows the heat flux from the current model and the Eicker and Dalibard work is shown in Figure 2.3. Since the radiators, wind speeds, and ambient temperatures are not the same, the Eicker and Dalibard measurements would not be the same as those from the annual simulation in Daggett, CA. However the comparison is encouraging because the order of magnitude of the heat flux is the same and the increasing trend with water-to-sky temperatures is the same.

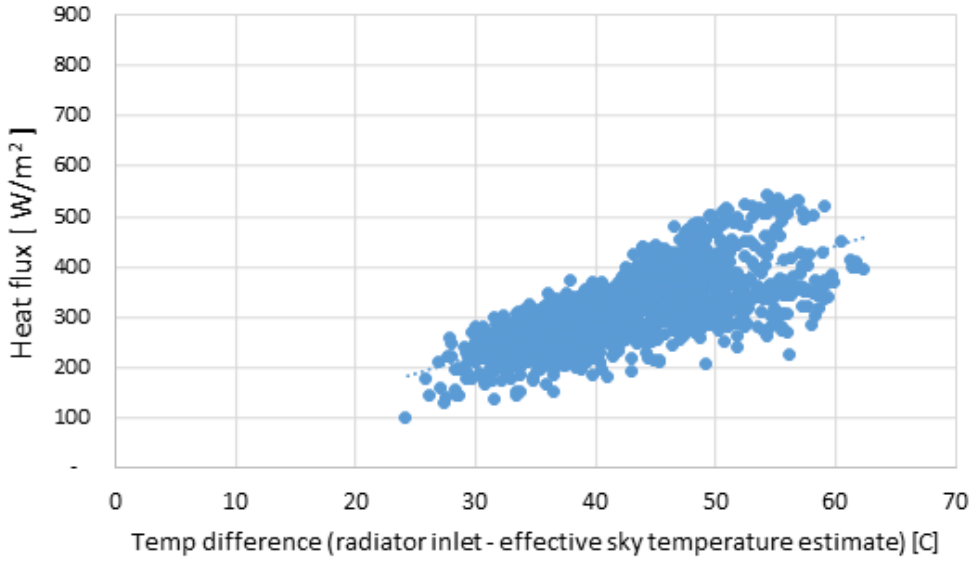

Figure 3.4: The heat flux from a two dimensional finite difference model of a black, uncovered radiator operating at night over one year in Daggett, CA is shown.

Erell and Etzion [2000] tested three different radiator designs for nighttime comfort cooling in Israel. Two of the radiator designs apply for validation of the nighttime radiator model. The data from Erell and Etzion [2000] were available and in this section they are used to test the heat transfer model of the radiator.

Experiments by Erell and Etzion

Erell and Etzion use a commercial Lordan LSC-F solar collector with the convection cover removed. The key dimensions are provided in Table 3.4.

Table 3.4: Physical characteristics of Lordan LSC-F collector used in experiments

Construction	Metal 'leaves' attached to tubes
Materials	Copper tubes, stainless steel absorber plate
Size	2.18 m x 1.27 m (2.77 m^2)
Number of tubes	12
Tube length	2.1 m
Tube diameter	1.59 cm (5/8 inch)
Tube spacing	10 cm
Bottom insulation	25 mm polyurethane foam with reflective aluminum foil

The ambient conditions during the single night test period are shown in Figure 3.5.

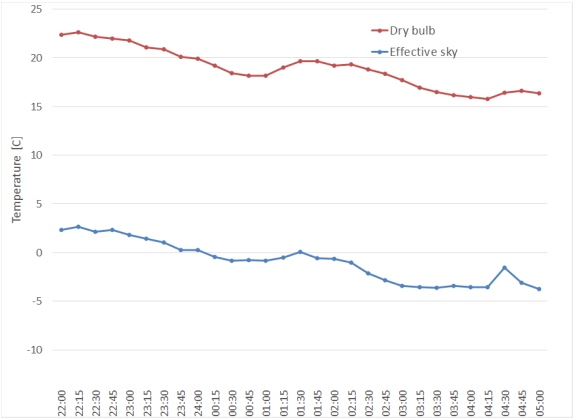

Figure 3.5: Ambient conditions.

The cooling performance of the radiator was determined by measuring the inlet temperature, outlet temperature, and mass flow rate. The temperatures were measured in the inlet and outlet by two redundant PT-100 RTD sensors that were calibrated to a differential error of less than 0.1°C. The mass flow rate of the water

through the radiators was measured using electro-magnetic pulse inducers with a resolution of 1 L. Ambient conditions (dry bulb, relative humidity, wind speed, wind direction, global horizontal radiation, net radiation (0.25 to 60 micrometers)) were also measured. The paper states that the mean wind velocity was 1.5 m/s but the data set does not include the measurements. The emissivity of the panel facing upward was assumed to be 0.9.

Additional details were uncovered from communication with the author:

- The hourly wind speed measurements are not available, but the site experiences a regular wind pattern with winds driven by sea breeze during the day and evening, and winds dying down to 0-2 m/s overnight. The wind speed of 1.5 m/s represents a consistent average; the author provided an example of the diurnal pattern of the wind that agrees with the description.

- The leaves that make up the absorber plate were welded or soldered to the edge of the riser tubes on either side. They are about 45 mm in length. The length of the collector is 2.1 m, as stated in the paper, but the individual riser tubes are approximately 2 m in length once the manifold at the entrance and exits are taken into account. The panel thickness about 0.4 to 0.6 mm.

- Water flow measurements were done using domestic water meters to determine the volume of water pumped during the overnight period. Approximately 0.5-1.5 m^3 of water was circulated per evening, and the resolution of the water meter is 0.001 m^3. The flow rate was said to be constant over the evening period. Documentation for similar meters from the same company (Arad) cite errors of 2% to 5%.

- The panel emissivity was not measured but were standard construction with black collector paint. They were not regularly cleaned and are known to have been covered in a thin layer of dust.

The outlet temperature was measured with an uncertainty of 0.1°C. The cooling power produced is determined from:

$$Q_u = \dot{m} c_p (T_{f,i} - T_{f,o}) \tag{3.28}$$

Given the uncertainties in the temperatures and assuming a 5% uncertainty in the mass flow rate, the uncertainty in the calculated heat transfer is determined using the law of uncertainty propagation. If the uncertainty around a value is normally distributed, then the usual law of propagation of uncertainty is used. If T is the value of the variable of interest such as temperature, and x_i are the independent variables, then the uncertainty in T, U_T due to uncertainties U_{x_i}, is:

$$U_T^2 = (\frac{dT}{dx_1})^2 U_{x_1}^2 + (\frac{dT}{dx_2})^2 U_{x_2}^2 + (\frac{dT}{dx_3})^2 U_{x_3}^2 \tag{3.29}$$

If available, U_{x_i} can be the standard deviation of , the value x_i. If standard deviation determined from statistical methods is not available, estimations for U_{x_i} can be made by converting the given uncertainty to an estimated standard deviation, depending on how it was given. See Taylor and Kuyatt [1994] for methods to use depending on if the given uncertainty is a confidence interval around x_i or range of values for x_i.

The heat transfer was on the order of 200 W and the error was about 20 W (results detailed below).

Model of Erell and Etzion's system

A two dimensional finite difference model was used to predict the outlet temperature (and cooling rate) from the insulated panel given the known geometry, inlet water temperature, flow rate, and ambient conditions.

The panel is assumed to be perfectly insulated so that no heat transfer happens from the back; initial testing with variable insulation thicknesses showed that this assumption was reasonable. The tube length was 2 m. The average heat transfer coefficient was determined from the turbulent Sartori correlation (see Chapter 2) given a characteristic length of 2 m (as the panel is relatively square and the wind speed is low, the impact of the wind direction and associated heat transfer coefficient

impact were not important in the overall performance). The numerical model was implemented using 30 elements in the flow direction and 30 elements in the fin direction. The strength of free convection from the top of the panel was considered but in all cases was small relative to forced convection. The internal convection coefficient within the riser tubes was determined from standard correlations. The flow is laminar with the flow rate of 0.032 kg/s divided between 12 tubes of diameter 1.59 cm.

The parameters included in the uncertainty analysis are shown in Table 3.5 along with the associated uncertainty contribution to temperature and heat transfer for the first measurement point in the dataset (beginning 22:00) for the insulated panel. Note that for convection heat transfer the uncertainty is from the measured wind speed, not the prediction of the convection correlation, though both exist. This is justified in the following sub-section.

Table 3.5: The uncertainty of the finite difference model accounted for the measurement uncertainty of the inlet temperature and mass flow rate as well as the possible variance in parameters that were not directly measured in the original paper. The portion of the uncertainty in the temperature prediction at the first hour and the heat transfer prediction at the first hour are provided. The total temperature uncertainty is 0.175°C of 294.4 K (21.3 C). The total heat transfer uncertainty is 19.16 W of 175.2 W.

	Value	Units	Uncertainty	Uncertainty units	Portion of uncertainty in T	Portion of uncertainty in Q
u	1.5	m/s	1	m/s	.231	.344
$T_{f,i}$	measured	C	0.1	C	.228	0
ϵ	0.85	-	.05	-	.150	.224
$\dot{m}$	0.032	kg/sec	5	%	.111	0
W	10	cm	10	%	.277	.413
th	0.5	mm	0.1	mm	0.000	0

Convection uncertainty components

The uncertainty in convection heat transfer increases with increasing wind speed and is impacted by uncertainties in wind speed measurement as well as the uncertainty in the correlations which predict convection heat transfer coefficients. The

uncertainty in the wind speed measurement depends on the measurement device; the uncertainty in the correlation is approximately 20%. The convection correlation used in this work is the turbulent Sartori equation based on flow over a flat plate:

$$h = 5.73u^{0.8}L_c^{-0.2} \tag{3.30}$$

Using Gaussian error propagation, the contribution to Q uncertainty due to uncertainty U_u in the measurement of u is:

$$(\frac{dQ}{du})^2 U_u^2 \tag{3.31}$$

The contribution to Q uncertainty due to uncertainty U_h in the correlation's prediction of h is:

$$(\frac{dQ}{dh})^2 U_h^2 \tag{3.32}$$

To determine the magnitudes of these two uncertainties under different wind conditions, an expression for each as a function of u can be developed. The heat transfer rate Q is approximated by the following, assuming a plate temperature T_p and a plate which is insulated on the back.

$$Q = \sigma\epsilon A(T_p^4 - T_s^4) + hA_c(T_p - T_a) \tag{3.33}$$

Using the expression for h with an uncertainty U_h of 20% and evaluating the derivatives of Q, a ratio of the two uncertainty contributions is developed:

$$\frac{(\frac{dQ}{dh})^2 U_h^2}{(\frac{dQ}{du})^2 U_u^2} = \frac{0.050u^{(6/5)}}{U_u^2} \tag{3.34}$$

This uncertainty can be plotted for different values of the uncertainty in measured wind speed and for varying wind speeds. As shown in Figure 3.6, for a relatively high uncertainty in wind speed of 1 m/s, as is the case in the Erell validation in this section, the uncertainty in the wind speed itself causes significantly more than does the 20% uncertainty in the convection correlation at the typical nighttime wind

speed of 1.5 m/s observed at the test location.

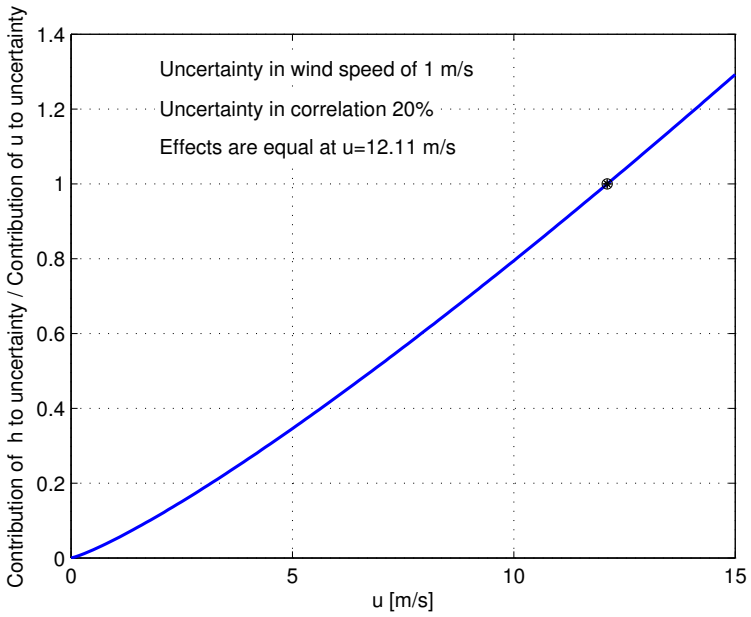

Figure 3.6: When the wind speed measurement uncertainty is high, this uncertainty contributes much more to the uncertainty of the heat transfer than does the 20% uncertainty in the convection correlation.

Figure 3.7 shows that when the uncertainty in the wind speed is only 0.1 m/s, the dominating effect is that of the correlation's uncertainty.

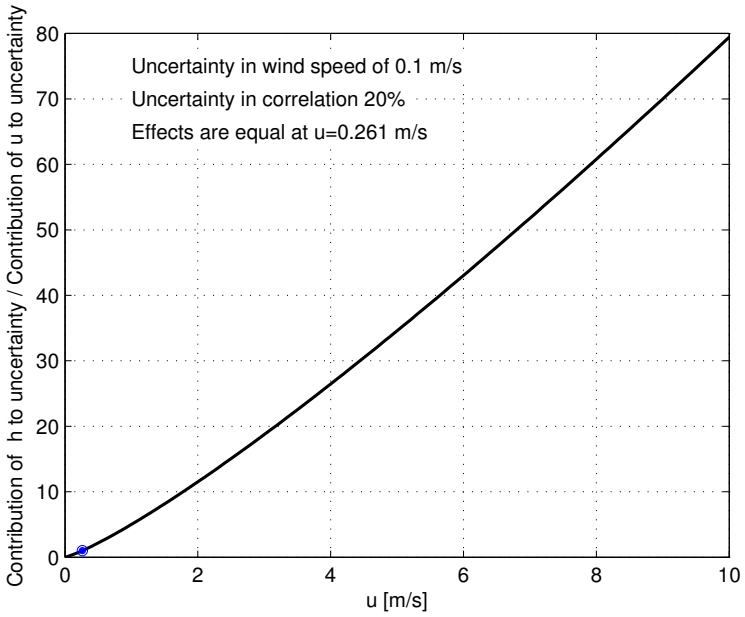

Figure 3.7: When the wind speed measurement uncertainty is 0.1 m/s, the 20% uncertainty in the convection correlation contributes much more to the uncertainty of the heat transfer than does the wind speed measurement.

The uncertainties resulting from wind speed measurement and convection correlations both contribute to uncertainty in heat transfer. As shown in this section, depending on the individual uncertainties, including only one of the effects can be justified in an analysis.

Fluctuations in wind speeds less than the typically reported hourly average value also exist. As described in Chapter 2, the use of hourly averages provides a conservative estimate of the hourly average convection heat transfer coefficient.

Comparison

The measured and modeled temperatures and heat transfer rates are shown in Figures 3.8 and 3.9. The error bars represent the uncertainties derived from the law of uncertainty propagation. It is assumed that all of the individual errors in Table

3.5 represent one standard deviation. The errors bars shown in these results are then the propagated uncertainty of all of the individual errors.

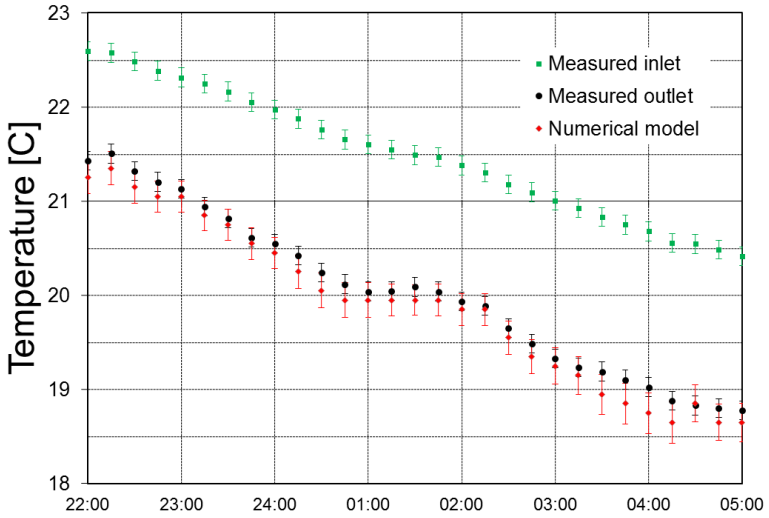

Figure 3.8: The measured inlet temperature, measured outlet temperature, and modeled outlet temperature are provided.

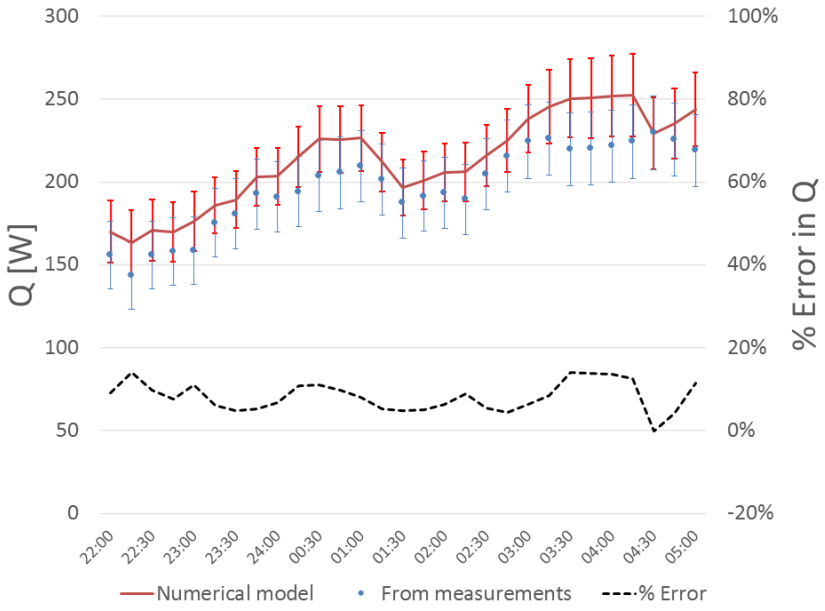

Figure 3.9: The measured and modeled heat rejection are shown along with the percent error in the modeled heat transfer compared to the measurements.

From the numerical model, the portions of heat transfer by convection and radiation are determined. As expected in these low wind speed conditions, the heat transfer is almost completely due to radiation, with convection initially providing a small negative transfer (heat gain) at the beginning of the night due to high ambient temperatures. (This results in greater than 100% radiation).

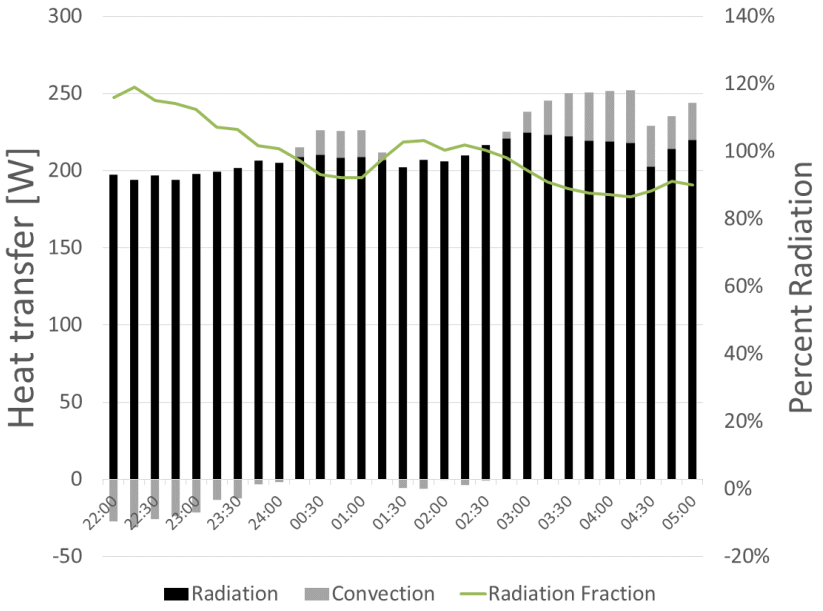

Figure 3.10: Stacked bars indicate heat transfer by radiation and conduction and the line is percent radiation determined by the model. In these low wind speed conditions, most of the heat transfer was by radiation.

The close match of the measured and predicted temperatures and heat transfer rates indicate that the two dimensional finite difference model is a good way to estimate the performance of a black, uncovered radiator. The experimental conditions only included low wind speeds, but conducting experiments in higher wind speeds would only add to the unavoidable uncertainty in the convection heat transfer prediction, as will be shown in the next section.

3.2.2 Experimental design

The validation done using data from Erell and Etzion was limited to the available data with low wind speeds. To examine the value of a new experiment to validate the heat transfer model of the radiator under a range of conditions, an experimental design is completed in this section.

Physical layout and measurement uncertainties

This experimental design considers a single panel radiator made of roll bond material. Roll bond panels are available for solar water heating. Typical panels have a width of about 1 meter and a length (flow direction) of 2 m. The bonded plate thickness is commonly 2 mm. Most manufacturers advertise that custom channel configurations are available. To get an estimate for the limits to manufacturability, the work done by Fraunhofer [2011] is useful. In the Bionicol project, roll bond solar thermal panels with fractal designs for minimized flow resistance were tested. The channel construction of a blown roll bond channel actually resembles an elongated hexagon as shown in the inset in Figure 3.11. Here the channels were modeled as square. According to the research done for the Bionicol project, practical channel heights are about 3 mm - any larger and the tube walls could not withstand the pressure.

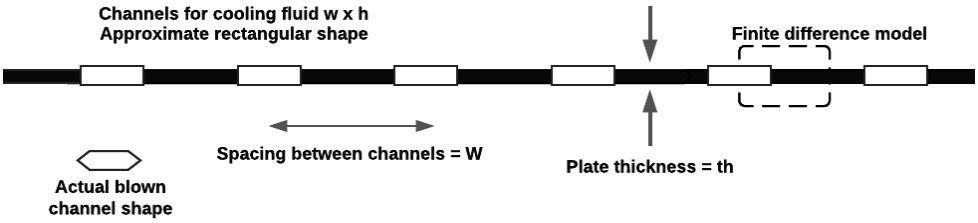

Figure 3.11: Roll bond geometry as modeled

20 tubes are distributed across the 1 m width for W= 5 cm spacing. The channel size is 3 mm by 10 mm, with a bonded plate thickness of th=2mm. The thickness and channel dimensions were reasonable compared to the Bionicol project and detailed drawing received from one vendor. The number of tubes (and therefore spacing over a 1 m panel) was reasonable compared to from vendor drawings. The flow rate was set at 0.1 kg/sec (divided between 20 tubes) in order to achieve significant temperature drop along the panels. This results in laminar flow. A higher flow rate could also be tested where turbulent flow would be achieved,

resulting in smaller temperature drops.

In an experiment the performance of the panel would be determined by measuring the inlet temperature, outlet temperature, and mass flow rate. Temperature measurements would use an RTD PT-100 type (resistance temperature detector using Platinum with 100 ohm resistance at 0 °C). An example of a general purpose RTD sensor is the Omega PR-10 probe which has an accuracy per the IEC 'Class A' standard. At 45°C the accuracy is +/- 0.24°C. At 0°C the accuracy is + 0.15°C. The uncertainty at 45°C will be used here. The mass flow would be measured using an electromagnetic flow meter; accuracy of better than 5% is achievable.

Environmental variables are measured for input to the heat transfer model. Ambient dry bulb temperature is measured using an RTD. Effective sky temperature is measured with a pyrgeometer such as Kipp & Zonen CGR4 which has a maximum uncertainty of 3% in measured downward longwave radiation (S_{down}), which is related to effective sky temperature by the equation:

$$S_{down} = \sigma T_s^4 \tag{3.35}$$

Solving for effective sky temperature, the relationship is:

$$T_s = \left(\frac{S_{down}}{\sigma} \right)^{1/4} \tag{3.36}$$

Therefore a 3% uncertainty in downward radiation can be propagated through to the uncertainty in effective sky temperature. Assuming that the 3% uncertainty is a standard deviation (conservatively; it could be a bound containing nearly all values, it is not specified by the manufacturer), there is a 1.9 °C uncertainty in the effective sky temperature at -23°C (250 K) and a 2.2°C uncertainty at 27°C (300 K). A 1% uncertainty relative to the effective sky temperature will be used in this analysis.

Wind speed can be measured with an anemometer and wind vane such as the Campbell Scientific 034B. This system measures wind speeds from 0.4 m/s to 10 m/s with a reported 'accuracy' of 0.1 m/s (higher speeds have larger uncertainties). More importantly, the calculated convection impact will have a 20% uncertainty. Given

the low uncertainty in wind speed measurements in this case, the 20% uncertainty in the correlation will dominate the convection impact as shown in Figure 3.7 for most wind speeds. For this analysis the 20% uncertainty in the convection coefficient will be used without calculating the uncertainty in the measured wind speed.

Model results

A two dimensional finite difference model is used to model the heat transfer over one of the sections of plate. A single typical condition (for Daggett, CA) is tested as a baseline. Table 3.6 shows the inputs and outputs to the model.

Table 3.6: Model results for baseline condition

Inputs	Outputs
T_a=299.3 K (26.15°C)	$T_{f,o}$=16.9 K (43.8°C)
T_s=280.9 K (7.75°C)	ΔT=2.408°C
$T_{f,i}$=319.3 K (46.15°C)	h_c=12.33 W/m^2-K
$\dot{m}$=0.1 kg/sec	v_{tube}=0.167 m/s
n=20 tubes	
L=2 m	
W=1 m	
w_c=10 mm	
$height_c$=3 mm	
th=2 mm	
u=3.1 m/s	

The uncertainties known are applied and the resulting effect on the outlet temperature modeled is shown in Table 3.7. Because what is of more interest is the temperature drop (and related total heat transfer), Table 3.8 also shows the impact on uncertainties on temperature drop uncertainty and Table 3.9 shows the impact on heat transfer.

Table 3.7: Contributions to total uncertainty in $T_{f,o}$ =317.32 of 0.31°C.

Variable	Uncertainty	Portion of total uncertainty
$T_{f,i}$	0.24 C	0.51
h_c	20%	0.37
$\dot{m}$	5%	0.09
T_s	1 %	0.03
T_a	0.24°C	<0.01

Table 3.8: Contributions to total uncertainty in ΔT =1.98 of 0.22°C. The inlet temperature has little effect on the temperature drop.

Variable	Uncertainty	Portion of total uncertainty
h_c	20%	0.74
$\dot{m}$	5%	0.19
T_s	1 %	0.06
$T_{f,i}$	0.24°C	<0.01
T_a	0.24°C	<0.01

Table 3.9: Contributions to total uncertainty in Q =829.9 W of 82.5 W. The mass flow rate has little effect on overall heat transfer.

Variable	Uncertainty	Portion of total uncertainty
h_c	20%	0.91
T_s	1 %	0.08
$T_{f,i}$	0.24°C	0.01
$\dot{m}$	5%	0.01
T_a	0.24°C	<0.01

The largest uncertainty in the modeled temperature drop in the baseline condition is due to convection. But the magnitude of convection heat transfer will vary with wind speed and its relative magnitude to the radiation heat transfer will change as the inlet temperature is controlled and as different ambient conditions are present. Next the uncertainties will be examined for a range of possible conditions.

Figures 3.12 and 3.13 show how the uncertainty in the temperature drop changes depending on the wind conditions and inlet temperature. For increasing wind speeds under the same ambient conditions and fixed inlet condition, the convection heat transfer is increasing while the radiation heat transfer is approximately the same. Therefore the temperature drop is increasing and the uncertainty is also increasing, Figure 3.12, as uncertainty is mostly due to the 20% uncertainty in the convection coefficient.

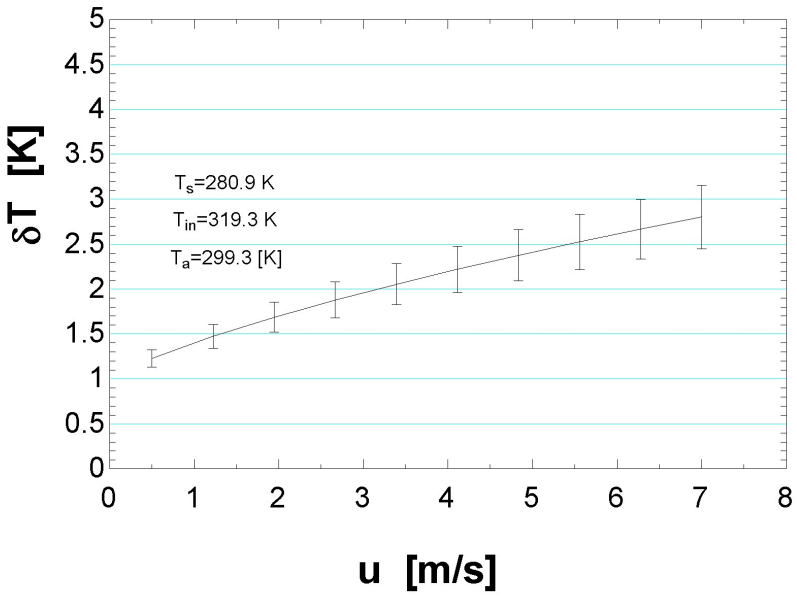

Figure 3.12: Increasing uncertainty in temperature drop with increasing wind speed.

In Figure 3.13 for increasing inlet temperatures under fixed ambient temperatures, the total temperature drop increases as both radiation and convection are enhanced. For a line of constant wind speed of u=5 m/s, as the inlet temperature increases the temperature drop increases from 1.5 to 5.7 K, with corresponding uncertainties from 0.2 K to 0.7 K. At the inlet temperature of 350 K, the heat flux is 33% radiation. The uncertainty in the temperature drop is 86% due to h_w and 14% due to mass flow uncertainties (less than 1% due to other). Sky temperature

contributed less than 1% to uncertainty because the heat transfer was dominated by convection. At the inlet temperature of 310 K, the heat flux is 47% radiation. The uncertainty in the temperature drop is 68% due to h_w, 18% due to mass flow and 11% due to sky temperature uncertainties. In this case the uncertainty in sky temperature was more significant because the fraction of heat transfer was nearly evenly split between convection and radiation.

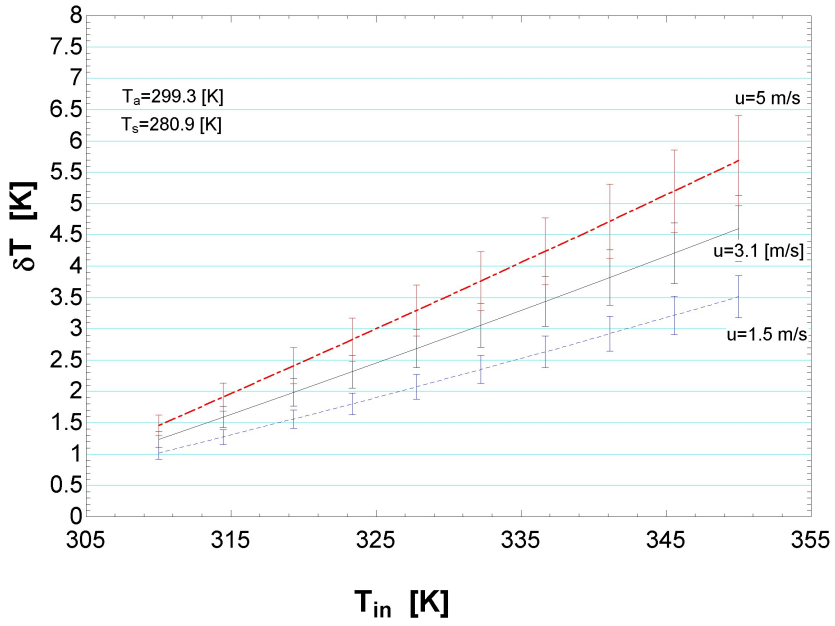

Figure 3.13: Increasing uncertainty in temperature drop with increasing inlet temperatures and wind speeds.

Considering a single medium wind speed of 3.1 m/s, Figure 3.14 shows the impact of the difference between sky and inlet temperatures on the radiation fraction. The fraction of heat transfer by radiation (Q_{rad}/Q) decreases with inlet temperature increase. When the sky temperature is close to ambient, the radiation is minimized and for this wind speed condition, the radiation fraction increases slightly as the inlet temperature increases.

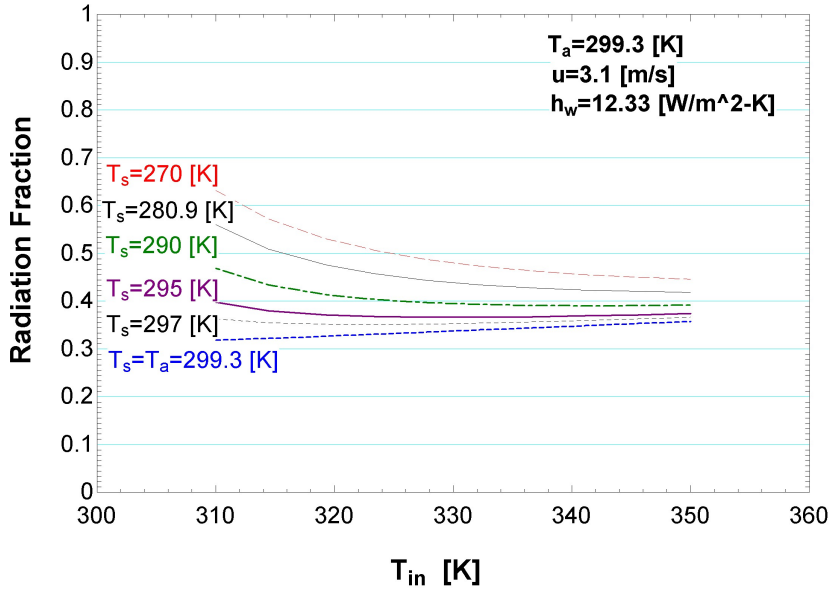

Figure 3.14: For a wind speed of 3.1 m/s and ambient temperature of 299.3 K, the fraction of the heat transfer by radiation generally decreases with increasing inlet temperatures except when the sky temperature is equal to the ambient temperature, in which case the fraction increases slightly with increasing inlet temperature.

Fraction of heat transfer by radiation decreases with increasing inlet temperature

The preceding discussion begins to show that in general, as the inlet temperature increases, the convection effect increases more quickly than radiation. This is somewhat counterintuitive because the radiation heat transfer rate is based on the difference in temperatures to the fourth power, while convection depends on the difference in temperatures. The exact contributions of radiation versus convection depend on the wind speed, ambient temperature, and sky temperature as well as inlet temperature. This section considers the radiation fraction for different conditions and analyzes the radiation fraction mathematically.

In this section the behavior of the radiation and convection heat transfer will be characterized not with a two dimensional finite difference model but using a

simplified mathematical approach. Equation 3.33 approximates the heat transfer from convection and radiation from the top of the panel if the average plate temperature T_p is assumed equal to $T_{f,i}$. The radiation and convection components are the first and second terms in Equation 3.33 and are defined as Q_{rad} and Q_{conv}. The radiation fraction is:

$$\text{RadiationFraction} = \frac{Q_{rad}}{Q_{rad} + Q_{conv}} = \frac{\sigma \epsilon A (T_{f,i}^4 - T_s^4)}{\sigma \epsilon A (T_{f,i}^4 - T_s^4) + hA(T_{f,i} - T_a)} \tag{3.37}$$

Figures 3.16 and 3.15 show how the radiation fraction decreases with inlet temperature increase under most conditions for the temperature range under consideration from about 310 to 330 K. The radiation fraction is high for low temperatures (convection to ambient goes to zero as the inlet temperature approaches dry bulb temperature) and decreases with temperature quickly before reaching a minimum and slowly increasing.

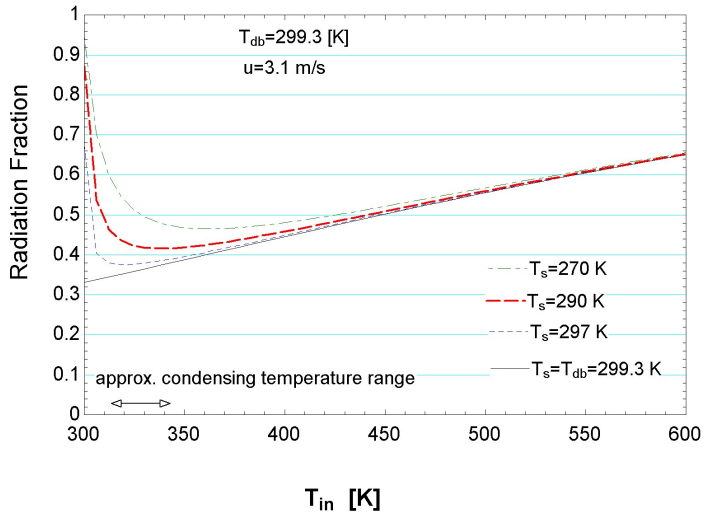

Figure 3.15: The fraction of heat transfer by radiation varies with ambient conditions and inlet temperature; here the radiation fraction is shown for a medium wind speed of 3.1 m/s.

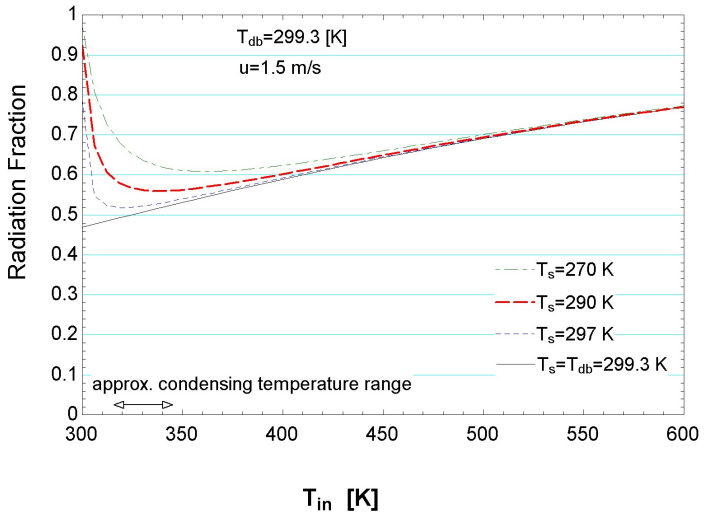

Figure 3.16: The fraction of heat transfer by radiation varies with ambient conditions and inlet temperature; here the radiation fraction is shown for a low wind speed of 1.5 m/s.

The effect of changing inlet temperature on heat transfer can be considered by taking the derivative of the radiative and convective heat transfer from Equation 3.33 with respect to inlet temperature. Again assuming that the inlet temperature approximates the average plate temperature, the derivatives of radiation and convection heat transfer with respect to inlet temperature are:

$$\frac{dQ_{rad}}{dT_{f,i}} = \sigma \epsilon A 4 T_{f,i}^3 \tag{3.38}$$

$$\frac{dQ_{conv}}{dT_{f,i}} = hA \tag{3.39}$$

Figures 3.17 and 3.18 show the relationships from Equations 3.39 and 3.38 for a range of conditions where the convection heat transfer coefficient is predicted by Equation 3.30. Unless wind speeds are under about 2 m/s, within the condensing temperature range of interest (which indicates range of inlet temperatures to

radiators) convection increases more quickly with inlet temperature than does radiation.

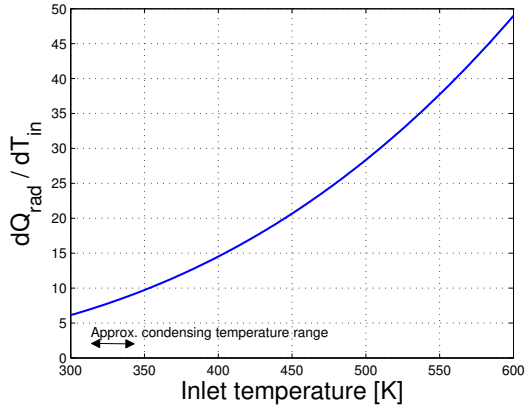

Figure 3.17: The rate of change of the radiation heat transfer with respect to inlet temperature varies with the cube of inlet temperature. A surface area A of one is assumed.

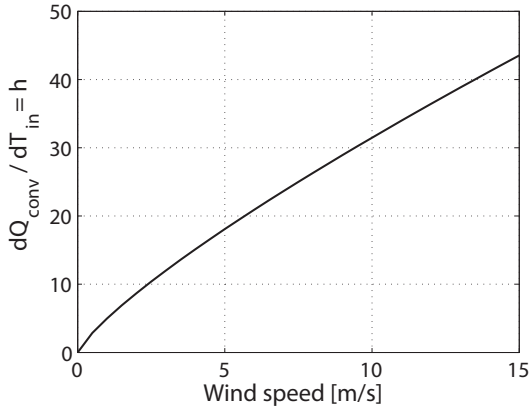

Figure 3.18: The rate of change of the convection heat transfer with respect to inlet temperature varies depends strongly on wind speed. A surface area A of one is assumed.

Referring back to Figure 3.14, for the wind speed of 3.1 m/s and an inlet temperature of 319.3 K, the derivative of the convection rate equation is 12.33 W/K.

The derivative of the radiation rate equation is 6.64 W/K. This explains why the radiation fraction is going down in most cases. But the radiation fraction does not strictly decrease with temperature. The change in radiation fraction as inlet temperature changes depends on the change in each component as well as its original magnitude relative to the total. The radiation fraction derivative is:

$$\frac{d}{dT_{f,i}}\mathtt{RadiationFraction} = \frac{Q_{conv}\frac{dQ_{rad}}{dT_{f,i}} - Q_{rad}\frac{dQ_{conv}}{dT_{f,i}}}{Q^2} \tag{3.40}$$

This expression is not easily generalized but it is useful to consider where the Radiation Fraction is minimized. Using equations 3.38, 3.39, and 3.33, and setting the radiation fraction equal to zero, the following equation is found:

$$3T_{f,i}^4 - 4T_a T_{f,i}^3 = -T_s^4 \tag{3.41}$$

The inlet temperature which characterizes minimum radiation fraction does not depend on wind speed, only ambient conditions. This is consistent with Figures 3.15 and 3.16 where the shape of the radiation fraction curve is consistent between wind speeds. (Though the magnitude of the radiation fraction is different.) The implication of these findings for the design of an efficient radiation-enhanced system is that raising the temperature of the radiator in the temperature range of interest for power plant condensers does not result in dominating radiation effects because convection is significant. The maximum radiation fractions are at lower temperatures where the overall heat transfer is low - this is not a desirable operating point. This analysis also confirms that raising the temperature of the radiator in an experimental design with operating temperatures below 350 K would not decrease, but rather increase the uncertainty as uncertainty is generally higher for convection than radiation.

The most general way to look at the impact of inlet temperature is to use a full year of weather data. For the SURFRAD monitoring station in Desert Rock, Nevada, measured ambient temperature, effective sky temperature, and wind speed are used here for the 2015 year. Considering only night time hours, Figure 3.19

shows histograms of the radiation fraction during the year for three different inlet temperatures. This shows that as the inlet temperature goes up, the fraction of heat transfer by radiation generally goes down.

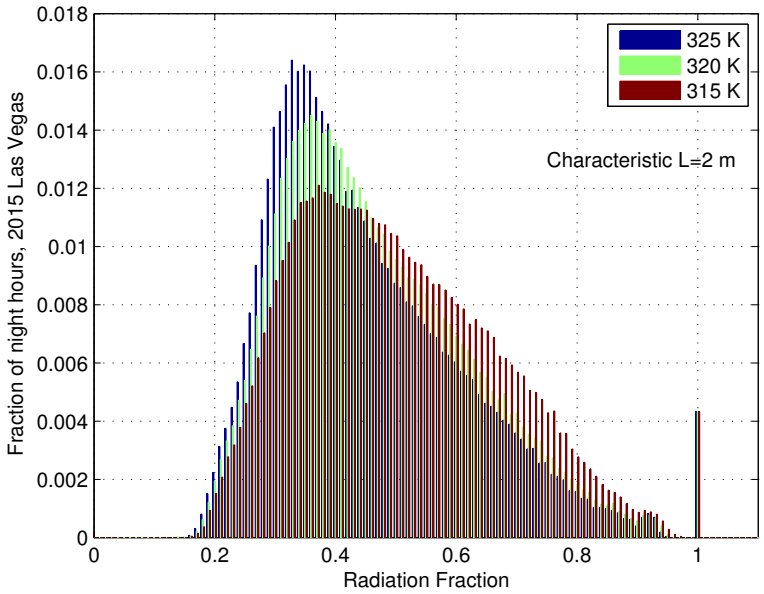

Figure 3.19: This figure shows the fraction of heat transfer by radiation from a 2 m square radiator with a uniform temperature over the panel equal to the inlet temperature. There is a spike in radiation fractions of one due to the zero wind speed conditions (here only forced convection is considered and assumed to be zero at zero wind speed; in reality free convection also occurs.)

3.2.3 Comparison of models

This section compares the analytical model using sky temperature reference and the analytical model using adiabatic temperature reference to the finite differences model. To illustrate the use of these models under a range of operating conditions and panel designs, the results are illustrated in three ways: 1) for a low-temperature cooling application for building comfort cooling over the course of one night, 2) for a high temperature operating condition with different panel designs, fluid flow

rates, and wind speeds, and 3) for a high temperature application under practical annual operating conditions.

Low temperature application

Erell and Etzion Erell and Etzion [2000] tested radiator designs for nighttime comfort cooling in Israel. In this section their radiator dimensions and test conditions are used to test the heat transfer model of the radiator in a typical low-temperature application representative of comfort cooling for buildings. Erell and Etzion used a commercial solar collector with the convection cover removed. The key dimensions are provided in Table 3.4. The wind speed was 1.5 m/s, emissivity from the top was 0.85, mass flow rate was 0.032 kg/sec, and the leaves were 2 mm thick. The panel is assumed to be perfectly insulated so that no heat transfers from the back; initial testing with variable insulation thicknesses showed that this assumption was reasonable. The average heat transfer coefficient was determined from the turbulent Sartori correlation Sartori [2006]. Because the panel is relatively square and the wind speed is low, the impact of the wind direction on characteristic length and associated heat transfer coefficient impact were not important in the overall performance. The numerical model was implemented using 30 elements in the flow direction and 30 elements in the fin direction. The strength of free convection from the top of the panel was considered but in all cases was small relative to forced convection. The internal convection coefficient within the riser tubes was determined from standard correlations and was laminar.

The percent difference in heat transfer for the analytical models compared to the numerical models was always $\pm$ 2.0%. (They also compared reasonably well to the experimental measurements of Erell and Etzion but given the inherent uncertainty in the convection coefficients ($\pm$20%), a direct comparison of measurements and model is not helpful for validation of the models). Since the three models agree well, the choice of model is not important in this case. But this represents a limited range of operating conditions and only tests one specific panel design. The following sections consider more general cases and higher temperature applications.

Different radiator designs operating in high temperature application

Using a set of different radiator designs that represent a range of panel efficiencies within the plausible realm, a set of basic assumptions were employed for comparing the models under a high temperature application. The radiator designs and conditions used are from Tables 3.2 and 3.3.

The results of the model comparisons (analytical vs numerical) are shown in Figure 3.20. The mean percent error from the analytical model referencing the adiabatic temperature to the numerical model using 20 nodes in the flow direction and 10 in the fin direction is -0.2% (minimum -0.5%, maximum 0.2%); these two models agree. The analytical model referencing the sky temperature has error up to 20%.

Figure 3.21 shows that the error in the sky temperature model is related to the collector heat removal factor F_R .

Percent error is correlated to F_R because the analytical model assumes that the fin efficiency and collector efficiency are constant over the panel's flow direction as its temperature decreases. In fact the fin efficiency varies over the flow direction and as the temperature drop of the panel increases (decreasing F_R and increasing ϵ_{HX}), the impact of this assumption is more significant. This error can be avoided by stringing multiple smaller models in series or by using the adiabatic temperature reference. In the analytical model referencing the adiabatic temperature, the overall loss coefficient, and therefore fin efficiency and collector efficiency, are only weakly dependent on the plate temperature (via the natural convection coefficient and linearized radiation coefficient).

Annual simulations of one radiator operating in high temperature application

Because different operating conditions exist with varying inlet temperature and ambient conditions, annual simulations are completed to observe the full range of

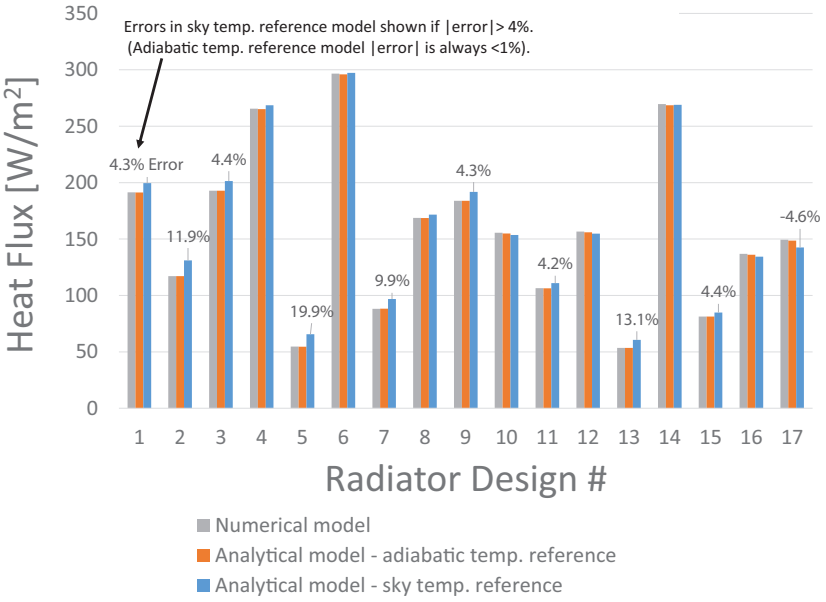

Figure 3.20: For 17 different radiator designs, the flux at typical conditions is calculated using three different models. The numerical model is always within ± 1% of the analytical model using the adiabatic temperature reference, while the sky temperature model can be off by as much as 20% depending on the geometry of the panel.

conditions. The annual simulation is for the high temperature application of heat rejection for a concentrating solar power plant. Using the heat rejection requirements and condensing temperatures from an air-cooled concentrating solar power plant, the stored cold water from the radiator system is used in a condenser to reject heat. The system design and calculations are documented in Dyreson and Miller [2016]. First, the system (solar collectors, power block, condenser, and cold storage) is modeled along with the finite differences model of the radiator. To determine the differences between the numerical and the two analytical models, the radiator operation is then isolated from the cold storage by taking the radiator inlet temperatures from the system simulation as fixed. The hourly annual inlet temperatures to the radiator were inputs to the analytical models under the concurrent ambient conditions (the actual effects of returning water temperature on cold storage are

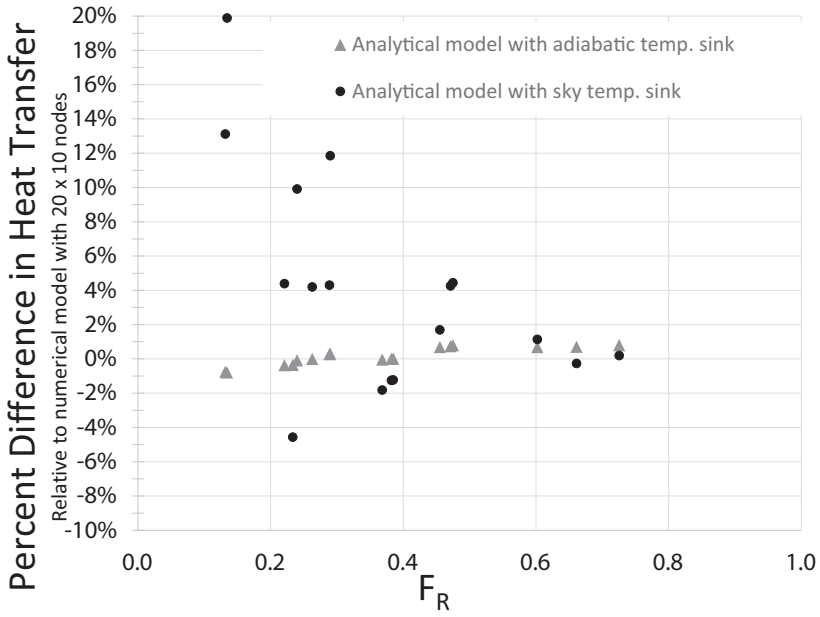

Figure 3.21: For 17 different radiator designs, the error in the heat transfer compared to the numerical model is plotted against the ratio F_R.

not fed back into the analytical models).

As described in Dyreson and Miller, there are 50 channels with D= 2 cm, th=2 mm, and *W*=0.1 m to give a 5 m wide panel. The length in this case is 200 m (actually split into multiple sections but because the axial conduction is not significant, can be modeled as one continuous length). The mass flow rate is 4.5 kg/sec, divided evenly between the 50 channels.

The annual results echo those of Section 3.2.3: the numerical and adiabatic temperature analytical models agree well. The sky temperature analytical model varies with F_R (Figure 3.22). Again when the F_R is low (reflecting large temperature drop over the radiator), the sky temperature analytical model error is high.

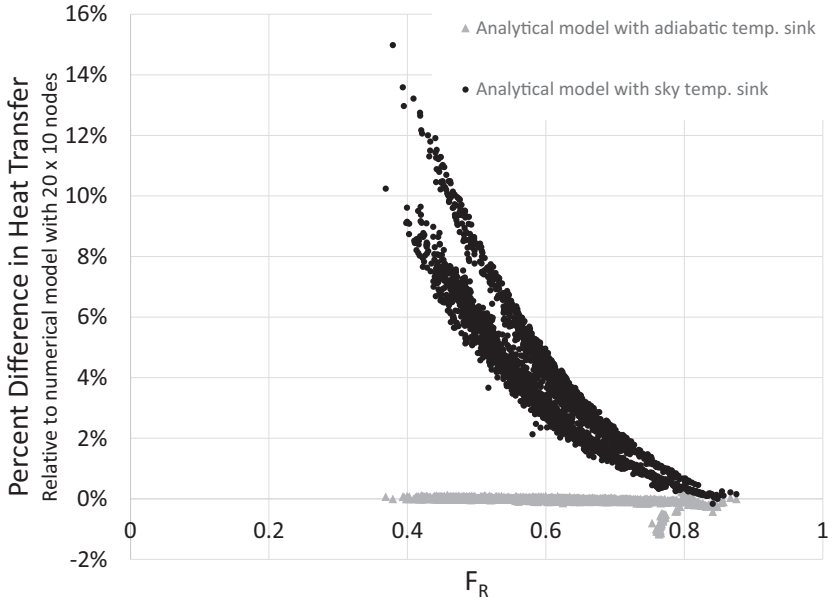

Figure 3.22: The three different models were tested for a one radiator design in an hourly annual simulation. Treating the numerical model as the baseline, the analytical model using the adiabatic temperature reference is always within $\pm$ 0.2% except when wind speed is zero and the differences in free convection models result in differences of about 1%. The percent error in the analytical model with reference to the sky temperature is up to 15%. Note that there are two operation conditions for the radiator system (taking inlet water from cold storage or warmer storage), making the error vs. F_R plot appear separated into two regions.

3.2.4 Summary and modeling recommendation

Using experimental data from the work of Erell and Etzion [2000], the two dimensional finite difference model has been validated under low wind speed conditions.

An experiment was designed to further test the models. An uncertainty analysis of the experiment showed that the uncertainties in the model depend on the conditions but are often high. The uncertainty in the model given the measurement uncertainties of the model's input values plus the uncertainty of the convection coefficient would in many conditions be much higher than the measurement uncertainty. Model uncertainty is up to 0.7 °C in the temperature drop from inlet to

outlet and the comparable measurement uncertainty is up to 0.2°C. New experiments would not provide higher confidence in the model; no new experiments are planned.

The two dimensional finite difference model was compared to the analytical solar collector-based heat transfer model and showed agreement. The analytical model based on the adiabatic temperature agrees well with the finite differences model, but because of the simplicity of the adiabatic temperature model, it is selected for use in the current work. The analytical model based on the reference temperature of the effective sky temperature is not recommended for modeling radiative cooling panels.

The comparison of radiative-cooled and air-cooled solar power plants in this project will quantify any differences in power cycle thermodynamic performance and reductions in cooling system parasitic loads. In order to capture condensing pressure effects on the cycle performance, it is important to accurately model the off design performance. This section details the power cycle models as well as the regression of those power cycles for use in annual simulations.

For this work, the off-design impacts of varying turbine backpressure (the exit pressure of the last stage turbine before the condenser) are captured in a cycle model implemented in IPSEPro [SimTech, 2017]. This software was chosen as one of several process simulation software packages that include turbine exhaust losses and other component level off-design models. Exhaust losses are a key to modeling the backpressure effect on the cycle because exhaust losses tend to counteract the increases in efficiency due to reducing condensing pressure (described further in this section). IPSEPro is an equation oriented solver. It is an open-equation system; most of the engineering equations can be viewed and changed by the user. The exception are certain library codes including the off-design steam turbine operation. A summary description of the modeling of the components is provided in this section. In some cases the component models as documented here are based on convention or the experience of the software users. Details of each component are available in the IPSE help files.

4.1 Modeling a benchmark power cycle with IPSEpro

To validate the modeling process, first a cycle is modeled in IPSE and compared against a published example. This subsection describes the benchmark model and details the component-level models used. The benchmark model is based on a parabolic trough Rankine cycle plant as in Appendix D of the SolarPACES Bankability report [Yildiz, 2017]. That Appendix provides guidance on the power

cycle modeling in order to provide guidance for more standardized CSP power cycle modeling. A reference heat cycle is described and modeled in process simulation software (not specified). In this subsection, a cycle model is developed to closely represent the benchmark cycle and the performance is checked against the design and off-design results provided by Yildiz.

4.1.1 Detailed power block model -design point

This section describes the design point model shown in Figure 4.1. The benchmark cycle provided in Yildiz represents state of the art for a 100 MW plant with six feedwater preheaters for regeneration, high pressure (HP) and low pressure (LP) turbines, and sliding evaporator pressure down to 30 bar for part load conditions. The heat transfer fluid (HTF) temperature supplied is 379 °C from storage or 393 °C supplied directly from solar field. The steam conditions at this higher (design) value are 103 bar and 383 °C at the solar steam generator and 21.5 bar and 383 °C at reheat. The ratio of initial pressure (103 bar) to reheat pressure (21.5 bar) is 0.21, which is in the optimal range per El-Wakil [1984]. IPSE is used to model a plant that closely matches the specifications in Yildiz for the case where HTF is delivered from the solar field at 393 °C. In addition to basic cycle parameters given in Yildiz, extraction pressures, flow rates, and turbine configurations were determined for the IPSE model. The specific inputs used are shown in Figure 4.2.

Three pressures constrain the problem: the boiler pressure 103 bar, the extraction pressure for reheat at 23.5 bar, and the condensing pressure (determined from condenser model) at 77.9 mbar. Optimal extraction pressures for the low pressure turbine are determined by evenly spacing the related saturation temperatures between the high and low temperature sources per El-Wakil. The high pressure in this turbine is 23.5 bar (corresponding condensing temperature of 220.7 °C) and the low side is 77.9 mbar (41 °C). The four extractions should be spaced by 36 °C. For the three low pressure feedwater heaters, this is accomplished by setting the extraction pressures at 0.4183 bar, 1.577 bar, and 4.611 bar. For the open feedwater heater, the extraction pressure is iterated until the cycle model shows the exit temperature of

the open feedwater heater is optimally spaced (184.8 °C).

For the high pressure turbine, the high side is 103 bar / 313.2 °C and the low side is 23.5 bar / 220.7 °C. The extractions should be spaced by saturation temperature differences of 46 °C. So the high pressure extraction would provide optimal cycle thermal efficiency at 52.44 bar / 267 °C. However, this extraction pressure was instead selected as part of the cycle heat balance. Given an incoming HTF temperature of 393 °F, a required gross power output at the generator of 100 MW, and cooling water at 28 °C, the highest extraction pressure and HTF mass flow rates in the reheat and solar steam generator loops can be selected to balance overall efficiency and HTF mass flow requirements. This trade off is important because the cost of the HTF system is significant. An optimizer in IPSE can be used to solve the problem, but in this case as the goal was to approximate the model of Yildiz, the values were selected to best match the HTF mass flow rate in Yildiz. The model determined a first extraction pressure of 26.15 bar / 226 °C saturation temperature.

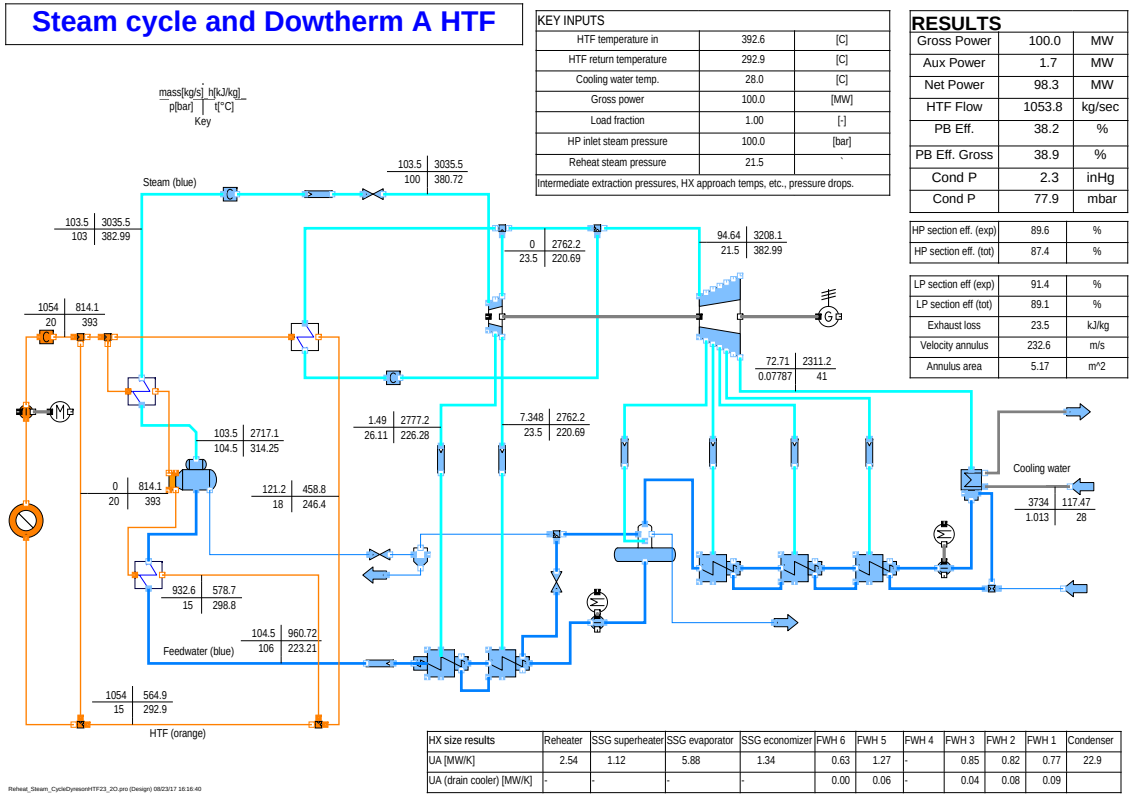

Figure 4.1: The process diagram and results for a water-cooled 100 MW power block and HTF delivery based on example plant per Yildiz.

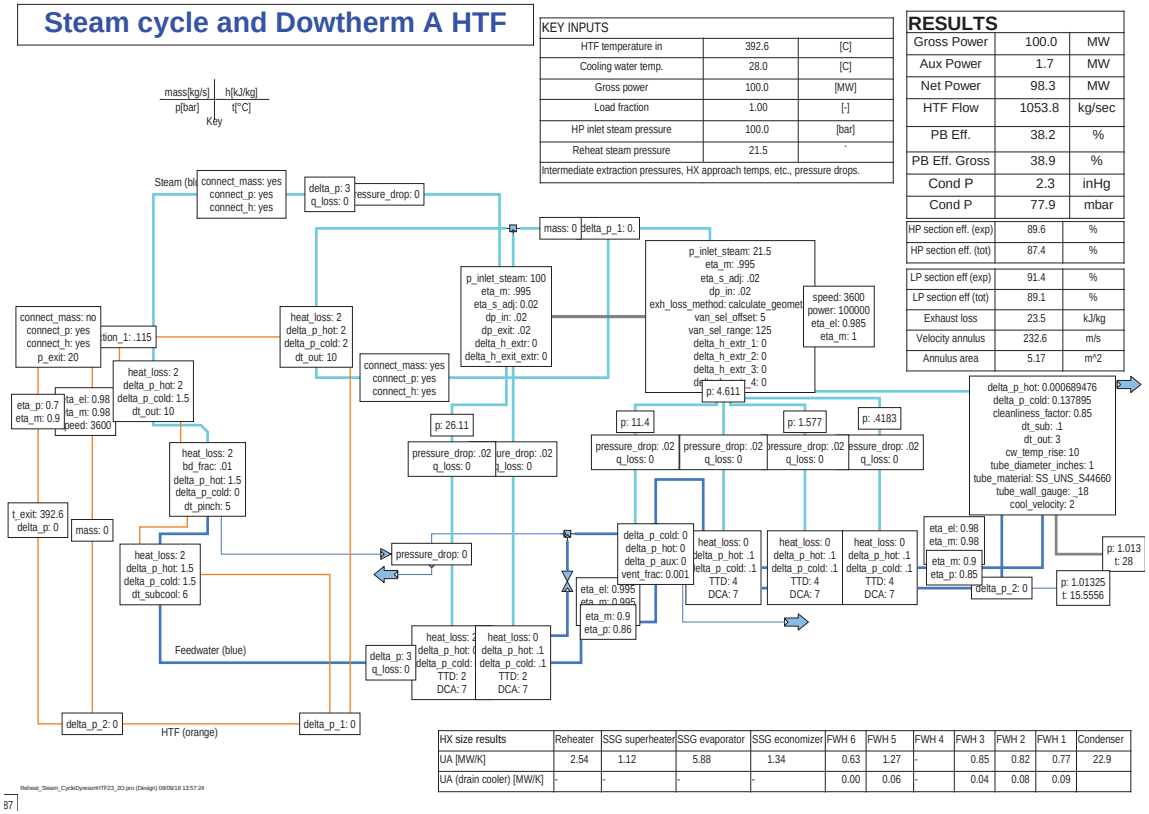

Figure 4.2: The process diagram shows the specific inputs values used for each component.

4.1.2 High pressure turbine

Modeling of turbine components is based on the Spencer-Cotton-Cannon methods, which are accepted in industry as representative of turbine characteristics. The methods will be referred to as "SCC methods" and are described in Spencer et al. [1974] unless otherwise noted. The high pressure turbine type selected is an intermediate pressure (IP) turbine. An IP turbine model is used because this cycle uses floating pressure instead of throttling for off-design operation, so the turbine model does not include a governing stage nor partial arc throttling. There are four main states at four different pressures of interest for determining the turbine efficiency : inlet ($p_{hp,in}$), just after inlet at the bowl (p_b), expansion line end point ($p_{hp,ELEP}$), outlet ($p_{hp,out}$). The temperature (T) and enthalpies (h) here use the same subscript notation. The pressure decreases from the inlet (100 bar) to the bowl pressure per a fraction specified (here 0.02). The isentropic expansion efficiency ($\eta_{hp,exp}$) from the bowl to the expansion line end point (ELEP) is determined from SCC. This method determines the efficiency of an intermediate pressure turbine based on the pressure ratio (bowl to exhaust) and volumetric flow rate at the bowl. A standard 2% improvement in this efficiency is added to account for modern improvements in turbine design [Cotton, 1998]. The exhaust pressure (here 23.5 bar) is set by the reheat pressure requirement and the known reheater pressure drop. The expansion line end point is a higher pressure than the exhaust by the fractional pressure drop specified (here 0.02). Thus the enthalpy at the expansion line end point can be determined:

$$\eta_{exp} = \frac{h_{bowl} - h_{ELEP}}{\Delta h_s} \tag{4.1}$$

Where Δh_s is for isentropic expansion from the bowl to the ELEP pressure. The enthalpy at the exit is the same as that at ELEP. An overall efficiency relative to the isentropic expansion from the inlet to the exhaust pressure is also calculated ($\eta_{hp,tot}$) for reference.

$$\eta_{tot} = \frac{h_{in} - h_{out}}{\Delta h_{s,x}} \tag{4.2}$$

Where $\Delta h_{s,x}$ is for isentropic expansion from the inlet to the exhaust pressure. Intermediate extraction point enthalpies are determined directly from the expansion line at the extraction pressure. For the intermediate turbine this is a simple linear h-s relationship along the expansion line. The expansion line is taken from SCC methods for a non-reheat turbine stage. The extraction fractions are determined based on the overall cycle heat balance.

Low pressure turbine

The low pressure turbine selected in IPSE is a low pressure turbine with five extraction points and exhaust losses. The inlet pressure is specified (21.5 bar) and the exhaust pressure is based on the cooling water temperature and condenser design. Again the bowl pressure is less than the inlet pressure by a fraction specified (here 0.02). SCC methods are used as follows. First, the turbine expansion efficiency from the bowl to a standard 1.5 in Hg backpressure is determined ($\eta_{s,1.5}$). The efficiency is adjusted for volumetric flow, initial steam conditions, and finally adjusted by the standard 2% increase for modern machines. Next, this efficiency is used to calculate the ELEP enthalpy and then the enthalpy is adjusted for the actual backpressure (here 2.3 in Hg) depending on the moisture content of the theoretical 1.5 in Hg ELEP state. The expansion efficiency (η_{exp}) for the actual backpressure is then calculated per Equation 4.1.

A key part of the model is incorporation of exhaust losses in the last stage of the turbine to account losses that are not included in a simple isentropic efficiency. The exhaust losses are for several effects, but the main effect is from the the lost kinetic energy from the leaving steam velocity to the condenser. This so-called 'leaving loss' increases with lower condensing pressures (i.e. higher velocities). For a discussion of the loss modes included in the exhaust losses in SCC, see Bartlett [1958]. Exhaust losses can counteract the condensing pressure effect on cycle efficiency, so capturing them is important. Exhaust losses depend on the turbine backpressure and last stage geometry. The turbine component in IPSE uses the turbine characteristics from SCC to select the last stage geometry for relatively favorable exhaust losses. Figure 4.3

shows the exhaust losses for the low pressure section for this design with a leaving annulus area of 5.16 square meters. The program chooses the smallest turbine possible where the leaving velocity (annulus velocity) falls within a specified range on that turbine's exhaust loss curve. If the exiting velocity is too high for the largest available turbine, the program chooses a double or triple flow configuration (two to three turbines in parallel). Note that the acceptable annulus velocity range is slightly higher than the annulus velocity for minimum exhaust losses. Depending on the backpressure expected during off-design operation, this may not be optimal, so an alternative approach that could be used is to specify the exhaust losses or the last stage geometry. The enthalpy leaving the turbine component h_{out} is the expansion line end point (ELEP) enthalpy less exhaust losses:

$$Exhaustloss = h_{ELEP} - h_{out} \tag{4.3}$$

An overall section efficiency is determined that accounts for exhaust losses ($\eta_{lp,tot}$) per Equation 4.2.

Intermediate extraction enthalpies for last stage turbines are determined from the expansion line as in SCC methods. Given an extraction pressure and steam properties to relate the entropy, enthalpy, and pressure of the extraction steam, the entropy at defined by Equation 4.4. B indicates the end of the expansion line and the constant H_0 is given in English units in SCC as 650 Btu/lb for reheat sections and 450 for nonreheat sections.

$$s_E/4.1868 = 10^{(h_B/2.326-(h_E/2.326+H_0))/371.0} + R_O(h_E - h_B)/2.326 + s_B/4.1868 - 0.0177 \tag{4.4}$$

The constant R_O [1/K] is provided in Equation 4.5 where A indicates the start of the expansion process.

$$R_O = \frac{(s_A - s_B)/4.1868 + 0.0177 - 10^{(h_B/2.326-(h_A/2.326+H_0))/371.0}}{(h_A - h_B)/2.326} \tag{4.5}$$

Equations 4.4 and 4.5 assume properties are in SI units. (Enthalpy conversion is 2.326 kJ/kg = 1 Btu/lbm. Entropy conversion is 4.1868 kJ/kg-K = 1 Btu/lbm-F.)

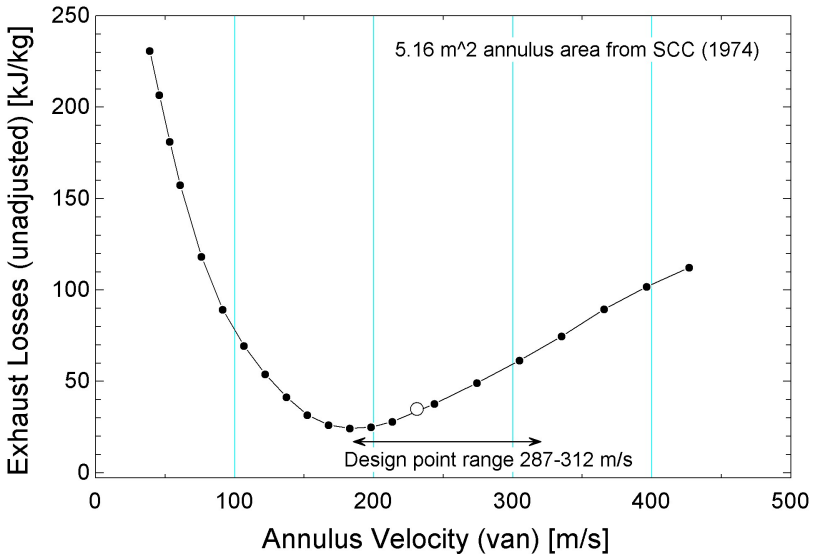

Figure 4.3: The exhaust loss curve for a 3600 rpm condensing section is shown. As an example a leaving velocity of 231 m/s gives exhaust losses of 35 kJ/kg. The exhaust losses must then be adjusted for the moisture level per SCC to give exhaust losses at design conditions of 23 kJ/kg.

Condenser

The condenser is a shell-and-tube type surface condenser. Figure 4.4 shows the condenser and relevant state points for the steam and cooling water. Cooling water is provided to the condenser at 28 °C as in the benchmark design. The condenser incorporates the return from the extraction streams from the LP turbine with the incoming steam from the main LP turbine exit. The condenser is specified in the current model by the cooling water range (Equation 4.6, here 10 °C), approach temperature difference (Equation 4.7, here 3 °C), and amount of subcooling of the condensate (here 0.1 °C). With this information and the known cooling water temperature, the entering and leaving temperatures, LMTD, and heat transferred are known.

$$\mathrm{Range}_{\mathrm{cond}} = \mathrm{T}_{\mathrm{CWout}} - \mathrm{T}_{\mathrm{CWin}} \tag{4.6}$$

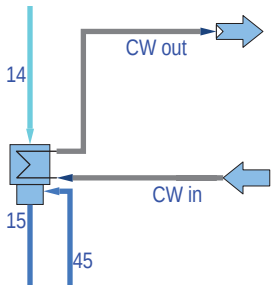

Figure 4.4: Condenser diagram from IPSE process model. The steam enters at state 14, is cooled by the cooling water (CW), mixed with the return water from the extractions (45) and leaves subcooled (15).

$$Approach_{cond} = T_{14} - T_{CWout} \tag{4.7}$$

The LMTD method is then used to determine the UA product. In order to determine physical size (A), the conductance (U_{cond}) water side is determined from the cold water inlet temperature, specified tube sizing, flow velocity in tubes, and material based on HEI methods. HEI methods from Heat Exchange Institute [1995] for surface condensers are based on calculation of the conductance U from:

$$U_{cond} = U_1 F_W F_M F_C \tag{4.8}$$

The unadjusted heat transfer coefficient U_1 is based on the fluid velocity from tabular data in the standards. The constants F_W, F_M, F_C, are corrections for water inlet temperature, tube material/gauge, and cleanliness, respectively, also given from tables.

Closed feedwater heaters

Figure 4.1 shows five closed feedwater heaters with drain cooling sections. The condensing section is a shell-and-tube type surface condenser. Figure 4.5 shows a closed feedwater heater and state points. In the current model, the terminal temper-

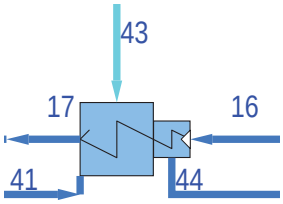

Figure 4.5: A closed feedwater heater is shown from the IPSE process model. Steam enters at 43 and is mixed with the recycled condensate from the upstream feedwater is state 41. Condensate exits at 44. The feedwater stream is 16 and 17.

ature difference (TTD, 2 or 4 °C) and drain cooler approach (DCA, 7 °C) are specified. TTD is the difference between the saturated steam (saturation temperature at p_{43}) and leaving feedwater (T_{17}). DCA is the difference between the subcooled condensate (T_{44}) and entering feedwater (T_{16}). The LMTD is determined for each section (condensing and drain cooler) and the size of each section is determined.

Open feedwater heater

Figure 4.1 shows one open feedwater heater in the cycle. Figure 4.6 shows a detailed view and state points. Extraction steam is mixed with feedwater and the resulting stream is required to be saturated liquid. Blowdown from the evaporator is also mixed and a small stream equal to a fixed fraction of the incoming feedwater (0.001) of the heater fluid is exhausted as saturated vapor. The open feedwater heater is analyzed with a simple energy balance.

Solar Steam Generator and Reheater

The solar steam generator is made up of the economizer, evaporator, and superheater. Figure 4.7 shows the four heat exchangers and state points. The economizer, superheater, and reheater components are all heat exchangers between water (steam) and the solar heat transfer fluid. For each component, temperature differences are specified and an LMTD approach is used to determine the heat exchanger UA required.

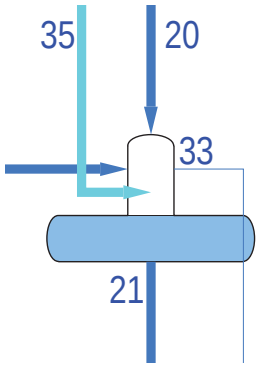

Figure 4.6: An open feedwater heater from the IPSE process model shows incoming extracted steam at 35 mixed with feedwater (20) and boiler blow-down water (not labeled, left). The exiting condensate is stream 21. Steam 33 is the exhaust stream.

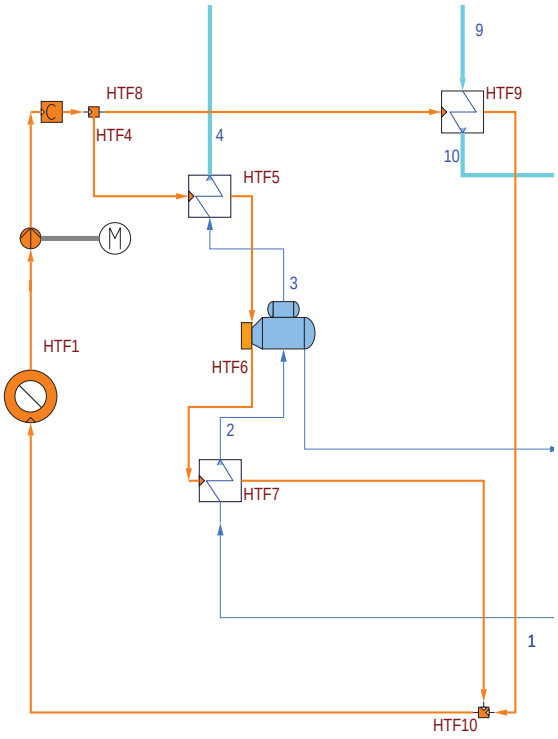

Figure 4.7: Detail of HTF loops and solar steam generator train and reheater from IPSE process model.

Economizer. In the economizer component, the feedwater is heated to a set amount of subcooling before entering the evaporator.

Superheater and reheater. In the superheater and reheater, the approach temperature (difference between hot inlet and cold exit) is set. For example, the approach temperature difference in the superheater is defined as:

$$\mathrm{Approach}_{\mathrm{sph\,t}} = T_{HTF4} - T_4 \tag{4.9}$$

Evaporator. In the evaporator, the pinch point is set and the exiting steam at state 3 is saturated vapor. The pinch point temperature difference is:

$$PPT = T_{HTF6} - T_3 \tag{4.10}$$

A blowdown fraction is set in the evaporator to determine the mass flow of saturated liquid that is exhausted at the drain pressure (0.01 of the incoming steam mass flow rate).

4.1.3 Detailed power block model: off-design point

Next, the off-design performance is analyzed with IPSE to compare to the benchmark cycle off-design thermal efficiency. The thermal input is varied by allowing the HTF mass flow rate and HTF return temperature to vary to capture thermal inputs from 20 to 100 % of the design value (257.4 MWth) in 10 % increments. The cycle is configured to handle lower thermal inputs by reducing the evaporator pressure. Cooling water input temperatures are also varied from the design value (28 °C) by 2 °C increments down to 14 °C.

IPSE handles the off-design operation by modeling how each component will operate under off-design operation. The off-design system models (datasets) are linked to the design dataset and have the same physical components but use more complex formulations to capture off-design behavior. After changing the component models to off-design versions as necessary, six datasets were created that use different guess values that allowed the solver to capture the 72 unique conditions.

The PSXLink toolbox in Microsoft Excel was used to run these six datasets for the 72 conditions. Licensed by SimTech, this toolbox allows Excel to call IPSE and record only a subset of key results. The results were then compiled and graphed using Visual Basic in Excel.

This section describes any differences between the design- and off-design component models and the results of the off-design analysis under a range of operating conditions. Note that the open feedwater heater does not require an off-design model because it is modeled with a simple energy balance that does not change under off-design conditions.

Shell-and-tube heat exchanger off-design modeling

Most of the heat exchangers used in the solar power cycle are shell-and-tube type. In this section, the basic modeling scheme for off-design performance is detailed before the IPSE models are presented.

The conductance-area product UA includes the resistances to heat transfer for internal convection in the tube (convection coefficient h_i over heat transfer area A_i), conduction through the tube wall, fouling effects, and external convection in the shell (convection coefficient h_o over heat transfer area A_o). The resistance to heat transfer via convection in the tube wall is negligible compared to the fluid resistances. Also neglecting fouling, the conductance-area product is estimated by:

$$\frac{1}{UA} \approx \frac{1}{h_i A_i} + \frac{1}{h_o A_o} \tag{4.11}$$

For a detailed model of a heat exchanger's physical size and cost, dimensions are needed to evaluate each heat transfer coefficient. For the purpose of performance modeling, however, some simplifications are useful. First, the heat transfer areas A_i and A_o are assumed equal and denoted A. The tube diameter is D. In the design load calculations, the heat exchanger is sized by selecting the UA based on relevant temperature differences for the desired performance. In the off-design load calculations, the change in UA from the design case is sufficient to understand off-design performance. The Nusselt number is the dimensionless convection

coefficient $Nu = hD/k$, making Equation 4.11:

$$\frac{1}{UA} \approx \frac{1}{\frac{Nu_i k_i}{D} A} + \frac{1}{\frac{Nu_o k_o}{D} A} \tag{4.12}$$

The internal convection coefficient is based on forced convection in a tube. Dittus-Boelter predicts the convection heat transfer coefficient for turbulent flow via the Nusselt number as:

$$Nu_i = 0.023 Re_i^{0.8} Pr_i^{0.3} \tag{4.13}$$

Where the Prandtl exponent 0.3 is for cooling and 0.4 for heating of fluid, and i indicates the internal dimensionless parameters Nusselt Nu, Reynolds Re and Prandtl Pr.

Tube side resistance dominates. In the case of the condenser, the evaporator in the solar steam generator, or the condensing section of a feedwater heater, the shell-side fluid is undergoing a phase change so the resistance to heat transfer is dominated by the tube side. Equations 4.12 is then:

$$\frac{1}{UA_{evap}} \approx \frac{1}{\frac{Nu_i k_i}{D} A} \tag{4.14}$$

Using Equation 4.13:

$$\frac{1}{UA_{evap}} \approx \frac{1}{\frac{0.023 Re_i{}^{0.8} Pr_i^n k_i}{D} A} \tag{4.15}$$

The ratio of design to off-design conductance-area products in the evaporator is quantified and simplified by assuming that the tube side properties do not change between design and off-design conditions. The design condition is the reference condition *REF*.

$$\frac{UA_{evap}}{UA_{evap,REF}} = \frac{\frac{0.023 Re_i^{0.8} Pr_i^n k_i}{D} A}{\frac{0.023 Re_{i,REF}^{0.8} Pr_i^n k_i}{D} A} \approx \left(\frac{Re_i}{Re_{i,REF}} \right)^{0.8} \tag{4.16}$$

Noting that the Reynolds number is $(4\dot{m})/(\pi\mu D)$ and again that properties do not change significantly, the conductance-area product is simply related to the mass flow rate as:

$$\boxed{\frac{UA_{evap}}{UA_{evap,ref}} \approx \left(\frac{\dot{m}_i}{\dot{m_{i,ref}}}\right)^{0.8}} \tag{4.17}$$

This is a useful relationship for the case where a phase change occurs on the shell side.

Shell side resistance dominates. In the superheater, superheated steam on the shell side of the heat exchanger has significantly higher resistance to heat transfer than the fluid on the tube side. From Equation 4.12, the conductance-area product is then:

$$\frac{1}{UA_{spht}} \approx \frac{1}{\frac{Nu_o k_o}{D} A} \tag{4.18}$$

For the shell side of the heat exchanger, the convection heat transfer is based on external flow over a bank of tubes. The Zukauskas correlation [Incropera and DeWitt, 2002] provides the Nusselt number relationships.

$$Nu_o = CRe_{D,max}^{m_z} Pr_o^{0.36} \left(\frac{Pr_o}{Pr_s}\right)^{1/4} \tag{4.19}$$

The Reynolds number $Re_{D,max}$ is evaluated at the maximum velocity as described in Incropera and DeWitt. All properties are evaluated at the average of inlet and outlet temperatures except the Pr_s which is evaluated at the surface temperature. This correlation applies for configurations with at least 20 tubes, Prandtl number from 0.7 to 500, and Reynolds number from 1000 to 2x10e6. The constants C and m_z depend on the Reynolds number and geometry of the bank of tubes. The constant m_z may take values of 0.4, 0.63, 0.6, or 0.84. The Reynolds number for the flow over a bank of tubes is $(\rho V_{max} D)/(\mu)$. The maximum velocity V_{max} is related to the average velocity and the tube bank geometry. For this analysis it is useful to note that the maximum velocity is proportional to the average velocity, and therefore proportional to the mass flow rate. Here a constant C_2 is defined to account for the

proportionality, finally giving the Reynolds number for the bank of tubes as:

$$Re_{D,max} = C_2 \frac{\rho \dot{m} D}{\mu} \tag{4.20}$$

Applying the correlation and Reynolds number definition to 4.18:

$$\frac{1}{UA_{spht}} \approx \frac{1}{\frac{C(C_2 \frac{\rho \dot{m} D}{\mu})^{m_z} Pr_o^{0.36} \left(\frac{Pr_o}{Pr_s}\right)^{1/4} k_o}{D} A} \tag{4.21}$$

In the design and off-design case, the properties, constants, and geometry values are assumed constant. The ratio of the design and off-design conductance-area products is then simply related to the mass flow rates.

$$\boxed{\frac{UA_{spht}}{UA_{spht,REF}} \approx \left(\frac{\dot{m}_o}{\dot{m}_{o,REF}}\right)^{m_z}} \tag{4.22}$$

This relationship is for the case of gas on the shell side where m_z takes values from 0.4 to 0.84 depending on the Reynolds number and tube alignment (staggered or aligned).

Both shell and tube side resistances relevant. For the case where both sides have sensible heat transfer such as the economizer and the drain cooling sections of the condenser and feedwater heaters, the analysis proceeds from Equation 4.12. The internal convection heat transfer coefficient is from Equation 4.13 and the shell side is from Equation 4.19. The conductance-area product is then:

$$\frac{1}{UA} \approx \frac{1}{\frac{0.023 Re_i^{0.8} Pr_i^n k_i}{D} A} + \frac{1}{\frac{C Re_{D,max}^m Pr_o^{0.36} \left(\frac{Pr_o}{Pr_s}\right)^{1/4} k_o}{D} A} \tag{4.23}$$

The ratio of design and off-design values is again of interest. The dimensions D and A appear in all terms and cancel. It is assumed that the fluid properties do not change significantly between the design and off-design conditions but the flow

rates (Reynolds numbers) do.

$$\frac{UA}{UA_{REF}} \approx \frac{\frac{1}{0.023Re_{i,REF}^{0.8}Pr_i^n k_i} + \frac{1}{CRe_{D,max,REF}^m Pr_o^{0.36}\left(\frac{Pr_o}{Pr_s}\right)^{1/4} k_o}}{\frac{1}{0.023Re_i^{0.8}Pr_i^n k_i} + \frac{1}{CRe_{D,max}^m Pr_o^{0.36}\left(\frac{Pr_o}{Pr_s}\right)^{1/4} k_o}} \tag{4.24}$$

Reynolds number definitions are substituted into Equation 4.24.

$$\frac{UA}{UA_{REF}} \approx \frac{\frac{1}{0.023(\frac{4\dot{m}_{i,REF}}{\pi\mu D})^{0.8}Pr_i^n k_i} + \frac{1}{C(C_2\frac{\rho\dot{m}_{o,REF}D}{\mu})^m Pr_o^{0.36}\left(\frac{Pr_o}{Pr_s}\right)^{1/4} k_o}}{\frac{1}{0.023(\frac{4\dot{m}_i}{\pi\mu D})^{0.8}Pr_i^n k_i} + \frac{1}{C(C_2\frac{\rho\dot{m}_o D}{\mu})^m Pr_o^{0.36}\left(\frac{Pr_o}{Pr_s}\right)^{1/4} k_o}} \tag{4.25}$$

The constant terms inside the tube are consolidated into the term C_i and those outside are C_o:

$$C_i = 0.023(\frac{4}{\pi\mu D})^{0.8}Pr_i^n k_i \tag{4.26}$$

$$C_o = C(C_2\frac{\rho D}{\mu})^m Pr_o^{0.36}\left(\frac{Pr_o}{Pr_s}\right)^{1/4} k_o \tag{4.27}$$

Equation 4.25 is then:

$$\boxed{\frac{UA}{UA_{ref}} \approx \frac{\frac{1}{C_i\dot{m}_{i,REF}^{0.8}} + \frac{1}{C_o\dot{m}_{o,REF}^m}}{\frac{1}{C_i\dot{m}_i^{0.8}} + \frac{1}{C_o\dot{m}_o^m}}} \tag{4.28}$$

If the heat exchanger tube diameter and tube bank geometry is known, the off-design UA can be calculated. But without a set geometry, Equation 4.28 cannot be simplified any further because the Reynolds number exponents are not the same. For the sake of simplifying the problem, here it is assumed that the constant m takes a value of 0.8 (which is within the range of values provided).

$$\frac{UA}{UA_{ref}} \approx \frac{\frac{1}{C_i\dot{m}_{i,REF}^{0.8}} + \frac{1}{C_o\dot{m}_{o,REF}^{0.8}}}{\frac{1}{C_i\dot{m}_i^{0.8}} + \frac{1}{C_o\dot{m}_o^{0.8}}} \tag{4.29}$$

It is often reasonable to assume that the ratio of mass flow rates on the tube side and shell side of the heat exchanger is constant in all operating conditions. This ratio is κ:

$$\frac{\dot{m}_i}{\dot{m}_o} = \frac{\dot{m}_{i,ref}}{\dot{m}_{o,ref}} = \kappa \tag{4.30}$$

Each term in Equation 4.29 is then multiplied by $\kappa^{0.8}$ to give:

$$\frac{UA}{UA_{ref}} \approx \frac{\frac{1}{C_i \dot{m}_{o,REF}^{0.8}} + \frac{1}{C_o \dot{m}_{o,REF}^{0.8}} \kappa^{0.8}}{\frac{1}{C_i \dot{m}_o^{0.8}} + \frac{1}{C_o \dot{m}_o^{0.8}} \kappa^{0.8}} \tag{4.31}$$

Constant terms are separated to give:

$$\frac{UA}{UA_{ref}} \approx \frac{\frac{1}{\dot{m}_{o,REF}^{0.8}} \left(\frac{1}{C_i} + \frac{1}{C_o} \kappa^{0.8} \right)}{\frac{1}{\dot{m}_o^{0.8}} \left(\frac{1}{C_i} + \frac{1}{C_o} \kappa^{0.8} \right)} \tag{4.32}$$

Canceling terms, the result is:

$$\boxed{\frac{UA}{UA_{ref}} \approx \left(\frac{\dot{m}_o}{\dot{m}_{o,ref}} \right)^{0.8}} \tag{4.33}$$

Given the proportionality of shell and tube side mass flow rates, Equation 4.30, the ratio of conductance -area products can also be stated in terms of the internal mass flow rates as in Equation 4.17. Equations 4.17 or 4.33 apply for shell-and-tube heat exchangers with sensible heat transfer on both sides where the ratio of mass flow rates on the shell to tube sides is constant and the shell side and tube side heat transfer coefficients are both proportional to $Re^{0.8}$.

4.1.4 Pressure drop

Pressure drop at the design point in each component is specified typically by a percent loss. In the off-design cases, this pressure drop is scaled by the mass flow, pressure, and/or temperature.

The pressure drop is expressed in terms of the dimensionless friction factor f:

$$f = \frac{-(dp/dx)D}{\rho u_m^2/2} \tag{4.34}$$

Where x is the axial position along the flow, D is the diameter, and u_m is the mean velocity. Thus the pressure drop is related to the mass flow rate squared and the friction factor. The friction factor depends on surface roughness. Multiple correlations and the Moody chart are available to estimate the friction factor.

4.1.5 High pressure turbine: off-design

The high pressure turbine is an intermediate pressure type turbine, as described in the design case. Here the system uses sliding pressure, allowing the cycle's high pressure side to float from 100 bar at design down to as low as 30 bar in low load conditions. The reduced pressure steam has a higher specific volume and lower mass flow rate. The off-design model of this turbine is identical to the design model with two exceptions. The pressure drops (inlet-bowl) and (2-exit) specified for the design case are adjusted for off-design operation according Stodola's law principles. The extraction pressures are no longer specified. Instead Stodola's law is used to determine the extraction pressures given the design values and the new adjusted flow conditions.

4.1.6 Low pressure turbine: off-design

The low pressure turbine off-design model is nearly identical to the design model. Extraction pressures are determined based on Stodola law (i.e. Law of the Ellipse, see Stodola and Loewenstein [1945]) given reduced steam mass flow rate. The off-design model applies SCC methods using the off-design conditions to determine the expansion efficiency and exhaust losses. The turbine geometry is determined in the design phase. The inlet pressure drop (inlet-bowl) specified in the design case is adjusted for off-design operation also using Stodola law.

4.1.7 Condenser: off-design

The off-design condenser model is based on the same LMTD approach as the design case, but instead of setting the temperature differences, the surface area A is known (same as design case) and the conductance U_{cond} is adjusted based on off-design conditions.

The condenser U_{cond} is determined from the design value of U_{cond} and the off-design values of cold water inlet temperature, flow velocity, and cleanliness factor based on HEI methods. Cleanliness factor is here assumed constant in the design and off-design cases. The cooling water flow velocity is the same as the design case here because the mass flow of cooling water is not varied in this case. The cooling water inlet temperature is an input for the off-design cases depending on availability from cooling source such as cooling tower or cold water storage. Decreasing water inlet temperatures increase the conductance U_{cond} slightly via the correction factor F_W in the HEI method.

The subcooling is scaled from the design case by the UA product.

Solar steam generator and reheater: off-design

Economizer. In the economizer's off-design model, instead of specifying the amount of subcooling at the economizer exit, the UA product is set. The pressure drops and UA product are scaled using the off-design mass flow rates. For the pressure drop on the cold side, using state points from Figure 4.7:

$$\frac{p_1 - p_2}{p_{1,design} - p_{2,design}} = \left(\frac{\dot{m}_{steam}}{\dot{m}_{steam,design}}\right)^{1.84} \tag{4.35}$$

For the pressure drop on the hot side, again using state points from Figure 4.7:

$$\frac{p_{HTF6} - p_{HTF7}}{p_{HTF6,design} - p_{HTF7,design}} = \left(\frac{\dot{m}_{HTF}}{\dot{m}_{HTF,design}}\right)^{1.84} \tag{4.36}$$

The UA of the economizer can be scaled in IPSE using the mass flow rates on both the hot and cold side compared to their design values. The scaling coefficients can

be customized in IPSE, so in this case according to Equation 4.17:

$$\frac{UA_{econ}}{UA_{econ,design}} = (\frac{\dot{m}_{HTF}}{\dot{m}_{HTF,design}})^{0.8} \tag{4.37}$$

Note that this assumes that the Reynolds number exponents for both the shell side is 0.8 and that the flow rates are proportional. To determine the most accurate m_z value from 0.4 to 0.84 according to the correlation for flow over a bank of tubes, the actual geometry of the heat exchanger could be modeled and tested over the range of operating conditions. The assumption that flow rates are proportional on the inside and outside is not exactly true for this cycle.

Evaporator. For the evaporator's off-design calculations, instead of setting the pinch point as in the design case, the UA product is set. The pressure drop on the hot side is scaled by the off-design and design mass flow rates, pressures, and temperatures. Using the states from figure 4.7, the pressure drop on the hot side is:

$$\frac{p_{HTF5} - p_{HTF6}}{p_{HTF5,design} - p_{HTF6,design}} = (\frac{\dot{m}_{HTF6}}{\dot{m}_{HTF6,design}})^{-1}(\frac{p_{HTF6}}{p_{HTF6,design}})^{1.84}(\frac{T_{HTF6}}{T_{HTF6,design}})^{1} \tag{4.38}$$

The evaporator UA product is scaled by the hot side mass flow rate. Equation 4.17 for the evaporator is:

$$\frac{UA_{evap}}{UA_{evap,design}} = (\frac{\dot{m}_{HTF}}{\dot{m}_{HTF,design}})^{0.8} \tag{4.39}$$

Superheater and reheater. In the superheater and reheater, instead of specifying the approach temperature difference, the UA product is set in the off-design model. The pressure drop on the cold side, pressure drop on the hot side, and UA products at off-design conditions are formulated as for the economizer based on the design mass flow rates as Equation 4.22:

$$\frac{UA_{spht}}{UA_{spht,design}} \approx \left(\frac{\dot{m}_4}{\dot{m}_{4,design}}\right)^{0.8} \tag{4.40}$$

Note that this assumes that the Reynolds number exponent is 0.8.

Closed feedwater heater: off-design

In the off-design models of the closed feedwater heaters, instead of setting the drain cooler approach temperature for the sub-cooling region and the terminal temperature difference for the condensing region as done in the design case, the UA product of each region is set. The pressure drops and UA products are determined from the following relations, using the state points in Figure 4.5.

$$\frac{p_{43} - p_{44}}{p_{43,design} - p_{44,design}} = \left(\frac{\dot{m}_{43}}{\dot{m}_{43,design}}\right)^2 \tag{4.41}$$

$$\frac{p_{16} - p_{17}}{p_{16,design} - p_{17,design}} = \left(\frac{\dot{m}_{16}}{\dot{m}_{16,design}}\right)^2 \tag{4.42}$$

For the condensing section, only the mass flow rate of the cold feedwater is needed to determine the UA product in off-design conditions because the resistance to heat transfer of the condensing steam is zero. Unlike the evaporator, a Reynolds number exponent of 0.6 is chosen here based on convention.

$$\frac{UA_{FWH,cond}}{UA_{FWH,cond,design}} = \left(\frac{\dot{m}_{16}}{\dot{m}_{16,design}}\right)^{0.6} \tag{4.43}$$

For the drain cooling section, the mass flow rates of both streams are required to determine the UA product of the drain cooler section. State 16 represents the mass flow of the feedwater and state 43 is the condensed steam mass flow in the drain cooler.

$$\frac{UA_{FWH,dc}}{UA_{FWH,dc,design}} = 2\frac{\left(\frac{\dot{m}_{16}}{\dot{m}_{16,design}}\right)^{.6}\left(\frac{\dot{m}_{43}}{\dot{m}_{43,design}}\right)^{.6}}{\left(\frac{\dot{m}_{16}}{\dot{m}_{16,design}}\right)^{.6} + \left(\frac{\dot{m}_{43}}{\dot{m}_{43,design}}\right)^{.6}} \tag{4.44}$$

This standard formulation in IPSE is not customizeable in the existing component (though the user can create new components), but note that if the proportionality of Equation 4.30 holds true, then:

$$\frac{\dot{m}_{16}}{\dot{m}_{43}} = \frac{\dot{m}_{16,design}}{\dot{m}_{43,design}} = \kappa \tag{4.45}$$

This simplifies Equation 4.44 to:

$$\frac{UA_{FWH,dc}}{UA_{FWH,dc,design}} = \left(\frac{\dot{m}_{16}}{\dot{m}_{16,design}}\right)^{0.6} \tag{4.46}$$

4.2 Results and validation for benchmark cycle

4.2.1 Comparison to SolarPACES benchmark

As described in this section, the design point for the cycle used the specified gross power production, initial pressure, HTF supply temperature, cooling water temperature, and reheat pressure from Yildiz. In addition to these key parameters, a partial list of heat exchanger specifications and pressure drops was given. The design point model compares to the benchmark from Yildiz as follows:

Table 4.1: Key cycle design outputs for comparison.

	Benchmark model	Current IPSE model
Gross efficiency	38.97 %	38.85 %
HTF flow rate	1055 kg/sec	1054 kg/sec
HTF return temp	293.1 °C	292.9 °C

This is sufficient to validate the design point modeling strategy.

4.2.2 Off design performance results

For comparison to the SolarPACES benchmark model, the power cycle operation is summarized by varying the cooling water temperature and load fraction (defined as fraction of full load HTF mass flow rate). The HTF supply temperature is assumed constant at 393 °C by control of the solar collectors for this case. This section reports the key outputs of the model for the range of conditions tested. The results are compared to those of the benchmark model provided at the same off-design points in Yilidiz. Figure 4.8 shows that the peak efficiency of 39% is approximately constant

at full load regardless of the cooling water temperature. This is despite the fact that the condensing pressure is lower for lower cooling water temperatures as shown in Figure 4.9. The benefit of lowering the condensing pressure on the thermal efficiency is offset by the increased exhaust losses for lower condensing pressures as shown in Figure 4.10. This can be changed by adjusting the design point of the turbine relative to the exhaust loss curve. Figures 4.8 through 4.12 provide results for key outputs over the range of load and cooling water temperatures. Figure 4.10 shows that the exhaust losses are minimal for low loads and moderate cooling water temperatures. Bends in the curves show where the limits of the typical exhaust loss curve are reached and the SCC method provides a method to extend the curves. For example for 14 °C cooling water at full load, the annulus velocity is higher than the maximum of 426 m/s so the discontinuity is evident in the curve. Comparing these results to the results provided by Yildiz [2017], the gross efficiency is within 1% (raw efficiency points) for all cases. The percent difference in the Yilidiz and current model's HTF mass flow rate is within 1% for all cases. This exercise validates the off-design modeling. Next, the cycle model will be adjusted to meet the needs of the radiative cooling with cold storage system.

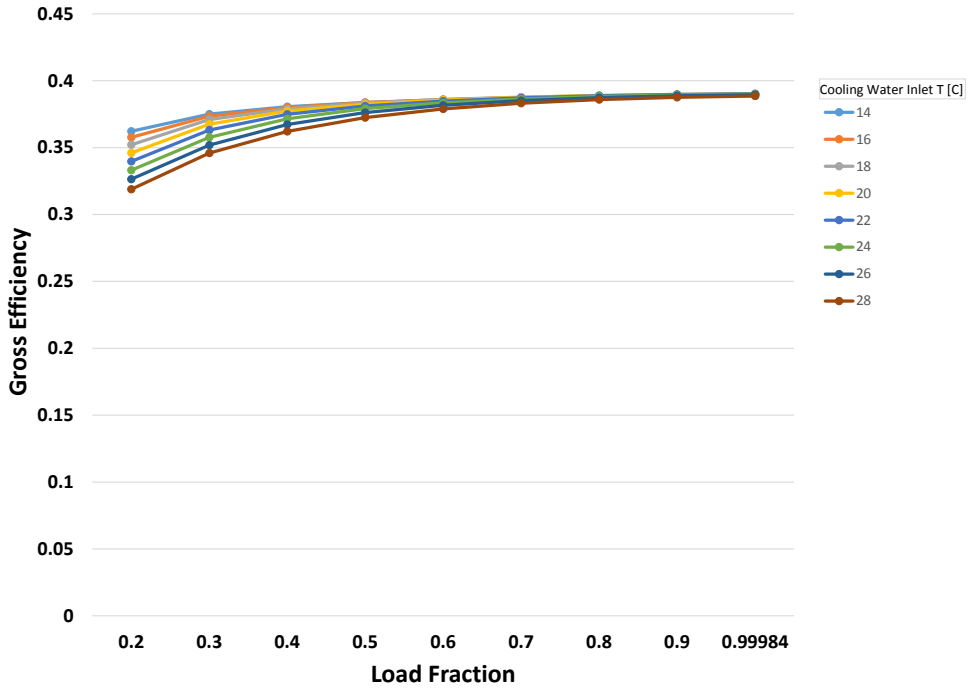

Figure 4.8: The gross efficiency is maximum at full load and decreases towards lower load cases and higher cooling water temperatures.

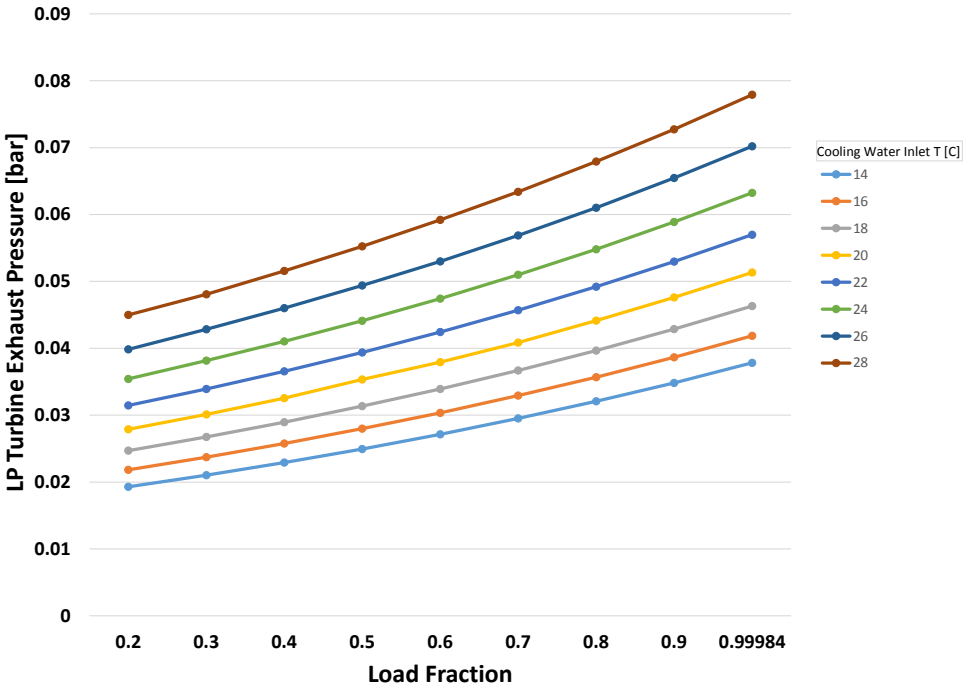

Figure 4.9: The condensing pressure decreases according to cooling water temperature and load fraction.

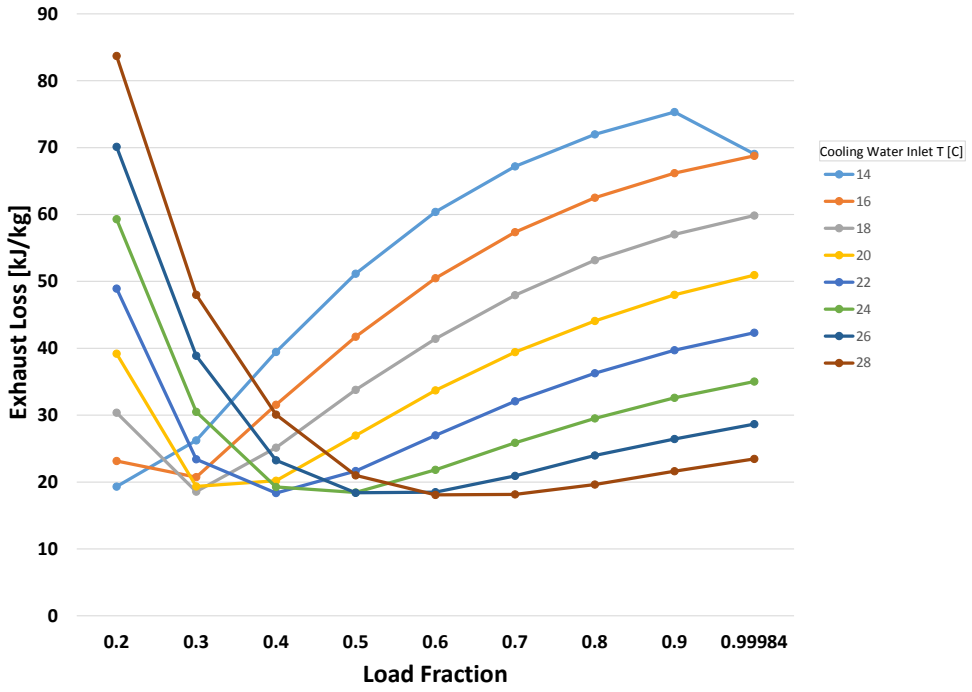

Figure 4.10: The exhaust losses reflect the exhaust loss curve for the last stage turbine blade. The last stage turbine blade was chosen so that at 28 °C cooling water temperature and 100 % load, exhaust losses are near the minimum level.

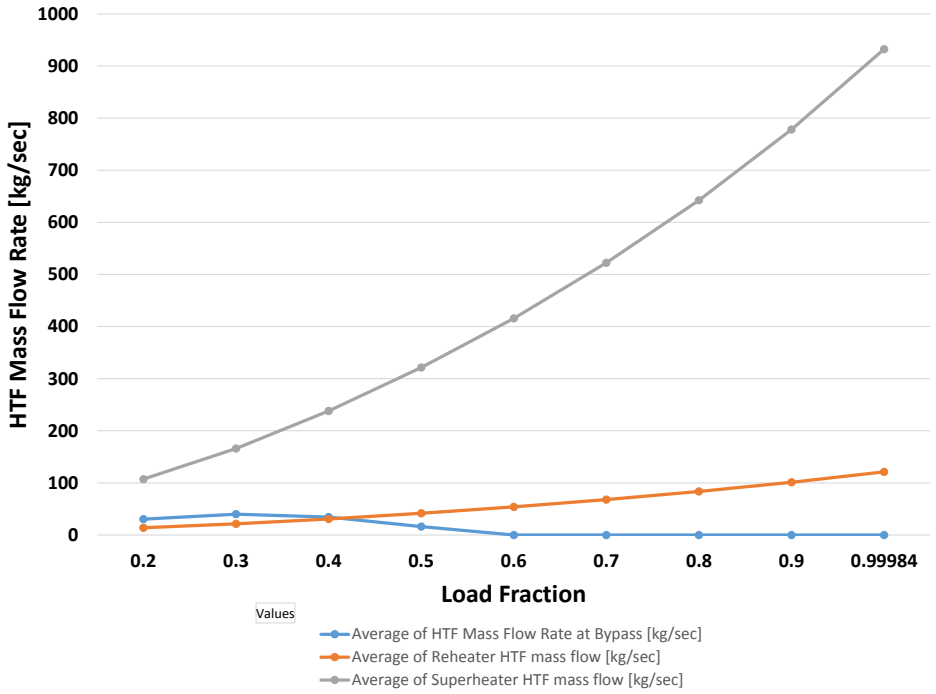

Figure 4.11: The HTF mass flow rate is directly related to the load fraction.

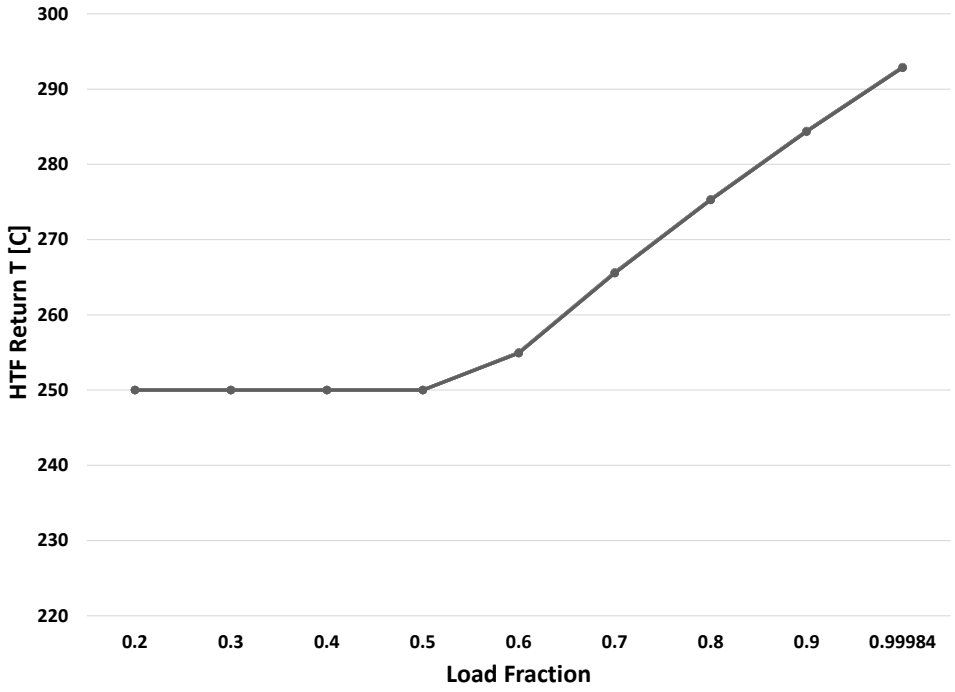

Figure 4.12: The HTF return temperature is related to the load fraction and the system is controlled to maintain a minimum of 250 °C temperature at low loads.

4.3 Modeling a custom power cycle

Next the validated Rankine cycle model is adjusted to create two custom power cycle models that are designed for the air- and radiative- cooled CSP plants in this project. CSP systems that utilize power towers for solar collection instead of parabolic troughs can achieve higher temperatures because they are not limited by the need to move the HTF through the trough field. The current configuration

of power towers most common is using molten salt in the receiver. The molten salt can withstand high temperatures and, like parabolic trough configurations, is a good material for energy storage. The molten salt transfers heat from the hot thermal storage to the power cycle, where a steam Rankine cycle is operated. The major difference in the Rankine cycle from the parabolic trough configuration is the operating temperature. Currently, molten salt is heated up to 565 °C and creates steam at up to 540 °C in the cycle. Mehos et al. [2017] provides an overview of the current technology and research aimed at increasing the receiver temperature above 700 °C. For the purpose of this work, the molten salt power tower configuration is most relevant. A recent plant of this type is the Crescent Dunes plant in Nevada. This is used roughly as the model for a power tower plant in this work. It is a 125 MW (gross) plant with steam generation at 115 bar.

The cycle configuration and components are as described in the SolarPaces benchmark cycle, with the exception of the condenser, which is modeled as a simple fixed UA. This simplification allows the cycle to be modeled over a complete range of condensing pressures regardless of condenser limitations. This captures the exhaust loss and condensing pressure effects on the cycle using the IPSE model, while leaving the details of the condenser operation to be modeled in System Advisor Model software (SAM) as described in Chapter 5. In order to correlate cycle performance for use in SAM, the condensing pressure is set instead of the cooling water delivery temperature. The cooling water flow rate is fixed. Thus the main cycle inputs are HTF temperature, HTF flow rate, and condensing pressure. The cycle is designed for 566 °C HTF delivery at 3 in Hg condensing pressure with a flow rate to meet 125 MW gross output.

Low pressure cycle for radiative cooling

A cycle is first modeled for use with radiative cooling. Because of the importance of turbine selection on exhaust losses and overall cycle performance, two different turbines are selected and compared. The first cycle uses an annulus area as selected automatically by IPSEPro. This is a 3.82 m^2 annulus area. Next the annulus area is

manually changed to 5.16 m ^{2}. Figure 4.13 shows how the design point lies on the exhaust loss curve for the two cases. The best choice depends on how much time the cycle will operate above or below the design point.

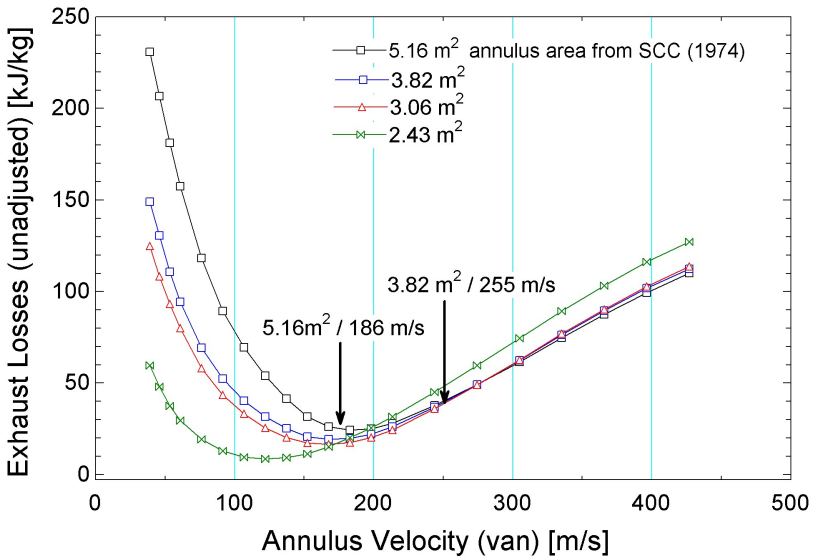

Figure 4.13: Selection of a smaller annulus area for the last stage turbine results in slightly higher exhaust losses but leaves room for the condensing pressure to increase (lower leaving velocities) while maintaining low exhaust losses.

Table 4.2: The design values of the three main factors for the low pressure cycle.

	3.82 m^2	5.16 m^2
HTF flow rate	734.3 kg/sec	728.6 kg/sec
HTF supply temp	566 °C	
Condensing pressure	3 in Hg	

The operating points are different in this power tower cycle compared to the benchmark parabolic trough cycle due to the higher HTF temperature. Using methods from El-Wakil as described for the benchmark cycle, the reheat pressure is set at 25 bar with extraction pressures selected to evenly space the associated satura-

tion temperatures between the condensing temperature and steam evaporation temperature.

The HTF loop is configured to split the high temperature HTF evenly between the reheater and superheater.

Figures 4.14 shows the IPSEPro models for the larger turbine. The smaller annulus area is leads to a slightly less efficient cycle at the design point (gross efficiency 43.3 versus 43.7 %). At low back pressure values the annulus velocity of the last stage turbine increase significantly and it is necessary to check that they do not exceed 426 m/s. Though the SCC methods provide adjustment factors to handle these cases, the exhaust losses predicted may be conservative and so these points are assumed to be outside of the desired operating range. For the larger turbine, the full range of 1.25 to 8 in Hg was feasible. For the smaller 3.82 m^2 last stage turbine annulus area, the annulus velocities exceed 426 m/s and the operation of this turbine would be limited to 1.75 in Hg. Since the goal of modeling a cycle for radiative cooling is to allow for low condensing pressures, the larger turbine is chosen.

High pressure cycle for air-cooling

Using the same design principles and model components, a cycle is also designed for an air-cooled power cycle for comparison of the air-cooled system to radiative cooling. The basis for this design is an ITD of 16 °C on an outdoor air temperature of 40 °C. The design point was modeled in IPSE using both an air-cooled condenser and also using the same once-through cooling system modeled for the radiative cooling system as shown in Figures 4.15 and 4.16, respectively.

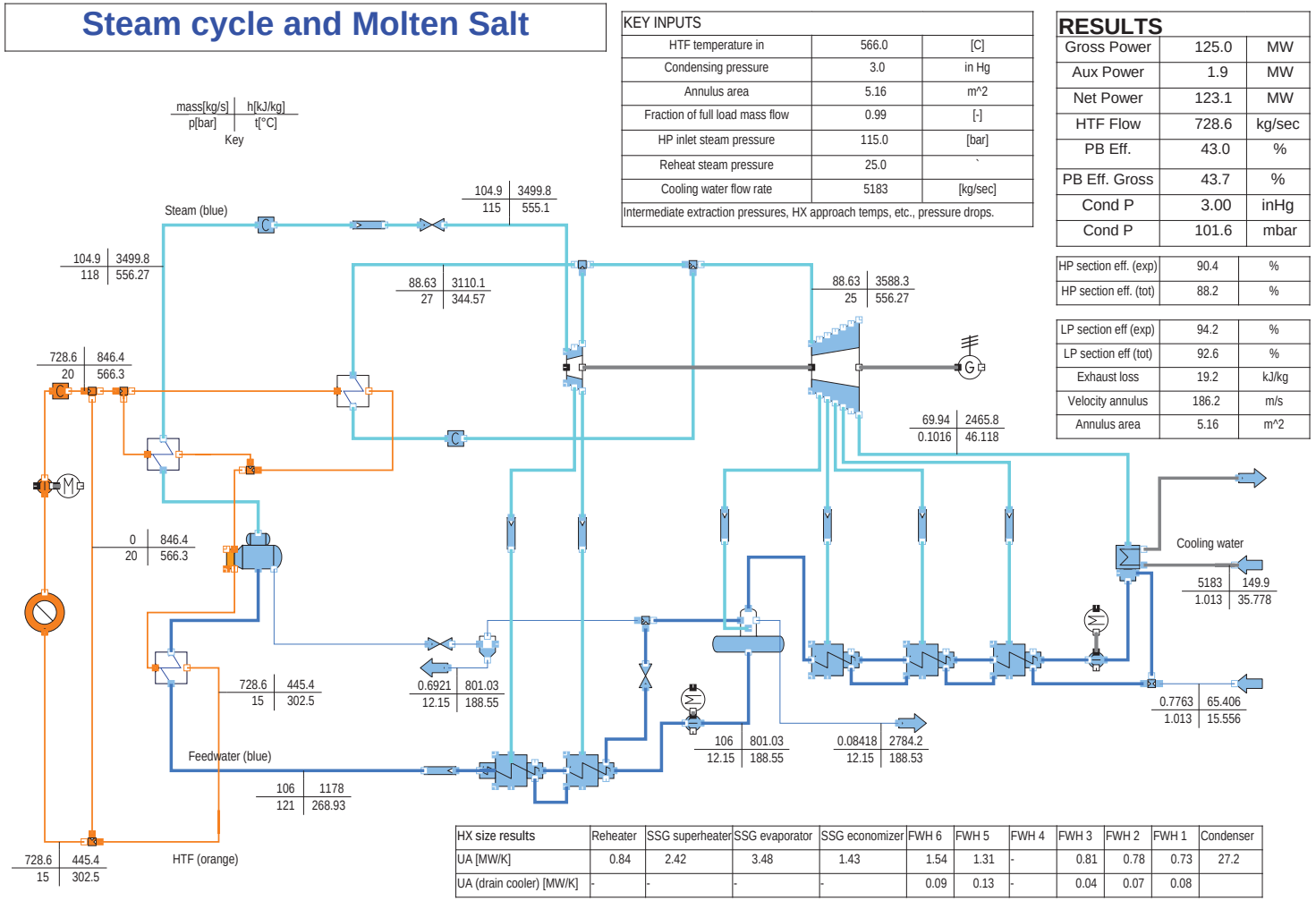

Figure 4.14: The cycle design solution from IPSEPro is shown for a 5.16 m ^{2} annulus area on the last stage turbine.

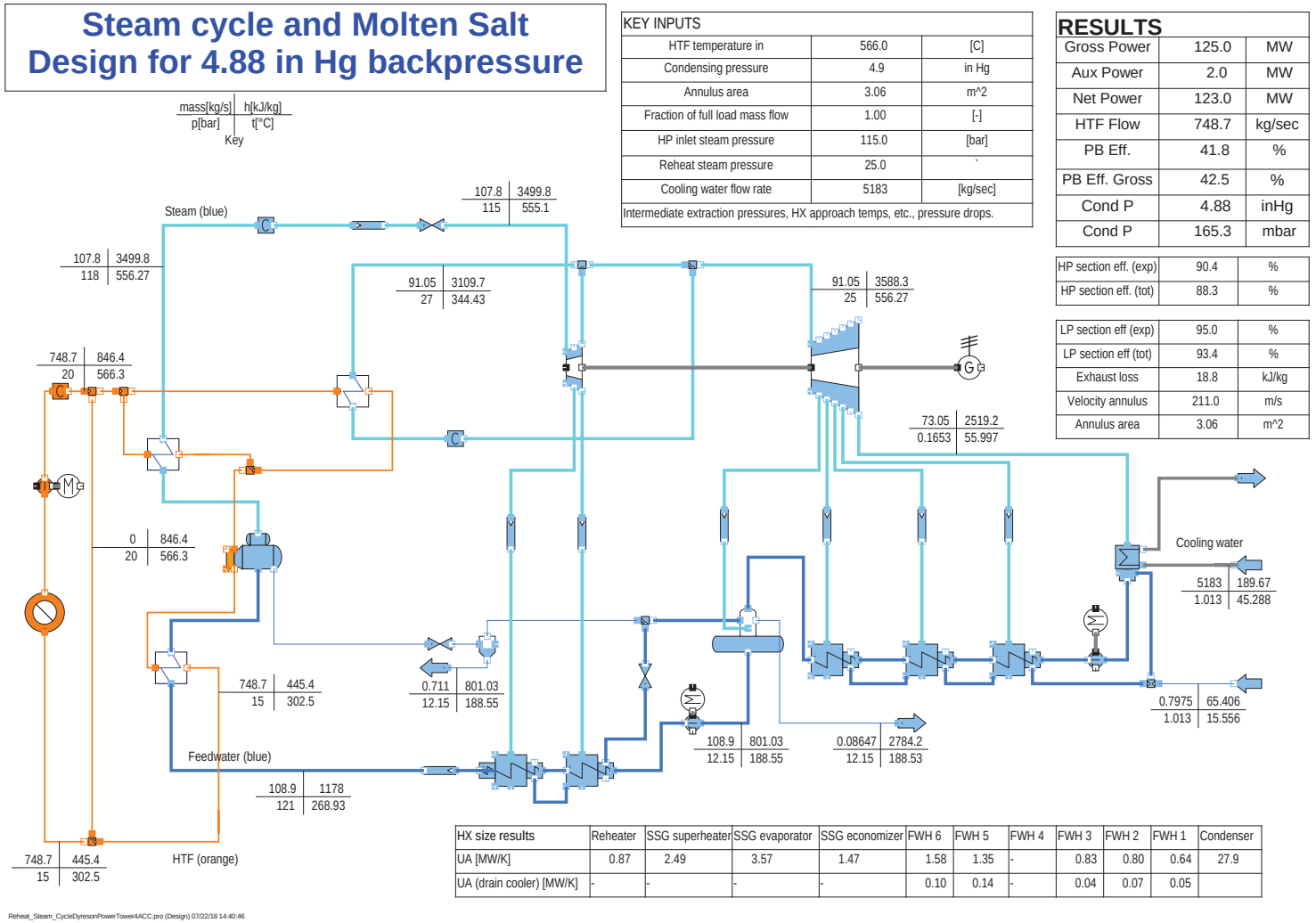

Figure 4.15: The cycle design solution from IPSEPro is shown for a 3.06 m ^{2} annulus area on the last stage turbine using a surface condenser model.

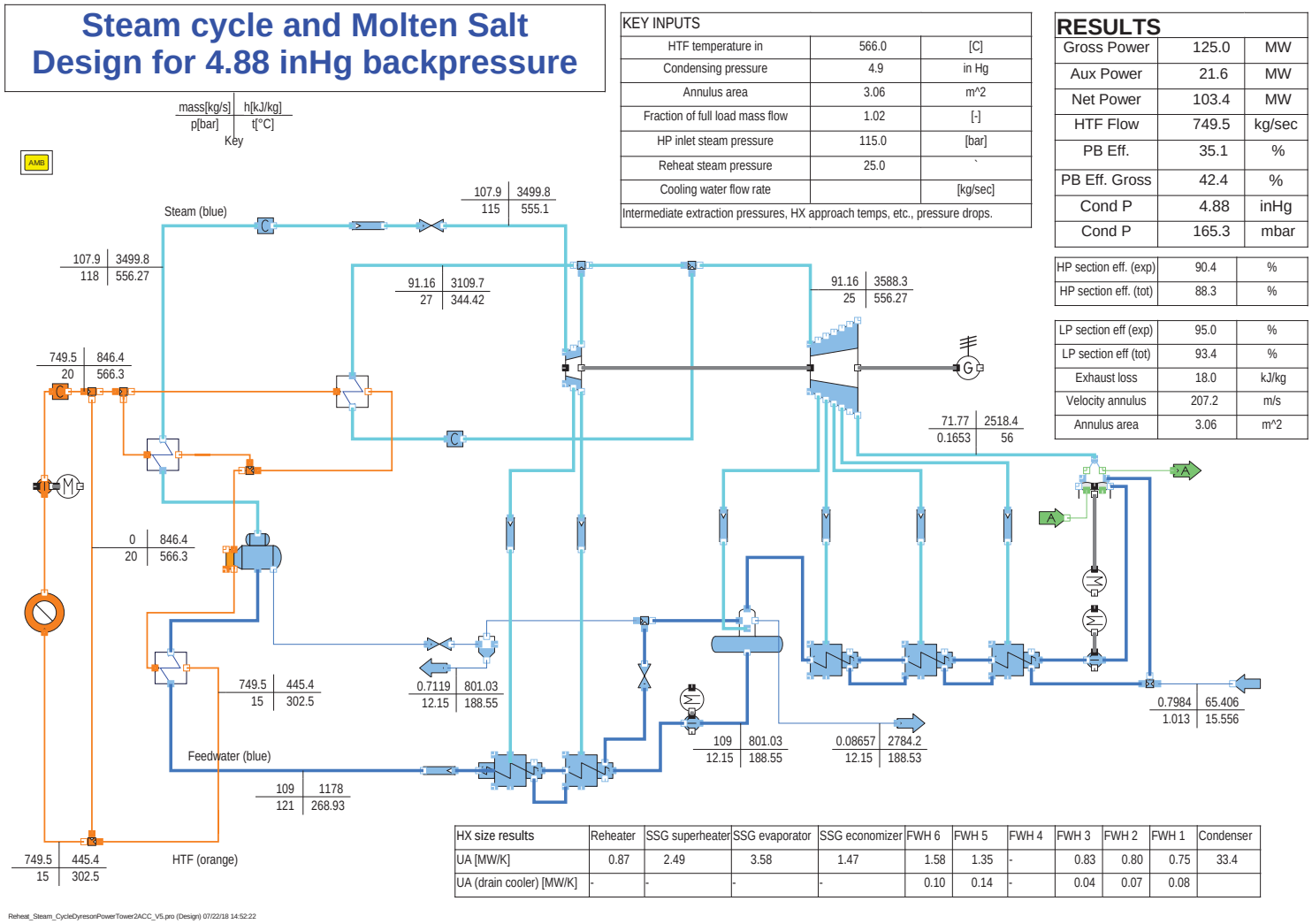

KEY INPUTS		
HTF temperature in	566.0	[C]
Condensing pressure	4.9	in Hg
Annulus area	3.06	m^2
Fraction of full load mass flow	1.02	[-]
HP inlet steam pressure	115.0	[bar]
Reheat steam pressure	25.0	
Cooling water flow rate		[kg/sec]
Intermediate extraction pressures, HX approach temps, etc., pressure drops.		

RESULTS		
Gross Power	125.0	MW
Aux Power	21.6	MW
Net Power	103.4	MW
HTF Flow	749.5	kg/sec
PB Eff.	35.1	%
PB Eff. Gross	42.4	%
Cond P	4.88	inHg
Cond P	165.3	mbar

HP section eff. (exp)	90.4	%
HP section eff. (tot)	88.3	%

LP section eff (exp)	95.0	%
LP section eff (tot)	93.4	%
Exhaust loss	18.0	kJ/kg
Velocity annulus	207.2	m/s
Annulus area	3.06	m^2

HX size results	Reheater	SSG superheater	SSG evaporator	SSG economizer	FWH 6	FWH 5	FWH 4	FWH 3	FWH 2	FWH 1	Condenser
UA [MW/K]	0.87	2.49	3.58	1.47	1.58	1.35	-	0.83	0.80	0.75	33.4
UA (drain cooler) [MW/K]	-	-	-	-	0.10	0.14	-	0.04	0.07	0.08	

Figure 4.16: The cycle design solution from IPSEPro is shown for a 3.06 m ^{2} annulus area on the last stage turbine using an air-cooled condenser model.

The gross performance, capturing the trade off between exhaust losses and condensing pressure effects is nearly the same for the two models: IPSE selects a 3.06 m^2 last stage turbine giving a gross efficiency at 3.88 in Hg back pressure of 42.4 or 42.5 %. The once through cooling model is used for off design performance modeling for simplicity. This 3.06 m^2 cycle is limited to 2.25 in Hg backpressure, which is acceptable for a cycle designed for high backpressure operation.

The objective of modeling these cycles was to get operating points over the full range of feasible values of HTF temperature, mass flow, and condensing pressure. The HTF temperature is limited by a practical range supplied by the receiver and thermal storage. The HTF mass flow is not; it is tested over a range from 20% of design value to 120%. The condensing pressure depends on the limitations of the condenser and turbine. The higher end of the range was 8 in Hg, which is higher than practical for air-cooled condensing. The lower end of the range (1.25 in Hg) was set based on practical limitations for steam velocities as described in SAM Technical Manual, except where limitations on the turbine require a higher limit, as described in this section. The simulations were completed for the cases:

- HTF Delivery temperature 550, 566, and 574 °C.
- HTF mass flow rates from 20% to 120% of design mass flow rate in 10% increments.
- Condensing pressures from 1.25 in Hg (2.25 for the 3.06 m^2 cycle) to 8 in Hg in 0.50 in Hg increments or smaller.

Based on experience modeling the radiative cooled cycle, the increments of the pressure values in the air-cooled cycle was increased from 0.25 to 0.50 in Hg. This gives 924 cases for the radiative cooling cycle and 396 for the air-cooled cycle.

4.4 Results for custom power cycles

The two custom power cycles were modeled over their range of operation. Figure 4.17 and 4.18 shows that the leaving velocity begins to exceed the expected range

only in a few high load cases.

The simulations are completed by using the IPSE Process Simulation Environment to solve the full load case for each condensing pressure in order to establish guess values. Then the IPSEpro-PSXLink add-on for Microsoft Excel is used to sequentially solve each of the other load cases and HTF supply temperatures, updating the guess values automatically.

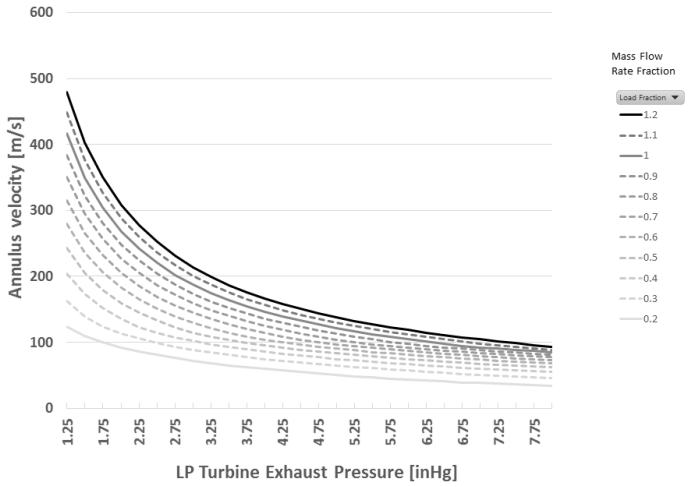

Figure 4.17: The last stage leaving velocity is exceeds 426 m/s only for high load cases (>1) and low condensing pressures for the 5.16 m^2 turbine at the design HTF temperature of 566 C.

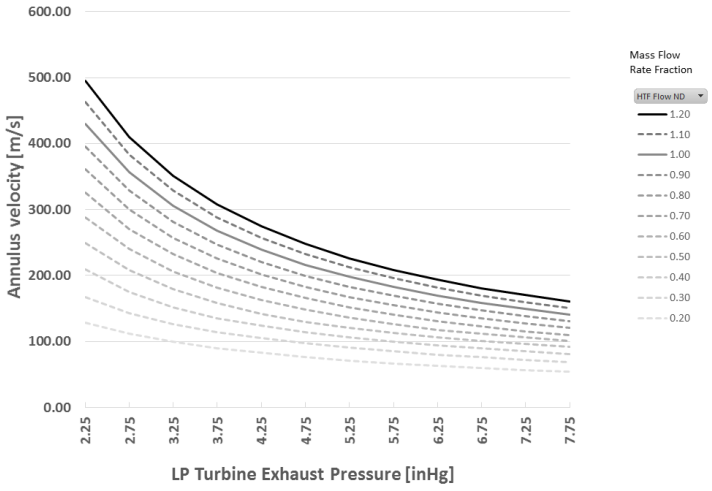

Figure 4.18: The last stage leaving velocity exceeds 426 m/s for the lower condensing pressures for the 3.06 m^2 turbine at the design HTF temperature of 566 C.

The exhaust losses for the two cycles are shown in Figure 4.19 and 4.20. The varying exhaust loss curves contribute to cycle performance and are reflected in the cycle efficiency curves in Figures 4.21 and 4.22. For the radiative cooled cycle there is a 5% difference between the lowest and highest condensing pressure at full load while the difference for the air-cooled cycle is only 1.3% . Figure 4.23 and 4.23 shows the two efficiency curves.

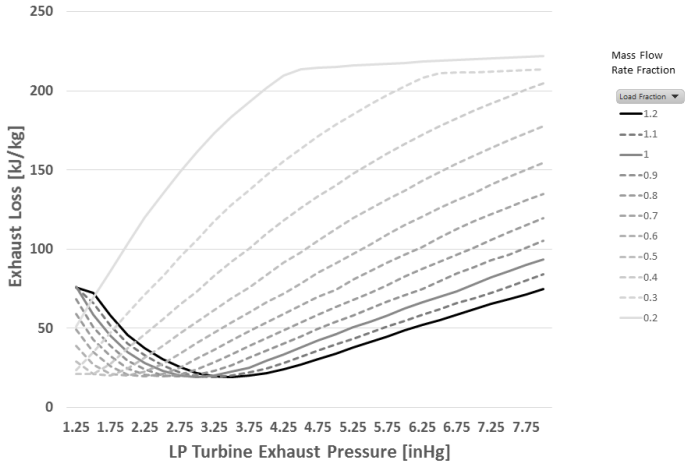

Figure 4.19: The exhaust losses at the 5.16 m^2 turbine for HTF delivery temperature of 566 °C are shown for a range of mass flow rate (loads) and condensing pressures.

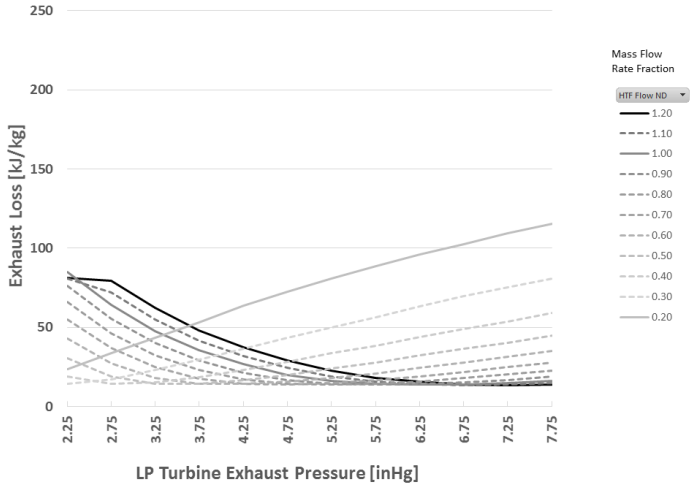

Figure 4.20: The exhaust losses at the 3.06 m^2 turbine for HTF delivery temperature of 566 °C are shown for a range of mass flow rate (loads) and condensing pressures.

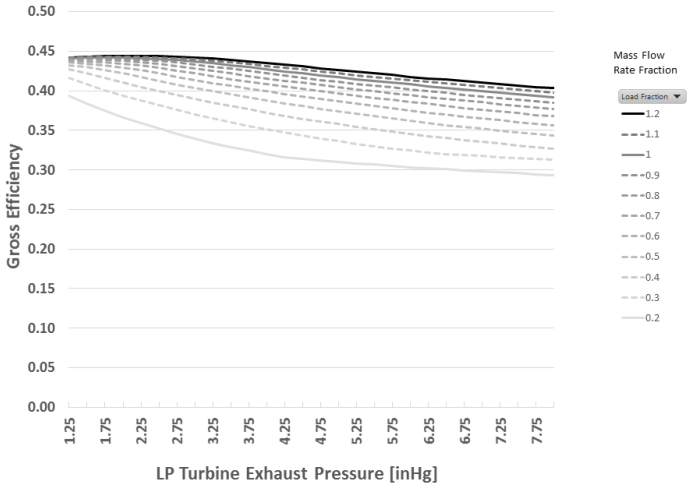

Figure 4.21: The efficiency with the 5.16 m^2 turbine for HTF delivery temperature of 566 °C are shown for a range of mass flow rate (loads) and condensing pressures.

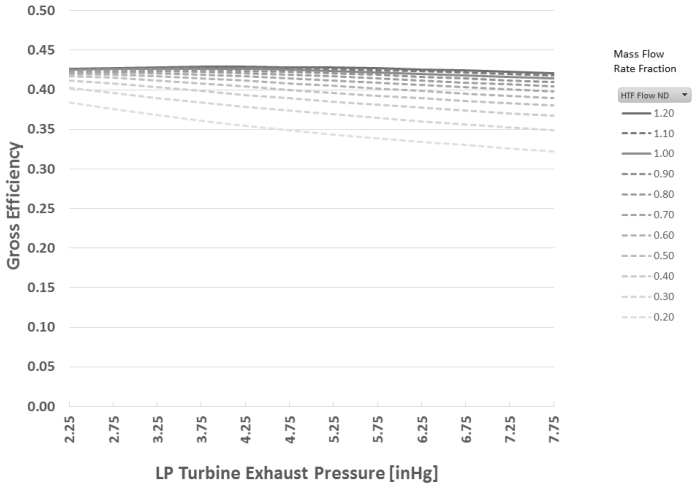

Figure 4.22: The efficiency with the 3.06 m^2 turbine for HTF delivery temperature of 566 °C are shown for a range of mass flow rate (loads) and condensing pressures.

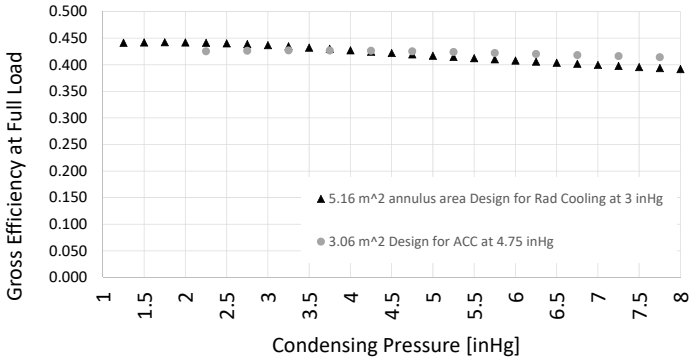

Figure 4.23: The two cycles have different efficiency profiles at full load and 566 °C HTF temperature.

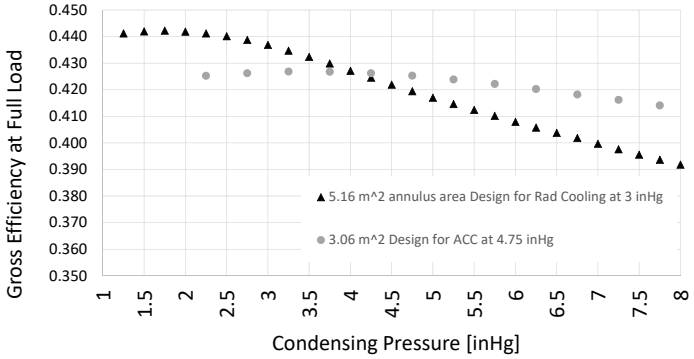

Figure 4.24: The efficiency profiles of both cycles where y-axis starts at 0.35 efficiency to emphasize the differences between the cycles.

To illustrate the condensing pressure effect on its own, a simple Rankine cycle is modeled in EES over the same pressure range. The condensing pressure effect is 4.3%. Fully modeling the exhaust losses shows that the variation of the cycle efficiency with condensing pressure depends on the choice of design point and turbine sizing. A simple cycle model predicts a continuously decreasing efficiency while the IPSE model predicts a wider range where the efficiency is nearly constant. (Note that the maximum efficiency of the EES cycle is less than the IPSE cycle models because the EES cycle does not include the six feedwater heating stages nor reheat, making the cycle overall less efficient.)

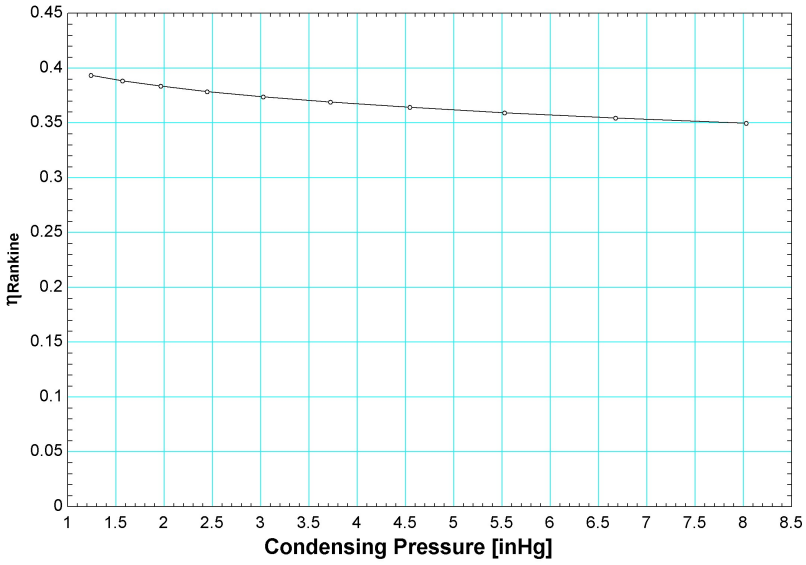

Figure 4.25: The condensing pressure effect for a simple Rankine Cycle with constant turbine efficiency for hot side temperature of 566 °C is shown.

4.5 Approximation of Power Cycle in System Adviser Model

Representing the power block model in SAM is done via a design of experiments approach as described in Wagner and Kutscher [2010] and Wagner [2008]. This creates a fast model that accounts for multiple effects. For the purpose of this work, the goal is simply to get an accurate translation of the full off design power cycle model that is useable in the existing SAM framework. In this section the design of experiments approach is detailed as used for this project, which is uses different interaction pairs than Wagner describes and so requires some changes to the SAM open source code. Power and heat input are the response variables and the factors are HTF mass flow rate, HTF temperature, and condensing pressure. Each variable except condensing pressure is non dimensionalized (indicated *).

$$\dot{W}^* = \frac{\dot{W}}{\dot{W}_{design}} \tag{4.47}$$

$$\dot{Q}^* = \frac{\dot{Q}}{\dot{Q}_{design}} \tag{4.48}$$

$$\dot{m}^* = \frac{\dot{m}}{\dot{m}_{design}} \tag{4.49}$$

$$T_{in}^* = \frac{T_{in} - T_{ref}}{T_{in,design} - T_{ref}} \tag{4.50}$$

The reference temperature is the saturation temperature at the boiler pressure of 115 bar, or 321 °C. As described in Wager, since most of the heat is added in the superheat section, this provides a reference for the temperature at which heat is added. The experimental design requires nine runs as described in Table 4.3.

A response variable Y (power or heat input) is calculated from:

Table 4.3: Series of cycle simulations required to represent cycle fully using two factor interactions. A variable can be set at its low value (-), design point (0) high value (+), or varied from low to high.

T_{in}^*	P_c	$\dot{m}^*$	Gives
vary	-	0	$Y_{INT}(P_c^- > T_{in}^*)$
vary	0	0	$Y_{ME}(T_{in}^*)$
vary	+	0	$Y_{INT}(P_c^+ > T_{in}^*)$
0	vary	-	$Y_{INT}(\dot{m}^{*-} > P_c)$
0	vary	0	$Y_{ME}(P_c)$
0	vary	+	$Y_{INT}(\dot{m}^{*+} > P_c)$
-	0	vary	$Y_{INT}(T_{in}^{*-} > \dot{m}^*)$
0	0	vary	$Y_{ME}(\dot{m}^*)$
+	0	vary	$Y_{INT}(T_{in}^{*+} > \dot{m}^*)$

$$Y = [(Y_{ME}(T_{in}^*) - 1)Y_{INT}(T_{in}^* > \dot{m}^*) + 1] \\ [(Y_{ME}(P_c) - 1)Y_{INT}(P_c > T_{in}^*) + 1] \\ [(Y_{ME}(\dot{m}^*) - 1)Y_{INT}(\dot{m}^* > P_c) + 1] \quad (4.51)$$

The main effects Y_{ME} are interpolated from a table of the value of Y for given factor level, given that the other two factors are at their design value. For example $Y_{ME}(T_{in}^*)$ is the value of Y at T_{in}^* given that P_c and $\dot{m}^*$ are at their design levels. The interaction effects account for how the variation of a second variable affects the first given that the third is held at design value. For example, $Y_{INT}(\dot{m}^* > P_c)$ depends on P_c and accounts for how Y varies with P_c under a changing mass flow rate. Y_{INT} is the average of an interaction calculated at the high setting and low setting of the interacting variable $\dot{m}^*$. The actual values of the response Y calculated with the full IPSE simulation at $\dot{m}^*$ and P_c are compared to an estimated value using only the main effects of each. The values are normalized relative to the main effect of pressure and their ratio is the interaction factor. For the high setting and low settings of $\dot{m}^*$:

$$Y_{INT}(\dot{m}^{*+} > P_c) = \frac{Y_{act}(\dot{m}^{*+}, P_c) - Y_{ME}(P_c)}{Y_{ME}(P_c)Y_{ME}(\dot{m}^{*+}) - Y_{ME}(P_c)} \tag{4.52}$$

$$Y_{INT}(\dot{m}^{*-} > P_c) = \frac{Y_{act}(\dot{m}^{*-}, P_c) - Y_{ME}(P_c)}{Y_{ME}(P_c)Y_{ME}(\dot{m}^{*-}) - Y_{ME}(P_c)} \tag{4.53}$$

Finally giving the interaction factor as:

$$Y_{INT}(\dot{m}^{*} > P_c) = \frac{Y_{INT}(\dot{m}^{*+} > P_c) + Y_{INT}(\dot{m}^{*-} > P_c)}{2} \tag{4.54}$$

A simplified version of the power cycles can be modeled using only the main effects:

$$Y = Y_{ME}(T^*_{in})Y_{ME}(P_c)Y_{ME}(\dot{m}^*) \tag{4.55}$$

Before implementing the custom power cycles, the default power cycles in SAM are tested. The SAM model is run with and without the interaction effects for a solar power tower configuration with fixed boiler pressure. The overall results for gross power output vary by less then 0.1%. This is because the interaction effects are not strong and the cycle operates most of the time near the design points. Typical values of the main effects are 1.05 to 1.10, while the interaction effects are from 1 to 1.001. However interaction effects are still used. The main effects for the custom IPSE cycles are shown in Figures 4.26 through 4.31.

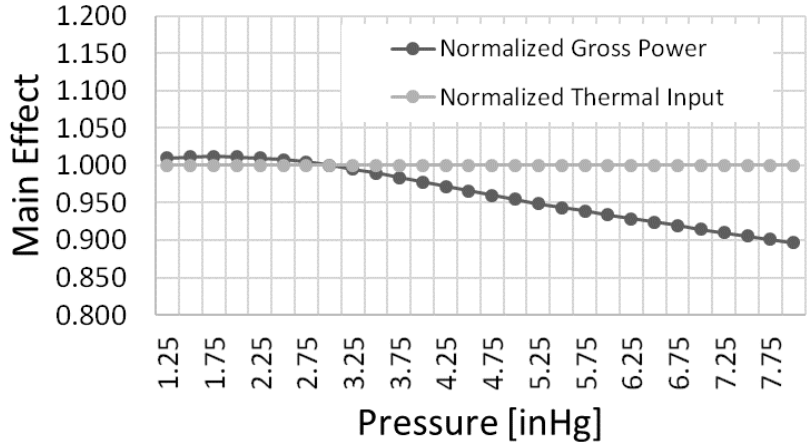

Figure 4.26: The main effects of pressure for the low pressure / 5.16 m^2 cycle.

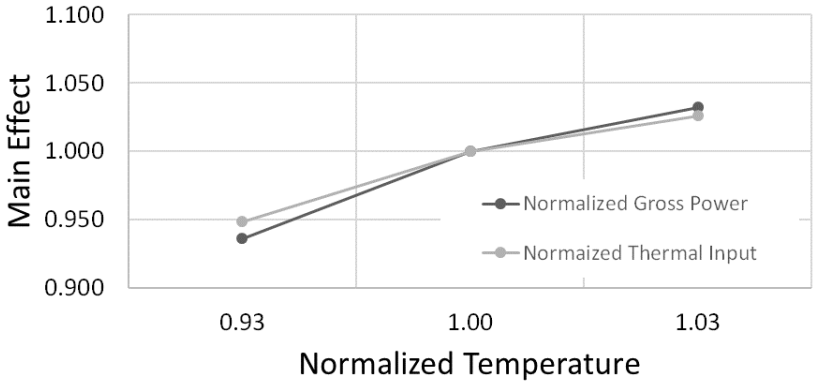

Figure 4.27: The main effects of temperature for the lower pressure/ 5.16 m^2 cycle.

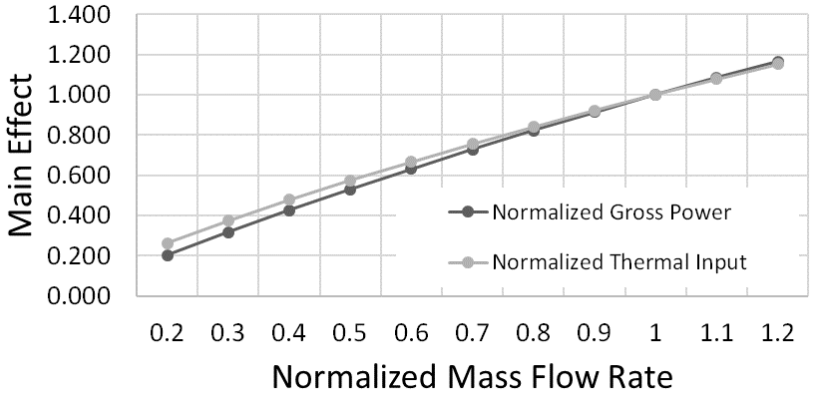

Figure 4.28: The main effects of mass flow for the low pressure/ 5.16 m^2 cycle.

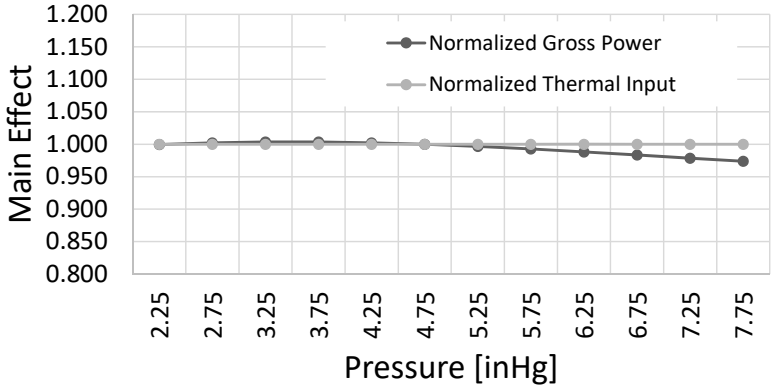

Figure 4.29: The main effects of pressure for the high pressure/ 3.06 m^2 cycle.

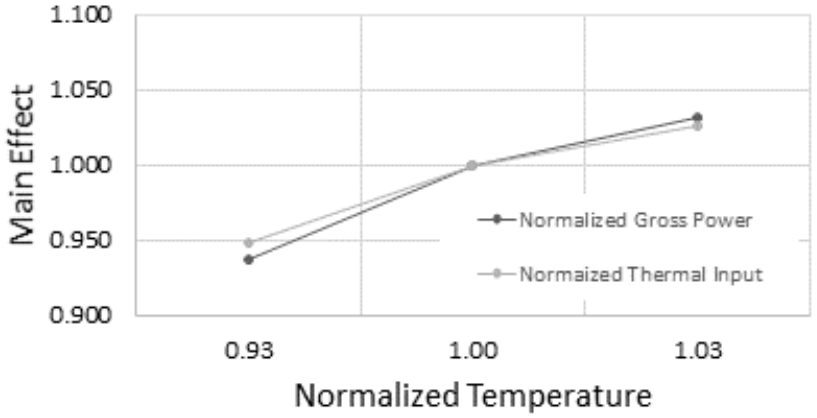

Figure 4.30: The main effects of temperature for the high pressure/ 3.06 m^2 cycle.

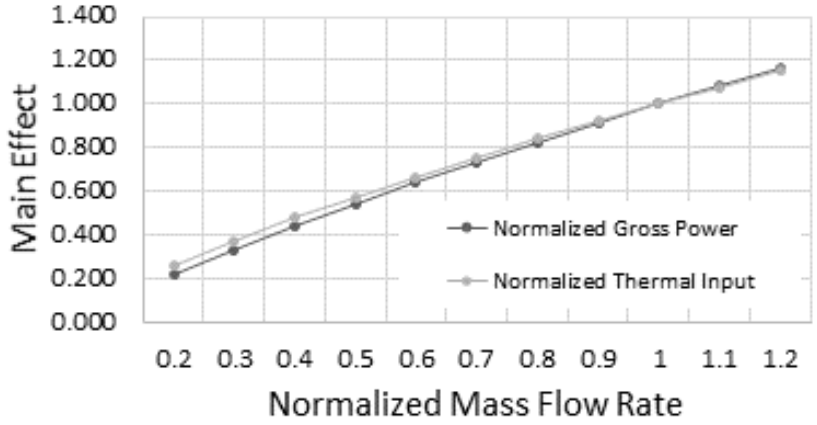

Figure 4.31: The main effects of mass flow for the high pressure / 3.06 m^2 cycle.

The resulting cycle performance of the regression model is here compared to the full IPSE runs by quantifying the percent difference between a full IPSE simulation and the regression-based estimation. Table 4.4 provides the upper and lower bound values tested for each cycle and interaction. The low pressure cycle (5.16 m^2) has 924 runs while the high pressure cycle (3.06 m^2) has 396 runs because it operates

over a smaller pressure range and the simulations were completed at 0.5 inHg condensing pressure increments instead of 0.25 inHg.

Figures 4.32 and 4.33 show the error at 566 °C input temperature. The error is significant only at low loads and even then falls in an acceptable range of less than approximately 10 percent for all cases except lowest load (0.2). The reason for some error at low load is partly because in the sliding pressure cycle, the boiler pressure is reduced as load is reduced, but there is a lower limit of 30 bar which is reached for the 20% load case for both cycles. The error is also quantified in Table 4.5. Cycle performance is fully described by not only the power output but also the thermal input. Errors are reported for normalized gross power only ($\dot{W}^*$) as errors in heat input are negligible (the thermal input error is at maximum 0.2%). Overall, this design of experiments approach adequately captures the cycle performance for use in the annual simulations.

Table 4.4: The range of the three factors are shown; note that the pressure limitations used for the interaction effect with temperature and pressure in the high pressure cycle is 2.75 - 7.75 in Hg even though the correlations are used over the complete range.

	Lower bound for interaction	Upper bound for interaction
$\dot{m}^*$	0.2	1.2
P_c	1.25 inHg / 2.75 inHg	8 / 7.75 inHg
T^*_{in}	550 C	574 C

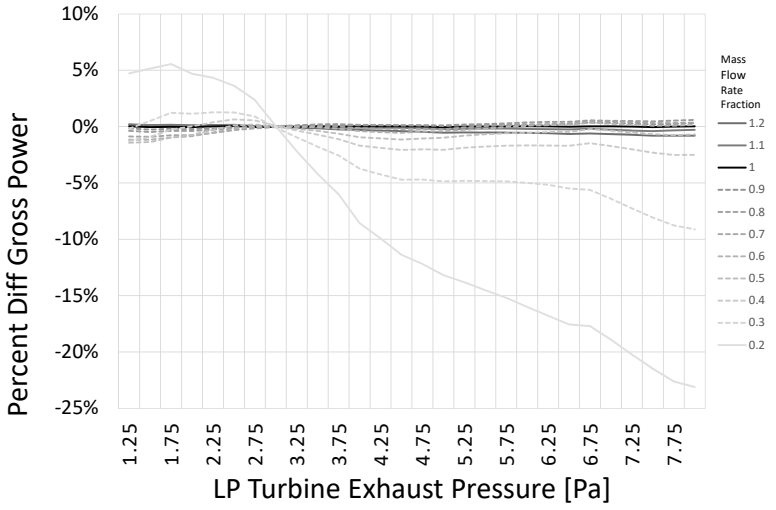

Figure 4.32: The error between the approximation of the cycle and the full IPSE runs at 566 °C HTF temperature is shown for the low pressure (5.16 m^2) cycle.

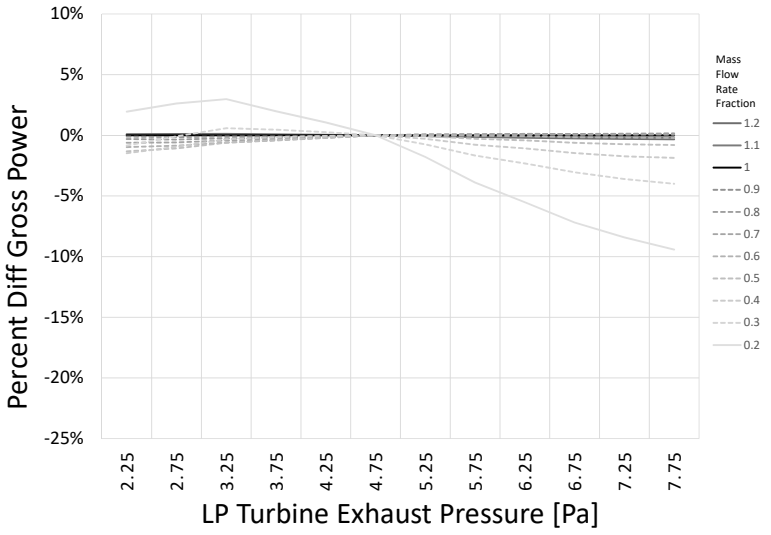

Figure 4.33: The error between the approximation of the cycle and the full IPSE runs at 566 °C HTF temperature is shown for the high pressure (3.06 m^2) cycle. Axis same as previous figure for comparison.

Table 4.5: The error between the full IPSE cycle runs for all cases available and the approximations are shown for normalized gross power. Including the interaction effects reduces the error.

	Mean Absolute Percent Error	Mean Absolute Error for 125 MW plant [MW]	Root Mean Square Error [MW]
Low pressure	1.9%	0.75	1.24
High Pressure	0.8%	0.43	0.68

For reference the main and interaction effects are documented in Appendix A.

5 CSP WITH NIGHTTIME COOLING ASSESSMENT

To compare concentrating solar power plants with different cooling systems, an annual model must capture the interaction between subsystems that impact energy production over the course of the year. The first section of this chapter describes the modeling which brings together the radiative-convective panel modeling (Chapter 3) and the power plant modeling (Chapter 4) using a system model in System Advisor Model (SAM) software. The second section describes implementation of the new SAM model for this project. Three solar power tower power plants are tested under a range of radiator field sizes and cold side storage sizes. Cost estimations are provided for each component. An air-cooled cycle is modeled as the baseline for each power plant. The final section of this chapter provides the results of that model.

5.1 Modeling the radiative-convective CSP cooling system in SAM

System Advisor Model is chosen for the annual simulations in order to take advantage of the built in capabilities of the program including the industry-accepted performance models that are used for the solar field. System Advisor Model is open source so the new functionalities that have been added during this project may be shared with other users interested in cold storage and/or radiative cooling systems.

5.1.1 Overview of system model

Existing SAM models are implemented for the heliostat field, receiver, thermal energy storage, condenser, and power plant control. SAM takes user inputs for major solar, power cycle, and hot side storage components and location information to run hourly simulations of CSP performance. For information about SAM, see

NREL (sam.nrel.gov) for general information, software download, and up to date references, Wagner and Gilman [2011] for component level algorithms, and Dobos et al. [2013] for discussion of the simulation core. SAM now has the capability to optimize the dispatch of CSP power tower plants [Wagner et al., 2017], but this capability is not used in the current work.

The novel part of this work is custom power cycle models, cold storage, and radiator models that are implemented in SAM using the open source code (C++) made available by NREL. Figure 5.1 and Figure 5.2 show different configurations of the new components. This section describes the new components added.

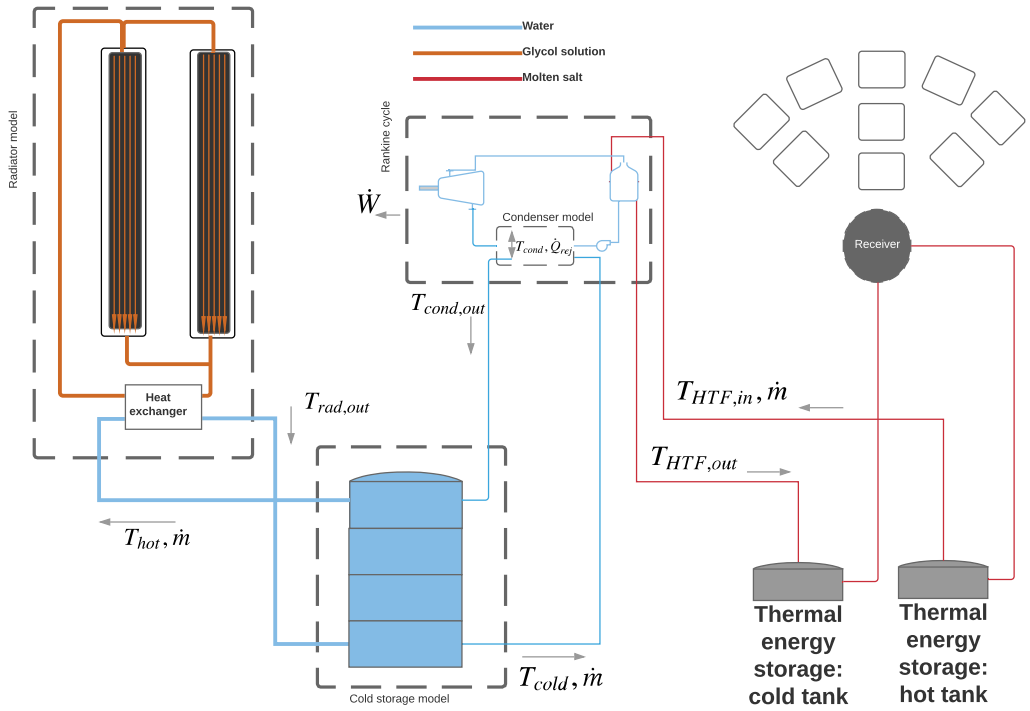

Figure 5.1: A conceptual schematic of the system using a stratified storage tank and a glycol cooled field connected via a heat exchanger to the cold storage. The variables shown are those that are passed between sub-systems.

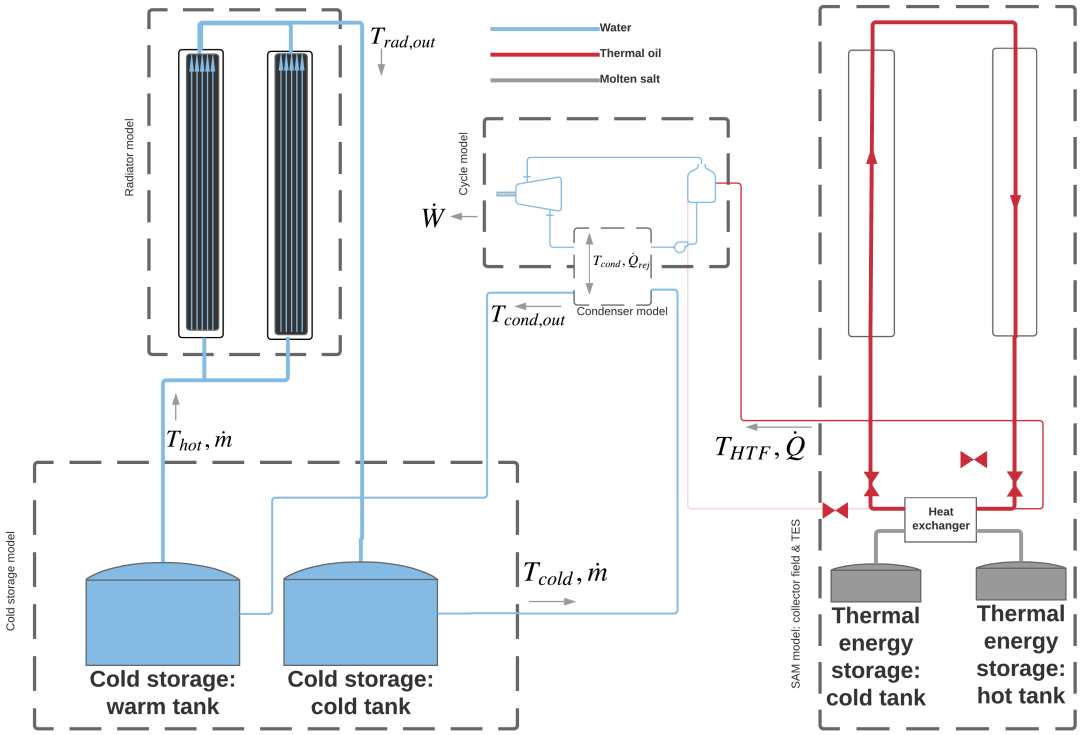

Figure 5.2: A conceptual schematic of the system showing a two tank cold storage system and a radiative field using water as the cooling fluid. This schematic shows a parabolic trough solar system; SAM has several solar options which could in theory be used with the radiative cooling though this work focuses on power tower plants only.

The user inputs are shown in Table 5.1. In the SAM GUI, if user selects 'radiative' as the condenser type, all of the radiative cooling inputs become relevant (otherwise they are ignored). Maximum flexibility is given to the user by allowing inputs of all the panel dimensions and design temperatures. Note that the pumping calculations use a pressure drop input in the GUI because the header design is highly dependent on design decisions for the field, as described in this chapter. The fluid volume calculation is also highly dependent on the header design and so the user must input a ratio of the total fluid volume to the volume within the panels (the volume

of fluid in the panels is known based on the entered dimensions).

Table 5.1: The inputs required in SAM to run the custom radiative cooled cycle are shown along with any nomenclature used in this document and clarifying notes.

Description in SAM GUI	Sym.	Notes
Radiator fluid (3=water, other=glycol)	-	Propylene Glycol at 20% concentration
Effectiveness of glycol-water HX ...	ϵ_{HX}	If water, this input is ignored.
Radiator multiplier	RM	Any value >0
Cold storage type (2=two-tank, 3=three-node...	-	Enter 0 if not using radiative cooling.
Equivalent full load hours cold storage	hrs_{CTES}	Hours of condenser operation
Tank loss coefficient	-	
Number of tank pairs in cold storage	-	Typically =1.
Cold tank design temp	$T_{cold,o}$	Cold tank design temperature [C]
Warm tank design temp	$T_{warm,o}$	Warm tank design temperature [C]
Cold tank initial temp	-	Cold tank initial temperature [C]
Warm tank initial temp	-	Warm tank initial temperature [C]
Percent of HTF in warm tank initially...	-	This value is only used in the two tank.
Cold storage tank height	-	Used to calculate the tank diameter. [m]
Minimum allowable tank height...	-	This value is only used in two tank model. [m]
Mass flow through single panel	$\dot{m}$	Mass flow for panel, split in n tubes.
Number of parallel tubes in panel.	n	
Center-to-center distance between tubes	W	m
Thickness of radiator panel	th	m
Inner diameter of radiator tubes	D	m
Length of row of radiator panels	-	Total length of series-connected panels [m]
Length of individual radiator panels	L	Length of a single panel m
Pressure drop through panel and distribution	ΔP	Pressure drop per loop. kPa
Cost of radiative panel	-	Cost of radiator panel $\$/m^2$
Installation cost of radiative panel	-	Installation cost radiator panels $\$/m^2$
Volumetric cost of cooling fluid	-	Cost of fluid - enter 0 if water \$/L
Ratio of fluid in distribution to fluid in panels	-	Total fluid volume/volume in panels
Volumetric cost of storage tanks	-	Cost of tanks \$/L

5.1.2 New components

Radiator components in SAM

The radiator model is based on Dyreson, Ana, Klein, S.A., Miller [2017] , described in Chapter 3, using the adiabatic temperature sink model and programmed into SAM as a new class. Two options are available. If water is selected as the heat transfer fluid, the model is implemented as in Dyreson et al. If glycol is instead chosen, then a combined radiator-heat exchanger model is implemented instead to account for the heat exchanger between the water in cold storage and the glycol in the radiative panels. This model is from Duffie and Beckman [2013], where

a solar collector is paired with a heat exchanger. Equation 3.11 is implemented with the adiabatic temperature reference the factor F'_R accounts for the panel and heat exchanger. This is Equation 5.1 where $T_{cw,i}$ is the inlet temperature of the cold water to the heat exchanger from the cold storage system side. U^*_L is the loss coefficient relative to the adiabatic temperature T^*, as described in Chapter 3.

$$Q_u = F'_R A_c U^*_L (T_{cw,i} - T^*) \tag{5.1}$$

The collector-heat exchanger factor F'_R is then:

$$F'_R = \frac{F_R}{1 + \frac{A_c F_R U^*_L}{(\dot{m}c_p)_{rad}} (\frac{(\dot{m}c_p)_{rad}}{\epsilon_{HX}(\dot{m}c_p)_{min}} - 1)} \tag{5.2}$$

Here subscript "rad" indicates the fluid on the radiative panel side of the heat exchanger and "min" indicates the minimum capacitance rate of the water storage side and radiative panel side. ϵ_{HX} is the heat exchanger effectiveness. Thus the performance penalty for the heat exchanger is easily added to the model. This assumes a constant effectiveness heat exchanger.

A 20% propylene glycol solution is used because it offers some freeze protection (freezing point -7.4 °C) and is more environmentally friendly than ethylene glycol. This fluid is commercially available.

Based on the initial technical feasibility described in Chapter 1, freeze protection will be required in the radiative field. If the model finds that the exiting water returning to the cold storage system (weather from the glycol cooled heat exchanger or directly from the field) reaches the freezing point of water, freeze protection is implemented. For glycol, the fluid simply stops circulating. For water, the loop continuously circulates to avoid freezing but the heat exchanger is valved off so that the cold storage side is not cooled. This scenario would in fact require some heat tracing as well to ensure no freezing in the lines, but this is not modeled.

Note that the radiator model is most accurate with measured sky temperature data. A weather data set is prepared specifically for this project and described in this Chapter. However the model will run with any SAM formatted weather file.

SAM's built in correlations for sky temperature are used if a custom weather file providing measured sky temperature is not available.

Cold storage model

The cold storage system models are created for both two-tank and stratified cold water storage. A two tank model is based on the existing SAM components for molten salt thermal energy storage as described in Wagner and Gilman [2011]. A new stratified tank model is built in SAM for a flexible number of nodes (3-6) using the multinode model described by Duffie and Beckman [2013].

Power cycle model

The power cycle models are as described in Chapter 4 for a high-pressure and low-pressure cycle. The two new choices for power cycles (high and low pressure) are in addition to the existing SAM power cycles for a fixed pressure Rankine cycle and sliding pressure Rankine cycle. All of the cycle models are compatible with the power tower regardless of condenser choice, but for the purpose of this work the custom power cycles are used as these cycles are fully documented and are designed specifically for radiative cooling and air-cooling.

Component sizing

Once the components are specified from the GUI inputs, the new components in SAM calculate the number of panels in the radiative field, the physical size of the cold storage system, and the condenser water flow rate. These items are related as described in this section. The design value of the cooling water temperature (ΔT_{CW}) drop is the difference between the design cold and warm tank temperatures specified by the user. From power cycle specifications, the design power output $\dot{W}_{design}$ and cycle efficiency η_{design} are known. The heat rejection at design is then:

$$\Delta T_{CW} = T_{warm,o} - T_{cold,o} \tag{5.3}$$

$$\dot{Q}_{rej,design} = \frac{\dot{W}_{design}(1-\eta_{design})}{\eta_{design}} \tag{5.4}$$

And the mass flow rate in the condenser is:

$$\dot{m}_{cond} = \frac{\dot{Q}_{rej,design}}{c_p \Delta T_{CW}} \tag{5.5}$$

Where c_p is the specific heat of water.

The cold storage system is sized based on the condenser flow rate and number of hours of cold storage desired hrs_{CTES}. In order to ensure that the cold storage tank is large enough to supply all the condenser with cooled water operation during the peak summer, a reasonable rule is to set this equal to the number of hours that the power plant operates in one day in the peak of summer. In the peak summer time period, the night is shortest and so both the cooling availability is lowest and the power plant heat input from solar is highest. For stratified tanks, using a smaller tank is possible but will induce a penalty on the power block due to the warmer recirculated water in the stratified tank. The mass of cold water in storage is:

$$m_{storage} = \dot{m}_{cond} hrs_{cold} \tag{5.6}$$

For two tank storage, an additional volume is added to keep a minimum storage level. The minimum storage level calculations are automatically made in the model based on the minimum storage height specified by the user; this is exactly as the hot thermal energy storage tank model in SAM. Note that a two-tank model must have enough storage to cover the peak summer day, else the tank will empty and the power plant will not be cooled. Though the cycle could be controlled to avoid this, the current implementation of cold storage does not provide feedback to the power cycle on the availability of cooling.

The ratio of the radiator field surface area to heliostat field surface reflective

area is radiator multiple RM.

$$RM = \frac{A_{field}}{A_{solar}} \tag{5.7}$$

Where the solar field area A_{solar} is known based on user inputs to the solar model in SAM. The radiator field has a given geometry (user specified) that includes length of series-connected panels L, tube diameter D, number of tubes per panel n, width between tubes W, and mass flow rate through individual panel $\dot{m}_{rad}$. This specifies the area of a series-connected panel, A_{row}. The number of rows connected in parallel N_p is then determined based on the required field size and row size:

$$A_{row} = nWL \tag{5.8}$$

$$N_p = \frac{A_{field}}{A_{row}} \tag{5.9}$$

The value is rounded up to the nearest integer. The flow rate for water between the cold storage system and radiative field ($\dot{m}_{storage}$) is set so that the cold storage tank will be fully cooled during the shortest night of the year (hrs_{night}=9 hours in Las Vegas, Nevada).

$$\dot{m}_{storage} hrs_{night} = m_{storage} \tag{5.10}$$

Note that the GUI inputs to the radiator model allow the user to determine the size of the radiator field and the size of the storage field. The flow rate for the field and the storage system are not necessarily the same. Both flow rates are constant. Typically a balanced heat exchanger is desirable between the glycol and water, but this is not enforced by the model. Equations 5.3 through 5.10 allow calculation of those flow rates based on user inputs. The user also supplies a heat exchanger effectiveness. The NTU of the heat exchanger given the specified mass flow rates should be checked to ensure a reasonable heat exchanger. If there is no heat exchanger because the radiative field uses water, the field must be designed to match the flow rate through the storage calculated in SAM.

5.2 Implementation of radiative cooled and air-cooled plant models

5.2.1 Power plant test cases

Solar thermal power plants can be configured with varying thermal energy storage capacities and solar multiples (SM). A plant that is configured for meeting more baseload energy requirements has a high solar multiple and larger thermal energy storage systems. This way the captured solar energy can be stored and turned into electricity at a relatively constant rate throughout the day. On the other extreme, a plant can be configured to mostly meet peak energy requirements by having a power cycle that produces energy when solar insolation is available and without much energy storage. Though currently not common, the peaker configuration is receiving more interest as the increasing levels of wind and solar PV on the electric grid require more flexibility. Price et al. [2017] designed a flexible CSP plant and showed its value in the Arizona market. Three cases are examined as in Table 5.2. In all cases the power block is 125 MW.

Table 5.2: Three SAM cases for solar power tower plant configurations were tested for both radiative- and air-cooled plants.

	SM	TES [hrs]
Baseload	3	15
Intermediate	2	9
Peaker	1	6

Each of the three plants is simulated with different size radiative cooling systems, as described in this Chapter. The baseline system is an air-cooled plant of the same SM and TES configuration. The air-cooled and radiative-cooled plants of a given plant (for example, baseload) have the exact same heliostat field and are dispatched on the same schedule. The only differences are the power plant model and condenser. As described in Wagner and Gilman [2011], SAM iterates between the

power block and condenser to find the condensing pressure for a given HTF mass flow rate and temperature supplied to the power block and cold sink availability. The difference between the air-cooled and radiative-cooled operation is that given their individual power cycle models and hourly cold sink temperatures (dry bulb temperature or cold storage temperature), the condensing pressure and condenser parasitic loads are different. They key differences in the air- and radiative- cooled systems inputs are summarized in Table 5.3.

Table 5.3: Key power cycle inputs for SAM are provided that differentiate the two systems. The high and low backpressure cycles are those described in IPSEpro modeling in Chapter 4.

	Air-cooled	Radiative-cooled
Peak cycle efficiency	0.425	0.437
Power cycle design backpressure	4.75 inHg	3 inHg
Minimum condensing pressure	2.25 inHg	1.25 inHg
Design temperature	39.3 C	28.11 C
Inlet temperature difference at design	16 C	
Approach temperature difference		5 C

5.2.2 Radiative cooling cases

For each of the three power plant types (baseload, intermediate, and peak) the impact of the size of the radiator field as well as the size of cold storage is tested by running the annual models with a range of storage and radiator field sizes. The radiator panel and field design are described in this Section for use in the SAM models.

Radiator panel design

The concepts of the radiator model described in Chapter 3 are used to design and model a panel for this study. The performance of a radiator panel can be quantified by an effectiveness relative to the adiabatic temperature T^* (Recall: the adiabatic temperature is the temperature at which a surface would be equally

heated by convection and cooled by radiation. Thus this is a logical cold sink temperature taking into account both convective and radiative heat transfer.) This panel effectiveness is:

$$\epsilon_{rad} = \frac{T_{in} - T_{out}}{T_{in} - T^*} \tag{5.11}$$

The effectiveness of a panel is correlated to the wind speed. This means that it is not necessary to compare the performance of different panel designs in annual simulations. The effectiveness at a single representative point can be used to compare designs. This is demonstrated by taking eight different radiative panels and running performance simulations of the panels for one year using the 2015 Las Vegas, Nevada weather data. The inlet temperature was fixed at 27 °C and the radiative panels used a 30% mass ethylene glycol solution transferring heat to the cold storage with a heat exchanger effectiveness of 0.9. The geometry of the panels are shown in Table 5.4 and the annual performance correlated to wind speed is in Figure 5.3. The correlation to wind speed exists because the sky temperature depression at any given condition (ambient minus sky temperature) is relatively constant throughout the year. This means that the main ambient condition that determines the heat transfer effectiveness relative to adiabatic temperature is the convection coefficient via the wind speed.

Table 5.4: 24 different designs are shown. The performance of eight different radiator designs (A-H) was tested using 2015 Las Vegas weather data. All 24 designs were used to test the effectiveness at design conditions. The range of tube velocities is 0.25-1.37 m/s (0.8-4.5 ft/s).

Design	n	W [m]	th [m]	D [m]	L [m]	$\dot{m}$ [kg/sec]
A	50	0.2	0.002	0.02	100	5.81
B	50	0.1	0.0002	0.02	200	5.81
C	50	0.2	0.002	0.02	100	8.72
D	50	0.1	0.0002	0.02	200	8.72
E	50	0.2	0.002	0.02	200	5.81
F	50	0.2	0.002	0.02	200	8.72
G	12	0.1	0.002	0.0159	2	1
H	12	0.1	0.002	0.0159	20	1
I	20	0.2	0.002	0.02	150	5.81
J	50	0.1	0.0002	0.02	150	5.81
K	20	0.2	0.002	0.02	150	8.72
L	50	0.1	0.0002	0.02	150	8.72
M	20	0.2	0.002	0.02	250	5.81
N	20	0.2	0.002	0.02	300	5.81
O	100	0.05	0.0002	0.01	250	2
P	100	0.05	0.0002	0.01	300	3
Q	40	0.1	0.0002	0.01	50	2.2
R	40	0.1	0.0002	0.015	50	3.5
S	40	0.1	0.0002	0.01	150	2.2
T	40	0.1	0.0002	0.015	150	3.5
U	50	0.1	0.0002	0.02	350	4
V	50	0.1	0.0002	0.02	350	5
W	20	0.2	0.02	0.02	400	2
X	20	0.2	0.02	0.02	400	3

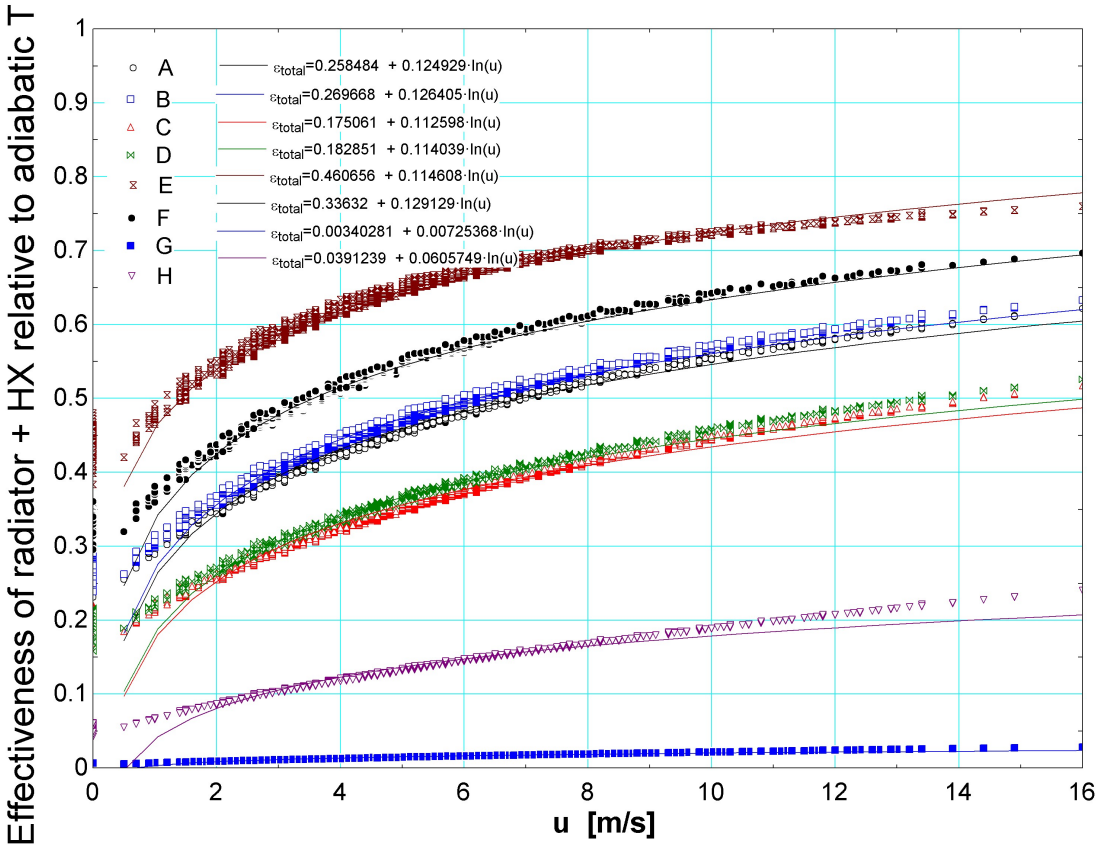

Figure 5.3: The effectiveness of panels during one year of nighttime operation is correlated to the wind speed.

With this simplification, the hour of 1AM on June 21 is chosen to further test radiator design performance. The wind speed at this hour is relatively high at 7.8 m/s and the adiabatic temperature is 15.9 °C; these conditions are typical for a June night in the test year.

To examine the range of radiator designs, 24 different geometries in Table 5.4 are now considered using the single representative condition. The fluid is propylene glycol at 20% concentration by mass with a heat exchanger to water at 0.9 effectiveness. A panel's performance is related to the dimensionless group

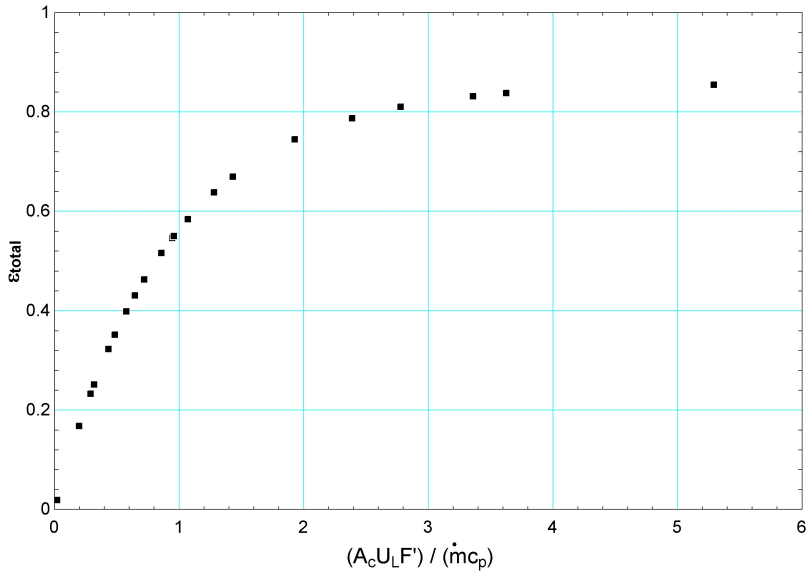

Figure 5.4: The dimensionless group relates to the effectiveness of the radiator panel using geometry parameters and the loss coefficient. The mass flow rate is that of the water side of the heat exchanger between the field and cold storage.

$(A_c U_L F')/(\dot{m}c_p)_{storage}$ as shown in Figure 5.4.This group is identified in Duffie and Beckman [2013] and used in the collector analytical solutions. Here the effectiveness also includes the effects of the water-glycol heat exchanger. This dimensionless group, paired with the panel effectiveness, provides an NTU-effectiveness relationship that is useful in understanding the performance of the panel.

In the dimensionless performance term $(A_c U_L F')/(\dot{m}c_p)$, the ratio of $A_c/\dot{m}$ appears. The collector efficiency factor F′ accounts for the fin efficiency and the resistance to heat transfer through the tube and tube walls. A cross section design should be selected for high F′. The loss coefficient U_L is mostly dependent on the ambient conditions though is does vary slightly with the plate temperature, which will decrease for more effective panels. Recall that for any configuration tested in the system model, the mass flow in the radiative field and total field area are fixed via the inputs $hrs_{storage}$ and RM, respectively. Assuming a high F′ and a given ambient condition, the ratio of $A_{field}/\dot{m}_{storage}$ and therefore $A_c/\dot{m}$, is set by the

RM and storage size, and the dimensionless performance term is also set. The field can be configured by varying the number of panels N_p , length of panels L and mass flow rate through individual panels $\dot{m}$, but the resulting effectiveness does not change except where the collector efficiency F′ is affected by the flow within the tube. This means that for the purpose of this study, the exact dimensions of the selected design are not important, only the collector efficiency F′.

A cross section is selected for the radiator using the dimensions in Table 5.5. This cross section provides a high fin efficiency and for turbulent flow, a high collector efficiency. Figure 5.2.2 shows how the choice of fluid and mass flow rate through the given tube diameter affect performance. If the flow through the channels is just beyond the turbulent transition, optimal heat transfer will be achieved but pumping loads within the tubes increase significantly with mass flow in the turbulent regime. Two mass flow rates are selected to test the heat transfer-pumping trade off. The final design has good fin efficiency (F 0.99) and collector efficiency (F′ 0.97) under the turbulent regime (Re=3091) and under the laminar regime (F′0.86; Re=1932). The laminar case will require a greater number of panel rows with shorter row length to meet the mass flow requirement for a given storage system than the turbulent case.

Table 5.5: The dimensions chosen for the radiator panel. The section length is the length of a single section for practical purposes. Each row of panels is made up of many sections in series.

n	100
W	0.05 [m]
D	0.02 [m]
$\dot{m}_{tube}$	0.08 [kg/sec] (turbulent)
$\dot{m}_{tube}$	0.05 [kg/sec] (laminar)
th	2 [mm]
$L_{section}$	10 [m]

Given the effectiveness curve as in Figure 5.4, there is a limit to the size of the field that will improve the effectiveness of the system. This is because as the panels get longer, the effectiveness of the panels (rows) asymptotically approaches the

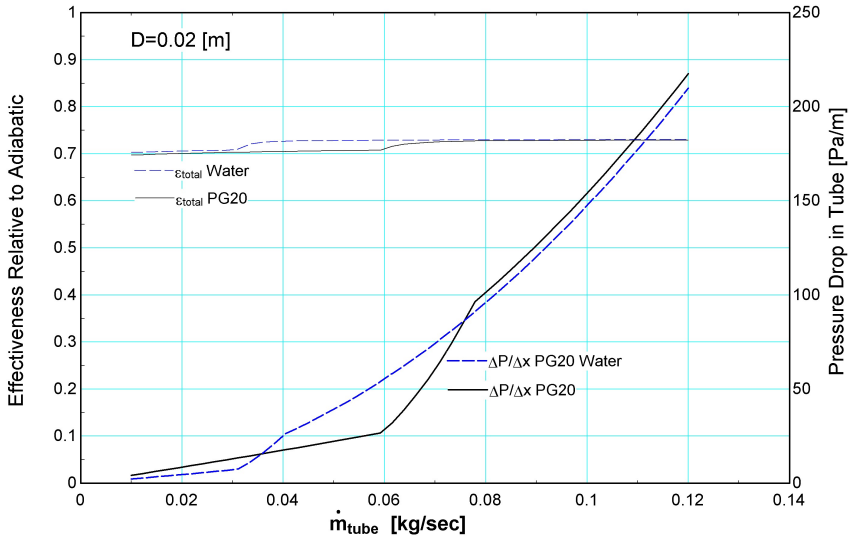

Figure 5.5: The heat transfer for turbulent flow is slightly better but pumping loads increase significantly.

heat exchanger effectiveness. For the test condition, the loss coefficient U_L is about 28 W/m^2-K, and the collector efficiency F′ is 0.93 for turbulent flow. The specific heat of water is 4183 J/kg-K. A reasonable goal for the dimensionless performance group is 2 based on Figure 5.4. Based on the air-cooled simulations, the peak, intermediate, and baseload plants runs 11, 21, and 24 hours per day in the peak of summer.

Table 5.6: For each plant, given the peak summer storage requirement, the radiator multiplier is shown which provides reasonable field performance.

Plant	Cold Storage Hours	Flow rate [kg/sec]	Maximum useful area [m^2]	Equivalent RM
Peak	11	4,704	1,511,000	**2.9**
Intermediate	21	8,981	2,885,370	**2.6**
Baseload	24	10,264	3,297,566	**2.0**

The field area is varied from 1 to 3 times the solar field area for each plant

(radiator multiplier from 1 to 3) to capture the range of values of interest. The cold storage sizes are are tested for each plant from plus and minus several hours from the ideal amount of storage.

Radiator field design

The storage size and radiator field are related. For each storage size, the cold storage flow rate is determined in SAM based on Equation 5.10. For this study a balanced heat exchanger is chosen and so the number of panels required N_p given the selected panel mass flow rate $\dot{m}$ is determined based on balancing the capacitance rate of the water side and glycol side of the heat exchanger:

$$N_p \dot{m} c_{p,PG20} = \dot{m} c_{p,water} \tag{5.12}$$

Given the available field area (from RM), the length of the panel rows is then set for each case. Table 5.7 shows the number of panel rows and total field flow rates for each storage size. Figure 5.6 shows the lengths required for the peak plant for turbulent flow in the tubes. In each case the length is determined by the solar area times the radiator multiplier (giving the total radiator field area) divided by panel width and the number of panels. The baseload and intermediate plants (not shown) have row lengths ranging from 240-930 m (baseload) and 170 - 780 m (intermediate).

Piping design and pressure drop

For each configuration, the pumping power requirement is determined. Because the pumping requirements of header piping are expected to be significant, each field is split into four subfields, arranged around the cold storage system. A header system is designed with stepped diameters the inlet to each row of radiators. The diameters decrease from the first to last panel (right to left) on delivery of warm fluid and increase on return of the cold fluid. The piping design was done to balance the pressure drop, pipe size, and fluid residence time (time to travel to and from the storage tank through the field). The diameters are selected for each storage size so that the largest header pipe is 2.6 meters. The velocity is constant through

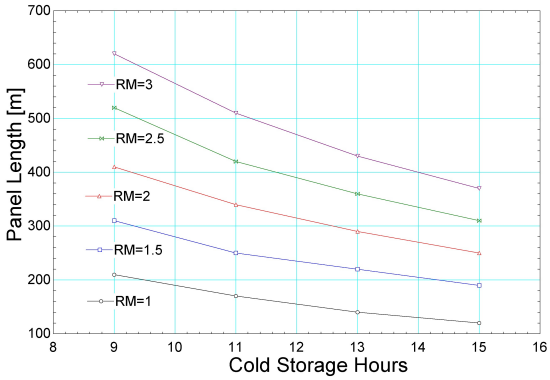

Figure 5.6: The length of the radiator panels tested depending on the cold storage size and radiator multiplier is shown for the peaking plant.

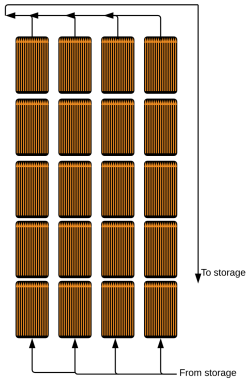

Figure 5.7: Radiators are set up in series connections (here, shown as rows of 5 panels) which are in parallel in a field (here, 4 rows in parallel make up the field).

the header and return system at 0.5 m/s. This provides a reasonable residence time in the system (1-2 hours) with a reasonable pressure loss (described below).

At each panel the flow is split into the individual tubes. The related pressure drop is approximated by a branched tee where the flow is diverted to each individual tube. A pressure drop approximating the splitters within the panels is calculated as 1.7 kPa for each panel. The pressure drop in the actual tubes with turbulent flow is 101 Pa/m or approximately 1 kPa per 10 m radiator panel. The pressure drop in the

distribution system accounts for the pressure drop through each individual header section, three 90 degree bends in the return line, the pressure loss in the return line, and minor entrance and exit losses. The header pressure loss is generally a small part of the total pressure loss, though for smaller fields the headers are a larger fraction because the panels are shorter.

Table 5.7: The flow requirements and header design for example storage sizes are provided. The flow rates and number of panels are total values for the system; each system is split into four subfields to determine the header size and pressure drop.

Cold storage hours	Storage Flow Rate [kg/sec]	Field (PG20) Flow Rate [kg/sec]	Largest Diameter Header [m]	Number of Rows	Pressure Drop in Headers
11	4,704	4,930	1.8	620	8.5 kPa
21	8,981	9,413	2.4	1180	12.4 kPa
24	10,264	10,757	2.6	1348	13.5 kPa

An example of the pumping load is provided for the smallest field and storage size (9 hours of storage with RM=1 on the peak power plant). These calculations assume 1 meter of space between each 5 m panel (or 2 m in every other row, for better access). The pumping power uses a pump efficiency of 0.75 and motor efficiency of 0.85. The header and return lengths provided assume four subfields make up the radiator field total.

Table 5.8: The pumping power requirement for the smallest system is summarized.

Length of Row	210 m
Number of panels in row	21
Pressure Drop per Row with minor losses	62.2 kPa
Header Length in each subfield	762 m
Pressure Drop in Headers	7.5 kPa
Return Length in each subfield	972 m
Pressure Drop in Return	4.1 kPa
Other minor losses in distribution	1 kPa
Total Pressure Drop	74.5 kPa
Pressure Drop in Row / Total	83 %
Total mass flow rate	4,034 kg/sec
Travel time	1.2 hour
Pumping Power	470 kW

Figure 5.8 shows the pumping requirements for fields with an of different sizes. The simulation will determine the total energy input based on when the pumps operate. With propylene glycol is the fluid, the pumps do not circulate when the system gets cold enough to freeze water through the glycol-water heat exchanger, so the operating hours is less than simply the night hours. However, as a rough order of magnitude, pumping power over 6,250 kW may be considered excessive as this is 5% of the output of the 125 MW power plant. Air-cooled condensers use 2-5 % of peak power depending on the size of the condenser. The configurations here have peak pumping requirements of 1-3%.

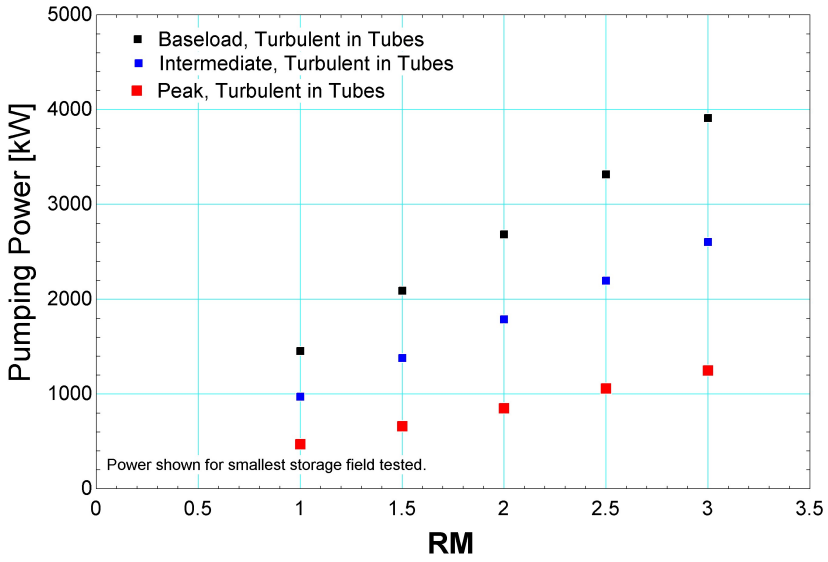

Figure 5.8: The power requirement to pump propylene glycol 20% concentration through the field of radiator in the smallest storage size tested for each power plant is shown.

Note that for a given radiator field area (RM relative to a solar field), a larger mass flow rate requires more, shorter panels, increasing the fraction of the pressure drop that is due to the distribution system.

5.2.3 Preparation of weather data for Las Vegas, Nevada

To model the radiative cooing resource, a weather station is chosen in Las Vegas, Nevada where infrared radiation is measured using a pyrgeometer. (Chapter 2 describes pyrgeometer measurements for effective sky temperature). The SURFRAD measurement site at Red Rocks, Las Vegas provides all the necessary data fields to run System Advisor Model for CSP as well as pyrgeometer data. The SURFRAD data is downloaded in individual daily weather data files where measurements are reported as 1-minute averages. The 1-minute data is distilled into hourly data in MATLAB using the following process:

- Missing data (flagged as -9999 in the original file if individual measurements are missing or as a missing entry if all measurements are missing) are coded as NaN. There are 353 days where at least some data is recorded each minute. There are 7 days where only one minute was entirely missing and for the remaining five days less than 40 minutes were missing (so at least one minute was recorded of every hour of the year).
- For temperatures, pressures, zenith wind speed, and radiation measurements, the hourly average is calculated by ignoring any NaN values.
- For the month, day, hour, and minute fields, the first measured value in the hour is recorded in the hourly dataset.
- For wind direction, the median measured value in the hour is recorded.
- The effective sky temperature is calculated from the measured downwelling infrared S by

$$S = \sigma T_s^4$$

.

- The hourly average dry bulb, pressure, and relative humidities are converted to dew point and wet bulb temperatures in EES so that dew point and wet bulb values are added to the hourly database for use in SAM.
- The hourly data are compared to the TMY3 format data for this site from SAM and the statistical description of the variables is similar. (Table 5.9)
- For the hours where no data was available, the values are infilled by interpolation between surrounding values or using periods of data from surrounding hours or days. The substituted values are taken from days that are roughly similar in DNI patterns.
- Negative DNI values are filled in as zero.

Table 5.9: Statistical summary of the hourly input data for Desert Rock Station from 2015, prior to infilling the missing hourly data. Items marked (*) are not from the SURFRAD dataset, instead they are derived from that data. The fraction of the data that is complete on an hourly and minute basis is shown.

	Complete by Hour	Complete of 525,560 min-utes	Min	Mean	Median	Max	Std
Dry bulb	0.991	0.990	-4.34	19.22	19.13	40.67	9.76
Dew point*			-20.50	-1.51	-2.00	17.41	6.55
Wet bulb*			-6.82	8.79	9.10	20.72	5.48
Relative hum.	0.991	0.990	3.16	29.15	23.92	98.63	18.80
Wind speed	0.991	0.989	0.18	3.74	3.05	16.17	2.51
Wind dir.	0.991	0.989	0.00	143.54	124.58	348.65	87.19
Pressure	1.000	1.000	888.10	902.20	901.67	917.28	5.22
DNI	0.993	0.992	-4.79	306.57	1.75	1068.12	391.76
Effective sky*	0.993	0.993	242.50	271.67	272.04	296.79	10.84

Table 5.10: Statistical summary of the hourly input data for Desert Rock Station from 2015, after to infilling the missing hourly data.

	Min	Mean	Median	Max	Std
Dry bulb	-4.34	19.22	19.13	40.67	9.76
Dew point*	(20.50)	(1.55)	(2.05)	17.41	6.53
Wet bulb*	(6.82)	8.74	9.04	20.72	5.48
Relative humidity	3.16	29.15	23.98	98.63	18.70
Wind speed	0.18	3.76	3.06	16.17	2.53
Wind direction	-	143.14	124.08	348.65	87.11
Pressure	888.10	902.20	901.67	917.28	5.22
DNI	-	307.68	-	1,068.12	392.48
Effective sky*	242.50	271.59	271.89	296.79	10.85

The Las Vegas weather data is used to simulate power plant performance in SAM. The TMY3 data from the site (as available in SAM) is to determine to what extent the 2015 weather data provides above or below normal insolation. For a 35

MW power plant with SM=2, TES-6 hrs using the default SAM parameters for all components, the annual production is 107 GWh with the 2015 data or 109 GWh with the TMY3 data, indicating that the yearly production is reasonable.

5.2.4 Component cost estimates

Based on the initial cost assessment described in Chapter 1, the key cost driver was the size of the cold storage tank for two, fully-mixed storage tanks. Stratified storage is chosen to minimize storage cost. Other important costs are the estimated cost of the air-cooled condenser (not needed in a radiative cooled plant) and the cost of the radiative field and fluid. Land costs are much smaller. The cost of a surface condenser for the radiative cooled plant was not considered in the initial cost estimation but is shown here to be relatively small. Radiator and storage costs are determined in a scalable way because the size of those components effects plant performance and so it is necessary to study the effects of changing the radiator and storage size systematically in the final results.

Conservative (high) cost estimates are chosen for each component and then the effect of cost reductions is explored in the results.

Radiator material and installation costs

The cost for the radiator field materials is based on roll bond panels for solar water heating as this is the same construction. Cost quotes were obtained for quantities of 20-50 panels from two different vendors. The costs were $ 13 to 21 per square meter. These are likely conservative as they do not represent nearly the volume that would be required for this project. A cost of $13 per square meter was used for the conservative cost estimate.

In addition to the material cost, installation costs for the radiator field are also included. Solar photovoltaics installation costs are estimated in Fu et al. [2017]. The installation cost including racking for large scale (1MW) PV plants in Q1 of 2017 was $ 0.13 per Watt of panel capacity. This model assumes a 17.5 % efficient panel. To convert this to an area specific cost, the 17.5% efficiency is applies to 1000

W / m^2 design irradiance, giving a 175 W capacity per square meter. The cost of installation is then $22.75 per square meter exclusive of the actual panels, which are priced separately as described above.

Radiator land

Land costs for the radiative panels are added to the land costs for the solar field. The default land cost in SAM of $10,000 per acre is used ($2.5 per m^2).

Freeze protected fluid costs

Propylene glycol and 20% mass concentration is selected for freeze protection. A bulk cost of $1.29 / gallon ($0.335/L) is used for the conservative cost estimation. This cost estimate is based on discussions with industry, where a bulk price of $0.95 / pound of concentrated propylene glycol was recommended, less an estimated 20% bulk discount. Another point of reference for the cost of this fluid is $3,199 for a 275 gallon purchase of inhibited propylene glycol at 95% concentration [ChemWorld, 2018]. This comes out to $2.44 per gallon of 20% solution. A bulk price for over 1 million gallons required in this application would be easily half.

Cold storage costs

Costs for above ground water storage tanks are based on industry expert [Andrepont, 2016]. An estimate for tanks over 12 million gallons is $0.5 to 0.7 / gallon ($0.13 to 0.18 / L). The tanks in the current study are 25 -54 million gallons, depending on the number of hours of storage. Tank costs are assumed to be $0.7/L for the conservative cost estimation.

Air-cooled condenser cost savings

The power block cost for CSP simulations in SAM is based on a $/kWe input for the entire powerblock. The default value is $1,100 / kWe. The component-level cost estimation that originally went into this calculation shows that the air-cooled

condenser cost was 17% of the total, or \$187 / kWe (see Turchi and Heath [2013] and provided spreadsheets). So the power block unit cost is reduced by \$200 / kWe for radiative-cooled plants.

To put these costs in perspective, the cost per UA of the ACC and radiator field can be compared. Based on the IPSE design point model for an ACC plant, the ACC UA is 33.4 MW/K with a total cost of \$25 million or \$0.75 per W/K. The radiative field cost estimate is \$35.75 per m^2 (including panels, structures, and installation as described above). The equivalent UA quantity for the radiator field is $U_L^* A_c$. For the design conditions, the selected radiator design has U_L^* of 27.7 W/m^2-K . The UA cost is then \$1.29 per W/K. However, the radiative system requires cold storage, making the cost of the system significantly more, as the results in this section show.

Surface condenser costs

A surface condenser must be added to the power cycle in place of the previous air-cooled condenser. EPRI [2004] provided a correlation of surface condenser costs based on heat transfer surface area. Using the surface condenser UA as determined in the detailed cycle models (see Chapter 4), the surface area is 88,757 ft^2. The EPRI correlation gives a cost of \$847,863 or \$6.78 / kWe. As expected the surface condenser is an insignificant part of the cost compared to the air-cooled condenser.

Economic outputs

System Advisor Model includes financial modeling. For the purpose of this work, the Levelized Cost of Energy (LCOE) in real \$/kWh is used. LCOE is a common metric taking into account the total lifetime costs (capital, operation, financing, etc.) over the total lifetime energy production.

$$\mathrm{LCOE} = \frac{\sum_{y=0}^{N} \frac{C_y}{(1+d)^y}}{\sum_{y=1}^{N} \frac{Q_y}{(1+d)^y}} \tag{5.13}$$

Where C_y is the costs in year y, d is the discount rate, Q_y is the energy produced in year y and N is the project lifetime. This formula discounts the costs from year zero (for installation) to N and levelizes costs over the production period of the plant from year one to year N. The plants were all assessed over a 25 year period. SAM's economic models including LCOE are documented in SAM help files NREL (sam.nrel.gov).

The real (constant dollar) LCOE is also used in the DOE's SunShot goals, so this metric is chosen for the main output from this work. The Power Purchase Agreement (PPA) price is also available to provide insight into time-of-day pricing impacts, but as the results show the time of day benefits of the radiative-cooled system were ultimately not significant.

5.3 Results

This first part of this section summarizes the energy performance results. The second part of this section provides economic results that demonstrate the configurations which make radiative cooling with cold storage competitive with air-cooling.

5.3.1 Energy Results

Energy performance depends on condensing pressure/cycle performance improvements and the parasitic power difference between air-cooled condensers and the radiative-cooling pumping system. The performance improvements are reflected in the gross energy production of the cycle and both performance and parasitics are reflected in the net energy. Figure 5.9 shows the energy results for the peak power plant over all configurations. In all cases there is a energy benefit in both gross and net energy to radiative cooling compared to air cooling. As the size of the field (RM) increases, the pumping load increases. At the same time the gross output is increasing, but unlike the continuous increase in pumping, the gross output levels off after RM of 2.

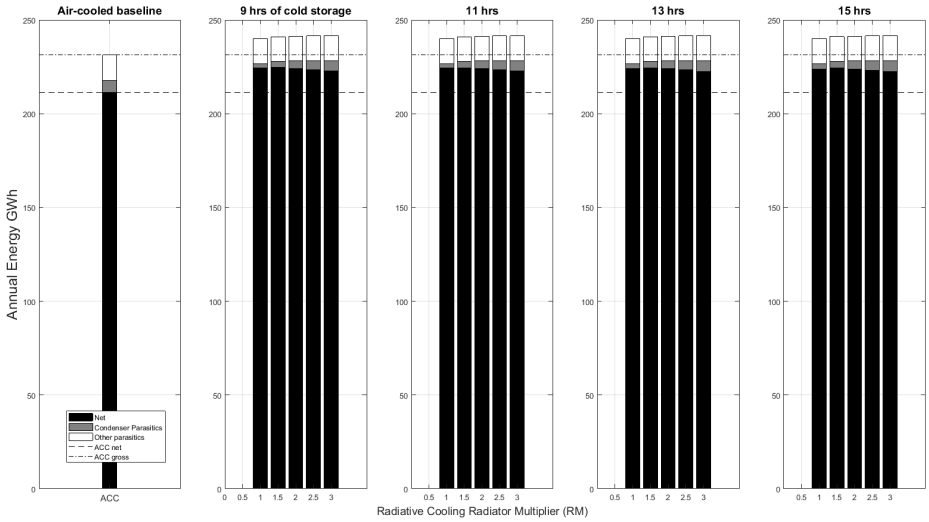

Figure 5.9: The performance of an air-cooled system compared to radiative-cooled are shown. The total height of the stacked bars shows gross output. Sections of the bar indicate the losses to condenser operation and other parasitics. Finally the net energy production for each case is shown.

Figures 5.10, 5.11, and 5.12 show the net and gross energy increases for all of the feasible configurations of a radiative cooled plant compared to air cooled. The gross energy results show that gross energy benefits of radiative cooling level out after RM or approximately 2. The maximum gross energy improvement is 3%, 4%, and 4.5 %, for the baseload, intermediate, and peaking plants, respectively at RM=3. The maximum net energy improvement is 4%, 5% and 6% for the same plants. The net energy improvement is always maximized at RM of 1.5. This reflects the fact that the parasitic loads increase with RM, so the performance improvement from a larger field size after RM 1.5 is eclipsed by the higher pumping loads. These results show that the improvement over air-cooling is highest for the peak power plant in terms of both net and gross energy.

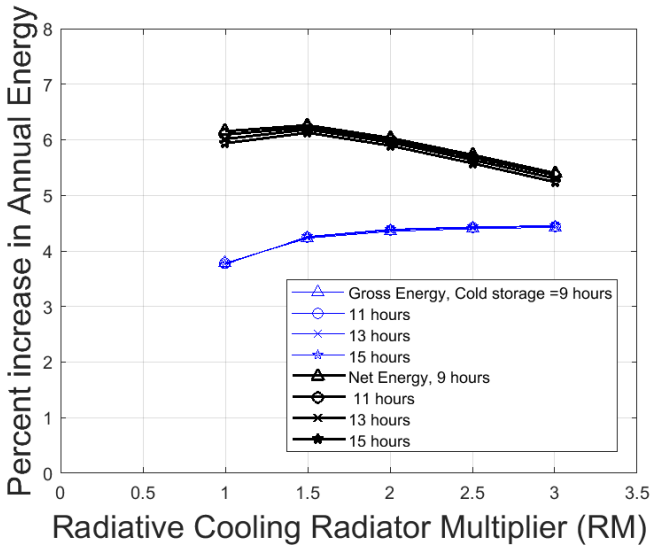

Figure 5.10: The gross and net output for a peak plant relative to the air-cooled cycle are shown.

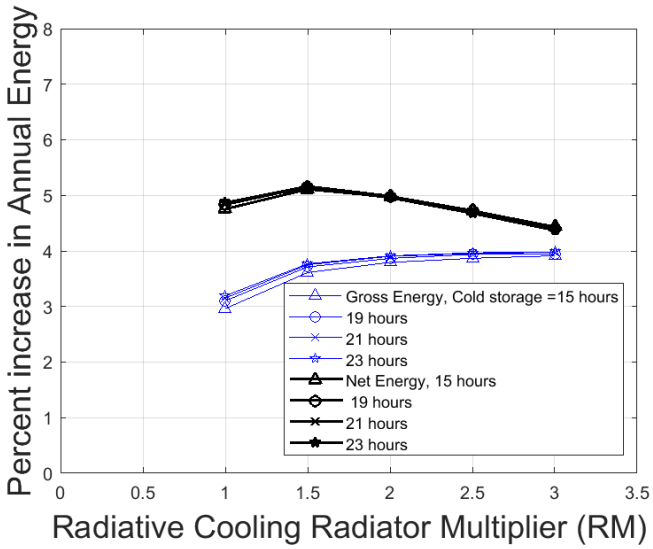

Figure 5.11: The gross and net output for an intermediate plant relative to the air-cooled cycle are shown.

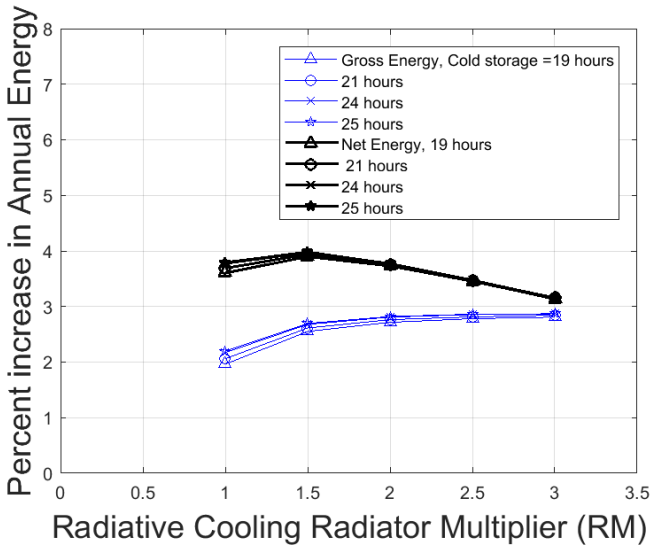

Figure 5.12: The gross and net output for a baseload plant relative to the air-cooled cycle are shown.

5.3.2 Economic Results

The levelized cost of energy results are less subtle; since the radiator field costs are a significant increase in the total cost, the lowest cost of energy production is always from the physically smallest radiator field, and for that field, the smallest storage size. Figure 5.13 shows the LCOE results for each configuration. Note that the peaking plant operates with a capacity factor of only 21.4%, so its LCOE is higher than the other configurations. When comparing air-cooling with radiative cooling, note that the size of the air-cooled condenser and cost is fixed across all scenarios along with the power block. Radiative cooling, however, scales with the size of the solar field (not linearly, depends on RM and storage). **The radiative-cooled peak power plant becomes cost-competitive with air-cooling for three cases**. The combinations of RM=1 with storage of 9 hours, RM=2 with 11 hours, and RM=1.5 with 9 hours all have an LCOE of less than the air-cooled plant's value of 16.1 cents. Note that 9 hours of storage is less than the assumed 11 hours of storage that would ideally use since it operates 11 hours per day in the peak of summer. So the 9 hour

tank has a performance penalty during some periods in the summer, but the overall impact on energy was not significant. It's important to recognize that CSP plants are not typically designed in this peaking configuration, but could be in the future if there are increased flexibility requirements for renewable generators.

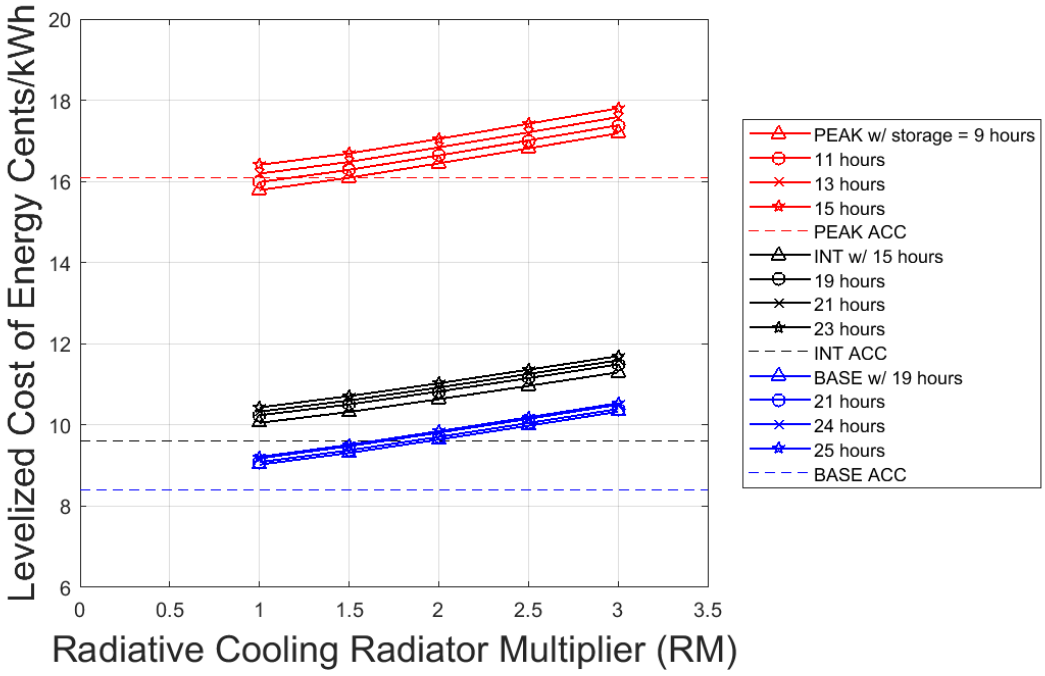

Figure 5.13: The LCOE for a peak plant of the smallest radiative-cooled system size makes this configuration cost-competitive.

SAM provides a detailed LCOE calculation for each simulation, but the results can be understood by simply comparing the increase in direct costs (not including O&M, depreciation, etc., which are accounted for in SAM) to the increase in net energy production. The increase in total direct costs for each configuration compared to air cooling is provided in Figures 5.14 to 5.16. Note that the direct cost increases do not include land area though those are ultimately factored into LCOE. Comparing these cost increases to Figures 5.10 through 5.12, the only configurations

where the increase in total direct costs is not significantly higher than the increase in net energy production are the smallest radiative-cooled systems for the peak power plant. That is why the peak power plants achieve at or near LCOE cost-effectiveness in Figure 5.13.

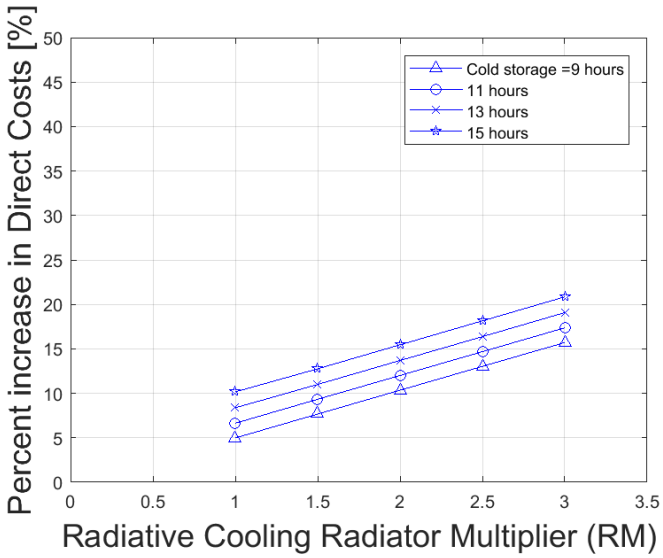

Figure 5.14: The increase in total direct costs for a Peak radiative-cooled plant compared to an air-cooled plant.

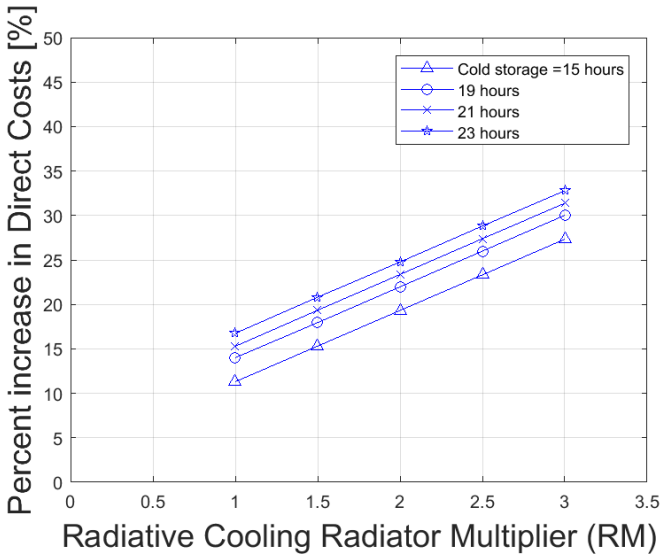

Figure 5.15: The increase in total direct costs for a Intermediate radiative-cooled plant compared to an air-cooled plant.

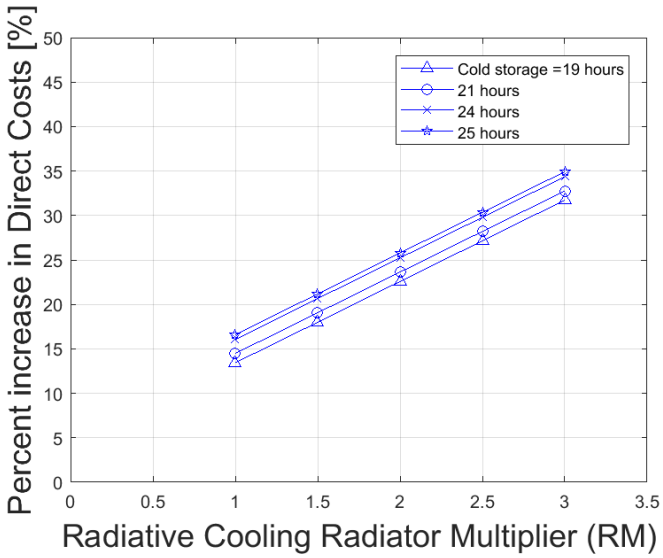

Figure 5.16: The increase in total direct costs for a Baseload radiative-cooled plant compared to an air-cooled plant.

All of the economic estimates provided thusfar depend on the conservative cost estimates which were made for each component of the radiative-cooled system. Economies of scale will likely make the system less expensive than these estimates show. Figures 5.17 through 5.19 show the cost breakdowns for each major component of the radiative-cooled system as well as an estimate of the cost that would be required to meet air-cooled LCOE for each configuration given its performance. These estimates are made by simply requiring that the percent increase in costs equal the percent increase in net energy (which is known based on the simulations).

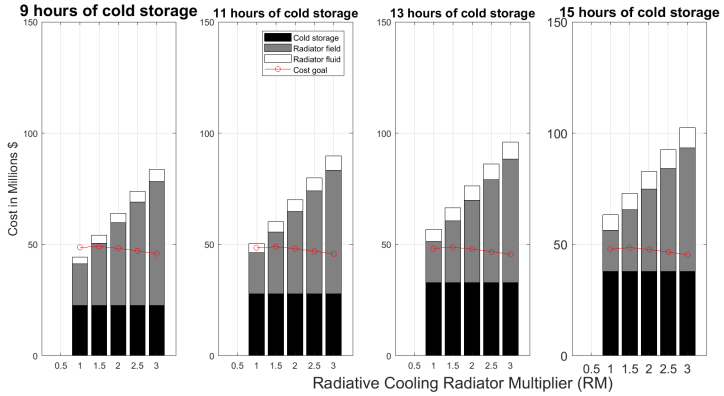

Figure 5.17: The cost of each configuration for a peak power plant is shown along with the estimated radiative-cooling cost to reach LCOE competitiveness with air-cooling.

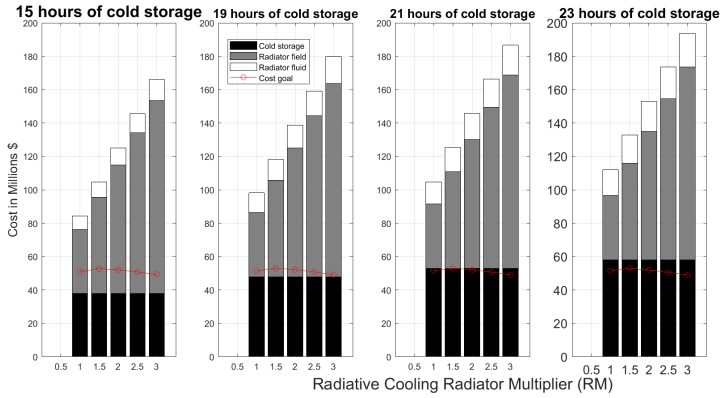

Figure 5.18: The cost of each configuration for a Intermediate power plant is shown along with the estimated radiative-cooling cost to reach LCOE competitiveness with air-cooling.

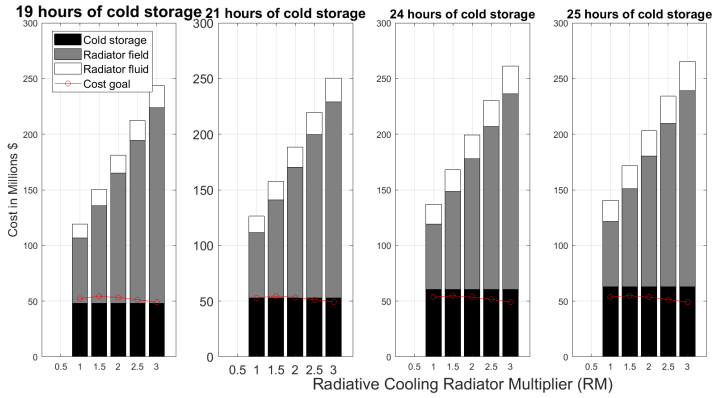

Figure 5.19: The cost of each configuration for a Baseload power plant is shown along with the estimated radiative-cooling cost to reach LCOE competitiveness with air-cooling.

Another way of looking at the uncertainty in costs for these projects is running actual simulations with reduced costs and observing the LCOE result. For each case, a 20% reduction in each of the three major costs (field, fluid, and storage) is assumed. Figures 5.20 shows the results. The radiative-cooled system is now cost-competitive with the air-cooled system for any of the RM=1 cases and for three of

four RM=1.5 cases as well as one case with RM=2. In the intermediate and baseload plants, the 20% cost reduction is not significant enough to move any configuration into competitiveness. However, given the uncertainties in cost estimations at this phase of the concept, it is not unreasonable to imagine cost reductions of more than 20% that could make the projects competitive.

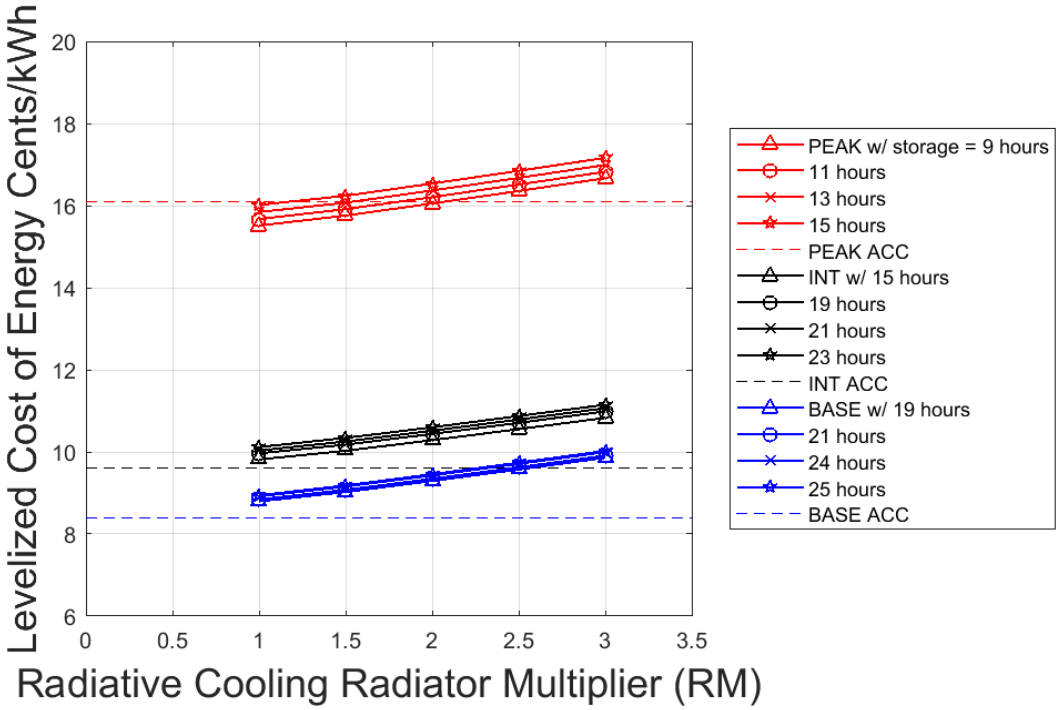

Figure 5.20: The LCOE of the peak power plant with the initial cost estimations and a 20% decrease in costs is shown. More configurations reach cost-competitiveness.

5.3.3 Performance Sensitivity

The sensitivity of the system's performance to flow conditions within the tube and the balancing of the glycol-water heat exchanger is tested. Allowing the flow rate to drop below turbulent within the tubes will have more resistance to heat transfer within the tubes. In addition, assuming the panel length does not change, the total

field amount of cooled glycol produced by a given field is reduced. However reduced flow rates make a panel more effective (reaching colder outlet temperatures). Laminar flow within the tube also reduces the pumping power.

To test these competing effects, the flow through an individual panel is varied for the intermediate power plant with RM=2 and 15 hours of cold thermal energy storage. The panel row length is held constant at 515 m. Thus the field's flow rate varies and the glycol-water heat exchanger becomes unbalanced. Figure 5.21 shows the effects on pressure drop through the tubes and effectiveness for a range of capacitance rates (CR) for the heat exchanger. Table 5.11 shows the impacts of these effects in the annual simulation. The 8 kg/sec flow rate represents the balanced case used in the main results in this Chapter for this particular plant. There is slight benefit to reducing the flow rate of the glycol loop slightly ($0.01 / kWh LCOE savings). Unbalancing the heat exchanger further results in significant decrease in gross energy production which is not compensated by pumping savings, so the LCOE falls. Unbalancing the heat exchanger by increasing the glycol flow rate (minimum capacitance rate on the water side) is a loss both in gross output and pumping. These results show that a radiative cooled system may ultimately be designed for laminar flow in the tubes, but overall the performance and LCOE results are not significantly changed.

Table 5.11: The trade off between pumping and performance is tested in annual simulations. The LCOE is reduced by 0.01 cent/ kWh.

Panel mass flow [kg/sec]	Press Drop [kPa]	Fluid Vol. Ratio	Direct Costs M$	Gross Output [GWh]	Net Output [GWh]	LCOE [cents/kWh]
5	75.4	2.54	565	520	490	10.10
6	75.54	2.85	566	522	492	10.06
7	83.04	3.15	567	524	493	10.05
8	92.87	3.46	567	525	493	10.06
9	98.81	3.77	568	525	492	10.09

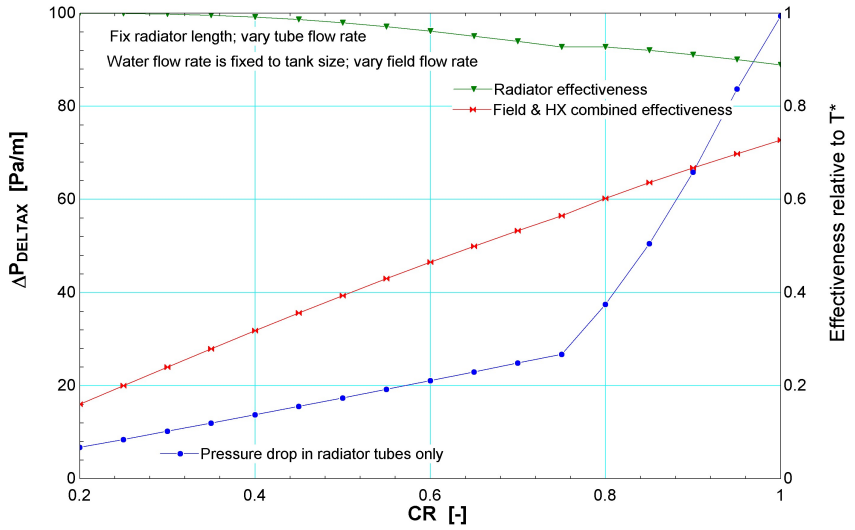

Figure 5.21: The tube pressure drop, radiator effectiveness, and radiator-HX combined effectiveness are shown for varying CR. The minimum capacitance rate is the glycol side.

6 CONCLUSION

6.1 The potential for radiative cooling of CSP power plants

Returning to the basic research question in this project: **What is the potential of a black, uncovered radiator panel system with cold storage to provide cooling for CSP power plants? What are the economic and energy benefits of the system (if any) compared to air cooled condensers?**

Results of the specific research goals are first stated:

1. An initial feasibility assessment of radiative-cooled CSP plants showed that using radiative surface area about the same size as the solar aperture area of the solar plant, a radiative-convective system could provide adequate power cycle cooling in all but the highest heat rejection load hours. Cold storage costs volumes with two tank, fully mixed storage tanks are likely too high; stratified tanks are needed.
2. An analytical model for radiative-convective cooling is detailed and validated with a finite differences model. Existing data was used to validate the models and an experimental design showed that the impacts of convection uncertainty make further model validation not valuable.
3. Detailed Rankine cycle modeling showed that optimized cycles, accounting for exhaust losses from last stage turbines, do not exhibit strong condensing pressure effects on efficiency. Two cycles are modeled and regressed for use in annual simulations to show the difference between a cycle optimized for low pressure and high.
4. A system-level simulation using accepted CSP modeling methods in System Advisor Model is completed for air-cooled cycles of three different power plant types. New components are added to the software to model radiative cooling with cold storage.

The major results of this work, back to the original research question, are that a radiative-cooled system performs slightly better in terms of gross energy output

compared to an air-cooled cycle. Though the condensing pressure effect is not strong, the radiative cooled cycle optimized to run at low condensing pressures does indeed have a higher gross energy output throughout the year by 1-4%, depending on the size of the radiator field. After accounting for pumping losses, the net energy gain from a radiative cooled system is still significant. Up to 6% in net energy increase is found for a peak type solar power plant with a small radiative cooled system (1.5 x the solar field aperture area). After accounting for the cost of radiator panels, installation, cold storage, heat transfer fluid, and additional land area, the radiative system is significantly more expensive than an air-cooled system. However there are a few cases where the radiative-cooled system is competitive with air-cooling based on LCOE. Based on initial conservative cost estimates, only the smallest radiative cooled plant (1x the solar aperture area) is cost competitive. But with a (not unrealistic) 20% cost savings in these estimates, several cases of the peak power plant are competitive.

6.2 Future Work

Given the new models in SAM described in Chapter 5, it is now possible to study the impacts of several different configurations of a radiative-cooled plant. Given the results of the current work (gross and net energy production are improved with radiative cooling and in some cases LCOE, compared to air-cooling), the following studies are of interest:

- Water as cooling fluid: Water can be modeled as the cooling fluid in the radiative panels. The performance of the system will improve if a heat exchanger is not used to separate the field and cold storage water systems. Water treatment will be required for the circulating water to avoid scaling in the tubes. The cost of this treatment should be compared to the propylene glycol fluid. The additional head pressure due to pumping the fluid through the cold storage tanks must also be added to the pressure drop in the field.

- Peak Summer performance: The cold storage system could be sized to meet a majority, but not all, of the load hours. In the current work the tank is sized for the summer day with the shortest cooling hours and longest power cycle run hours. Instead the tanks could be sized to meet 90 % of the load hours or similar. The time of day impacts of this can be modeled in SAM using time-of-day price multipliers and PPA as an economic output.

- Two-tank system: Though more expensive, the two tank system has thermodynamic performance benefits. A system with two, fully-mixed tanks could be cost-competitive with the stratified tank system if cost saving measures are taken such as reducing the required tank volume (for example, by considering peak summer performance as described above).

- Solar power plant for radiative cooling: Because the solar power plant design (solar multiple and hours of thermal energy storage) impacted the comparison of air- and radiative- cooling in the results of this work (Chapter 5), one could consider what power cycle would benefit most from radiative-cooling. A cycle that operates only at night, for example, would require no cold storage system for radiative cooling. A cycle that is used only for peak morning, afternoon, and evenings would minimize the amount of cold storage and maximize the performance benefit compared to air cooling.

- Power cycle design point: The power cycles used in this work are optimized for their expected design operation point. A last stage turbine annulus area was selected for best efficiency given the exhaust loss- condensing pressure trade off over expected operating range. Other design points could be used and the last stage turbine annulus area can be varied to slightly change the power cycle.

Items of interest related to this project but not currently possible in the existing SAM model (as described in Chapter 5) are:

- Direct Cooling: Fluid cooled by the radiative field could be directly used for the power cycle surface condenser during night hours, while storing

additional fluid for daytime use. This would minimize the cold storage system size. The directly used fluid would provide a lower operating temperature for the power cycle during the night and the cold storage tank temperature would be slightly higher for daytime. The tradeoffs of any performance penalty on the power cycle compared to the cost savings in cold storage can be quantified.

- Hybrid Cooling: A radiative cooling system paired with an air-cooled condenser operating in series would allow cooling at a more consistent temperature throughout the year. The size of the two systems could be optimized based on their respective costs and the paired performance of the system. This could have advantages for a power cycle that is optimized to run at a consistent back pressure as well.
- Other applications: This radiative cooling system with cold storage could be useful for any thermal power cycle. It is interesting to consider its application for supercritical CO2 Brayton cycles used for CSP because air-cooling is typically chosen and they also operate in desert regions.

A APPENDIX: POWER CYCLE REGRESSION COEFFICIENTS

Coefficients for determining power output and thermal input based on HTF mass flow, HTF temperature, and condensing pressure for the two custom power cycles in Chapter 4.

Table A.1: Effects of temperature for the low pressure cycle.

T_{in}^*	0.935	1.000	1.033
$\dot{W}_{ME}(T_{in}^*)$	0.936	1.000	1.032
$\dot{Q}_{ME}(T_{in}^*)$	0.948	1.000	1.026
$\dot{W}_{INT}(P_c > T_{in}^*)$	1.227	1.000	0.906
$\dot{Q}_{INT}(P_c > T_{in}^*)$	1.032	1.003	0.984

Table A.2: Effects of temperature for high pressure cycle.

T_{in}^*	0.935	1.000	1.033
$\dot{W}_{ME}(T_{in}^*)$	0.935	1.000	1.033
$\dot{Q}_{ME}(T_{in}^*)$	0.948	1.000	1.026
$\dot{W}_{INT}(P_c > T_{in}^*)$	1.639	1.000	0.759
$\dot{Q}_{INT}(P_c > T_{in}^*)$	0.937	0.989	1.067

Table A.3: Pressure effects for the low pressure cycle for min pressure to 16090 Pa.

P_c [Pa]	4233	5080	5926	6773	7619	8466	9313	10160	11010	11850	12700	13550	14390	15240	16090
$\dot{W}_{ME}(P_c)$	1.010	1.011	1.012	1.011	1.010	1.008	1.004	1.000	0.995	0.990	0.984	0.978	0.972	0.966	0.960
$\dot{Q}_{ME}(P_c)$	1.000	1.000	1.000	1.000	1.000	1.000	1.000	1.000	1.000	1.000	1.000	1.000	1.000	1.000	1.000
$\dot{W}_{INT}(\dot{m}^* > P_c)$	0.948	0.955	0.961	0.970	0.977	0.983	0.990	1.000	1.008	1.016	1.022	1.030	1.035	1.039	1.041
$\dot{Q}_{INT}(\dot{m}^* > P_c)$	1.000	1.000	1.000	1.000	1.000	1.000	1.000	1.000	1.000	1.000	1.000	1.000	1.000	1.000	1.000

Table A.4: Pressure effects for the low pressure cycle from 16090 Pa to max pressure.

P_c [Pa]	16930	17780	18620	19470	20320	21170	22020	22870	23700	24550	25400	26250	27100
$\dot{W}_{ME}(P_c)$	0.954	0.949	0.944	0.939	0.934	0.929	0.924	0.920	0.915	0.910	0.905	0.901	0.897
$\dot{Q}_{ME}(P_c)$	1.000	1.000	1.000	1.000	1.000	1.000	1.000	1.000	1.000	1.000	1.000	1.000	1.000
$\dot{W}_{INT}(\dot{m}^* > P_c)$	1.044	1.045	1.047	1.048	1.050	1.052	1.054	1.054	1.057	1.060	1.063	1.065	1.067
$\dot{Q}_{INT}(\dot{m}^* > P_c)$	1.000	1.000	1.000	1.000	1.000	1.000	1.000	1.000	1.000	1.000	1.000	1.000	1.000

Table A.5: Pressure effects for the high pressure cycle.

P_c [Pa]	7619	9313	11010	12700	14390	16090	17780	19470	21170	22870	24550	26250
$\dot{W}_{ME}(P_c)$	1.000	1.002	1.003	1.003	1.002	1.000	0.997	0.993	0.988	0.983	0.979	0.974
$\dot{Q}_{ME}(P_c)$	1.000	1.000	1.000	1.000	1.000	1.000	1.000	1.000	1.000	1.000	1.000	1.000
$\dot{W}_{INT}(\dot{m}^* > P_c)$	0.967	0.972	0.978	0.986	0.993	1.000	1.008	1.016	1.023	1.029	1.034	1.038
$\dot{Q}_{INT}(\dot{m}^* > P_c)$	1.000	1.000	1.000	1.000	1.000	1.000	1.000	1.000	1.000	1.000	1.000	1.000

Table A.6: Mass flow effects for the low pressure cycle.

$\dot{m}^*$	0.20	0.30	0.40	0.50	0.60	0.70	0.80	0.90	1.00	1.10	1.20
$\dot{W}_{ME}(\dot{m}^*)$	0.204	0.317	0.426	0.530	0.631	0.728	0.823	0.913	1.000	1.084	1.164
$\dot{Q}_{ME}(\dot{m}^*)$	0.262	0.374	0.477	0.574	0.666	0.754	0.839	0.921	1.000	1.077	1.152
$\dot{W}_{INT}(T^*_{in} > \dot{m}^*)$	1.053	0.986	0.973	0.979	0.987	0.995	0.997	0.998	1.000	1.002	1.004
$\dot{Q}_{INT}(T^*_{in} > \dot{m}^*)$	0.886	0.852	0.880	0.904	0.926	0.946	0.965	0.983	1.000	1.017	1.033

Table A.7: Mass flow effects for high pressure cycle.

$\dot{m}^*$	0.20	0.30	0.40	0.50	0.60	0.70	0.80	0.90	1.00	1.10	1.20
$\dot{W}_{ME}(\dot{m}^*)$	0.215	0.329	0.436	0.540	0.639	0.735	0.827	0.915	1.000	1.081	1.160
$\dot{Q}_{ME}(\dot{m}^*)$	0.262	0.374	0.477	0.574	0.666	0.754	0.839	0.921	1.000	1.077	1.152
$\dot{W}_{INT}(T^*_{in} > \dot{m}^*)$	1.030	0.965	0.969	0.977	0.984	0.990	0.994	0.997	1.000	1.005	1.011
$\dot{Q}_{INT}(T^*_{in} > \dot{m}^*)$	0.887	0.852	0.880	0.905	0.926	0.946	0.965	0.983	1.000	1.016	1.033

B APPENDIX: FEASIBILITY STUDY PAPER

The feasibility study begins on the next page. This is published in the journal *Applied Energy*.

NIGHT SKY COOLING FOR CONCENTRATING SOLAR POWER PLANTS

Ana Dyreson[1,*], Franklin Miller

Department of Mechanical Engineering, Solar Energy Lab, University of Wisconsin - Madison, 1500 Engineering Drive Madison, WI 53706

Abstract

Concentrating solar power (CSP) plants are currently designed with either cooling towers or air-cooled condensers. These two alternatives have a trade off: cooling tower evaporative cooling systems use water, which is a scarce resource in the desert environments where CSP is implemented, but air-cooling results in decreased power plant performance. In this paper, a radiation-enhanced cooling system for thermal power plants is analyzed with a detailed heat transfer model and shown to be feasible for CSP. The proposed system consumes no water and has the potential to out-perform air-cooling. Heat transfer occurs by convection and radiation to the cold night temperatures of desert environments. The radiators are uncovered black panels with tubes of cooling fluid circulated to a cold storage system. The radiators' performance is modeled using a two-dimensional finite difference model and the complete power plant system is modeled on an hourly basis using a standard power plant with thermal energy storage. If the night sky cooling system is the same size as the solar collector field, annual simulation shows that the system can provide over 90% of the required cooling. In addition, performance is improved compared to traditional air-cooling because the parasitic load for circulating water in the radiator system is about 1% of gross energy production while the parasitic load for an air-cooled power plant is about 4%. The night sky cooling system is a potential solution to the water issues that face CSP power plants and other power plants located in desert environments.

Keywords: concentrating solar, radiation, heat rejection, air-cooling, night sky, water

1. Introduction

There is a great need for more efficient low-water cooling sources for thermoelectric power plants, especially for concentrating solar power (CSP). This paper provides a comprehensive analysis using a detailed hourly simulation to show that the proposed radiation-enhanced nighttime cooling system is feasible. The system takes advantage of the low nighttime temperatures and clear skies in the regions where CSP is typically

*Corresponding author

Email addresses: adyreson@wisc.edu (Ana Dyreson), fkmiller@wisc.edu (Franklin Miller)

deployed. This type of black (non-selective), uncovered system of flat panels has been considered for building cooling applications in the past but has not been studied for the potential to provide power plant cooling (see Section 1.3).

1.1. The energy-water issue

CSP lives at the crossroads of the energy-water nexus; as water usage requires energy (for treatment, pumping, etc.) so energy usage requires water (for fossil fuel mining and refining, thermal power plant cooling, etc.) The water consumption of electricity produced in the US is estimated at 1.9 L (0.5 gallon) per kWh (Diehl and Harris, 2014). As water constraints become tighter, especially in the western U.S., the energy-water issue becomes more important. Moreover, the water issues for CSP are magnified because the solar resource is best in deserts where water is especially scarce.

CSP power plants have typically used evaporative cooling in cooling towers to cool a liquid stream which is circulated through a condenser to provide heat rejection from the power cycle. (Here this is also referred to as wet-cooling though other types of wet-cooling exist.) Most new plants such as Shams I (100MW parabolic trough, United Arab Emirates) and Ivanpah (377 MW power tower, United States) employ air-cooled condensers to reduce water use. Water consumption was quantified for several CSP plant designs and locations by Turchi et al. (2010) and the wet-cooled plants consumed 3.5 L per kWh compared to 0.3 L per kWh for dry-cooled (some water consumption still occurs due to mirror cleaning and other plant operations). Macknick et al. (2012) reviews and consolidates data from many sources to estimate the water footprints of different electricity generation sources in the US. The median water consumption for wet-cooled parabolic trough CSP is 3.3 L per kWh and for dry cooled it is 0.3 L per kWh. About 3 L per kWh can then be attributed to wet-cooling. This 3 L per kWh can be confirmed from first principles using the enthalpy of vaporization of water and a power plant thermal efficiency of 0.33. Turchi et al. (2010) point out that CSP plants tend to operate at a lower efficiency and with more start-up and shut-down periods than base load fossil fueled steam cycles, making their average efficiency lower and water consumption higher than would be expected for a typical steam cycle.

Though eliminating water usage for cooling, air-cooled condenser systems don't perform as well as wet-cooled systems. First, the parasitic load from the fans on an air-cooled condenser are much higher than the fan and pumping loads for a cooling tower system. Second, the condensing temperature of an air-cooled system is limited by the outdoor dry bulb temperature (for CSP this issue is magnified in the hot desert during the day). Wet-cooled systems, however, can approach the wet bulb temperature instead, allowing for lower condensing temperatures and therefore higher efficiency in the Rankine steam cycle. Thus, when choosing between air-cooled condensers and cooling towers, there is a trade off between performance and water usage. Currently most new plants are built with air-cooled condensers because the water use issue is paramount, but the plants suffer from the performance penalty as well as the increased capital cost of air-cooled condensers.

1.2. CSP power plant cooling

Because the energy-water issue for CSP power plants is critical, some have proposed alternative low-water cooling systems. Wagner and Kutscher (2014) analyzed a hybrid

cooling system composed of parallel evaporative and air-cooled systems for CSP and such a system is implemented at the Crescent Dunes power tower plant (SolarReserve, 2015). Muñoz et al. (2012) proposed an air-cooled condenser that operates at night with cold storage at a CSP plant, taking advantage of low nighttime ambient temperatures. Goswami (2011) analyzed using underground channels to pre-cool air for an air-cooled condenser at a CSP plant. Heller cycle indirect cooling with dry cooling towers has been proposed USDOE (2001). Work is currently underway by Martin and Pavlish (in USDOE (2013)) for a desiccant-based cooling system for CSP plants to reduce water usage compared to wet cooling. Of these proposals, the hybrid system is the most practical and has already been implemented. But it is not a complete solution because there is still some water consumption and since the systems operate in parallel, the condensing temperature of the cycle is limited by the air-cooled condenser.

1.3. Radiative cooling

Radiative cooling has been investigated in detail for building cooling and a few publications consider radiative cooling for power plants. A fundamental difference between these two categories is the temperature of the radiator surface. For comfort cooling a building is maintained below ambient while a power plant condenser generally operates above ambient unless the cooling system allows cooling below ambient (such as a cooling tower which approaches ambient wet bulb).

As summarized by Eicker and Dalibard (2011), a great amount of work has been reported on passive radiation cooling for buildings. Radiation cooling for buildings has been proposed using open tanks, dedicated thermal panels, and now photovoltaic-thermal (PVT) panels. (PVT panels are typically used to cool PV panels and to collect thermal energy during the day but as a passive cooling panel they can be used at night to cool water.) Radiating surfaces can be covered, uncovered, selective, or black. Most relevant to the current work are black, uncovered radiating surfaces. Based on a review of the literature (Eicker and Dalibard (2011), Tevar et al. (2015), Erell and Etzion (2000), Hosseinzadeh and Taherian (2012)), the heat flux from experiments on uncovered black surfaces used for comfort cooling averages between 50 and 100 W/m^2 . One study included a demonstration of heat fluxes of up to 800 W/m^2 when the inlet temperature is higher, up to 55 C (Eicker and Dalibard, 2011).

Radiation cooling for power plants has also been suggested in the literature, though not nearly as widely as radiation cooling for building comfort cooling. Olwi et al. (1992) propose a white covered pond to provide passive cooling for thermal power plants in the desert during both day and night. One typical day (September) is modeled using hourly steady-state conditions. Water at 50 C enters the pond in the upper layer, that is separated by a screen from the lower (cold) layer of water. A net heat rejection is available all day, although it is higher at night. According to the model, the total available heat rejection is about 150 W/m^2 (about 50 W/m^2 radiation and 100 W/m^2 convection). The experimental implementation of this model Sabbagh et al. (1993) showed that the average heat rejection by radiation was about 50 W/m^2 . The major problem encountered during testing was that it was difficult to prevent an air gap from being present between the water in the pond and the cover. The presence of an air gap increases the resistance to heat transfer. Similar to the work of Olwi et al. (1992), a nighttime cooling system for a supercritical organic Rankine cycle was proposed by Vidhi (2014) using radiative cooling from a covered or uncovered pond. Due to a lack of experimental data the results

were inconclusive, but it is expected that a cooling pond would be subject to the same problems of daytime heat gain and lack of good heat transfer through pond cover as found by the experimental work of Sabbagh et al. (1993).

Du Marchie Van Voorthuysen and Roes (2013) propose flat radiating surfaces within the parabolic trough structure of the solar collectors. These radiating surfaces would provide cooling both day and night using selective surfaces. The radiating surfaces are aluminum mirrors coated in titanium dioxide in order to be transparent to far infrared radiation. The surfaces are also cooled by convection to ambient air. Water would circulate from the condenser through a water tube below the parabolic trough and be stored in a cold storage basin. This water tube would be thermally connected to the cold radiating surfaces with heat tubes. The total insolation for a June day along with average daytime temperature, nighttime temperature, average sky temperature suppression (25 C), and two point estimates for wind speeds are used to analyze the performance. The average heat flux from the radiating surfaces is found to be sufficient to cool a 33% efficient Rankine power cycle fueled by the parabolic trough solar plant. Off-design conditions, heat tube performance, condenser performance, and cold water storage tank size were not addressed.

Zeyghami and Khalili (2015) propose using a selective surface to provide daytime radiative cooling as supplemental cooling for air-cooled supercritical carbon dioxide cycles for solar thermal power. The selective surface reflects solar insolation and emits in the atmospheric window of 8 -13 micrometers. Based on modeled operation, the net output of the cycle is improved by 3 to 8% depending on cycle configuration and temperature.

1.4. Night sky cooling: dry and efficient

In light of the already water-stressed energy system, the water use of CSP for cooling is a significant detractor from the benefits of the technology. By taking advantage of the desert conditions where CSP is deployed, the proposed radiation-enhanced cooling system offers a promising solution. Under clear sky conditions the sky temperature is about 20 C colder than the ambient air temperature. In the proposed system a cooling fluid (nominally water) is circulated during the night through a field of black radiative panels. The water is cooled by radiation to the night sky and convection to the ambient air. Cold water storage tanks are used so that the power plant can operate at any time day or night. The parasitic loads for pumping are less than those of an air-cooled condenser and water is not consumed. Though not included in this analysis, the condensing temperature of the steam cycle can be adjusted to match the available cooling from this system, improving cycle performance under some conditions.

The cooling system proposed in this paper is a promising new alternative that consumes no water and has the potential to out-perform air cooling. The proposed system is novel; cooling power plants primarily with nighttime radiation cooling has not been well studied. An uncovered, non-selective surface operating at night has not been analyzed in previous literature. In addition, the hourly annual simulation presented is the most comprehensive analysis of a radiation cooling system for power plants to date.

This paper demonstrates the feasibility of uncovered, black radiators with cold storage to provide CSP plant cooling using a radiator surface area equal to the aperture area of the solar collector field. Constraining the surface area ensures that the land area required for cooling will not be significantly larger than for the solar field. It is also possible that the radiating surfaces could be on the back of the solar collectors, thereby requiring no

additional land area. (This alternative would require solar collectors that could rotate 180 degrees from solar noon position and a collector frame designed to handle the additional loading while maintaining the precise focus of the parabolic trough.)

2. Selection of location and weather data

To demonstrate the feasibility of the proposed cooling system, two plants were modeled at locations in the United States which are close to existing CSP plants therefore demonstrate realistic locations and weather conditions: Daggett, California and Tucson, AZ. The plant capacities are 35 MW, chosen to be representative of some existing parabolic trough CSP plants. The plant design is also typical for new plants with storage (solar multiple of two and thermal energy storage capacity (TES) of six hours). Weather conditions are modeled using the Typical Meteorological Year (TMY3) data set (Wilcox and Marion, 2008).

3. Methods

The feasibility of the night sky cooling system is analyzed by creating a detailed model of the radiator's performance and linking it to the required heat rejection of an air-cooled CSP plant with thermal energy storage (TES). A cold storage system is also modeled. Since all components of the CSP plant are standard, the focus of the work is on the radiator's performance (Section 3.2), while other components of the system are modeled using a standard model (Section 3.1).

3.1. Model of CSP system

The complete system consists of a radiator field, cold storage, and CSP plant. The CSP plant is typical: a solar collector field of parabolic troughs collects solar radiation in a circulating heat transfer fluid during daylight hours and the heat is transferred to molten salt thermal storage with a heat exchanger. When the power plant operates, the stored energy in the molten salt is transferred to the steam cycle via a heat exchanger. The power block is a steam Rankine cycle. The unique components of the proposed system are the radiator field and cold storage. The power block rejects heat to the cooling fluid from cold storage that is cooled using the radiator field. Figure 1 shows the system layout.

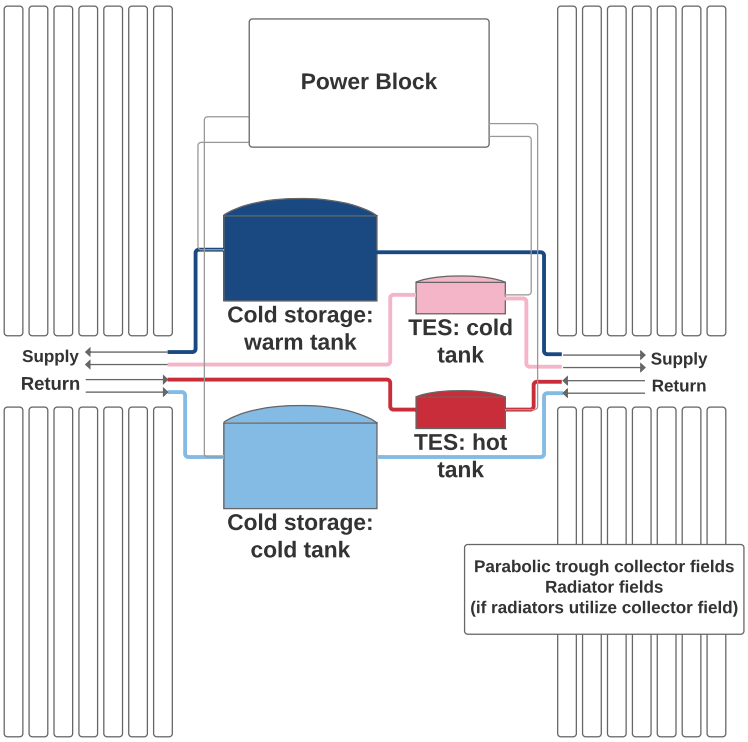

Figure 1: The complete system includes typical CSP components: solar collectors, power block, and thermal energy storage, plus the radiators (assumed to be co-located with the solar collectors in this figure) and cold side storage.

For this feasibility analysis of the radiation cooling technology, it was assumed that heat rejection load from the CSP plant had the same magnitude (MW thermal) and was at the same temperature as an air cooled plant. (In reality, the operation of a power plant and cooling system are connected in that when lower cooling temperatures are available, power block operation would be adjusted to take advantage of those temperatures for improved efficiency.) A reference air cooled power plant is modeled using the System Adviser Model (SAM) program (see NREL (2015) and Wagner and Gilman (2011)). SAM simulates operation over one year at an hourly timescale using TMY3 data. The heat input to the power block and cycle thermal efficiency are output from SAM for use in the analysis of the proposed cooling system. The hourly required heat rejection is calculated from:

$$Q_{load} = Q_{thermal}(1 - \eta_{gross})$$

The plant modeled in SAM has 584 Solargenix SGX-1 collectors. A collector is 100 m long and has a width of 5 m. (One 100 m collector actually consists of 12 sub-modules.) Eight of the collectors are connected in series to make an 800 m loop. 73 loops of eight collectors are connected in parallel. The solar field is configured in two sub-fields as shown in the left and right hand side sub-fields in Figure 1. Although many configurations could be implemented in a CSP plant, this configuration is one realistic reference case. Details of the SAM model and results are in Table 1.

Table 1: SAM CSP plant model summary. The air-cooled system parasitic load is 4% of gross energy output. The total parasitic load is 10% of gross output.

	Tucson	Daggett
Collector aperture area	274,655 m^2	
Power block condensing temperature	40 to 55 C	39 to 63 C
Hot side molten salt storage volume	8,282 m^3	
Power output, gross	116 GWh	122 GWh
Parasitic cooling load, air cooled condenser	4,670 MWh	4,873 MWh
Parasitic Loads, all other	6,950 MWh	7,210 MWh

The mismatch of availability of cooling (nighttime) and solar thermal energy collection (daytime) in the proposed system requires storage. Hot storage alone, as is implemented in many solar thermal power plants, would require that the power block run only at night when cooling is available and only at the rate at which cooling is available. Since such limitations on the availability of power detract from the flexibility of CSP (an important characteristic that distinguishes it from many other renewable energy generators), cold side storage is implemented so that the power block can be operated at any time night or day.

A two tank system is modeled where a hot tank feeds the nighttime cooling radiators and a cold tank stores the cooled water for use in the power block condenser. When the radiator operates, water is moved from the hot to cold tank. When the condenser operates, water is moved from the cold to hot tank. If the hot tank gets low in the winter because there are more nighttime hours than sunshine hours, then the system recirculates cold water from the cold tank back through the radiators to further reduce the cold tank temperature. The two tanks are modeled as fully mixed tanks and thermal losses and gains are not included. The total water volume is 50,000 m^3 ; the impact of changing the water volume is discussed in Section 4.3.

The overall heat transfer coefficient-area product (UA) of the power block condenser is designed for the typical summertime conditions, and then the UA of the condenser is used in the hourly simulation to determine performance at other conditions. The reference heat rejection load was 63 MW for a steam condensing temperature of 325 K and a cold tank temperature of 300 K. The cooling water mass flow rate through the condenser is 772.9 kg/second, determined by balancing the mass flow rates of the hot and cold tanks during a peak summertime week. The condenser flow rate was variable based on available water temperatures and required cooling load. When the cooling load required by the power cycle exceeds that available from the tank system, excess cooling must be met by additional radiator field area or by an auxiliary system working in parallel. Such an auxiliary system could be air cooled or water cooled. This is similar to the hybrid cooling proposed by Wagner and Kutscher (2014).

Like the 100 m solar collectors which are composed of 12 modules, the 200 m long radiator is composed of 24 individual radiators in series. Figure 2 shows that over the length of an 800 m loop of solar collectors, four 200 m radiator groups are plumbed in parallel to most efficiently use the available surface area. This configuration allows the radiators to use the same structure as the solar collectors.

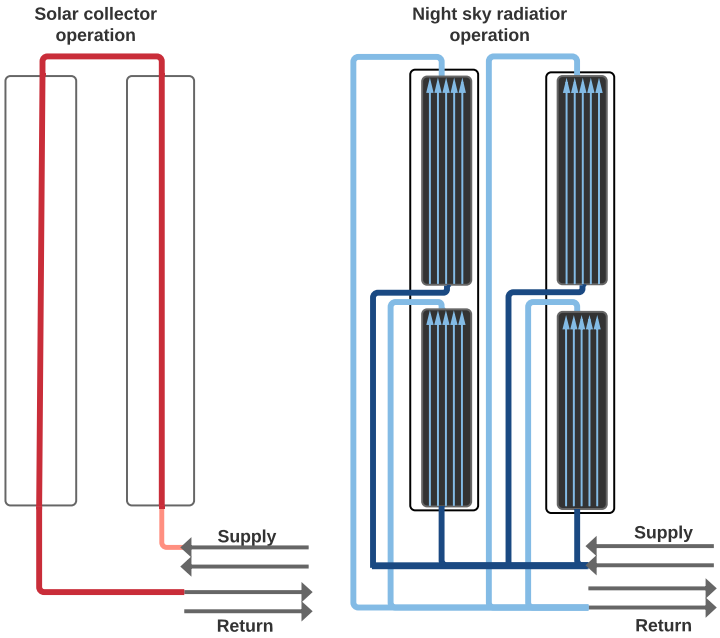

Figure 2: Assuming that the radiator field has a footprint equal to the solar collectors (possibly the radiators are on the back of the solar collectors), the area used for a single 800 m solar collector loop is composed of four shorter radiation loops in parallel.

3.2. Model of the night sky radiator

This section describes the design and modeling of a radiator panel. Tubes are integral in the panel structure and the plate area between tubes provides radiation and convection surface area (Figure 3). This geometry could be obtained using a roll-bonding process to bond aluminum plates. The panel section connecting the tubes is designed to act as a fin. The radiator is designed to maximize radiation from the top of the panel using a black surface, but the bottom of the panel also will have radiative heat exchange with its surroundings. This radiative heat exchange could either result in a heat gain or loss depending on the temperature of the ground and other structures. To minimize these impacts, the back surface has a reflective coating.

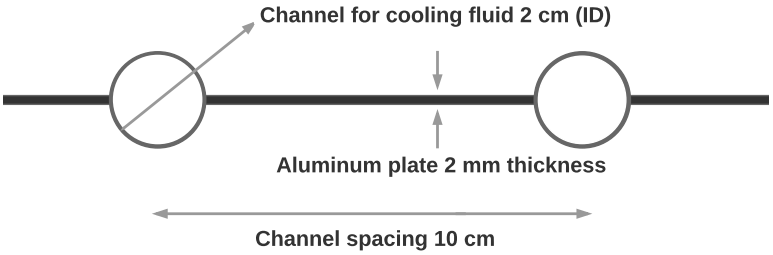

Figure 3: A cross section of the radiator shows the major dimensions. The radiator section continues such that 50 channels are connected across one radiator. The radiator is 200m long (into the page).

The dimensions of one radiator section are 200 m by 5 m.The aluminum radiator has 50, 2 cm inner diameter tubes over the 5 m width. Plate thickness is 2 mm. The mass flow rate through the tubes must be high enough to obtain turbulent conditions within the tube for best convection heat transfer. Higher flow rates will increase the pressure drop and pumping loads, however, and the pumping loads are addressed in Section 4.2. The mass flow rate is 4.5 kg/second, which is divided between 50 tubes. At nominal temperature of 27 C, the flow is turbulent in the tubes (Re=6700).

3.2.1. Two dimensional finite difference model

The radiator was modeled using a two-dimensional finite difference approach. A single lengthwise section of the radiator modeled has a length of 200 m and a width of 5 cm (from the center of one tube to the midpoint between two tubes). A summary of the equations of the finite difference model are provided in the Appendix.

Since the convection coefficients, sky temperature, and radiation properties are not exactly known, convection models and radiation properties are varied in Section 3.2.2 in order to select inputs for the full system simulation. The coefficients and radiation properties that were used to develop the two dimensional model are described here. For initial modeling of the radiator and to test performance sensitivity to key inputs in Section 3.2.2, one typical summer night hour was considered where ambient temperature was 26 C (79 F), clear sky temperature was 7.8 C (46 F), wind speed was 3.1 m/s (6.9 mph), and the incoming fluid was 46.2 C (115 F).

Forced convection over the top surface is determined from correlations for standard forced convection over a flat plate (Nellis and Klein, 2009). It is assumed that the wind approaches the panels along the smaller dimension of 5 m and has laminar flow transitioning to turbulent depending on the wind speed. Free convection on the bottom is modeled with an assumed convection coefficient of 5 W/m^2-K . The emissivity of the black panel approaches 1. The emissivity of the ground and back panels are estimated based on sand and aluminum foil from Incropera and DeWitt (2002) as 0.9 and 0.07, respectively. The ground temperature is equal to the ambient temperature. The night sky temperature is estimated from a correlation for clear sky temperatures by Berdahl and Martin (1984), detailed in Section 3.2.2.

Because the radiator model was designed to be applicable for different radiator geometries, the number of nodes required was examined using a thickness of 1 mm, tube diameter of 2 cm, and with 25 tubes on a 5 m plate. Compared to the high performance

radiator chosen for the annual simulations and described above, this makes the section between tubes much thinner and longer, resulting in a less efficient fin. This is a good test of the model because it increases importance of the two dimensional model; if the plate is well designed it will act as an efficient fin and have a nearly uniform temperature in the x-direction (lateral) and therefore be approximated well with a one dimensional model. In order to determine how many elements the two dimensional model needs to have to adequately capture the behavior of the radiator, different variations of the number of nodes in both the flow (y) and lateral (x) directions are considered. Figure 4 shows the results: five nodes in the x-direction and 20 nodes in the y-direction were chosen to maintain the error (compared to 100 nodes in each direction) less than 1%.

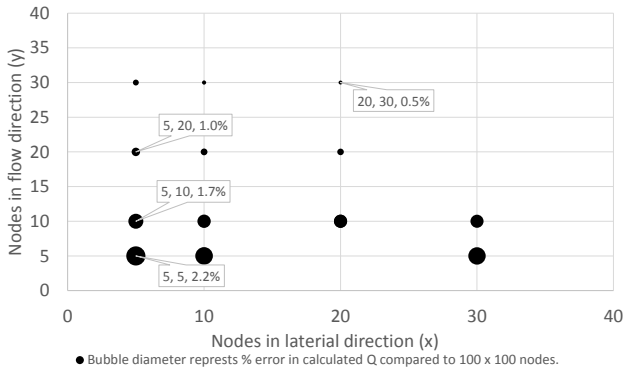

Figure 4: The number of nodes used in the x (lateral) and y (flow) directions along the radiator is plotted along with the error compared to using 100 x 100 nodes.

Another modeling simplification was made at this point: in order to increase computational efficiency, the internal convection coefficient within the tube is calculated based on the incoming fluid temperature instead of taking into account the changing fluid temperature along the radiator's length. This adds a small error so that the total percent difference between the full two dimensional model with 100 x 100 nodes is 1.1%.

3.2.2. Sensitivity of radiator model to key inputs

The sensitivity of the model to key inputs is tested by examining the radiator's performance under typical ambient conditions. Key inputs examined are the external convection coefficients, effective sky temperature, and radiation material properties. Based on the sensitivity analysis, the most realistic yet conservative assumptions are selected for annual simulations. Figure 5 shows the change in the heat rejection from a radiator panel compared to the baseline model described in Section 3.2. The key inputs are described in this section.

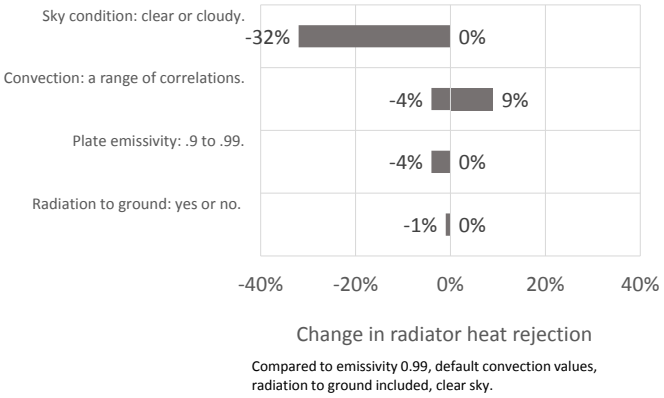

Figure 5: During a typical operation hour in the summer, the radiator's performance is impacted most by the sky conditions. The convection coefficients used also have an impact of less than ten percent increase or decrease in heat transfer.

Sky temperature. Several correlations are available for sky temperature for clear skies and some correlations also consider partly cloudy conditions. During completely cloudy periods the sky temperature can be approximated by the ambient temperature. For a full treatment of the available correlations, see Aubinet (1994) or Eicker and Dalibard (2011). Eicker and Dalibard (2011) compare correlations against short term measurements of sky temperature based on pyrgeometer data. They show that clear sky models follow measurements well during clear periods and that none of the models can represent the hourly sky temperatures in cloudy periods. For the current work the clear sky correlation of Berdahl and Martin (1984), which performed well during clear periods tested by Eicker and Dalibard (2011), is used when skies are clear. The correlation was tested in the original work (Berdahl and Martin, 1984) against measured clear sky temperatures in six locations including two desert environments. This correlation is actually a clear sky emissivity correlation which is allows for an estimate of effective clear sky temperature. The effective sky temperature (T_s) per Duffie and Beckman (2013) is:

$$T_s = T_{db}\left(0.711 + 0.0056T_{dp,C} + 0.000073T_{dp,C}^2 + 0.013\cos\left(15t\right)\right)^{1/4} \quad (1)$$

Since the true sky temperatures could be as low as the clear sky temperature or as high as the ambient temperature, the radiator performance was bounded by looking at these two extremes. Figure 5 shows that the night sky temperature has a large impact on the results. Since it is relatively unknown, a sensitivity to sky temperature will be included in the annual results. The TMY3 data includes an hourly total cloud cover fraction. For the Daggett, CA site the data documentation shows these data were from measurements for 40% of the nighttime hours, were linearly interpolated 23% of the

hours, and were modeled or estimated 36% of hours. Though an inexact data point, we expect that the TMY3 cloud cover fraction (f_{cloud}) would give a reasonable estimate of the cloudy or clear conditions. It is used in the annual simulations to determine what portion of the sky should be considered completely clear (and rely on clear sky estimates for sky temperature) versus what portion of the sky should be considered cloudy (and use ambient temperature as the effective sky temperature for radiation). Figure 6 shows the nighttime average clearness by month at the Daggett location. To roughly estimate the clearness, the clearness fraction is adjusted by plus or minus 0.2 around the reported value. The five cases shown are used as a sensitivity in the annual simulation.

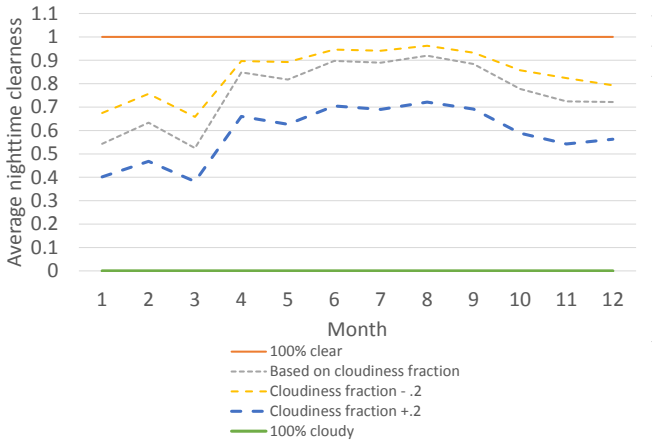

Figure 6: The TMY3 data shows that skies are generally clear during the night in the summer. The cloudiness fraction from the TMY3 data is adjusted up and down by 0.2 to provide a range of estimates of cloudiness. Completely clear or completely cloudy skies are the extreme cases.

Convection effects. Many have completed tests to attempt to correlate observed convection coefficients over solar thermal panels or PV panels, which indeed resemble the exposed convection surface of the radiator panel relatively well other than that they are at some angle to the horizontal. Nonetheless the work that has been done for solar thermal and PV panels is relevant because correlations often consider a range of mounting angles including completely horizontal. For a discussion of the available correlations see Kumar and Mullick (2010). Individual correlations often do not replicate observed convection coefficients in different experimental setups. Sartori (2006) argues that this is because correlations depend on the given solar collector geometry and nearby wind obstructions. Instead Sartori proposes simplified versions of the standard flat plate convection correlations.

Kaplani and Kaplanis (2014) study the impact of convection over PV panels on panel temperature. Their work includes comparing forced convection correlations. The Sartori correlation is one of two recommended correlations based on their experiments.

Kaplani and Kaplanis also provide simplified free convection correlations and a method for accounting for mixed free and forced convection over horizontal plates. Kaplani and Kaplanis account for the varying wind direction by calculating the path of the wind over a panel depending on direction. In the case of a radiator, which is oriented with the solar field such that its long dimension is north-south, a southerly wind would blow straight along the 200 m length and the turbulent convection coefficient theoretically would decrease continuously along the length of the panel. On the other hand, an easterly wind would be parallel to the shorter dimension and would therefore have a higher average turbulent convection coefficient. The impact of varying convection coefficients was tested for combinations free and forced convection estimates for the top and bottom of the radiator at the test condition with a wind speed of 3.1 m/s. Table 2 shows the combination of assumptions which were tested for the top and bottom:

Table 2: Convection estimates for top and bottom of panel considered in sensitivity analysis. The assumptions that were used in the baseline as presented in Figure 5 are indicated.

	Top	Bottom
Forced convection transitioning from laminar to turbulent assuming the path of the wind is over shortest dimension. Free convection effects at zero wind speed not included.	Baseline	No
Fixed 5 W/m^2-K free convection coefficient.	No	Baseline
Free convection only. Determined from correlation.	No	Yes
Consideration of combined free & forced convection. Turbulent convection. Path of the wind is determined by calculating the length of the panel along the wind direction.	Yes	Yes
Consideration of combined free & forced convection. Turbulent convection assuming the path of the wind is over shortest dimension.	No	Yes

The convection treatment for the final model is chosen from these alternatives. For convection from the top of the panel, combined free and forced convection are included. Where free convection is appreciable, it is estimated using the correlation used by Kaplani and Kaplanis (2014) for the Nusselt number $Nu_{free,top}$:

$$Nu_{free,top} = 0.13Ra^{1/3} \tag{2}$$

Because the local wind field over the radiator field is expected to be interrupted by the rows of radiators as well as surrounding equipment, forced convection is represented

by turbulent convection. The Sartori turbulent convection correlation h_{forced} is:

$$h_{forced} = 5.73u^{0.8}L_c^{-0.2} \tag{3}$$

The effective plate length (L_c) is based on wind direction reported in TMY3 data assuming that the long dimension of the radiators is oriented north-south. The combined effect of free and forced convection from the top surface (here h_w) is estimated as Kaplani and Kaplanis (2014) and using the definition of Nusselt number $Nu = \frac{hL_c}{k_{air}}$. For convection from the bottom panel only free convection is considered. In reality some forced movement of air underneath the panels will occur but it will depend on the height of the panels and the interference of the supporting structure. Including only free convection provides a conservative estimate of performance. The Nusselt number for free convection $Nu_{free,bottom}$ from the bottom is estimated using the correlation used by Kaplani and Kaplanis (2014) for a downward facing heated plate:

$$Nu_{free,bottom} = 0.58Ra^{1/5} \tag{4}$$

The related free convection coefficient on the bottom is h_g.

The accuracy of the wind speed measurements are also important; TMY3 data provides measured wind speed at a typical height of 6-10m from the ground. The wind speed at the radiator surface will depend on the exact height of the radiator as well as the local wind field characteristics and the importance of this deviation will depend on the hourly wind speed. This is considered as a sensitivity in the annual simulations.

Radiation properties. The emissivity of the black surface can be very high using specifically designed coatings such as Ball Aerospace InfraRed Black Coating (emissivity of 0.96 at 25 C). For the sensitivity analysis the emissivities of 0.99 (baseline) was compared to 0.90. The radiator's performance was impacted by 4% with the change in properties (Figure 5), therefore a moderate plate emissivity is 0.95 is chosen. The radiative heat exchange from the back panel to the surroundings is minimized by design using a reflective surface. An insulating surface could be used instead though the convection from the back surface would then be reduced. In order to observe the importance of the radiative heat exchange from the back, the model is run including the radiative heat exchange (baseline) and excluding it. The ground temperature is assumed to be equal to ambient. The ground and panel back emissivities were assumed to be 0.9 and 0.07, respectively. The radiation to the ground had very little impact and is included in the final model.

4. Results and Discussion

The system's operation over one year is simulated in two different locations to determine what portion of the required CSP plant cooling could be provided via night sky cooling using an area equal to the aperture area of the solar collectors. The pumping loads and the storage water volume are estimated.

4.1. Night sky cooling can provide most of the required power plant cooling

The night sky cooling system can meet 93% of the power plant's heat rejection load at the Daggett location. During the winter months, 100% of the load is met, while during

the summer months it is lower. Figure 7 shows the temperature of the hot tank, cold tank, ambient dry bulb and estimated clear sky temperature for Daggett. Figure 8 shows the monthly portion of heat rejection achieved with night sky cooling. This same analysis is completed in Tucson, AZ and the heat rejection provided is 91% of total (Figure 9).

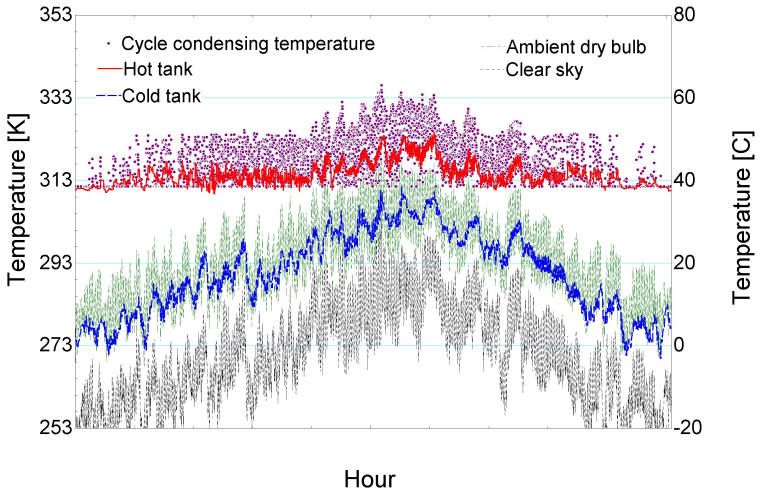

Figure 7: During the winter months in Daggett the cold tank temperature closely follows the minimum ambient temperature, while during the summer months the cold tank tends to be warmer than nighttime minimums but is still never as warm as daytime highs.

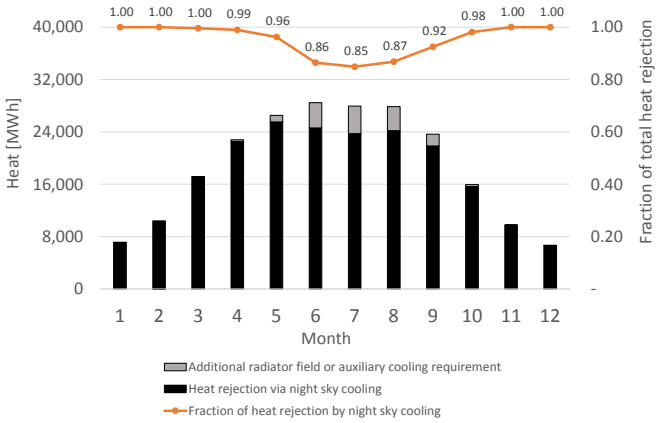

Figure 8: In Daggett the night sky cooling system provides all of the required cooling in the winter, and 80-90% in the summer.

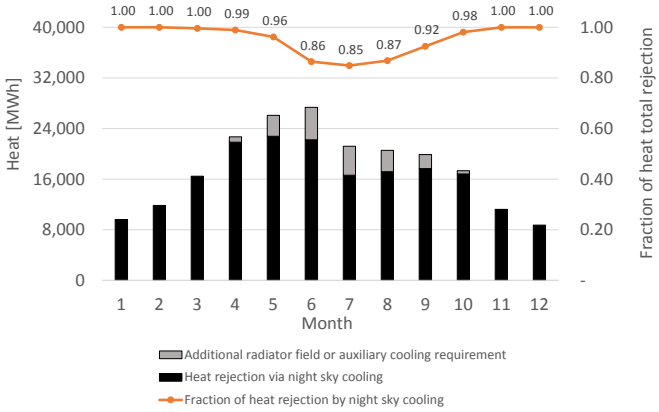

Figure 9: In Tucson the night sky cooling system provides all of the required cooling in the winter, and 80-90% in the summer.

The remainder of the discussion focuses on the Daggett location. Hourly results show that during 39 hours the cooling available is below 50% of the load. This occurs

because the condensing temperature (per the modeled air cooled cycle) has decreased in the night following the ambient temperature, while the cold tank temperature has remained constant and so the temperature of the cold water is not low enough to provide the necessary cooling with the design condenser. In reality, the power block's operation would be varied based on the available cooling. The radiative cooling system would provide a more constant temperature heat sink compared to the air cooled system. There are additionally 30 hours when the supply of cold water is exhausted so no cooling can be met with the system. This occurs during the summer months.

During 6% of the radiator's operating hours the cooling liquid is below the freezing temperature of water (Figure 7). As such, a freeze protection strategy would need to be implemented.

64% of cooling from the radiator field is achieved by radiation during the year (the remainder being convection). The radiation fraction varies seasonally as shown in Figure 10.

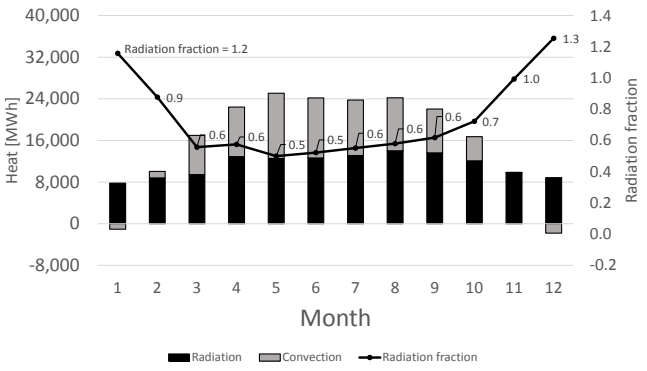

Figure 10: In Daggett, during the winter the radiation accounts for a majority of the cooling because the circulating water temperature is close to or below the ambient temperature and so convection loss is weak or is negative (heat gain). A radiation fraction of greater than one indicates some convection heat gain. During the summer hours the heat transfer is split between radiation and convection.

Since the sky temperature has a large impact on the results as described in Section 3.2.2, the sensitivity of the annual results to sky temperature is also analyzed. Table 3 shows the annual fraction of cooling achieved and Figure 11 shows the monthly fraction. During the winter months all of the cooling can be achieved regardless of the sky condition assumption while during the summer the sky condition impacts the portion of cooling achieved. If the skies are always completely cloudy and the radiation heat transfer is to the ambient night time air, the June heat rejection is about 70% of the requirement. However this is an unrealistic case; the sky conditions are generally clear in the summer

and the heat rejection obtained on a monthly basis expected to be between 80 and 90% as predicted by the models which use the measured cloudiness fraction.

Table 3: Several night time sky clearness assumptions were tested and the heat rejection is between 92 and 93% of the annual load at the Daggett location. At the limit of completely cloudy skies (not realistic) the heat rejection is 85% of annual load.

Description	Percent of annual heat rejection met	Average nighttime clearness percent
Assuming always clear	94.0	100
Based on cloudiness fraction	93.2	75.1
Based on cloudiness fraction -0.2	93.6	83.3
Based on cloudiness fraction +0.2	91.7	57.5
Assuming always cloudy	85.2	0

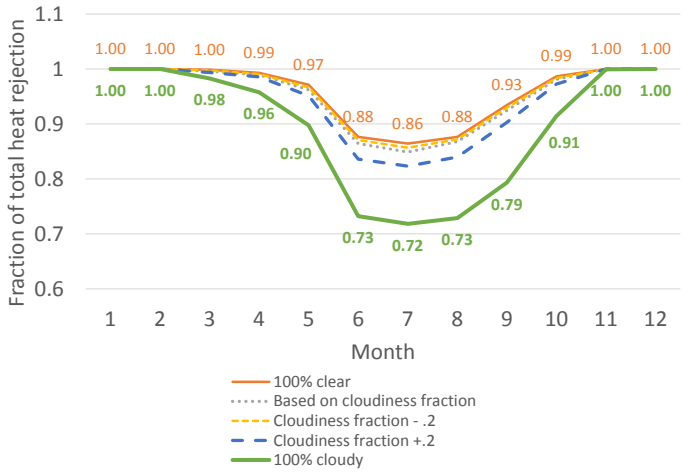

Figure 11: In Daggett, regardless of the sky condition assumed, the cooling load can be met in the winter. During the summer months, the sky conditions based on reported cloudiness fraction plus or minus 0.2 show similar results; the cooling achieved is between 80 and 90%.

As discussed in Section 3.2.2, the wind speed at the height of the panel will be less than at measurement height in the TMY3 dataset. To examine the importance of this effect, the annual simulation is completed assuming that the top of the radiator is 4 m above the ground and adjusting the wind speeds using the power law with an exponent of 1/7. The wind speed is adjusted down from the 6 m or 10 m height (wind measurement height varied within the data set). Using the cloudiness fraction as reported in the TMY3 data set, radiation cooling provided 92.9% of the total cooling load after wind speeds were adjusted compared to 93.2% with unadjusted wind speeds.

4.2. Pumping loads are low

A simple piping layout was completed to approximate parasitic pumping loads for the system. As described in Section 3.1 and illustrated in Figure 2, each of the collector loops has four, 200 m radiators in parallel. The significant components and their relevant dimensions and pressure drop contribution for one sub-field are shown in Table 4. The largest component of the pressure loss is from the medium sized distribution sections because these sections include the complex header system within the radiator field.

Table 4: The pressure loss estimate for one of the two sub-fields is determined from pressure losses in pipe runs and minor losses in each of the significant sections of the distribution system.

Section	Description	Pressure Drop [kPa]
Large distribution pipe from storage to radiators	Two main lines, each approximately 555 m for each of two field sections. Pipe diameter 0.8 m.	31.9
Medium distribution sections delivering to individual radiations plus 90 degree bends for routing piping, and header sections within radiators.	Piping to deliver to radiators is 200-400 m depending on radiator position in field. Headers include inlet, tees, and exit for 24 sections which make up one radiator. Pipe diameter is 10 cm.	71.6
Small tube sections within radiators	Each radiator is 200 m length composed of 24 smaller sections. Exit from individual tubes is included. The tube diameter is 2 cm.	24.2

The pump power is determined from the pressure drop with an assumed 75% pump efficiency and 85% motor efficiency. The total parasitic power for the two sub-fields when the radiators are operating is 330 kW. For Daggett (4328 cooling hours), the total parasitic load is 1,428 MWh which is 1.1% of the gross plant energy output over the year. For Tucson (4344 cooling hours), the total parasitic load is 1,434 MWh or 1.2% of gross output. This estimate of pumping power puts the parasitic loads for the radiator system at about 1% compared to the SAM estimates of air-cooled condenser operation which were 4% of annual gross output.

4.3. Water requirement is large but water consumption is zero

The volume of water in the system is 50,000 m^3 . However the combined size of the hot and cold tanks required to operate during the year is about twice that; in the summer most of the water is in the hot tank while in the winter most of the water is in the cold tank. The water volume was varied to determine what the impact of under- or oversizing the system would be. A larger volume of water provides little benefit (0.1% additional annual cooling load can be met with 60,000 m^3 of water). A slightly smaller water volume could be used at little penalty but 20% less annual cooling load would be met if the total water volume were reduced significantly to 30,000 m^3 . The 50,000 m^3 would likely be implemented as a group of smaller tanks. In addition the current model

assumes fully mixed tanks to achieve the coldest temperatures. To reduce the water volume requirement, stratified tanks could be used instead.

The water consumption of a wet-cooled plant is about 3 L per kWh produced (see Section 1). As a point of reference, the reference SAM cycle had a gross output of 122 GWh and net 110 GWh. The water consumption for a wet-cooled plant of this size is about 330 million L or 330,000 m^3 for one year of operation. It would take about 2 months of operation of a wet-cooled plant to use the 50,000 m^3 of water that should serve the cooling purposes of the proposed cooling system for the life of the plant. The volume of water required for cold storage in the proposed system is much less than the volume of water consumed over the life of a wet-cooled power plant.

5. Conclusion

A night sky cooling system which uses radiation and convection heat transfer to cold ambient and yet colder sky temperatures in desert environments can provide over 90% of the cooling required for a CSP power plant. The feasibility of the system is shown using a two-dimensional finite difference heat transfer model of the radiator and considering the sensitivity of the model to the uncertainties in sky temperature, wind convection coefficients, and radiation properties. The detailed radiator model is linked to a generic air-cooled CSP plant and the size of the night sky cooling system is limited to the aperture area of the parabolic trough collectors. The largest uncertainties in the performance of the system are in the effective sky temperature and wind convection coefficients.

Night sky cooling is a promising method for cooling CSP power plants without the consumption of water. Such a cooling system could be used to retrofit an existing wet-cooled plant or in new plant construction. Beyond CSP, the concept could be used to provide auxiliary cooling to any thermal power plant where water use is a concern.

Nomenclature

A_p area of panel, m^2

dx node width in lateral direction, m

dy node with in flow direction, m

ϵ emissivity of top of panel

ϵ_g emissivity of ground

ϵ_p emissivity of back of panel

f_{cloud} cloud cover fraction

h_f internal forced convection coefficient, W/m^2-K

h_{forced} forced convection coefficient from top of panel, W/m^2-K

h_g convection coefficient from back of panel, W/m^2-K

h_w convection coefficient from top of panel, W/m^2-K

k conductivity of radiator panel W/m-K

k_{air} conductivity of air, W/m-K

L_c characteristic length of panel, m

η_{gross} gross efficiency of power plant

$Nu_{free,bottom}$ Nusselt number for free convection from the bottom of the panel

$Nu_{free,top}$ Nusselt number for free convection from the top of the panel

Q_{load} heat rejection load from power plant, MW-hr

$Q_{thermal}$ thermal energy input to power plant, MW-hr

$\dot{q}_{cond,x}$ rate of conduction heat transfer from one node to another in the x-direction, W

$\dot{q}_{cond,y}$ rate of conduction heat transfer from one node to another in the y-direction, W

$\dot{q}_{conv,bot}$ rate of convection heat transfer from the top of the panel to surroundings, W

$\dot{q}_{conv,int}$ rate of internal convection heat transfer from the fluid in tube, W

$\dot{q}_{conv,top}$ rate of convection heat transfer from the top of the panel to surroundings, W

$\dot{q}_{conv,top}$ rate of convection heat transfer from the top of the panel to surroundings, W

$\dot{q}_{conv,tube}$ rate of convection heat transfer from the surface of the tube, W

$\dot{q}_{fluid}$ rate of change of internal energy of the fluid, W

$\dot{q}_{rad,bottom}$ rate of radiation heat transfer from the bottom of the panel to surroundings, W

$\dot{q}_{rad,top}$ rate of radiation heat transfer from the top of the panel to surroundings, W

$\dot{q}_{rad,tube}$ rate of radiation heat transfer from the surface of the tube, W

Ra Rayleigh number

Re Reynolds number

σ Stephan-Boltzmann constant for radiation heat transfer, W/m^2-K^4

T_{db} dry bulb temperature, K

$T_{dp,c}$ dew point temperature, C

$T_{i,j}$ node temperature, K

T_s sky temperature, K

t hours after midnight, hr

u wind speed, m/s

Acknowledgments

The authors are grateful for the advice of S.A. Klein. Funding: This work was supported by The Dow Chemical Company.

REFERENCES

Aubinet, M., 1994. Longwave Sky Radiation Parameterizations. Solar Energy 53 (2), 147–154.

Berdahl, P., Martin, M., 1984. Emissivity of clear skies. Solar Energy 32 (5), 663–664.

Diehl, T., Harris, M., 2014. Withdrawal and Consumption of Water by Thermoelectric Power Plants in the United States , 2010. Tech. rep., US Geological Survey.

Du Marchie Van Voorthuysen, E., Roes, R., 2013. Blue sky cooling for parabolic trough plants. Energy Procedia 49, 71–79.
URL http://dx.doi.org/10.1016/j.egypro.2014.03.008

Duffie, J., Beckman, W., 2013. Solar Engineering of Thermal Processes, 4th Edition. John Wiley & Sons, Inc., Hoboken, New Jersey.

Eicker, U., Dalibard, A., 7 2011. Photovoltaic thermal collectors for night radiative cooling of buildings. Solar Energy 85 (7), 1322–1335.
URL http://www.sciencedirect.com/science/article/pii/S0038092X11000983

Erell, E., Etzion, Y., 5 2000. Radiative cooling of buildings with flat-plate solar collectors. Building and Environment 35 (4), 297–305.
URL http://www.sciencedirect.com/science/article/pii/S0360132399000190

Goswami, J., 2011. Dry Cooling in Solar Thermal Power Plants. In: Proceedings of the ASME 2011 5th International Conference on Energy Sustainability. pp. 1–8.

Hosseinzadeh, E., Taherian, H., 2012. An Experimental and Analytical Study of a Radiative Cooling System with Flat Plate Collectors. International Journal of Green Energy 9 (April), 766–779.

Incropera, F., DeWitt, D., 2002. Fundamentals of Heat and Mass Transfer, 5th Edition. John Wiley & Sons, Inc.

Kaplani, E., Kaplanis, S., 9 2014. Thermal modelling and experimental assessment of the dependence of PV module temperature on wind velocity and direction, module orientation and inclination. Solar Energy 107, 443–460.
URL http://linkinghub.elsevier.com/retrieve/pii/S0038092X14002771

Kumar, S., Mullick, S., 6 2010. Wind heat transfer coefficient in solar collectors in outdoor conditions. Solar Energy 84 (6), 956–963.
URL http://linkinghub.elsevier.com/retrieve/pii/S0038092X10001076

Macknick, J., Newmark, R., Heath, G., Hallett, K. C., 2012. Operational water consumption and withdrawal factors for electricity generating technologies: a review of existing literature. Environmental Research Letters 7 (4), 045802.
URL http://iopscience.iop.org.lib-ezproxy.tamu.edu:2048/1748-9326/7/4/045802/article/

Muñoz, J., Martínez-Val, J., Abbas, R., Abánades, A., 4 2012. Dry cooling with night cool storage to enhance solar power plants performance in extreme conditions areas. Applied Energy 92, 429–436.
URL http://linkinghub.elsevier.com/retrieve/pii/S0306261911007276

Nellis, G., Klein, S., 2009. Heat Transfer. Cambridge University Press.

NREL, 2015. System Advisor Model.
URL https://sam.nrel.gov/

Olwi, I., Sabbagh, J., Khalifa, A., 1 1992. Mathematical modeling of passive dry cooling for power plants in arid land. Solar Energy 48 (5), 279–286.
URL http://www.sciencedirect.com/science/article/pii/0038092X9290055F

Sabbagh, J. A., Khalifa, A. M. A., Olwi, I. A., 1993. Development of passive dry cooling system for power plants in arid land. Solar Energy 51 (6), 431–447.

Sartori, E., 9 2006. Convection coefficient equations for forced air flow over flat surfaces. Solar Energy 80 (9), 1063–1071.
URL http://linkinghub.elsevier.com/retrieve/pii/S0038092X05003701

SolarReserve, 2015. Crescent Dunes.
URL http://www.solarreserve.com/en/global-projects/csp/crescent-dunes

Tevar, J. F., Castaño, S., Marijuán, a. G., Heras, M., Pistono, J., 2015. Modelling and experimental analysis of three radioconvective panels for night cooling. Energy and Buildings 107, 37–48.
URL http://linkinghub.elsevier.com/retrieve/pii/S0378778815301377

Turchi, C., Wagner, M., Kutscher, C., 2010. Water Use in Parabolic Trough Power Plants : Summary Results from WorleyParsons ' Analyses. Contract (December).
URL http://www.solaripedia.com/files/971.pdf

USDOE, 2001. Concentrating Solar Power Commercial Application Study: Reducing Water Consumption of Concentrating Solar Power Electricity Generation Report to Congress. Tech. rep.

USDOE, 2013. SunShot Concentrating Solar Power Program Review 2013. U.S. Department of Energy, Phoenix, AZ.
URL http://www1.eere.energy.gov/solar/pdfs/58484.pdf#page=44

Vidhi, R., 2014. Organic Fluids and Passive Cooling in a Supercritical Rankine Cycle for Power Generation from Low Grade Heat Sources.
URL http://scholarcommons.usf.edu/etd/5322

Wagner, M. J., Gilman, P., 2011. Technical Manual for the SAM Physical Trough Model, NREL/TP-5500-51825. Tech. Rep. June.

Wagner, M. J., Kutscher, C., 2014. The Impact of Hybrid Wet/Dry Cooling on Concentrating Solar Power Plant Performance. In: Proceedings of the ASME 2010 4th International Conference on Energy Sustainability. pp. 1–8.

Wilcox, S., Marion, W., 2008. Users Manual for TMY3 Data Sets NREL/TP-581-43156. Tech. rep., National Renewable Energy Laboratory.

Zeyghami, M., Khalili, F., 2015. Performance improvement of dry cooled advanced concentrating solar power plants using daytime radiative cooling. Energy Conversion and Management 106, 10–20.
URL http://linkinghub.elsevier.com/retrieve/pii/S0196890415008511

Appendix A. Finite difference heat transfer model

This Appendix summarizes the equations for the two dimensional finite difference model used to determine the hourly performance of the radiators. Figure A.12 shows the cross section of a radiator and indicates the reduction of the problem based on symmetry to one single half-tube and fin section. Edge effects are assumed minimal and are not included. Figure A.13 shows a top view of the same section of the radiator. The fin is modeled with nodes indexed by i in the x-direction and j in the y-direction. The fin tip, which is the midpoint between two tubes, is modeled as adiabatic.

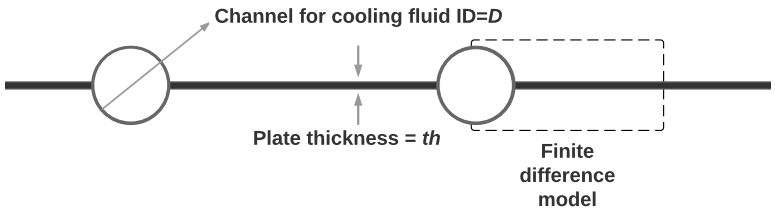

Figure A.12: A cross section of the roll bond radiator panel is shown along with the section which is modeled in the two dimensional finite difference model.

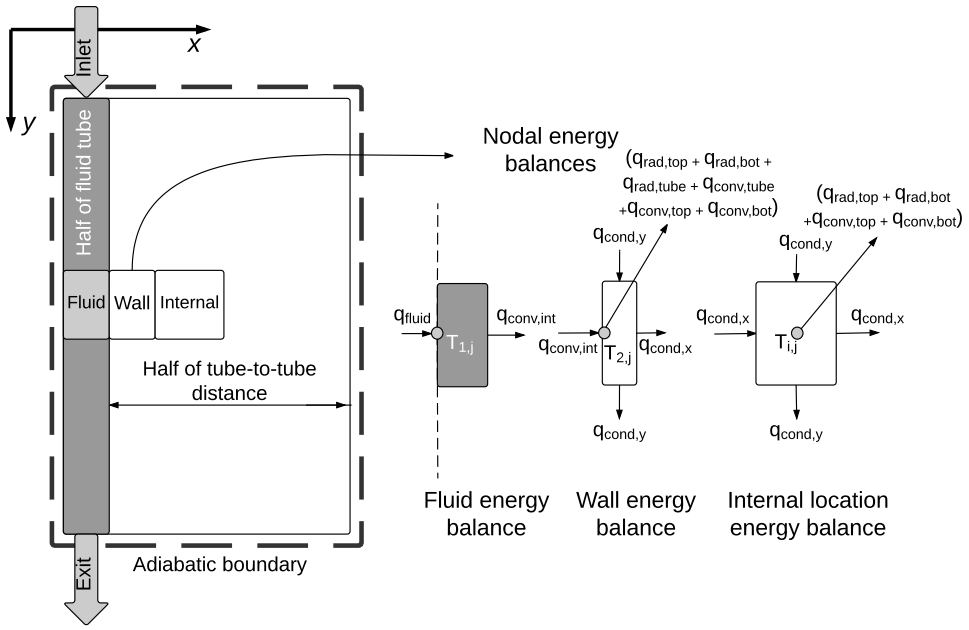

Figure A.13: A top view of one section of the radiator panel shows examples of the energy balances completed depending on node location (insets in the figure).

On any given node at location (i, j) with temperature $T_{i,j}$, radiation and convection heat rates are determined from the node temperature. An energy balance on each control volume using two point finite differences for the temperature gradient is completed. The energy balance for any control volume can include convection to ambient, radiation to sky, conduction between adjacent nodes, and convection from fluid. Figure A.13 shows the three main control volume types and the heat transfer modes included. The distance between nodes in the x-direction is dx (except the distance from the first fluid node to the second wall node, which is exactly a distance of half of the tube diameter). The distance between nodes in the y-direction is dy. A conduction term in the x-direction on an internal control volume is:

$$\dot{q}_{cond,x} = kdyth\frac{1}{dx}\left(T_{i-1,j} - T_{i,j}\right) \tag{A.1}$$

Likewise a conduction term in the y-direction is:

$$\dot{q}_{cond,y} = kdxth\frac{1}{dy}\left(T_{i,j-1} - T_{i,j}\right) \tag{A.2}$$

The radiation heat transfer from the top of the panel on an internal control volume $\dot{q}_{rad,top}$ is determined from:

$$\dot{q}_{rad,top} = \sigma\epsilon(1 - f_{cloud})dxdy\left(T_{i,j}^4 - T_s^4\right) + \sigma\epsilon f_{cloud}dxdy\left(T_{i,j}^4 - T_{db}^4\right) \tag{A.3}$$

The convection heat transfer from the top is:

$$\dot{q}_{conv,top} = h_w dydx\left(T_{i,j} - T_{db}\right) \tag{A.4}$$

Radiation from the bottom of the panel to the ground is based on radiation exchange between two parallel surfaces:

$$\dot{q}_{rad,bot} = \frac{\sigma}{1/\epsilon_p + 1/\epsilon_g - 1} dydx \left(T_{i,j}^4 - T_g^4\right) \tag{A.5}$$

Convection from the bottom of the panel to the air is:

$$\dot{q}_{conv,bot} = h_g dydx \left(T_{i,j} - T_{db}\right) \tag{A.6}$$

At the fluid node, the rate of change in internal energy of the fluid is:

$$\dot{q}_{fluid} = \dot{m} c_p \Delta T \tag{A.7}$$

Internal forced convection in the tube is based on the temperature difference between the fluid ($T_{1,j}$) and tube, which is assumed to be at the temperature of the bordering wall node ($T_{2,j}$). The area for heat transfer is half of the tube circumference times the control volume length dy.

$$\dot{q}_{conv,int} = h_f \frac{\pi D}{2} dy \left(T_{1,j} - T_{2,j}\right) \tag{A.8}$$

Energy balances in two dimensions are completed on each control volume, including convection, conduction, and radiation terms as appropriate depending on location. These energy balances are shown in Figure A.13 for the fluid control volume, wall control volume, and generic internal control volume. Note that at the wall node, the energy balance includes convection and radiation from the projected half surface of the tube (radius), since this area is also exposed to the same ambient conditions and the tube is assumed to be at the same temperature as the wall node. The special radiation and convection terms for the tube surface (top and bottom together) are:

$$\begin{aligned}\dot{q}_{rad,tube} = \sigma\epsilon(1 - f_{cloud}) \frac{D}{2} dy \left(T_{i,j}^4 - T_s^4\right) + \sigma\epsilon f_{cloud} \frac{D}{2} dy \left(T_{i,j}^4 - T_{db}^4\right) \\ + \frac{\sigma}{1/\epsilon_p + 1/\epsilon_g - 1} \frac{D}{2} dy \left(T_{i,j}^4 - T_g^4\right)\end{aligned} \tag{A.9}$$

$$\dot{q}_{conv,tube} = h_w \frac{D}{2} dy \left(T_{i,j} - T_{db}\right) + h_g \frac{D}{2} dy \left(T_{i,j} - T_{db}\right) \tag{A.10}$$

In addition the control volume at the wall and is half the size of the internal control volumes so that the node is located exactly at the tube edge. The control volume at the edge of the fin (rightmost) is also half the size of the internal control volumes. To reflect this, in the energy balances at these locations the area $dxth$ in the y-direction conduction terms (Equation A.2) is replaced by $\frac{dx}{2}th$. In Equations A.3, A.4, A.5, A.6, the surface area $dxdy$ is replaced by $\frac{dx}{2}dy$.

Nodes at the mid-point between tubes (adiabatic fin tip) or at the beginning or ending radiator surfaces are considered adiabatic and so conduction terms are zero as appropriate on the boundaries. On the right side, the conduction term $\dot{q}_{cond,x}$ is zero exiting the node towards the right. On the top, the conduction term $\dot{q}_{cond,y}$ is zero entering the node. On the bottom, the conduction term $\dot{q}_{cond,y}$ is zero exiting the node.

C APPENDIX: RADIATOR MODELING PAPER

The technical brief paper regarding radiator modeling published in ASME Journal of Solar Engineering is attached.

Modeling Radiative-convective Panels for Nighttime Passive Cooling Applications

Ana R. Dyreson
Solar Energy Laboratory
Department of Mechanical Engineering
University of Wisconsin - Madison
1337 Engineering Research Building
1500 Engineering Drive
Madison, WI 53706-1687
Email: adyreson@wisc.edu

S.A. Klein
Solar Energy Laboratory
Department of Mechanical Engineering
University of Wisconsin - Madison
1343 Engineering Research Building
1500 Engineering Drive
Madison, WI 53706-1687
Email: saklein@wisc.edu

Franklin K. Miller
Solar Energy Laboratory
Department of Mechanical Engineering
University of Wisconsin - Madison
1341 Engineering Research Building
1500 Engineering Drive
Madison, WI 53706-1687
Email: fkmiller@wisc.edu

ABSTRACT

Passive cooling by combined radiation-convection from black panels at night is a potential source of significant energy-efficient cooling for both homes and industry. Assessing the technology requires system models that connect cooling load, passive cooling technology performance, and changing weather conditions in annual simulations. In this paper the performance an existing analytical model for a passive cooling panel is validated using a full two dimensional finite differences model. The analytical model is based on a solar hot water collector model but uses the concept of adiabatic surface temperature to create an intuitive, physically meaningful sink temperature for combined convection and radiation cooling. Simulation results are reported for cooling panels of different sizes and operating in both low temperature (comfort cooling) and high temperature (power plant) applications. The analytical model using adiabatic minimum temperature agrees with the high-fidelity finite differences model but is more practical to implement. This model and the validations are useful for the continued study of passive cooling technology, in particular as it is integrated into system-level models of higher complexity.

1 Introduction

Passive radiation cooling can help meet the worldwide need for energy efficient cooling for both buildings and industry. In the United States, air conditioning accounts for about 13% of home electricity use and nearly 90% of homes are now air conditioned [1]. Around the world, access to energy as well as the increase in extreme temperatures are driving the adoption of air conditioning [2]. Cooling is also important for industry and power plants - thermoelectric generators require fan or pump-driven cooling systems and their operation reduces annual energy output by several percent [3]. In addition to the energy cost of power plant cooling systems, many systems are driven by evaporative cooling towers and so are also large consumers of water. This paper focuses on the modeling of a simple method of passive cooling that uses uncovered, non-selective panels to cool water overnight. Such cooling systems can help meet air conditioning and industrial cooling demands.

Heat transfer from uncovered black panels is a combination of radiation to the night sky and convection to the ambient air. The radiation is readily determined given the effective sky temperature (T_s), which is the effective black body temperature of the atmosphere determined from measurements of the sky radiance using a pyrgeometer. Convection depends on the ambient dry bulb and convection coefficients over the flat surface. In desert environments at night, the atmosphere is dry and the air far above the ground is cold. This results in an effective sky temperature that can be significantly lower than the ambient temperature, often 20°C lower at night, which drives the radiation cooling effect. Non-selective surfaces, the focus of this work, provide cooling only at night. During the day, the sun warms the exposed surface, requiring an initial cool down period at night. Work on solar hot water collectors has shown that the heat capacity of the collector structure, which is similar to a radiative-convective panel structure, is small and energy wasted during start-up periods is small [4].

Many researchers have recognized radiative-convective cooling's potential in desert environments that have high cooling loads and relatively cold night temperatures, but it is not widely used [5]. As summarized by Eicker and Dalibard [6], radiation cooling for air conditioning of buildings has been proposed using open tanks, dedicated thermal panels, and photovoltaic-thermal (PVT) panels. (PVT panels are typically used to cool PV panels and to collect thermal energy during the day, but as a passive cooling panel they can be used at night to cool water.) Radiative cooling has also been proposed by several authors for power plant cooling using selective surfaces, non-selective surfaces, and ponds, as reviewed by Dyreson and Miller [7]. Dyreson and Miller presented a radiative cooling system for a concentrating solar power plant that used cooling water circulating through black surfaces exposed to the night sky. The radiative panels proposed are similar to those of the systems used for building cooling, being uncovered, non-selective surfaces.

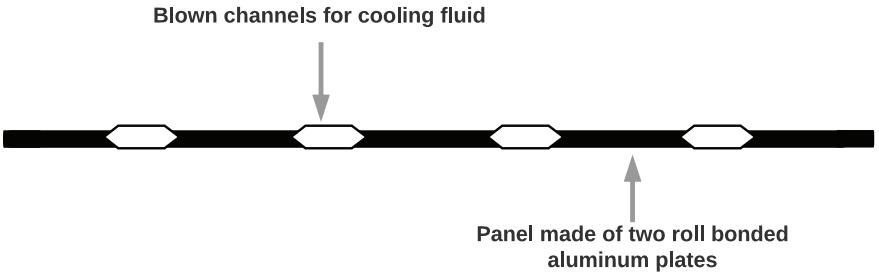

Fig. 1: The cross section of an example radiative-convective panel using a roll bond type construction where plates are bonded together. The panel is painted black for maximum emissivity and is uncovered to allow convection cooling.

Radiative-convective cooling panels typically consist of flat plates made of high conductivity, high emissivity material thermally connected to tubes for circulation of cooling fluid (i.e. Figure 1 and Figure 2). Many papers have formulated the heat transfer problems using the approach described in Duffie and Beckman for solar hot water collectors which are physically similar, except having one or more convective covers. The following works cited use this approach in some form: Erell and Etzion propose flat plate solar collectors to provide nighttime cooling for a building [8] . They highlight several differences between a solar collector and a flat plate radiator including that convection effects can work to the advantage of the radiator instead of being considered a loss mechanism so a transparent cover is not needed. Also, the heat flux is for a cooling panel significantly less than for a hot water collector and so the ideal solar collector geometry is not the ideal radiator geometry. Farmahini Farahani et al. model cooling panels made of uncovered flat-plate radiators with copper tubes for use in a multi-stage cooling system for buildings [9] . Eicker and Dalibard use a PVT panel with the cover removed to provide nighttime cooling [6] . Al-Zubaydi et al. model and test nighttime radiator performance including a radiator made of an aluminum panel with grooved channels for water circulation [10]. Hosseinzadeh and Taherian use similar

radiative-convective panels with the copper tubes painted white [11] . Most recently, Tevar et al. consider three different 'radio-convective' panels designed for use in building cooling [12] . The three uncovered panels tested were 1) a panel with complex geometry and high emissivity 2) a selective surface plate and 3) a white metallic panel.

Ito and Miura utilize an alternative formulation of the solar collector model [13]. They studied radiative cooling from uncovered commercial solar collectors made of two steel plates. This model was based on a different thermal sink temperature, referred to as the adiabatic minimum temperature, in place of the ambient temperature. The adiabatic minimum temperature is the surface temperature at which the net radiative and convective heat transfer is zero; it is a temperature below ambient where convection provides some heating and radiation provides some cooling. This formulation is used for radiative air coolers by [14] as well as [15], but otherwise is not widely adopted.

This paper compares two analytical models for uncovered radiative-convective cooling panels with a numerical model. The three models are tested for both high temperature and low temperature cooling applications in the desert. The models apply to uncovered, high conductivity, high emissivity plates with single flow circulating fluid and can be extended to include other plate geometries (see [4] or [16] for other geometries). Based on the results herein, the analytical model based on the classic solar collector model by Duffie & Beckman [4] as modified by Ito & Miura [13] is recommended. It is more accurate than the classic formulation of the analytical model for a variety of designs and operating conditions. In addition, it is more computationally efficient than a finite differences model. Passive cooling for both homes and industry continues to see attention in the literature due to its energy and, in the case of power plant cooling, water saving potential. The results presented here and the provided heat transfer code are useful for modelers investigating potential for passive cooling systems for both comfort cooling and industrial applications.

2 Basic analytical formulation

The first of three models in this paper is an analytical model closely based on the solar model from Duffie & Beckman [4] as detailed by Eicker and Dalibard [6] for radiative-convective cooling panels. One notable difference, discussed further in Section 3.3, is that the reference temperature here is the effective sky temperature T_s instead of ambient. The general equation for useful heat loss rate is written in terms of the temperature difference $(T_p - T_s)$.

$$Q_u = A_c U_{L,s} (T_p - T_s) \tag{1}$$

Where T_p is the representative temperature of the plate, $U_{L,s}$ is the overall loss coefficient, and A_c is the area of the collector surface.

Figure 2 shows a cross section of a radiative-convective panel that is uncovered and uninsulated and example temperature profiles along the lateral (x) and flow (y) directions. Tubes in the panel circulate the cooling fluid. The geometry of the collector is described by the number of tubes in parallel in one collector n, the center-to-center distance between tubes W, the tube diameter D, the length of the plate L, and the thickness of the absorber plate th. The area of the collector surface is $A_c = nWL$.

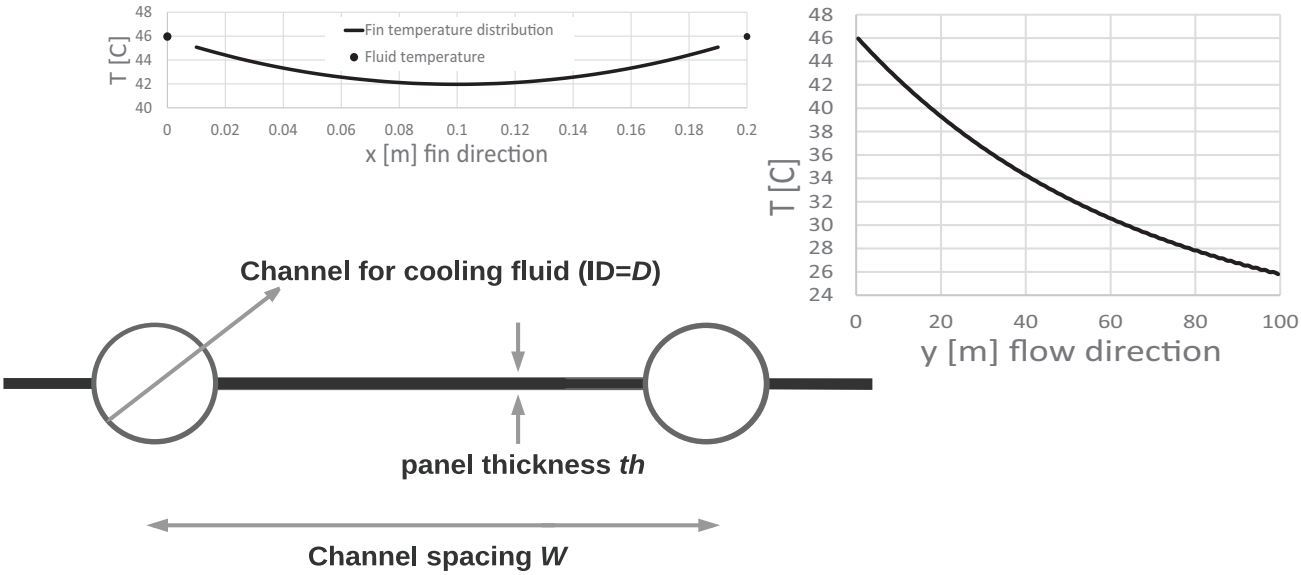

Fig. 2: A cross section of a radiative-convective panel (bottom left). The temperature is lowest in the midpoint between tubes (top left). The temperature of the fluid in the tubes decreases along the panel length (right).

Radiative and convective heat transfer coefficients are defined relative to the difference between the plate temperature and the effective sky temperature. The radiation heat transfer from the top of the collector to the effective night sky T_s is determined by radiation transfer between a small convex object (plate) and a large enclosure (sky). Only the emissivity (ε) of the small surface, in this case the panel, is relevant; the large enclosure acts as a blackbody. Dividing the heat flux rate by $(T_p - T_s)$ to reference the plate-sky temperature difference, the radiation coefficient relative to the sky temperature is:

$$h_{r,t} = \sigma \cdot \varepsilon \cdot \frac{T_p^4 - T_s^4}{T_p - T_s} = \sigma \cdot \varepsilon \cdot (T_p^2 + T_s^2)(T_p + T_s) \tag{2}$$

The Stephan-Boltzmann constant is σ. Other formulations linearize the heat transfer coefficient as described in [4], but the formulation in Equation 2 is simply an algebraic operation and does not make any approximations to linearize radiation heat transfer. Assuming that the radiator surface is exposed to the ground on the back side, the radiation heat transfer from the bottom of the plate to the ground temperature (T_g) is based on radiation exchange between two flat infinite plates. The panel back has emissivity ε_b and the ground has emissivity ε_g. The heat transfer coefficient relative to the sky temperature is:

$$h_{r,b} = \sigma \cdot \frac{1}{\frac{1}{\varepsilon_b} + \frac{1}{\varepsilon_g} - 1} \cdot \frac{T_p^4 - T_g^4}{T_p - T_s} \tag{3}$$

The convection coefficients from the top ($h_{c,t}$ to ambient air) and bottom ($h_{c,b}$ to ground) are determined from convection correlations for a given condition per standard methods. Depending on the conditions the convection may be forced or free (natural). The coefficients are normalized to the plate-sky temperature difference:

$$h_{c,t,s} = h_{c,t} \frac{T_p - T_a}{T_p - T_s} \tag{4}$$

$$h_{c,b,s} = h_{c,b} \frac{T_p - T_g}{T_p - T_s} \tag{5}$$

Radiation and convection act in parallel for heat transfer from the top of the panel and bottom of the panel. With these four resistances acting in parallel relative to the temperature difference ($T_p - T_s$), the overall loss coefficient ($U_{L,s}$) is a sum of the four individual coefficients.

$$U_{L,s} = h_{r,t} + h_{c,t,s} + h_{r,b} + h_{c,b,s} \tag{6}$$

A fin analysis is used to model the temperature variation between tubes. The collector efficiency (F') combines the traditional fin efficiency (F) with the resistance of the tube wall and internal flow resistance to represent the lateral direction temperature variation in the x-direction as in Figure 2 (inset). The reader is referred to Duffie and Beckman for F and F'.

Next the temperature distribution in the flow direction (y-direction) is examined. The fluid outlet temperature ($T_{f,o}$) at $y = L$ is then written (using $A_c = nWL$) :

$$T_{f,o} - T_s = (T_{f,i} - T_s) exp(-\frac{A_c F' U_{L,s}}{\dot{m} c_p}) \tag{7}$$

Where the inlet temperature is $T_{f,i}$, the mass flow rate is $\dot{m}$, and the specific heat capacity of the fluid is c_p. As noted in [4], this distribution of temperatures assumes that the fin efficiency and loss coefficient are constant over the flow direction of the plate. The collector heat removal factor (F_R) is defined to account for the flow direction temperature variation in the y-direction as in Figure 2 (inset). F_R is the ratio of the useful heat rejection to the useful heat rejection that would take place if the whole collector were at temperature $T_{f,i}$ and the loss coefficient was unchanged.

$$F_R = \frac{\dot{m} c_p (T_{f,i} - T_{f,o})}{A_c U_{L,s} (T_{f,i} - T_s)} \tag{8}$$

For reference a heat exchanger effectiveness can also be defined for the panel. The effectiveness relative to the sink temperature (here T_s) and relationship to F_R is:

$$\varepsilon_{HX} = \frac{Q}{Q_{max}} = \frac{T_{f,i} - T_{f,o}}{T_{f,i} - T_s} = F_R \frac{A_c U_{L,s}}{\dot{m} c_p} \tag{9}$$

Equations 8 and 7 can be used to eliminate $T_{f,o}$ and $T_{f,i}$ and finally write the heat removal factor as:

$$F_R = \frac{\dot{m} c_p}{A_c U_{L,s}} (1 - exp(-\frac{A_c U_{L,s} F'}{\dot{m} c_p})) \tag{10}$$

The total heat rejection is then written in terms of F_R, A_c, $U_{L,s}$, T_s and the inlet fluid temperature $T_{f,i}$:

$$Q_u = F_R A_c U_{L,s} (T_{f,i} - T_s) \tag{11}$$

Finally the outlet temperature is determined from the total heat rejection:

$$Q_u = \dot{m} c_p (T_{f,i} - T_{f,o}) \tag{12}$$

The collector operation is thus parameterized so that given inlet temperature, mass flow rate, geometry, and ambient conditions, the total heat rejection can be determined. An iterative solution method is required because of the dependence of $U_{L,s}$ on the plate mean temperature. Equations 1, 10, 11, and 12 are solve iteratively along with the formulations for $U_{L,s}$, F, and F', appropriate for given geometry and wind conditions.

In order to most accurately evaluate fluid properties in the tubes, a mean fluid temperature is calculated by Duffie

& Beckman. In this paper the mean fluid temperature is estimated by the inlet fluid temperature because fluid property differences along the tube are not critical for the problem.

3 Analytical formulation using adiabatic reference temperature

In this section the adiabatic temperature is defined and used as a reference temperature in a reformulated solar collector model. The issue of reference temperature choice and implications for modeling is discussed.

3.1 Adiabatic temperature concept

Ito and Miura [13] present an adiabatic minimum temperature that provides realistic sink temperature reflecting the strength of radiation and convection heat transfer to the ambient. The adiabatic temperature is the surface temperature at which there is zero net heat transfer. For a plate being cooled, the adiabatic temperature provides a lower bound for the desirable outlet temperature; if the outlet temperature is less than the adiabatic minimum, the plate begins to approach the adiabatic adiabatic state.

To derive the adiabatic temperature, the total heat transfer is written using expanded and linearized radiation terms. Radiation heat transfer is linearized using the average of the plate and ambient temperatures ($\bar{T}_{p,a}$) (as in [17] and other texts). The radiation from the top of the panel to the sky is expanded and linearized:

$$Q_{r,t} = \sigma\varepsilon\left(T_p^4 - T_s^4\right) = \sigma\varepsilon\left(T_p^4 - T_a^4\right) + \sigma\varepsilon\left(T_a^4 - T_s^4\right) = \sigma\varepsilon(T_a^4 - T_s^4) + \sigma\varepsilon 4\bar{T}_{p,a}^3(T_p - T_a) \tag{13}$$

The radiation to the ground is treated similarly. Summing the radiation and convection to the top and bottom and collecting terms in $(T_p - T_a)$, the heat transfer rate is:

$$\begin{aligned} Q = A_c\sigma\varepsilon(T_a^4 - T_s^4) + A_c\sigma\frac{1}{\frac{1}{\varepsilon_b}+\frac{1}{\varepsilon_g}-1}(T_a^4 - T_g^4) + h_{c,b}A_c(T_a - T_g) + \\ A_c\left(4\sigma\varepsilon\bar{T}_{p,a}^3 + 4\sigma\frac{1}{\frac{1}{\varepsilon_b}+\frac{1}{\varepsilon_g}-1}\bar{T}_{p,a}^3 + h_{c,b} + h_{c,t}\right)(T_p - T_a) \end{aligned} \tag{14}$$

When the plate temperature equals the adiabatic temperature (T_{ad}), the total rate of heat transfer Q is zero. These substitutions ($Q = 0$ and $T_p = T_{ad}$) are made in Equation 14. Because the radiation terms have been linearized for $(T_p - T_a)$, it is simple to then solve for the adiabatic temperature, except that the average of the adiabatic and ambient ($\bar{T}_{ad,a}$) remains. For the case of an uninsulated, uncovered panel, the adiabatic temperature is given by Equation 15:

$$T_{ad} = T_a - \frac{\sigma\varepsilon(T_a^4 - T_s^4) + \sigma\frac{1}{\frac{1}{\varepsilon_b}+\frac{1}{\varepsilon_g}-1}(T_a^4 - T_g^4) + h_{c,b}(T_a - T_g)}{4\sigma\left(\varepsilon + \frac{1}{\frac{1}{\varepsilon_b}+\frac{1}{\varepsilon_g}-1}\right)\bar{T}_{ad,a}^3 + h_{c,b} + h_{c,t}} \tag{15}$$

Note that this equation is implicit in adiabatic temperature because the radiation heat transfer rate depends on the surface temperature. Given ambient conditions and convection coefficients, one can solve iteratively for the adiabatic minimum temperature. Free convection coefficients do depend on the plate temperature, but since free convection is typically small compared to forced and to the radiation heat transfer, approximations for plate temperature are acceptable.

The adiabatic temperature provides a physically meaningful temperature on which to base the analytical solution; it is always less than the ambient dry bulb temperature and greater than the sky temperature. The adiabatic temperature is closer to the air temperature for higher wind speeds and it approaches the sky temperature when the wind is calm.

3.2 Adiabatic reference temperature model

An analytical formulation based on that of Ito and Miura is presented. In the current formulation, the adiabatic temperature is replaced with the plate temperature in Equation 15 (in the term $\bar{T}_{ad,a}$) . This substitution allows for implementation of the solar model without making the approximation that $\bar{T}_{ad,a} = T_a$, as Ito and Miura originally did. (The approximation

is not good when the adiabatic temperature is far from the ambient, which occurs when the radiation heat transfer is strong compared to convection.) With this substitution, the approximate adiabatic minimum temperature (T^*) is:

$$T^* = T_a - \frac{\sigma\varepsilon(T_a^4 - T_s^4) + \sigma\frac{1}{\frac{1}{\varepsilon_b}+\frac{1}{\varepsilon_g}-1}(T_a^4 - T_g^4) + h_{c,b}(T_a - T_g)}{4\sigma\left(\varepsilon + \frac{1}{\frac{1}{\varepsilon_b}+\frac{1}{\varepsilon_g}-1}\right)\bar{T}_{p,a}^3 + h_{c,b} + h_{c,t}} \tag{16}$$

The overall heat transfer coefficient using the adiabatic minimum as the reference temperature is defined as:

$$U_L^* = 4\sigma\left(\varepsilon + \frac{1}{\frac{1}{\varepsilon_b}+\frac{1}{\varepsilon_g}-1}\right)\bar{T}_{p,a}^3 + h_{c,b} + h_{c,t} \tag{17}$$

The analytical model in Section 2 is applied to account for flow-direction and fin-direction temperature profiles using temperature difference $(T_p - T^*)$ instead of $(T_p - T_s)$. The fin efficiency, collector efficiency, and heat removal factor are defined with T_s replaced with T^* and U_L is replaced with U_L^* as appropriate. Substituting the overall heat loss coefficient Equation 17 and adiabatic temperature Equation 15 into Equation 1, the resulting heat transfer is indeed equivalent to Equation 14, the heat flux from a surface at temperature T_p.

The model is implemented by first estimating the plate temperature with the inlet fluid temperature in Equations 16 and 17. Implementation of the collector model then gives an estimate of the plate temperature. Iterations are repeated until the plate temperature converges (two iterations were sufficient here).

3.3 Importance of thermal sink reference temperature choice

The analytical model allows for both radiation heat transfer (to the effective sky temperature) and convection heat transfer (to the ambient air temperature) in a single loss coefficient by normalizing both the radiation and convection heat transfer coefficients to a single reference temperature. In Duffie & Beckman [4], the reference temperature is the ambient T_a and the heat transfer coefficients are referenced to the plate-ambient temperature difference. Sections 2 and 3.2 show that the analytical model can also be formulated using the effective sky temperature or the adiabatic minimum temperature. When applying the collector model for cooling applications, the choice of reference temperature becomes an important consideration. (This is not an issue for solar hot water collectors where losses are small compared to gains in the heat transfer.)

For a given choice of reference temperature, there is a related loss coefficient (U_L, U_L^*, or $U_{L,s}$, for ambient, adiabatic, or sky temperature references, respectively). Under some conditions the loss coefficient can be negative. Table 1 summarizes how the sign of the loss coefficient for each model depends on the plate temperature with reference to the ambient, adiabatic and sky temperatures. A model based on the adiabatic temperature has a positive loss coefficient U_L^* in any condition, while using the other two reference temperatures can at times result in a negative loss coefficient. Computationally, it is more difficult to find the solution to a problem where the loss coefficient may be either positive or negative. The effective sky temperature reference model has a positive loss coefficient in any cooling condition. The ambient air temperature reference has a negative loss coefficient during some net cooling conditions, so it is not implemented in the solar collector model in this paper.

Table 1: Depending on the plate temperature's value compared to the ambient and adiabatic temperatures, the loss coefficient can be negative. Here ambient (T_a and U_L), sky (T_s and $U_{L,s}$), and adiabatic minimum (T^* and U_L^*) are shown. The loss coefficient will be positive regardless of the choice of reference temperature when both radiation and convection are cooling the surface. When there is convective heating combined with radiative cooling, the loss coefficient can be negative.

	$T_s < T^* < T_a < \mathbf{T_p}$	$T_s < T^* < \mathbf{T_p} < \mathbf{T_a}$	$T_s < \mathbf{T_p} < \mathbf{T}^* < \mathbf{T_a}$
	Cooling by convection & radiation	Net cooling; convection heating + radiation cooling	Net heating; convection heating + radiation cooling
$Q_u = A_c U_L (T_p - T_a)$	$0 < U_L$	$U_L < 0$	$0 < U_L$
$Q_u = A_c U_{L,s} (T_p - T_s)$	$0 < U_{L,s}$		$U_{L,s} < 0$
$Q_u = A_c U_L^* (T_p - T^*)$	$0 < U_L^*$		

The solar collector model has been implemented for radiative-convective cooling applications in different ways in the literature. For example [6] and [9] use the ambient temperature while [13] use the adiabatic temperature. When applying a model, it is important to understand how radiation is accounted for and what thermal sink temperature has been defined.

4 Finite difference model

A two dimensional finite difference model of the radiative-convective panel solves the combined heat transfer problem numerically. This model is implemented here for validation of the analytical models because, with an adequately discretized grid, there are no assumptions made about the temperature distribution as is required in the analytical model (see Section 2). Thus this model is the accurate baseline against which the others are compared. The model is described in [7]. In that paper, a cloudiness factor f_{cloud} quantified the fraction of the sky covered by clouds. For the purpose of the model validation here, it was assumed that skies were clear (cloudiness fraction equal to zero). Because the numerical model accuracy depends on the number of nodes used to model the panel, first a test is completed to determine what node density would be accurate enough for a range of radiator sizes and designs. The panel geometries, flow rates tested are shown in Table 2 and represent a range of designs from large installations to small, roof-mounted cooling systems.

Table 2: Geometry and wind speed conditions tested along with fin efficiency for designs # 1 to 17. (F, F_R, and ε_{HX} are calculated using adiabatic temperature as reference temperature.)

		1	2	3	4	5	6	7	8	9	10	11	12	13	14	15	16	17
L	m	100	200	200	200	200	2	5	5	5	100	200	200	200	2	5	5	5
W	m	0.2	0.2	0.2	0.1	0.2	0.1	0.2	0.2	0.2	0.2	0.2	0.2	0.2	0.1	0.2	0.2	0.2
th	mm	2	2	2	0.2	2	2	2	2	2	0.2	0.2	0.2	0.2	0.2	0.2	0.2	0.2
$\dot{m}$	kg/s	2.25	2.25	4.5	4.5	1	0.03	0.01	0.03	0.03	2.25	2.25	4.5	1	0.03	0.01	0.03	0.03
D	cm	2	2	2	2	2	1.59	1.59	1.59	1.59	2	2	2	2	1.59	1.59	1.59	1.59
u	m/s	3.1	3.1	3.1	3.1	3.1	1.5	1.5	1.5	6	3.1	3.1	3.1	3.1	1.5	1.5	1.5	6
n	-	50	50	50	50	50	12	12	12	12	50	50	50	50	12	12	12	12
F_R	-	0.47	0.29	0.47	0.60	0.13	0.73	0.24	0.46	0.29	0.38	0.26	0.38	0.13	0.66	0.22	0.37	0.23
F	-	0.92	0.92	0.92	0.84	0.92	0.98	0.93	0.93	0.86	0.57	0.57	0.57	0.57	0.84	0.59	0.59	0.44
ε_{HX}	-	0.77	0.95	0.78	0.54	0.99	0.21	0.93	0.59	0.74	0.62	0.86	0.63	0.97	0.19	0.86	0.48	0.60

Table 3 documents the ambient conditions, materials, and convection assumptions that are used to demonstrate the

radiator models in this section. These ambient conditions are typical of those in the analysis of [7] in the desert region of Daggett, California, USA.

Table 3: Conditions and assumptions made for comparison of radiator models

	Symbol	Value for model testing
Ambient dry bulb temperature [K]	T_a	299.3
Effective sky temperature [K]	T_s	280.9
Wind direction	-	Across width W
Inlet water temperature [K]	T_{in}	319.3
Plate emissivity, top	ε	0.95
Plate emissivity, bottom	ε_b	0.07
Ground emissivity	ε_g	0.9
Convection coefficient, top [W/m^2-K]	$h_{c,t}$	Correlation for turbulent flow per [18]
Convection coefficient, bottom [W/m^2-K]	$h_{c,b}$	Correlation for heated plate
Conductivity of plate [W/m-K]	–	235

Each of the 17 designs are modeled with different node layouts from two to 20 in the fin direction (x) and five to 200 in the flow direction (y). The percent error is calculated for each design and node layout relative to the highest density grid (x=20, y=200) model.

The density of the baseline model (20 nodes in fin direction and 200 in flow direction) was selected because the heat transfer from a radiator converged within $\pm 0.2\%$ at or below this density for all designs; in other words this was more nodes than necessary. The error in the varying node layouts for the 17 different designs was examined and a model with ten nodes in the fin direction and 20 in the flow direction was within 0.2% error for all of the designs. The 10 x 20 node model was chosen as the minimum grid density for the numerical model.

5 Results

This section compares the analytical model using sky temperature reference and the analytical model using adiabatic temperature reference to the finite differences model. To illustrate the use of these models under a range of operating conditions and panel designs, the results are illustrated in three ways: 1) for a low-temperature cooling application for building comfort cooling over the course of one night, 2) for a high temperature operating condition with different panel designs, fluid flow rates, and wind speeds, and 3) for a high temperature application under practical annual operating conditions.

5.1 Low temperature application

Erell and Etzion [8] tested radiator designs for nighttime comfort cooling in Israel. In this section their radiator dimensions and test conditions are used to test the heat transfer model of the radiator in a typical low-temperature application representative of comfort cooling for buildings. Erell and Etzion used a commercial solar collector with the convection cover removed. The key dimensions are provided in Table 4. The panel is assumed to be perfectly insulated so that no heat transfers from the back; initial testing with variable insulation thicknesses showed that this assumption was reasonable. The average heat transfer coefficient was determined from the turbulent Sartori correlation [18]. Because the panel is relatively square and the wind speed is low, the impact of the wind direction on characteristic length and associated heat transfer coefficient impact were not important in the overall performance. The numerical model was implemented using 30 elements in the flow direction and 30 elements in the fin direction. The strength of free convection from the top of the panel was considered but in all cases was small relative to forced convection. The internal convection coefficient within the riser tubes was determined from standard correlations and was laminar.

Table 4: Physical characteristics of Lordan LSC-F described by [8]

Construction	Metal 'leaves' attached to tubes
Materials	Copper tubes, stainless steel absorber plate
Size	2.18 m x 1.27 m (2.77 m^2)
Number of tubes n	12
Tube length L	2.0
Tube diameter D	1.59 cm (5/8 inch)
Tube spacing W	10 cm
Bottom insulation	25 mm polyurethane foam with reflective aluminum foil
Wind speed u	1.5 m/s
Top emissivity ε	0.85
Total mass flow rate $\dot{m}$	0.032 kg/s
Thickness of 'leaves' th	0.5 mm

The percent difference in heat transfer for the analytical models compared to the numerical models was always $\pm$ 2.0%. (They also compared reasonably well to the experimental measurements of Erell and Etzion but given the inherent uncertainty in the convection coefficients ($\pm$20%), a direct comparison of measurements and model is not helpful for validation of the models). Since the three models agree well, the choice of model is not important in this case. But this represents a limited range of operating conditions and only tests one specific panel design. The following sections consider more general cases and higher temperature applications.

5.2 Different radiator designs operating in high temperature application

Using a set of different radiator designs that represent a range of panel efficiencies within the plausible realm, a set of basic assumptions were employed for comparing the models under a high temperature application. The radiator designs and conditions used are from Tables 2 and 3.

The results of the model comparisons (analytical vs numerical) are shown in Figure 3. The mean percent error from the analytical model referencing the adiabatic temperature to the numerical model using 20 nodes in the flow direction and 10 in the fin direction is -0.2% (minimum -0.5%, maximum 0.2%); these two models agree. The analytical model referencing the sky temperature has error up to 20%.

Figure 4 shows that the error in the sky temperature model is related to the collector heat removal factor F_R .

Percent error is correlated to F_R because the analytical model assumes that the fin efficiency and collector efficiency are constant over the panel's flow direction as its temperature decreases. In fact the fin efficiency varies over the flow direction and as the temperature drop of the panel increases (decreasing F_R and increasing ε_{HX}), the impact of this assumption is more significant. This error can be avoided by stringing multiple smaller models in series or by using the adiabatic temperature reference. In the analytical model referencing the adiabatic temperature, the overall loss coefficient, and therefore fin efficiency and collector efficiency, are only weakly dependent on the plate temperature (via the natural convection coefficient and linearized radiation coefficient).

5.3 Annual simulations of one radiator operating in high temperature application

Because different operating conditions exist with varying inlet temperature and ambient conditions, annual simulations are completed to observe the full range of conditions. The annual simulation is for the high temperature application of heat rejection for a concentrating solar power plant. Using the heat rejection requirements and condensing temperatures from an air-cooled concentrating solar power plant, the stored cold water from the radiator system is used in a condenser to reject heat. The system design and calculations are documented in Dyreson and Miller. First, the system (solar collectors, power block, condenser, and cold storage) is modeled along with the finite differences model of the radiator. To determine the differences between the numerical and the two analytical models, the radiator operation is then isolated from the cold storage by taking the radiator inlet temperatures from the system simulation as fixed. The hourly annual inlet temperatures to the radiator were inputs to the analytical models under the concurrent ambient conditions (the actual effects of returning water temperature on cold storage are not fed back into the analytical models).

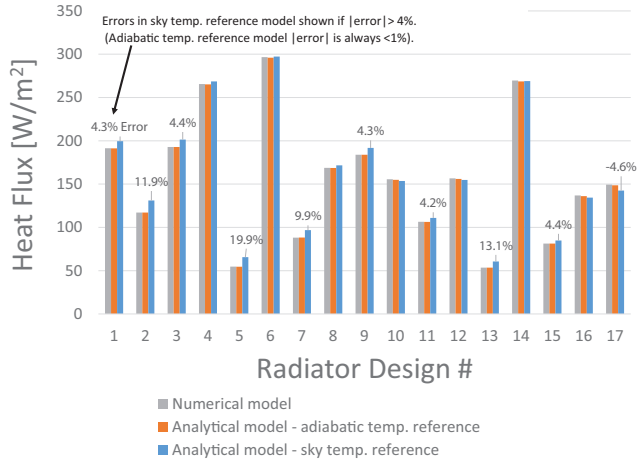

Fig. 3: For 17 different radiator designs, the flux at typical conditions is calculated using three different models. The numerical model is always within $\pm$ 1% of the analytical model using the adiabatic temperature reference, while the sky temperature model can be off by as much as 20% depending on the geometry of the panel.

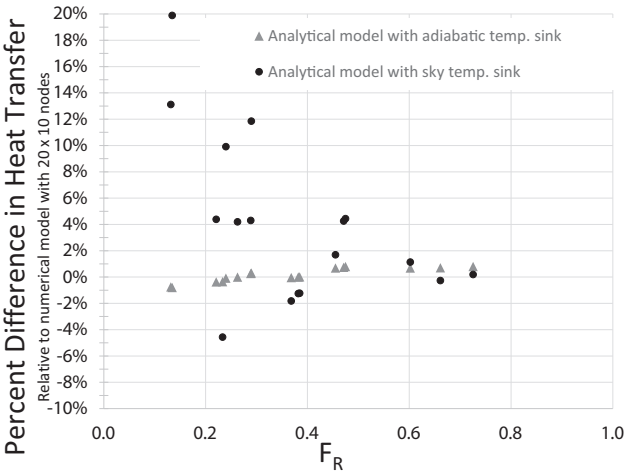

Fig. 4: For 17 different radiator designs, the error in the heat transfer compared to the numerical model is plotted against the ratio F_R.

As described in Dyreson and Miller, there are 50 channels with D= 2 cm, th=2 mm, and W=0.1 m to give a 5 m wide panel. The length in this case is 200 m (actually split into multiple sections but because the axial conduction is not significant, can be modeled as one continuous length). The mass flow rate is 4.5 kg/sec, divided evenly between the 50 channels.

The annual results echo those of Section 5.2: the numerical and adiabatic temperature analytical models agree well. The sky temperature analytical model varies with F_R (Figure 5). Again when the F_R is low (reflecting large temperature drop over the radiator), the sky temperature analytical model error is high.

6 Conclusion

Radiative-convective cooling is a promising passive cooling technology, especially in desert environments. It can be used for both building cooling and industrial uses such as power plant cooling. Modeling the passive cooling technology is a fundamental part of the larger models integrating system components, but there is not agreement on proper methods. This paper documents an alternative version of the original Duffie and Beckman analytical solar collector model adapted for cooling applications, first suggested by Ito and Miura in 1989, for modeling uncovered, non-selective passive cooling panels. A numerical model has been used for comparison and shows excellent agreement with the adiabatic reference temperature analytical model. Because the Ito and Miura model offers computational speed, accuracy, and stability, it is recommended for radiative-convective cooling from uncovered black surfaces. A program to implement adiabatic analytical model is available (see [19]).

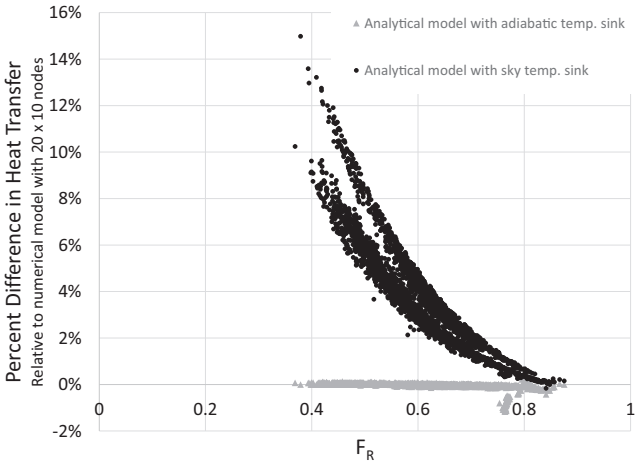

Fig. 5: The three different models were tested for a one radiator design in an hourly annual simulation. Treating the numerical model as the baseline, the analytical model using the adiabatic temperature reference is always within $\pm$ 0.2% except when wind speed is zero and the differences in free convection models result in differences of about 1%. The percent error in the analytical model with reference to the sky temperature is up to 15%. Note that there are two operation conditions for the radiator system (taking inlet water from cold storage or warmer storage), making the error vs. F_R plot appear separated into two regions.

Acknowledgments

Funding: This work was supported by The Dow Chemical Company.

References

[1] U.S. Energy Information Administration, 2009. Residential Energy Consumption Survey. Tech. rep.

[2] Davis, L. W., and Gertler, P. J., 2015. "Contribution of air conditioning adoption to future energy use under global warming.". *Proceedings of the National Academy of Sciences of the United States of America,* **112**(19), 5, pp. 5962–7.

[3] EPRI, 2004. Comparison of Alternate Cooling Technologies for U.S. Power Plants 1005358. Tech. rep.

[4] Duffie, J., and Beckman, W., 2013. *Solar Engineering of Thermal Processes*, fourth ed. John Wiley & Sons, Inc., Hoboken, New Jersey.

[5] Cook, J., ed., 1989. *Passive Cooling*. The MIT Press.

[6] Eicker, U., and Dalibard, A., 2011. "Photovoltaic thermal collectors for night radiative cooling of buildings". *Solar Energy,* **85**(7), 7, pp. 1322–1335.

[7] Dyreson, A., and Miller, F., 2016. "Night sky cooling for concentrating solar power plants". *Applied Energy,* **180**, pp. 276–286.

[8] Erell, E., and Etzion, Y., 2000. "Radiative cooling of buildings with flat-plate solar collectors". *Building and Environment,* **35**(4), 5, pp. 297–305.

[9] Farmahini Farahani, M., Heidarinejad, G., and Delfani, S., 2010. "A two-stage system of nocturnal radiative and indirect evaporative cooling for conditions in Tehran". *Energy and Buildings,* **42**(11), 11, pp. 2131–2138.

[10] Al-Zubaydi, A. Y. T., Dartnall, J., and Dowd, A., 2012. "Design, Construction and Calibration of an Instrument for Measuring the production of Chilled Water by the Combined Effects of Evaporation and Night Sky Radiation". In Proceedings of the ASME International Mechanical Engineering Congress and Exposition, pp. 1523–1532.

[11] Hosseinzadeh, E., and Taherian, H., 2012. "An Experimental and Analytical Study of a Radiative Cooling System with Flat Plate Collectors". *International Journal of Green Energy,* **9**(April), pp. 766–779.

[12] Tevar, J. F., Castaño, S., Marijuán, a. G., Heras, M., and Pistono, J., 2015. "Modelling and experimental analysis of three radioconvective panels for night cooling". *Energy and Buildings,* **107**, pp. 37–48.

[13] Ito, S., and Miura, N., 1989. "Studies of Radiative Cooling Systems for Storing Thermal Energy". *ASME Journal of Solar Energy Engineering,* **111**(3), pp. 251–256.

[14] Argiriou, A., Santamouris, M., and Assimakopoulos, D. N., 1994. "Assessment of the radiative cooling potential of a collector using hourly weather data". *Energy,* **19**(8), pp. 879–888.

[15] Bagiorgas, H. S., and Mihalakakou, G., 2008. "Experimental and theoretical investigation of a nocturnal radiator for space cooling". *Renewable Energy,* **33**(6), pp. 1220–1227.

[16] Bliss, R. W., 1959. "The derivations of several Plate-efficiency factors useful in the design of flat-plate solar heat collectors". *Solar Energy,* **3**(4), 12, pp. 55–64.

[17] Nellis, G., and Klein, S., 2009. *Heat Transfer*. Cambridge University Press.

[18] Sartori, E., 2006. "Convection coefficient equations for forced air flow over flat surfaces". *Solar Energy,* **80**(9), 9, pp. 1063–1071.

[19] University of Wisconsin - Madison, 2017. Solar Energy Lab website: sel.me.wisc.edu.

List of Tables

1 Depending on the plate temperature's value compared to the ambient and adiabatic temperatures, the loss coefficient can be negative. Here ambient (T_a and U_L), sky (T_s and $U_{L,s}$), and adiabatic minimum (T^* and U_L^*) are shown. The loss coefficient will be positive regardless of the choice of reference temperature when both radiation and convection are cooling the surface. When there is convective heating combined with radiative cooling, the loss coefficient can be negative. 8

2 Geometry and wind speed conditions tested along with fin efficiency for designs # 1 to 17. (F, F_R, and ε_{HX} are calculated using adiabatic temperature as reference temperature.) 8

3 Conditions and assumptions made for comparison of radiator models 9

4 Physical characteristics of Lordan LSC-F described by [8] 10

List of Figures

1 The cross section of an example radiative-convective panel using a roll bond type construction where plates are bonded together. The panel is painted black for maximum emissivity and is uncovered to allow convection cooling. 2

2 A cross section of a radiative-convective panel (bottom left). The temperature is lowest in the midpoint between tubes (top left). The temperature of the fluid in the tubes decreases along the panel length (right). . 4
3 For 17 different radiator designs, the flux at typical conditions is calculated using three different models. The numerical model is always within ± 1% of the analytical model using the adiabatic temperature reference, while the sky temperature model can be off by as much as 20% depending on the geometry of the panel. . 11
4 For 17 different radiator designs, the error in the heat transfer compared to the numerical model is plotted against the ratio F_R. 11
5 The three different models were tested for a one radiator design in an hourly annual simulation. Treating the numerical model as the baseline, the analytical model using the adiabatic temperature reference is always within ± 0.2% except when wind speed is zero and the differences in free convection models result in differences of about 1%. The percent error in the analytical model with reference to the sky temperature is up to 15%. Note that there are two operation conditions for the radiator system (taking inlet water from cold storage or warmer storage), making the error vs. F_R plot appear separated into two regions. 12

BIBLIOGRAPHY

J. Andrepont. Personal Communication, 2016.

M. Aubinet. Longwave Sky Radiation Parameterizations. *Solar Energy*, 53(2):147–154, 1994.

A. Balogh and Z. Szabo. HELLER System : The Economical Substitute for Wet Cooling. In *EPRI Workshop on Advanced Thermal Electric Power Cooling Technologies*, pages 1–45, Charlotte, NC, 2008.

R. Bartlett. *Steam Turbine Performance and Economics*. McGraw-Hill Book Company, Inc., 1958.

P. Berdahl and M. Martin. Emissivity of clear skies. *Solar Energy*, 32(5):663–664, 1984.

P. Berdahl, M. Martin, and F. Sakkal. Thermal performance of radiative cooling panels. *International Journal of Heat and Mass Transfer*, 26(6):871–880, jun 1983. ISSN 00179310. doi: 10.1016/S0017-9310(83)80111-2. URL `http://linkinghub.elsevier.com/retrieve/pii/S0017931083801112`.

X. Berger, D. Buriot, and F. Garnier. About the equivalent radiative temperature for clear skies. *Solar Energy*, 32(6):725–733, 1984. ISSN 0038092X. doi: 10.1016/0038-092X(84)90247-0.

R. W. Bliss. The Derivations of Several Plate-Efficiency Factors Useful in the Design of Flat-Plate Solar Heat Collectors. *Solar Energy*, 3(4):55–64, dec 1959. ISSN 0038092X. doi: 10.1016/0038-092X(59)90006-4. URL `http://linkinghub.elsevier.com/retrieve/pii/0038092X59900064`.

N. Bracken, J. Macknick, A. Tovar-hastings, P. Komor, M. Gerritsen, and S. Mehta. Concentrating Solar Power and Water Issues in the U.S. Southwest, NREL/TP-6A50-61376. Technical Report March, NREL, 2015.

J. J. Burkhardt, G. a. Heath, and C. S. Turchi. Life cycle assessment of a parabolic trough concentrating solar power plant and the impacts of key design alternatives. *Environmental science & technology*, 45(6):2457–2464, 2011. ISSN 1520-5851. doi: 10.1021/es1033266.

L. Camargo, M. Gitsham, and B. R. Baliga. Measurements of mean heat transfer coefficients for turbulent forced convection in a rectangular duct with uniformly spaced plate inserts. In *Proceedings of the 2009 ASME Summer Heat Transfer Conference*, San Francisco, CA, 2009. ASME.

N. T. Carter and R. J. Campbell. Water issues of concentrating solar power (CSP) electricity in the U.S. Southwest. Technical report, Congressional Research Service, 2009.

S. Catalanotti, V. Cuomo, G. Piro, D. Ruggi, V. Silvestrini, and G. Troise. The radiative cooling of selective surfaces. *Solar Energy*, 17(2):83–89, may 1975. ISSN 0038092X. doi: 10.1016/0038-092X(75)90062-6. URL http://www.sciencedirect.com/science/article/pii/0038092X75900626.

V. Cheang, R. Hedderwick, and C. McGregor. Benchmarking supercritical carbon dioxide cycles against steam Rankine cycles for Concentrated Solar Power. *Solar Energy*, 113:199–211, mar 2015. ISSN 0038092X. doi: 10.1016/j.solener.2014.12.016. URL http://www.sciencedirect.com/science/article/pii/S0038092X14006070.

ChemWorld. ChemWorld, 2018. URL https://www.chemworld.com/Inhibited-Propylene-Glycol-p/glacier-275.htm.

A. Colmenar-Santos, D. Borge-Diez, C. P. Molina, and M. Castro-Gil. Water consumption in solar parabolic trough plants: Review and analysis of the southern Spain case. *Renewable and Sustainable Energy Reviews*, 34:565–577, 2014. ISSN 13640321. doi: 10.1016/j.rser.2014.03.042. URL http://dx.doi.org/10.1016/j.rser.2014.03.042.

T. M. Conboy, M. D. Carlson, and G. E. Rochau. Dry-Cooled Supercritical CO 2 Power for Advanced Nuclear Reactors. *Volume 3B: Oil and Gas Applications; Organic Rankine Cycle Power Systems; Supercritical CO2 Power Cycles; Wind Energy*, 3B(1):V03BT36A001, 2014. ISSN 0742-4795. doi: 10.1115/GT2014-25079. URL http://www.scopus.com/inward/record.url?eid=2-s2.0-84922362200{&}partnerID=tZOtx3y1.

P. Cooper, E. Christie, and R. Dunkle. A method of measuring sky temperature. *Solar Energy*, 26(2):153–159, 1981. ISSN 0038092X. doi: 10.1016/0038-092X(81)90079-7. URL http://www.sciencedirect.com/science/article/pii/0038092X81900797.

K. Cotton. *Evaluating and Improving Steam Turbine Performance*. Cotton Fact, Inc., Rexford, New York, second edition, 1998.

N. Cur and E. Sparrow. Experiments on heat transfer and pressure drop for a pair of colinear, interrupted plates aligned with the flow. *International Journal of Heat and Mass Transfer*, 21:1069–1080, 1978.

N. Cur and E. Sparrow. Measurements of Developing and Fully Developed Heat Transfer Coefficients along a Periodically Interrupted Surface. *Journal of Heat Transfer*, 101(May 1979):211–216, 1979.

K. Damerau, K. Williges, A. G. Patt, and P. Gauché. Costs of reducing water use of concentrating solar power to sustainable levels: Scenarios for North Africa. *Energy Policy*, 39(7):4391–4398, 2011. ISSN 03014215. doi: 10.1016/j.enpol.2011.04.059.

T. Diehl and M. Harris. Withdrawal and Consumption of Water by Thermoelectric Power Plants in the United States , 2010. Technical report, US Geological Survey, 2014.

A. Dobos, T. Neises, and M. Wagner. Advances in CSP simulation technology in the System Advisor Model. *Energy Procedia*, 49:2482–2489, 2013. ISSN 18766102. doi: 10.1016/j.egypro.2014.03.263. URL http://dx.doi.org/10.1016/j.egypro.2014.03.263.

A. W. Dowling, A. Dyreson, F. Miller, and V. M. Zavala. Economic Assessment and Optimal Operation of CSP Plants with TES in California Electricity Market. In *SolarPACES 2016*, Abu Dhabi, United Arab Emirates, 2016.

A. W. Dowling, T. Zheng, and V. M. Zavala. Economic assessment of concentrated solar power technologies: A review. *Renewable and Sustainable Energy Reviews*, 72 (January):1019–1032, 2017. ISSN 18790690. doi: 10.1016/j.rser.2017.01.006. URL http://dx.doi.org/10.1016/j.rser.2017.01.006.

E. Du Marchie Van Voorthuysen and R. Roes. Blue sky cooling for parabolic trough plants. *Energy Procedia*, 49:71–79, 2013. ISSN 18766102. doi: 10.1016/j.egypro.2014.03.008. URL http://dx.doi.org/10.1016/j.egypro.2014.03.008.

J. Duffie and W. Beckman. *Solar Engineering of Thermal Processes*. John Wiley & Sons, Inc., Hoboken, New Jersey, fourth edition, 2013.

J. Dyreby, S. Klein, G. Nellis, and D. Reindl. Design Considerations for Supercritical Carbon Dioxide Brayton Cycles With Recompression. *Journal of Engineering for Gas Turbines and Power*, 136(10):101701, 2014. ISSN 0742-4795. doi: 10.1115/1.4027936. URL http://gasturbinespower.asmedigitalcollection.asme.org/article.aspx?doi=10.1115/1.4027936.

J. J. Dyreby. *Modeling the Supercritical Carbon Dioxide Brayton Cycle with Recompression*. Phd, University of Wisconsin - Madison, 2014.

A. Dyreson and F. Miller. Night sky cooling for concentrating solar power plants. *Applied Energy*, 180:276–286, 2016. ISSN 03062619. doi: 10.1016/j.apenergy.2016.07.118.

F. Dyreson, Ana, Klein, S.A., Miller. Modeling Radiative-convective Cooling Panels for Nighttime Passive Cooling Applications. *ASME Journal of Solar Energy Engineering*, 2017.

U. Eicker and A. Dalibard. Photovoltaic thermal collectors for night radiative cooling of buildings. *Solar Energy*, 85(7):1322–1335, jul 2011. ISSN 0038092X. doi:

10.1016/j.solener.2011.03.015. URL http://www.sciencedirect.com/science/article/pii/S0038092X11000983.

M. El-Wakil. *Powerplant Technology*. McGraw-Hill, Inc., 1984.

EPRI. Spray Cooling Enhancement of Air-Cooling Condensers. Technical report, EPRI, 2003. URL http://www.epri.com/abstracts/Pages/ProductAbstract.aspx?ProductId=000000000001005360.

EPRI. Comparison of Alternate Cooling Technologies for U.S. Power Plants 1005358. Technical report, EPRI, 2004.

E. Erell and Y. Etzion. Radiative Cooling of Buildings with Flat-Plate Solar Collectors. *Building and Environment*, 35(4):297–305, may 2000. ISSN 03601323. doi: 10.1016/S0360-1323(99)00019-0. URL http://www.sciencedirect.com/science/article/pii/S0360132399000190.

M. Farmahini Farahani, G. Heidarinejad, and S. Delfani. A two-stage system of nocturnal radiative and indirect evaporative cooling for conditions in Tehran. *Energy and Buildings*, 42(11):2131–2138, nov 2010. ISSN 03787788. doi: 10.1016/j.enbuild.2010.07.003. URL http://www.sciencedirect.com/science/article/pii/S0378778810002197.

Fraunhofer. Development of a Bionic Solar Collector with Aluminum Roll-bond Absorber. Technical report, Fraunhofer Institute for Solar Energy Systems, Freiburg, Germany, 2011. URL www.bionicol.eu.

R. Fu, D. Feldman, R. Margolis, M. Woodhouse, K. Ardani, R. Fu, D. Feldman, R. Margolis, M. Woodhouse, and K. Ardani. U . S . Solar Photovoltaic System Cost Benchmark : Q1 2017 NREL/TP-6A20-68925. Technical Report September, NREL, 2017.

GE. GateCycle.

O. Gliah, B. Kruczek, S. G. Etemad, and J. Thibault. The effective sky temperature: An enigmatic concept. *Heat and Mass Transfer/Waerme- und Stoffuebertragung*, 47 (9):1171–1180, 2011. ISSN 09477411. doi: 10.1007/s00231-011-0780-1.

R. Goldstein. A survey of water use and sustainability in the United States with a Focus on Power Generation 1005474. Technical report, Electric Power Research Institute (EPRI), 2003. URL `http://www.epri.com/abstracts/Pages/ProductAbstract.aspx?ProductId=000000000001005474`.

J. Goswami. Dry Cooling in Solar Thermal Power Plants. In *Proceedings of the ASME 2011 5th International Conference on Energy Sustainability*, pages 1–8, 2011.

H. Schlichting. *Boundary Layer Theory*. McGraw-Hill, Inc., seventh edition, 1979.

Heat Exchange Institute. Standards for Steam Surface Condensers, 1995.

G. Hewitt, editor. *Heat Exchanger Handbook Part 2: Fundamentals of Heat and Mass Transfer*. Begell House, Inc., 2008.

C. K. Ho. Computational fluid dynamics for concentrating solar power systems. *Wiley Interdisciplinary Reviews: Energy and Environment*, 3:290–300, 2014. ISSN 20418396. doi: 10.1002/wene.90.

E. Hosseinzadeh and H. Taherian. An Experimental and Analytical Study of a Radiative Cooling System with Flat Plate Collectors. *International Journal of Green Energy*, 9(April):766–779, 2012.

P. J. Hruska, G. F. Nellis, and S. A. Klein. Methodology of Modeling and Comparing the Use of Direct Air-Cooling for a Supercritical Carbon Dioxide Brayton Cycle and a Steam Rankine Cycle. *The 5th International Symposium - Supercritical CO2 Power Cycles*, 1:1–18, 2016.

F. Incropera and D. DeWitt. *Fundamentals of Heat and Mass Transfer*. John Wiley & Sons, Inc., fifth edition, 2002.

S. Ito and N. Miura. Studies of Radiative Cooling Systems for Storing Thermal Energy. *ASME Journal of Solar Energy Engineering*, 111(3):251–256, 1989. ISSN 01996231. doi: 10.1115/1.3268315. URL http://solarenergyengineering.asmedigitalcollection.asme.org/article.aspx?articleid=1454914.

C. M. Jubayer, K. Siddiqui, and H. Hangan. CFD analysis of convective heat transfer from ground mounted solar panels. *Solar Energy*, 133:556–566, 2016. ISSN 0038092X. doi: 10.1016/j.solener.2016.04.027. URL http://dx.doi.org/10.1016/j.solener.2016.04.027.

E. Kaplani and S. Kaplanis. Thermal modelling and experimental assessment of the dependence of PV module temperature on wind velocity and direction, module orientation and inclination. *Solar Energy*, 107:443–460, sep 2014. ISSN 0038092X. doi: 10.1016/j.solener.2014.05.037. URL http://linkinghub.elsevier.com/retrieve/pii/S0038092X14002771.

B. Kelly. Nexant Parabolic Trough Solar Power Plant Systems Analysis Task 2 : Comparison of Wet and Dry Rankine Cycle Heat Rejection, NREL/SR-550-40163. Technical Report July, 2006.

A. A. Kendoush. Theoretical analysis of heat and mass transfer to fluids flowing across a flat plate. *International Journal of Thermal Sciences*, 48(1):188–194, jan 2009. ISSN 12900729. doi: 10.1016/j.ijthermalsci.2008.03.010. URL http://linkinghub.elsevier.com/retrieve/pii/S1290072908000719.

B. Kimball. Cooling performance and efficiency of night sky radiators. *Solar Energy*, 34(1):19–33, 1985. ISSN 0038092X. doi: 10.1016/0038-092X(85)90089-1.

R. J. Kind, D. H. Gladstone, and A. D. Moizer. Corrective Heat Losses From Flat-Plate Solar Collectors in Turbulent. *Journal of Solar Energy Engineering*, 105(1):7–12, 1983.

Kipp&Zonen. CGR 4 Pyrgeometer Instruction manual, 2014.

S. Klein. Engineering Equation Solver (EES), 2016. URL www.fchart.com.

P. Kurup and C. S. Turchi. Parabolic Trough Collector Cost Update for the System Advisor Model (SAM). Technical Report November, 2015. URL http://www.nrel.gov/docs/fy16osti/65228.pdf.

J. Macknick, R. Newmark, G. Heath, and K. C. Hallett. Operational water consumption and withdrawal factors for electricity generating technologies: a review of existing literature. *Environmental Research Letters*, 7(4):045802, 2012. ISSN 1748-9326. doi: 10.1088/1748-9326/7/4/045802. URL http://iopscience.iop.org.lib-ezproxy.tamu.edu:2048/1748-9326/7/4/045802/article/.

J. Manwell, J. McGowan, and A. Rogers. *Wind Energy Explained*. John Wiley & Sons, Inc., 2nd edition, 2009.

M. Martin and P. Berdahl. Characteristics of infrared sky radiation in the United States. *Solar Energy*, 33(3-4):321–336, 1984. ISSN 0038092X. doi: 10.1016/0038-092X(84)90162-2.

M. Maupin, J. Kenny, S. Hutson, J. Lovelace, N. Barber, and K. Linsey. Estimated Use of Water in the United States in 2010. Technical report, US Geological Survey, 2010.

S. J. McColl, P. Rodgers, and V. Eveloy. Thermal management of solar photovoltaics modules for enhanced power generation. *Renewable Energy*, 82:14–20, 2015. ISSN 18790682. doi: 10.1016/j.renene.2014.09.015. URL http://dx.doi.org/10.1016/j.renene.2014.09.015.

M. Mehos, C. Turchi, J. Vidal, M. Wagner, Z. Ma, C. Ho, W. Kolb, C. Andraka, and A. Kruizenga. Concentrating Solar Power Gen3 Demonstration Roadmap NREL/TP-5500-67464. Technical Report January, NREL, Golden, CO, 2017.

M. Moser, F. Trieb, T. Fichter, J. Kern, H. Maier, and P. Schicktanz. Techno-economic analysis of enhanced dry cooling for CSP. *Energy Procedia*, 49(0):1177–1186, 2013. ISSN 18766102. doi: 10.1016/j.egypro.2014.03.127. URL http://dx.doi.org/10.1016/j.egypro.2014.03.127.

J. Muñoz, J. Martínez-Val, R. Abbas, and A. Abánades. Dry cooling with night cool storage to enhance solar power plants performance in extreme conditions areas. *Applied Energy*, 92:429–436, apr 2012. ISSN 03062619. doi: 10.1016/j.apenergy.2011.11.030. URL http://linkinghub.elsevier.com/retrieve/pii/S0306261911007276.

T. W. Neises. *Development and Validation of a Model to Predict the Temperature of a Photovoltaic Cell*. Master's thesis, University of Wisconsin - Madison, 2011.

G. Nellis and S. Klein. *Heat Transfer*. Cambridge University Press, 2009.

NREL. System Advisor Model. URL https://sam.nrel.gov/.

I. Olwi, J. Sabbagh, and A. Khalifa. Mathematical modeling of passive dry cooling for power plants in arid land. *Solar Energy*, 48(5):279–286, jan 1992. ISSN 0038092X. doi: 10.1016/0038-092X(92)90055-F. URL http://www.sciencedirect.com/science/article/pii/0038092X9290055F.

J. Palyvos. A survey of wind convection coefficient correlations for building envelope energy systems' modeling. *Applied Thermal Engineering2*, 28:801–808, 2008.

A. Patnode. *Simulation and performance evaluation of parabolic trough solar power plants*. Master's thesis, University of Wisconsin - Madison, 2006. URL http://www.minds.wisconsin.edu/handle/1793/7590.

J. A. Peterka, N. Hosoya, B. Bienkiewicz, and J. E. Cermak. Wind load reduction for heliostats SERI/STR-253-2859. Technical report, Solar Energy Research Institute, 1986.

A. Poullikkas, G. Kourtis, and I. Hadjipaschalis. An overview of CSP cooling systems. In *3rd International Conference on Renewable Energy Sources and Energy Efficiency*, number May, Nicosia, Cyprus, 2011. ISBN 9789963567027.

H. Price, D. Kearney, F. Redell, R. Charles, and F. Morse. Dispatchable Solar Power Plant. In *SolarPACES 2017*, Santiago, Chile, 2017.

J. A. Sabbagh, A. M. A. Khalifa, and I. A. Olwi. Development of passive dry cooling system for power plants in arid land. *Solar Energy*, 51(6):431–447, 1993.

E. Sartori. Convection coefficient equations for forced air flow over flat surfaces. *Solar Energy*, 80(9):1063–1071, sep 2006. ISSN 0038092X. doi: 10.1016/j.solener.2005.11.001. URL http://linkinghub.elsevier.com/retrieve/pii/S0038092X05003701.

E. Sartori. Comments on 'A thermal model for PV panels under varying atmospheric conditions', by S. Armstrong and W.G. Hurley, Applied Thermal Engineering 30 (2010), feb 2011. ISSN 13594311. URL http://www.sciencedirect.com/science/article/pii/S1359431110003261.

S. Sharples and P. Charlesworth. Full-scale measurements of wind-induced convective heat transfer from a roof-mounted flat plate solar collector. *Solar Energy*, 62 (2):69–77, 1998.

J. Shinners. *Analysis of Dual Loop Parabolic Trough Concentrating Solar Power Plants*. Master's thesis, University of Wisconsin - Madison, 2014.

SimTech. IPSEpro-PSE, 2017. URL www.SimTechnology.com.

J. Sment and C. K. Ho. Wind patterns over a heliostat field. *Energy Procedia*, 49: 229–238, 2013. ISSN 18766102. doi: 10.1016/j.egypro.2014.03.025.

C. G. Smith, Geoffrey B., Granqvist. *Green Nanotechnology : Solutions for Sustainability and Energy in the Built Environment*. Taylor and Francis Group, LLC, 2011.

SolarReserve. Crescent Dunes, 2015. URL http://www.solarreserve.com/en/global-projects/csp/crescent-dunes.

R. C. Spencer, K. C. Cotton, and C. N. Cannon. A Method for Predicting Performance of Steam Turbine Generators 16,500 kW and Larger Revised. Technical report, General Electric Company, 1974.

A. Stodola and L. Loewenstein. *Steam and Gas Turbines*. McGraw-Hill Book Company, Inc., New York, vol. 1 edition, 1945.

B. N. Taylor and C. E. Kuyatt. Guidelines for Evaluating and Expressing the Uncertainty of NIST Measurement Results. *Technology*, (1297):2, 1994.

F. Test, R. C. Lessmann, and A. Johary. Heat Transfer During Wind Flow ower Rectangular Bodies in the Natural Environment. *Transactions of the ASME*, 103 (May 1981):262–267, 1981.

J. F. Tevar, S. Castaño, a. G. Marijuán, M. Heras, and J. Pistono. Modelling and experimental analysis of three radioconvective panels for night cooling. *Energy and Buildings*, 107:37–48, 2015. ISSN 03787788. doi: 10.1016/j.enbuild.2015.07.027. URL http://linkinghub.elsevier.com/retrieve/pii/S0378778815301377.

C. Turchi, M. Wagner, and C. Kutscher. Water Use in Parabolic Trough Power Plants : Summary Results from WorleyParsons ' Analyses. *Contract*, (December), 2010. URL http://www.solaripedia.com/files/971.pdf.

C. S. Turchi and G. A. Heath. Molten Salt Power Tower Cost Model for the System Advisor Model (SAM) NREL/TP-5500-57625. Technical Report February, NREL, 2013.

USDOE. Concentrating Solar Power Commercial Application Study: Reducing Water Consumption of Concentrating Solar Power Electricity Generation Report to Congress. Technical report, 2001.

USDOE. SunShot Vision Study. Technical Report February, USDOE, 2012.

USDOE. SunShot Concentrating Solar Power Program Review 2013. Phoenix, AZ, 2013. U.S. Department of Energy. URL http://www1.eere.energy.gov/solar/pdfs/58484.pdf{#}page=44.

R. Vidhi. *Organic Fluids and Passive Cooling in a Supercritical Rankine Cycle for Power Generation from Low Grade Heat Sources*. PhD thesis, University of South Florida, 2014. URL http://scholarcommons.usf.edu/etd/5322.

M. J. Wagner. *Simulation and Predictive Performance Modeling of Utility-Scale Central Receiver System Power Plants*. Master's thesis, University of Wisconsin - Madison, 2008. URL http://sel.me.wisc.edu/publications/theses/wagner08.zip.

M. J. Wagner and P. Gilman. Technical Manual for the SAM Physical Trough Model, NREL/TP-5500-51825. Technical Report June, 2011.

M. J. Wagner and C. Kutscher. The Impact of Hybrid Wet/Dry Cooling on Concentrating Solar Power Plant Performance. In *ASME 2010 4th International Conference on Energy Sustainability, Volume 2*, volume v 2, pages 675–682. ASME, 2010. ISBN 978-0-7918-4395-6. doi: 10.1115/ES2010-90442. URL http://proceedings.asmedigitalcollection.asme.org/proceeding.aspx?articleid=1607643.

M. J. Wagner, A. M. Newman, W. T. Hamilton, and R. J. Braun. Optimized dispatch in a first-principles concentrating solar power production model. *Applied Energy*, 203:959–971, 2017. ISSN 03062619. doi: 10.1016/j.apenergy.2017.06.072. URL http://dx.doi.org/10.1016/j.apenergy.2017.06.072.

WorleyParsons. Analysis of Wet, Dry, and Parallel Condensing Parabolic Trough Power Plants with Fixed Solar Heat Input, NREL-2-ME-REP-0003 Rev 0. Technical report, 2009a.

WorleyParsons. Analysis of Wet and Dry Condensing 125 MW Parabolic Trough Power Plants NREL-2-ME-REP-0002 Rev 0. Technical report, 2009b.

WorleyParsons. Analysis of Wet, Dry, and Parallel Condensing Parabolic Trough Power Plants with Fixed Solar Heat input San Luis Valley, Colorado Site, NREL-2-ME-REP-0004 Rev 1. Technical report, 2010.

Z. Wu, B. Gong, Z. Wang, Z. Li, and C. Zang. An experimental and numerical study of the gap effect on wind load on heliostat. *Renewable Energy*, 35(4):797–806, 2010. ISSN 09601481. doi: 10.1016/j.renene.2009.09.009. URL http://dx.doi.org/10.1016/j.renene.2009.09.009.

E. Yildiz. Draft for an Appendix D - Power Block to the SolarPACES Guideline for Bankable STE Yield Assessment. Technical report, 2017.

M. Zeyghami and F. Khalili. Performance improvement of dry cooled advanced concentrating solar power plants using daytime radiative cooling. *Energy Conversion and Management*, 106:10–20, 2015. ISSN 01968904. doi: 10.1016/j.enconman.2015.09.016. URL http://linkinghub.elsevier.com/retrieve/pii/S0196890415008511.

H. Zhang, J. Baeyens, J. Degrève, and G. Cacères. Concentrated solar power plants: Review and design methodology. *Renewable and Sustainable Energy Reviews*, 22:466–481, jun 2013. ISSN 13640321. doi: 10.1016/j.rser.2013.01.032. URL http://linkinghub.elsevier.com/retrieve/pii/S1364032113000634.